2809077409

REFERENCE ONLY

UNIVERSITY OF LONDON THESIS

Degree PhD Year 2006 Name of Author WOLFF Angela Jean

COPYRIGHT

This is a thesis accepted for a Higher Degree of the University of London. It is an unpublished typescript and the copyright is held by the author. All persons consulting the thesis must read and abide by the Copyright Declaration below.

COPYRIGHT DECLARATION

I recognise that the copyright of the above-described thesis rests with the author and that no quotation from it or information derived from it may be published without the prior written consent of the author.

LOAN

Theses may not be lent to individuals, but the University Library may lend a copy to approved libraries within the United Kingdom, for consultation solely on the premises of those libraries. Application should be made to: The Theses Section, University of London Library, Senate House, Malet Street, London WC1E 7HU.

REPRODUCTION

University of London theses may not be reproduced without explicit written permission from the University of London Library. Enquiries should be addressed to the Theses Section of the Library. Regulations concerning reproduction vary according to the date of acceptance of the thesis and are listed below as guidelines.

A. Before 1962. Permission granted only upon the prior written consent of the author. (The University Library will provide addresses where possible).

B. 1962 - 1974. In many cases the author has agreed to permit copying upon completion of a Copyright Declaration.

C. 1975 - 1988. Most theses may be copied upon completion of a Copyright Declaration.

D. 1989 onwards. Most theses may be copied.

This thesis comes within category D.

☐ This copy has been deposited in the Library of UCL

☐ This copy has been deposited in the University of London Library, Senate House, Malet Street, London WC1E 7HU.

www.blissetts.com

Adsorption and Desorption of Mixed Molecular Ices from a Cosmic Dust Grain Analogue Surface

Angela Jean Wolff

Thesis for the degree of Doctor of Philosophy

UCL

2006

ProQuest LLC
789 East Eisenhower Parkway
P.O. Box 1346
Ann Arbor, MI 48106-1346

Abstract

Surface science is playing an ever more prominent role in the field of astronomy. More than 220 different molecules have so far been observed in the interstellar medium (ISM), and for several of these molecules, the observed abundance is such that the molecules cannot be formed by gas phase reactions alone. Astronomers have proposed that they are instead formed by heterogeneous reactions that take place on the surface of dust grains.

The two alcohols methanol and ethanol are just two of the molecules typically observed in both the gas and solid phase in the ISM. In the solid phase, they are found frozen out with the more abundant water, as molecular ices on the surface of dust grains. Both alcohols can be viewed as evolutionary indicators in the vicinity of hot cores. Hot cores are compact objects found in close to newly formed massive stars; they are dense and relatively warm and show atypical gas-phase molecular compositions. The gas-phase composition, and therefore the evolutionary stage of the hot core, can be understood by considering the sublimation behaviour of molecular ices on the dust grains within the molecular cloud.

This thesis presents the results of investigations on the adsorption and desorption of methanol and ethanol in both the pure state and in combination with water. In each case the deposition occurs on a highly oriented pyrolytic graphite (HOPG) surface. HOPG is considered to be a suitable interstellar dust grain analogue, as dust grains in the ISM are composed of mainly carbonaceous and silicaceous material. Temperature programmed desorption (TPD) and reflection absorption infrared spectroscopy (RAIRS) studies of methanol and ethanol ices, mixed with water, are presented.

The adsorption and desorption of each species deposited on a layer of amorphous solid water ice is compared to those of codeposited ice layers. In all systems, there is evidence for molecular adsorption in a physisorbed state and for interactions between the investigated molecule and the water ice. As expected, the sequentially deposited systems show different behaviour when compared with the codeposited systems.
The information obtained from these experiments is of direct relevance to astronomers, as the measured desorption energies can be incorporated directly into astronomical models. This, in turn, helps to lead to a greater understanding of star formation, and hence of the Universe in which we live.

Acknowledgments

Thanks to:

Wendy Brown for her patient supervision and for giving me this opportunity.

The tea break crew for providing support, inspiration and most importantly, plenty of tea.

Shakti for pointing out that my space exploration chamber had gone “Kertoosh” for 3 years without once managing to escape the confines of the basement.

To escape criticism – do nothing, say nothing, be nothing.

Table of Contents

List of Figures

List of Tables

Chapter 1 Introduction

A cursory glance into the night sky reveals very little to the naked eye, but the interstellar medium (ISM), is far from empty. The ISM contributes ≈ 10% to the overall mass of the galaxy and is comprised of dust grains and gases in the form of clouds. It is the gravitational collapse of these clouds that gives rise to the birth of new stars.

It has been proposed that the surfaces of dust grains play an important role in the formation of molecules in the ISM. Many of these molecules are thought to form via addition reactions from simple constituents [1-5]. These dust grains are typically very cold (≈ 10 K) and so newly formed molecules, or those that collide with the grain, will tend to stick. This results in the accumulation of icy mantles on the dust grain surface which can act as a reservoir of gas phase molecules. Given that species are actually observed in the gas phase, there are clearly processes, such as ultraviolet and cosmic ray bombardment that act upon these ices resulting in the release of molecules from the grain.

A number of studies have been performed that suggest certain molecules, such as CO, HCN, N_2, O_2, Ar, CH_4 and CH_3OH, can show anomalous behaviour when enmeshed in a water rich, icy, mantle [6-11]. It has been suggested that these molecules can be trapped beyond the sublimation temperature for the pure species, thereby leading to unexpected compositions such as the high methanol abundances found in the relatively high temperature regions surrounding newly formed stars [12]. An understanding of the complex desorption behaviour of mixed molecular ices is required, in order to explain gas phase abundances in warm areas, such as hot cores, and to enable the prediction of the evolutionary stage of star formation [13].

1.1 Interstellar Medium

Our galaxy is a rotating spiral disk with a diameter in the order of 100,000 light years and a thickness of about 6000 light years. Within the galaxy are approximately 10^{11} stars separated by an average of 10 light years [2].

The ISM is a general term encompassing the whole of the space between the stars. Not surprisingly it is of a diverse nature. Although it has a mean density of 10^6 atoms m^{-3}, the range of densities and pressure conditions is wide. The predominant component of this region is H_2 followed by He, at 10% of the atoms while a further 0.1% consists of C, N and O atoms and simple molecules such as CO.

Most interstellar matter is accumulated in vast clouds some light years in size. These vary from particularly diffuse regions, unsurprisingly called diffuse clouds, through to areas of ever increasing density which culminate in the densest regions where stars are actually formed by the collapse of such clouds. *Table 1.1* summarises the physical and chemical properties of the different interstellar regions.

Table 1.1 Summary of the properties of clouds and other regions found in the interstellar medium [2].

Object	Properties*
H II Region	T = 10000 K. Dominant ion H^+, but C^+, N^+ and O^+ also present. $n \approx 10^2$-10^3 cm^{-3}. $r \approx$ 3-30 ly. Line and continuum radiation emitted.
Intercloud Medium	T = 10000 K. Dominant atom H. Dominant ion C^+. All atoms with ionisation potential < 13.6 eV ionized. $n \approx 0.1$ cm^{-3}. No molecules.
Diffuse Clouds	T = 100 K. Partial conversion of H into H_2. Dominant ion C^+. Other atoms partially neutral. $n \approx 100$ cm^{-3}. Molecules CO, H_2CO, and some others observed.
Dark Clouds	T = 10-20 K. Most H converted into H_2. $n \approx 10^4$ cm^{-3}. Little internal motion. $M = 10^2$-10^4 solar masses. $r \approx$ 16 ly. Many molecules observed.
Molecular Clouds	T = 50 K. Associated with regions of excitation. $n < 10^6$ cm^{-3}. Little internal motion. $M < 10^6$ solar masses. $r \leq$ 95 ly. Many molecules observed.
Compact H II Regions	T = 100-1000 K. Hot stars in dense clouds of gas and dust. Infrared and radio emission of gas and dust including molecules. Maser sources SiO, H_2O, OH. $n \approx 10^3$-10^4 cm^{-3}.
Giant Molecular Clouds	T = 10 K. Relatively low density ($n \approx 600$ cm$^{-3)}$. Very large mass. $M = 5 \times 10^5$ solar masses. Diameter 130 ly.

* T = kinetic temperature; n = number of H atoms cm^{-3} in all forms; M = mass; r = radius measured in light years (ly)

The diffuse clouds have low densities and a wide range of temperatures (100 - 10^6 K). The dark clouds are much denser and cooler, with number densities approaching 10^9-10^{10} molecules m^{-3} and a temperature of approximately 10 K. The densest areas are HII clouds, occurring near bright stars. Their densities exceed 10^{12} molecules m^{-3} and they have temperatures in the region of 300 K [14].

The more diffuse areas are made up of predominantly atomic species and molecular hydrogen, as the penetrating starlight easily photodissociates molecules. Interstellar molecules are particularly associated with the denser regions, such as the dark clouds, where they are shielded from UV radiation [15]. To date, more than 220 molecules have been categorised, ranging from simple diatomics to more complicated alcohols, carbohydrates and possibly even polycyclic aromatic hydrocarbons (PAH's). *Table 1.2* lists some of the species so far identified in the ISM.

Table 1.2 Some of the molecules detected in the ISM to date [16].

2 atoms	3 atoms	4 atoms	5 atoms	6 atoms	>6 atoms
H_2	H_2O	NH_3	CH_4	CH_3OH	CH_3C_2H
CO	H_2S	H_2CO	SiH_4	CH_3SH	CH_3CHO
CSi	HCN	H_2CS	CH_2NH	C_2H_4	CH_3NH_2
CP	HNC	C_2H_2	NH_2CN	CH_3CN	CH_2CHCN
CS	CO_2	HNCO	CH_2CO	CH_3NC	HC_4CN
NO	SO_2	HNCS	HCOOH	HC_2CHO	C_6H
NS	MgCN	H_3O^+	HC_2CN	NH_2CHO	CH_3COOH
SO	MgNC	$HOCO^+$	HCCNC	C_4H_2	$HCOOCH_3$
HCl	NaCN	C_3S	cyclic-C_3H_2	C_5H	CH_3C_2CN
NaCl	N_2O	H_2CN	linear-C_3H_2	C_5O	$(CH_3)_2O$
KCl	NH_2	cyclic-C_3H	CH_2CN		C_2H_5OH
AlCl	OCS	linear-C_3H	C_4H		C_2H_5CN
AlF	HCO	HCCN	C_4Si		CH_3C_4H
PN	C_3	H_2CO^+	C_5		HC_6CN
SiN	C_2H	C_2CN	HNCCC		$(CH_3)_2CO$
SiO	HCO^+	C_3O			CH_3C_4N
SiS	HOC^+	$HCNH^+$			NH_2CH_2COOH
NH	N_2H^+	CH_2D^+			HC_8CN
OH	HNO	SiC_3			$HC_{10}CH$
C_2	HCS^+				CH_2CHOH
CN	H_3^+				C_8H
HF	C_2O				$HC_{11}N$
CO^+	C_2S				HC_9N
SO^+	SiC_2				CH_3C_5N
CH	H_2D^+				$C_7HH_2C_6$
CH^+	CH_2				
FeO	AlNC				

1.1.1 Chemistry of the Interstellar Medium

For reactions to occur in the gas phase, collisions must occur between reacting species. Given the low number densities of the diffuse clouds, there can be millions of years between collisions, and as a result the chemistry in the ISM can be a slow process. As previously discussed, the ISM is a diverse region and therefore reaction rates will be very dependant on the prevailing local physical conditions. The dense stellar atmospheres are expected to demonstrate very fast chemistry, for example [17].

Reactions will need to be exothermic to prove significant at such low temperatures and densities. This will tend to favour reactions including ionised species, which can interact at larger distances than a typical collision cross-section, and will exclude many neutral-neutral reactions. Any formation mechanisms proposed must be efficient enough to counteract the destructive mechanisms caused by ultraviolet radiation. Photodissociation of molecules, see *Equation 1.1*, occurs in a typical time frame of 300 years [18]:

$$t_{diss} \approx 300yr(AB + hv \rightarrow A + B) \qquad \text{Equation 1.1}$$

Although molecules can be formed by grain decomposition and in stellar outflows, the rapid destruction of individual molecules enables us to disregard the proposition that observed molecular abundances can be explained by these processes alone [19]. The rate of destruction would far exceed the generation rate. The alternative proposition is that of in-situ formation mechanisms, either in the gas phase or grain surface catalysed.

Gas phase reactions are well understood and can be described by the following series of equations [17]. Considering simple gas phase reaction mechanisms such as A + B leads to a molecule with internal energy:

$$A + B \longrightarrow AB^* \qquad \text{Equation 1.2}$$

where A is an atom and B another atom or atomic ion.

Some process must occur to remove the excess energy, and thereby stabilize AB, or the particles will simply dissociate again. In radiative association, emission of radiation could occur if the contact time is long enough:

$$A + B \rightarrow AB + hv \qquad \text{Equation 1.3}$$

The contact time is actually very short, in the order of 10^{-13} s, which results in a low probability that a molecule AB can form through this pathway. In fact the probability of this reaction pathway occurring is around 10^{-5} per collision [14].

An alternative mechanism that could occur is a 3-body collision, where the third species can take away the excess energy as kinetic energy:

$$A + B + M \rightarrow AB + M$$ Equation 1.4

Given the low number densities in the ISM, 3-body collisions are negligible. However in *Equation 1.4*, species M could be substituted for a dust grain surface which would provide a pathway for release of the internal energy via heating of the grain.

Equations 1.2 - 1.4 show how reactions between atoms and/or atomic ions can proceed, whether by radiative association or on the surface of grains. As soon as molecules are present within the medium, much faster ion-molecule and neutral exchange reactions can begin. As molecular hydrogen is by far the most abundant molecule it is considered to be the key molecular initiator in many chemical pathways, e.g.

$$\begin{aligned} &C^+ + H_2 \rightarrow CH_2^+ + hv \\ &CH_2^+ + H_2 \rightarrow CH_3^+ + H \\ &CH_3^+ + e^- \rightarrow CH_2 + H \end{aligned}$$ Equation 1.5

Simulations have shown that gas phase chemistry can account for approximately 80% of all molecules observed in the gas phase [20-22]. However the hydrogen molecule formation is a distinct exception. Radiative association in the ISM is not a significant route to H_2 formation as the collision cross-section is too small to stabilise the transition [2]. The only feasible route to hydrogen formation is to consider catalytic synthesis on the surface of dust grains [23, 24]. Several larger molecules, such as CH_3OH, H_2O and NH_3, are also thought to be formed on the surface of dust grains [25].

1.2 Dust Grains

Although dust grains make up only approximately 1% of the mass of the ISM, it is now certain that they play a pivotal role in molecular hydrogen formation and in the formation of other molecules, including the small alcohols [2, 26].

1.2.1 Probing the Nature of Dust

Possibly the first observational evidence for the existence of stellar dust was a cause of some hindrance to astronomers. Large clouds of dusty gas can extinguish the background visible light, forming apparent holes in the sky and blocking the astronomers' view of the stars beyond. *Figure 1.1* shows an example of a dense cloud obscuring the starlight [19].

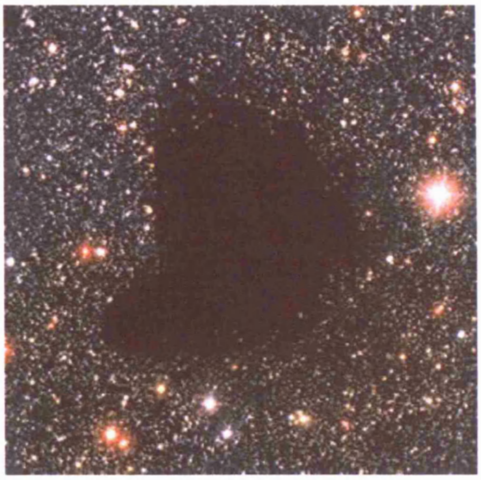

Figure 1.1 Image of the "Black Cloud" B68, illustrating the obscuration of starlight by the dusty cloud. http://antwrp.gsfc.nasa.gov/apod/ap990511.html

Evidence for the existence of dust grains in space also comes from a study of the extinction at different wavelengths of light compared to known and similar star types. This gives rise to the extinction curves shown in *Figure 1.2*, which shows a plot of absorption versus inverse wavelength [27].

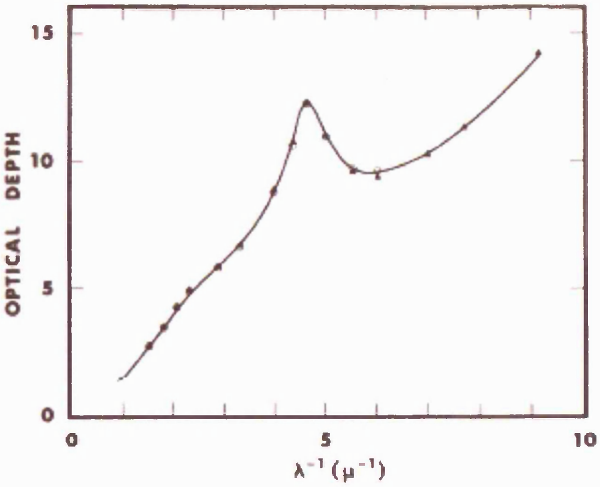

Figure 1.2 Typical interstellar extinction curve demonstrating how extinction varies with wavelength [27].

The typical curve shows an almost linear rise in the visible region where extinction is proportional to wavelength. A prominent bump at ≈ 4.6 μm^{-1} is followed by an upward curve into the far ultraviolet region of the spectrum. The curve is characteristic of differing particle sizes giving rise to the extinction, and typical grain sizes range from 5 nm to 0.2 μm [28]. The 4.6 μm^{-1}, or 2175 Å, bump is often cited as evidence for the carbonaceous composition of dust grains in the form of small graphite particles [29].

Grains are also implicated in the observed polarisation of starlight, which is a partial extinction in one plane of polarisation and can be explained by non-spherical grains aligned in the interstellar magnetic field [19, 30]. Several groups have worked with the extinction and polarisation curves to propose structural models for dust. Li and Greenberg [31] have proposed a trimodal dust model, see *Figure 1.3*, where the grain has 3 clear components:

1. A large silicate core with organic refractory materials in the mantle, which are responsible for the extinction features in the infra-red and visible regions.
2. Small carbonaceous materials, responsible for the hump at 4.6 μm^{-1}.
3. Polyaromatic hydrocarbons which can explain the far ultraviolet extinction.

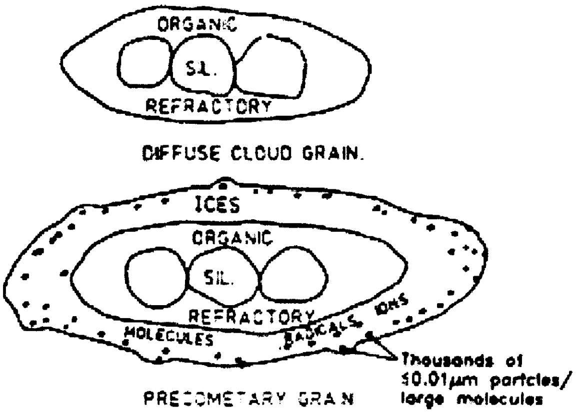

Figure 1.3 Proposed composition of the trimodal dust grain model. From: http://strw.leidenuniv.nl/~greenber/isd.html

Interstellar depletions provide further evidence for the chemical make-up of dust by assuming that atoms tied up in grains and ices are not present in the gas phase. Comparing a particular cloud with "typical" stellar abundances leads to interesting changes in the relative abundances. Our sun is usually taken as the standard reference as it is believed to be representative of the galaxy as a whole [14]. Depletions of the heavier elements C, N, O, Mg, Si and Fe are generally accepted as evidence for their inclusion in refractory solids [27].

Infrared observations provide the most convincing evidence for the composition of dust grains and, despite the difficulty encountered in collecting accurate data throughout all wavelengths, the Infrared Space Observatory (ISO) has identified several species. In particular, amorphous and crystalline silicates have been detected through their fingerprint vibrations in the 10 and 20 μm regions [15] and ices containing water, carbon dioxide and methanol have displayed characteristic absorption signals, see *Figure 1.4* [32, 33]. In contrast to extinction studies, infrared observations have not produced any evidence to suggest that graphite is present in the ISM, however graphite is not strongly infrared active [15].

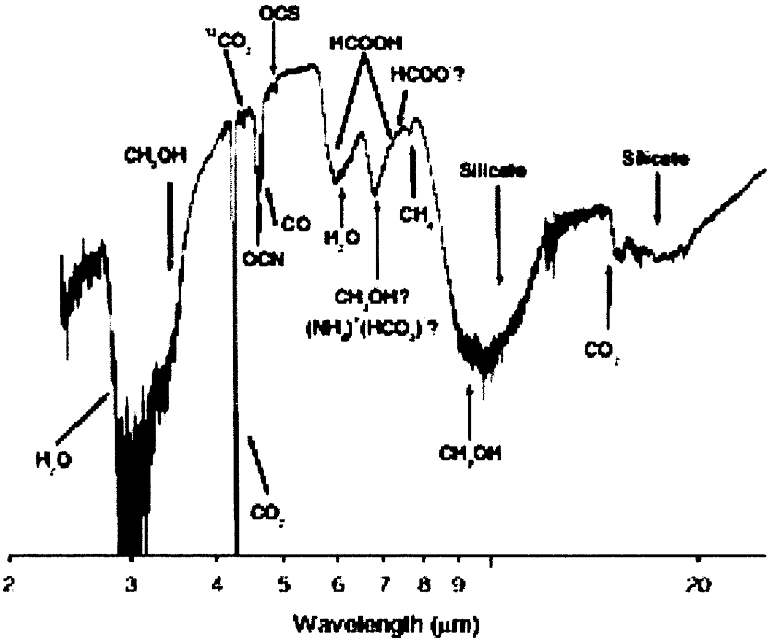

Figure 1.4 Interstellar IR spectrum from w33a showing the assignments of the major observed bands {Gibb, 2004 #352}.

A final source of information about the composition of interstellar dust grains is from studying interplanetary dust that has fallen to earth. This dust may have formed by the erosion of asteroids following impact and, as such, has often undergone harsh physical processing. There is sometimes also a component that appears unmodified and is thought to possibly be an example of interstellar dust [19]. It is fluffy, porous and contains carbonaceous and silicate material, see *Figure 1.5*.

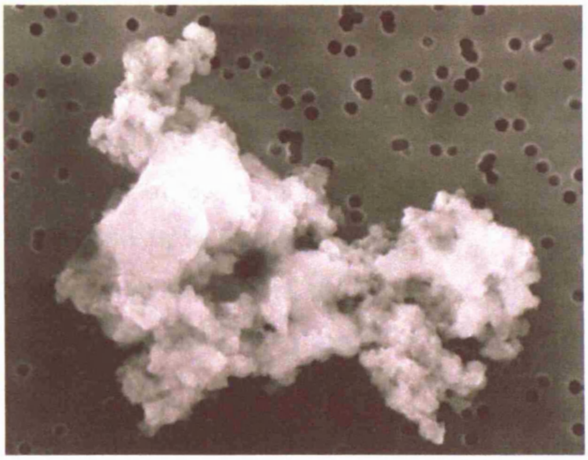

Figure 1.5 Interplanetary Dust. Photo credit: NASA.

Further interplanetary particles known as GEMS, glasses with embedded metal and sulphides, have been identified following collection by the Ulysses spacecraft [34]. They are of a glassy composition, made of iron and nickel sulphides, and are a size that is consistent with that expected for interstellar dust, see *Figure 1.6*.

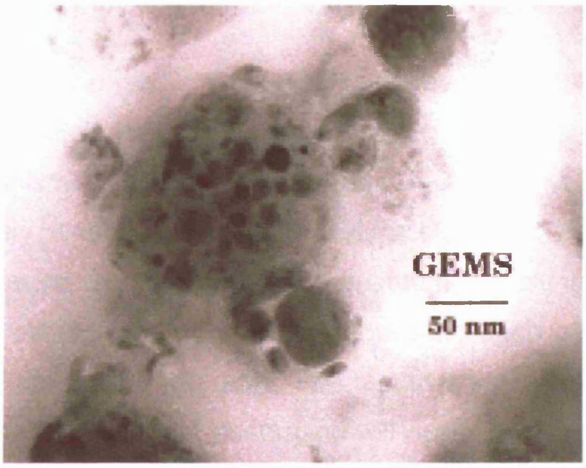

Figure 1.6 GEMS (glasses with embedded metal and sulphides). Courtesy of NASA http://stardust.jpl.nasa.gov/science/sd-particle.html

So far, indirect methods for determining both the structure and composition of interstellar dust grains have been described. In the near future we may have direct evidence of dust composition by way of samples from the NASA Stardust mission which can be followed at http://stardust.jpl.nasa.gov/.

1.3 Surface Chemistry

It is generally accepted that the surfaces of dust grains act as a necessary site of molecular formation in the ISM [30]. In order to understand the formation process it is necessary to probe the nature of chemical processes occurring on the grain surface. This will include the accretion or adsorption of the species onto the surface of the grain to form icy mantles, mobility across the surface, surface mediated reactions, processing and finally desorption from the grain.

At the low temperatures of the ISM, it is typically assumed that all atoms, molecules and ions that collide with a dust grain will adsorb on the surface [19, 35, 36]. For molecular formation to occur, an atom or ion must be adsorbed onto the surface of a grain and remain there long enough to come into contact with another species. The fate of the adsorbed species is in some part dependant on its mobility across the surface, and this in turn is dependant on the strength of the interaction between the adsorbate and the surface, as well as upon its size. Small molecules such as hydrogen are expected to be highly mobile, although the actual nature of the movement, whether by thermal hopping or quantum tunnelling, is less clear [37-39].

There are two surface based mechanisms to be considered, the Langmuir-Hinshelwood mechanism and the Eley-Rideal mechanism. The Langmuir-Hinshelwood mechanism is shown schematically in *Figure 1.7*. In the model the adsorbate is relatively weakly bound to the surface and is able to act as a two-dimensional gas, diffusing over the surface by quantum tunnelling or thermal hopping. Molecular formation occurs when two atoms approach each other and are able to transfer the heat of formation to the grain. The fact that this adsorption is necessarily weak will increase the chances that desorption will occur before molecular formation, but also allows the heat of formation to result in the newly formed molecule desorbing rapidly. Much experimental work has been carried out to study this mechanism and it is thought only to be efficient in a small range of interstellar temperatures, low enough to prevent evaporation before molecular formation and yet high enough to encourage appreciable diffusion across the surface [40].

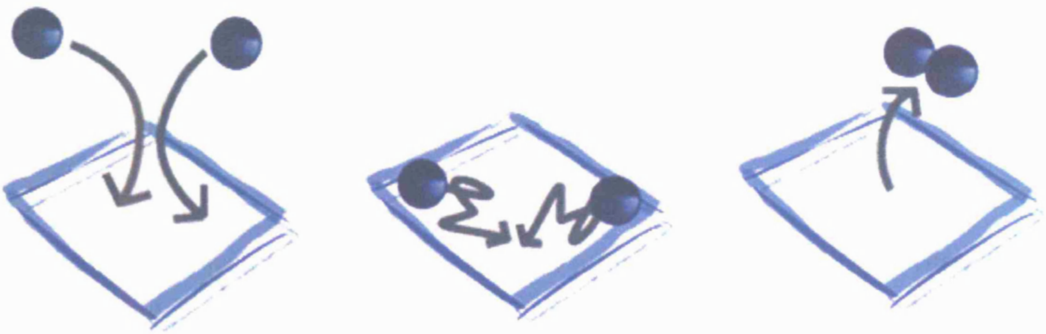

Figure 1.7 Schematic diagram of the Langmuir-Hinshelwood Mechanism.

In the Eley-Rideal mechanism, shown schematically in *Figure 1.8*, the atoms are bound more strongly to the surface and in this case both diffusion and evaporation will be low and monolayers will readily form. Molecule formation can then occur when another atom collides directly with a surface atom and desorption occurs from the surface.

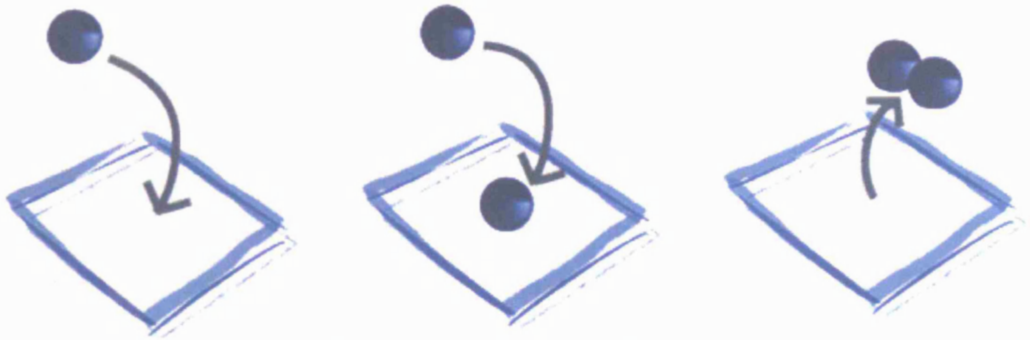

Figure 1.8 Schematic diagram of the Eley-Rideal Mechanism.

There have been a number of studies of the formation of molecular hydrogen on surfaces [37, 41-49]. The grain acts as a thermodynamic entity and is able to absorb the 4.5 eV binding energy that results from the combination of the two hydrogen atoms. In this way the grain effectively acts as the third body, as in *Equation 1.4*. Calculations by Farebrother et al [50] have provided support for the Eley-Rideal mechanism as a possible route to H_2 formation on graphitic surfaces.

Molecular hydrogen is not the only species thought to form on the surface of dust grains. Interstellar ices are thought to provide a guide to the larger molecules whose formation may also proceed on the grain surface. H_2O, CH_4, NH_3 and CH_3OH are found in ices and their gas phase abundances are not high enough to justify freeze out within appreciable time-scales [32, 51, 52]. It is assumed that, unlike in the gas phase, most formation reactions occurring on grain surfaces would be associative in nature [19] and, given the huge dominance of hydrogen atoms in the ISM, it is not surprising that many reactions are proposed to be sequential hydrogenation processes.

For example, it is hypothesised that methanol forms by the successive hydrogenation of CO to form formaldehyde and then methanol via the following scheme [53]:

$$\begin{aligned} &CO_a + H_a \rightarrow HCO_a \\ &H_a + HCO_a \rightarrow CH_2O_a \\ &CH_2O_a + H_a \rightarrow CH_3O_a \\ &CH_3O_a + H_a \rightarrow CH_3OH_a \end{aligned} \qquad \text{Equation 1.6}$$

On the other hand, water, the dominant molecule in interstellar ices, is thought to form via successive addition of O and H atoms:

$$\begin{aligned} &H_a + O_a \rightarrow OH_a \\ &OH_a + H_a \rightarrow H_2O_a \end{aligned} \qquad \text{Equation 1.7}$$

Interstellar ices formed on the surface of dust grains undergo significant processing as a result of interstellar shocks that lead to temperature increases and by ultraviolet and cosmic ray bombardment. This processing can influence molecular formation by providing the necessary energy to overcome activation barriers to reaction, and it is also the means by which icy grain mantles are returned to the gas phase [17].

Thermal processing plays an important role within Hot Cores which are small, relatively warm, dense clumps found in the vicinity of newly formed massive stars. They have a far richer chemistry than is found in the region of low mass stars, and are found in regions heavily populated with saturated molecules such as H_2O, H_2S, NH_3 and CH_3OH and other H rich nitrogen and oxygen bearing molecules such as CH_3CN and $HCOOCH_3$ [54].

1.4 Molecular Ices

Within the cold dense regions of the ISM, the sticking of gas phase species on to the surface of cold grains (≈ 10 K) is expected to be extremely efficient and results in the formation of an icy molecular mantle [8, 15, 55]. These mantles result in depletion from the gas phase forming a reservoir of solid state species. Processing and resultant sublimation of these mantles can have a profound affect on the gas phase abundances and, in certain circumstances, may provide a source of new molecules [13, 54].

1.4.1 Composition of the Molecular Ices

The following species are among those that have been detected and securely identified in the solid state by infra-red spectroscopy: H_2O, CO, CH_3OH, CO_2, CH_4 and NH_3. The following species are suspected to be present, but have either not yet been confirmed or have only been observed in isolated regions: OCS, H_2CO, HCOOH and OCN^- [33]. The relative abundances of these components have been argued but it is generally accepted that the ices consist mainly of amorphous water ice with other species present as impurities [33, 56, 57].

As already discussed, the composition of these molecular ices cannot be entirely explained by freeze out from the gas phase. Surface reactions have been invoked to explain the presence of enhanced abundances of deuterated species [58-61] or unexpectedly high abundances of molecules such as NH_3 and CH_3OH and the presence of complex organic molecules that cannot adequately be explained by gas phase chemistry [33, 55, 62, 63].

The icy mantle composition varies according to the prevailing physical conditions, but is not just a reflection of the gas phase composition. Surface reactions will lead to the formation of new species and these will depend to a certain extent on the local H/H_2 ratio. When the ratio is particularly high, as it is in the region of dense clouds, surface reactions involving H will predominate and will result in polar ices containing H_2O, NH_3 and CH_3OH. In more diffuse areas where the H/H_2 ratio is less than 1, apolar or hydrogen poor ices will form containing molecules such as CO, O_2 and N_2 [15, 64, 65].

Codeposition experiments will provide a more accurate model of the composition of molecular ices, as surface formation mechanisms are expected to result in an intimately mixed ice. However, the study of layered systems is still relevant for ices where simple accretion processes are dominant. In this thesis, studies of both codeposited and layered systems will be considered.

1.4.2 Trapping of Molecules within Molecular Ices

Water is the most abundant component of most molecular ices. The ability of water to trap volatile gases is well understood and a number of groups have performed preliminary studies of mixed ices of varying complexity.

Notesco, Bar-Nun and others from Tel-Aviv University have performed studies on the gas trapping properties of amorphous water ice. They were particularly concerned with the implications for comets and their proposed role in seeding volatile components on the early Earth, and so concentrated on the trapping of heavy noble gases, N_2, CO and CH_4 [11, 66-68]. Later work also considered the trapping of methanol, hydrogen cyanide and n-Hexane [9, 69].

The Tel-Aviv group studied binary systems, both sequentially dosed and codeposited and also more complex mixtures of up to 4 molecules codeposited with water. They described the release of trapped molecules in four temperature ranges [66]: at 30-60 K the frozen gas on the surface of the water evaporates, at 135-155 K trapped gas is squeezed out of the ice matrix as it transforms from amorphous to crystalline cubic ice, between 160 and 175 K they occasionally see a desorption peak attributed to the release of deeply buried gases during the cubic to hexagonal water transition and finally they report a release at 165-190 K that is simultaneous with the water desorption trace [66]. With methanol only, they assigned this final co-desorption trace to the release of a clathrate-hydrate structure [9, 69, 70].

Sandford and Allamandola at the NASA/Ames Research centre have presented a number of infrared vibrational studies of molecular ices, varying from single component ices to complex mixtures [71-73]. They determined binding energies for individual species such as methanol, water and ammonia and used these to calculate approximate residence times.

Recently, Collings et al [74] have performed a survey of a number of astrophysically relevant molecules and studied them in a) their pure form, b) sequentially adsorbed onto a pre-existing layer of water ice and c) co-adsorbed with water. They classified the species into three groups according to their desorption behaviour. CO – like species include the volatile species CO, N_2, O_2 and CH_4 and in the sequentially dosed experiments were shown to display monolayer, volcano and co-desorption peaks. The latter two peaks were assigned to trapped molecules. The volcano peak corresponded to the rapid release of molecules as the water ice crystallised and the co-desorption peak applied to the molecules so firmly trapped that they were only released as the bulk of the ice desorbed. Water-like species included NH_3, CH_3OH and HCOOH, and in the sequentially dosed system these demonstrated multilayer peaks and monolayer desorption traces coincident with the desorption of water. They found no evidence for trapping of water-like species within the ice layer. The final category was Intermediate species such as H_2S, CO_2 and CS_2 which demonstrated desorption behaviour some way between the previous two categories. In all cases the intermediate species showed evidence of trapping within the water ice.

This was an expansive study, performed in UHV conditions, which highlighted the importance of studying the desorption of molecular species in the presence of water ice if the kinetic results were to be interpreted for astronomical models. In all cases they found that the desorption characteristics of each species were dominated by the behaviour of the water, but stressed the need for more detailed studies to be performed on the individual molecules concerned.

Gibb et al [33] have undertaken a large study comparing the laboratory produced spectra of interstellar ice analogues with those from the Infrared Space Observatory in order to characterise a number of the observed ice bands. Many of the experimental results available to them were based on ices composed of a single molecule from which they extracted features pertaining to each component. There is therefore a requirement for more complex ice mixtures to be studied so that a more accurate characterisation of interstellar ice can be carried out.

1.5 Alcohol and Water in Space

Methanol and ethanol are found in the solid phase, frozen out with the more abundant water, as molecular ices on the surface of grains. In the gas phase, they are found in relatively high abundances in the vicinity of hot cores. Hot cores are compact objects found in or near newly formed massive stars; they are dense and relatively warm and show atypical gas-phase molecular compositions. The gas-phase composition, and therefore the evolutionary stage of the hot core, can be understood by considering the sublimation behaviour of molecular ices on the dust grains within the molecular cloud. Both of the alcohols can be viewed as evolutionary indicators so it is important to understand the surface processes that lead to their sublimation from the grain. This thesis presents the results of investigations on the adsorption and desorption of methanol and ethanol in both the pure state and in combination with water.

1.5.1 Water

The so-called "3 μm" band, attributed to the OH stretch of water, is ubiquitous in infrared observational spectra, where it is often the strongest band visible. Comparisons between observational and laboratory based spectra indicate that water is the most dominant constituent of ices in the dense clouds [75, 76].

Within the temperature range found in the ISM, water is known to occur in both amorphous and crystalline phases [77]. The amorphous form has also been isolated in both high and low density variants, with the transition from high to low between 38 K and 80 K [56]. It is generally accepted that the high density amorphous form is the most prevalent in interstellar ices, but both thermal and UV processing can result in structural transitions [56, 77].

1.5.2 Methanol

Methanol is thought to be one of the most abundant molecules in interstellar ices after H_2O and CO [26]. It has been observed in both the solid state and in the gas phase in dark clouds and is also found in abundance in the hot core regions associated with star formation. The quoted observational abundances can vary quite widely according to the source [78-80]. Skinner et al [81] and Ehrenfreund et al [82] suggest that these discrepancies could be explained by incomplete mixing, or by segregation of methanol and water along the observational line of sight.

1.5.3 Ethanol

Although ethanol has not been observed in dark clouds, it is present in the rich star forming regions [63, 83, 84], and is predicted to form on the surface of grains [26]. Both ethanol and methanol are important as they are implicated in the formation mechanisms of complex organics such as ethers and esters [26].

1.6 Motivation for this study

Much of our understanding of the nature and composition of the ISM comes from the interpretation of remote data, either from radio telescopes or by infrared spectroscopy. Infrared laboratory data of interstellar mixed ice analogues can be particularly useful in confirming (or disputing) the origin of the telescopic observations [33]. In addition, an understanding of the desorption characteristics of mixed ices enables astrophysicists to classify the evolution, and therefore the age, of stars [13]. This work aims to provide a comprehensive astrophysically relevant surface science study of the interaction of the small alcohols, methanol and ethanol, with a dust grain surface in water rich environments.

The investigations presented in this thesis use ultra high vacuum (UHV) technology, coupled with liquid nitrogen cooling, to mimic the low pressures and temperatures experienced in the ISM. Temperature programmed desorption (TPD) and reflection absorption infrared spectroscopy (RAIRS) techniques are used to probe the nature of the surface interactions for each system studied. The following systems have been studied:

1) Methanol deposited onto a pre-existing water ice to form a binary layered structure.
2) Methanol codeposited with water to form an intimately mixed system.
3) Pure ethanol.
4) Ethanol deposited onto a pre-existing water ice to form a binary layered structure.
5) Ethanol codeposited with water to form an intimately mixed system.

In each case the deposition occurs on a highly oriented pyrolytic graphite (HOPG) surface, which is considered to be a suitable interstellar dust grain analogue.

1.7 Bibliography

1. Dalgarno, A., Journal of the Chemical Society-Faraday Transactions, 1993. **89**(13): p. 2111-2117.

2. Duley, W.W. and Williams, D.A., *Interstellar Chemistry*. 1984: Academic Press.

3. Millar, T.J. and Williams, D.A., *Dust and Chemistry in Astronomy*. The Graduate Series in Astronomy, ed. R.J. Taylor and R.E. White. 1993: Institute of Physics Publishing.

4. Williams, D.A., IAU Symposia, 1987(120): p. 531-538.

5. Williams, D.A. and Taylor, S.D., Quarterly Journal of the Royal Astronomical Society, 1996. **37**(4): p. 565-592.

6. Collings, M.P., Dever, J.W., Fraser, H.J., and McCoustra, M.R.S., Astrophysics and Space Science, 2003. **285**(3-4): p. 633-659.

7. Sandford, S.A. and Allamandola, L.J., Icarus, 1988. **76**: p. 201-224.

8. Sandford, S.A. and Allamandola, L.J., Astrophysical Journal, 1993. **417**: p. 815.

9. Notesco, G. and BarNun, A., Icarus, 1997. **126**(2): p. 336-341.

10. Ayotte, P., Smith, R.S., Stevenson, K.P., Dohnalek, Z., Kimmel, G.A., and Kay, B.D., Journal of Geophysical Research-Planets, 2001. **106**(E12): p. 33387-33392.

11. Barnun, A., Kleinfeld, I., and Kochavi, E., Physical Review B, 1988. **38**(11): p. 7749-7754.

12. van der Tak, F.F.S., van Dishoeck, E.F., and Caselli, P., Astronomy and Astrophysics, 2000. **361**(1): p. 327-339.

13. Viti, S., Collings, M.P., Dever, J.W., McCoustra, M.R.S., and Williams, D.A., Monthly Notices of the Royal Astronomical Society, 2004. **354**(4): p. 1141-1145.

14. Dyson, J.E. and Williams, D.A., *The Physics of the Interstellar Medium*. 1980: John Wiley & Sons, Inc., New York.

15. Sandford, S.A., Meteoritics & Planetary Science, 1996. **31**(4): p. 449-476.

16. Wootten, A. *The 129 Reported Interstellar and Circumstellar Molecules*. [website] 2005 [cited; Available from: http://www.cv.nrao.edu/~awootten/allmols.html.

17. Hartquist, T.W. and Williams, D.A., *The Chemically Controlled Cosmos*. 1995: Cambridge University Press.

18. Watson, W.D., Reviews of Modern Physics, 1976. **48**(4).

19. Williams, D.A. and Herbst, E., Surface Science, 2002. **500**(1-3): p. 823-837.

20. Millar, T.J., Farquhar, P.R.A., and Willacy, K., Astronomy & Astrophysics Supplement Series, 1997. **121**(1): p. 139-185.

21. Le Teuff, Y.H., Millar, T.J., and Markwick, A.J., Astronomy & Astrophysics Supplement Series, 2000. **146**(1): p. 157-168.

22. Terzieva, R. and Herbst, E., Astrophysical Journal, 1998. **501**(1): p. 207-220.

23. Gould, R.J. and Salpeter, E.E., Astrophysical Journal, 1963. **138**: p. 393-407.

24. Hollenbach, D. and Salpeter, E.E., Astrophysical Journal, 1971. **163**: p. 155-164.

25. Hiraoka, K., Ohashi, N., Kihara, Y., Yamamoto, K., Sato, T., and Yamashita, A., Chemical Physics Letters, 1994. **229**(4-5): p. 408-414.

26. Charnley, S.B., Kress, M.E., Tielens, A., and Millar, T.J., Astrophysical Journal, 1995. **448**(1): p. 232-239.

27. Whittet, D.C.B., *Dust in the Galactic Environment*. Series in Astronomy and Astrophysics. 2003: Institute of Physics Publishing.

28. Greenberg, J.M., Astrophysics and Space Science, 1999. **269-270**: p. 33-55.

29. Draine, B.T., Annual Review of Astronomy and Astrophysics, 2003. **41**: p. 241-89.

30. Greenberg, J.M., Surface Science, 2002. **500**(1-3): p. 793-822.

31. Li, A. and Greenberg, J.M., Astronomy & Astrophysics, 1997. **323**: p. 566-584.

32. Whittet, D.C.B., Schutte, W.A., Tielens, A., Boogert, A.C.A., deGraauw, T., Ehrenfreund, P., Gerakines, P.A., Helmich, F.P., Prusti, T., and vanDishoeck, E.F., Astronomy and Astrophysics, 1996. **315**(2): p. L357-L360.

33. Gibb, E.L., Whittet, D.C.B., Boogert, A.C.A., and Tielens, A., Astrophysical Journal Supplement Series, 2004. **151**(1): p. 35-73.

34. Grun, E., Hamilton, D.P., Baguhl, M., Riemann, R., Horanyi, M., and Polanskey, C., Geophysical Research Letters, 1994. **21**(11): p. 1035-1038.

35. Meijer, A., Farebrother, A.J., Clary, D.C., and Fisher, A.J., Journal of Physical Chemistry A, 2001. **105**(11): p. 2173-2182.

36. Farebrother, A.J., Meijer, A., Clary, D.C., and Fisher, A.J., Chemical Physics Letters, 2000. **319**(3-4): p. 303-308.

37. Hiraoka, K. and Sato, T., Radiation Physics and Chemistry, 2001. **60**(4-5): p. 389-393.

38. Hiraoka, K., Sato, T., Sato, S., Hishiki, S., Suzuki, K., Takahashi, Y., Yokoyama, T., and Kitagawa, S., Journal of Physical Chemistry B, 2001. **105**(29): p. 6950-6955.

39. Katz, N., Furman, I., Biham, O., Pirronello, V., and Vidali, G., The Astrophysical Journal, 1999. **522**: p. 305-312.

40. Katz, N., Furman, I., Biham, O., Pirronello, V., and Vidali, G., Astrophysical Journal, 1999. **522**(1): p. 305-312.

41. Hiraoka, K., Sato, T., and Takayama, T., Science, 2001. **292**(5518): p. 869-870.

42. Hornekaer, L., Baurichter, A., Petrunin, V.V., Field, D., and Luntz, A.C., Science, 2003. **302**(5652): p. 1943-1946.

43. Cazaux, S. and Tielens, A., Astrophysical Journal, 2002. **575**(1): p. L29-L32.

44. Duley, W.W., Monthly Notices of the Royal Astronomical Society, 1996. **279**(2): p. 591-594.

45. Duley, W.W. and Williams, D.A., Monthly Notices of the Royal Astronomical Society, 1993. **260**(1): p. 37-42.

46. Pirronello, V., Biham, O., Liu, C., Shen, L.O., and Vidali, G., Astrophysical Journal, 1997. **483**(2): p. L131-L134.

47. Pirronello, V., Liu, C., Roser, J.E., and Vidali, G., Astronomy and Astrophysics, 1999. **344**(2): p. 681-686.

48. Pirronello, V., Liu, C., Shen, L.Y., and Vidali, G., Astrophysical Journal, 1997. **475**(1): p. L69-L72.

49. Kaiser, R.I., Chemical Reviews, 2002. **102**(5): p. 1309-1358.

50. Farebrother, A.J., Meijer, A.J.H.M., Clary, D.C., and Fisher, A.J., Chemical Physics Letters, 2000. **319**(3-4): p. 303-308.

51. Ehrenfreund, P., Space Science Reviews, 1999. **90**(1-2): p. 233-238.

52. Ehrenfreund, P. and Schutte, W.A., *Infrared observations of interstellar ices*, in *Astrochemistry: From Molecular Clouds to Planetary Systems.* 2000. p. 135-146.

53. Tielens, A. and Charnley, S.B., Origins of Life and Evolution of the Biosphere, 1997. **27**(1-3): p. 23-51.

54. Brown, P.D., Charnley, S.B., and Millar, T.J., Monthly Notices of the Royal Astronomical Society, 1988. **231**(2): p. 409-417.

55. Tielens, A. and Hagen, W., Astronomy and Astrophysics, 1982. **114**(2): p. 245-260.

56. Jenniskens, P., Blake, D.F., Wilson, M.A., and Pohorille, A., Astrophysical Journal, 1995. **455**(1): p. 389-401.

57. Tielens, A. and Allamandola, L.J., *Evolution of Interstellar Dust*, in *Physical Processes in Interstellar Clouds*, G. Morfill and M. Scholer, Editors. 1987, Reidel. p. 333-376.

58. Brown, P.D. and Millar, T.J., Monthly Notices of the Royal Astronomical Society, 1989. **240**(2): p. P25-P29.

59. Brown, P.D. and Millar, T.J., Monthly Notices of the Royal Astronomical Society, 1989. **237**(3): p. 661-671.

60. Olofsson, H., Astronomy and Astrophysics, 1984. **134**(1): p. 36-44.

61. Moore, E.L., Langer, W.D., and Huguenin, G.R., Astrophysical Journal, 1986. **306**(2): p. 682-690.

62. Brown, P.D. and Charnley, S.B., Monthly Notices of the Royal Astronomical Society, 1990. **244**(3): p. 432-443.

63. Millar, T.J., Olofsson, H., Hjalmarson, A., and Brown, P.D., Astronomy and Astrophysics, 1988. **205**(1-2): p. L5-L7.

64. Ehrenfreund, P. and Fraser, H.J. *Ice Chemistry in Space.* in *Proceedings of the NATO Advanced Study Institute on Solid State Astrochemistry.* 2000. Sicily, Italy.

65. Ehrenfreund, P., Boogert, A., Gerakines, P., and Tielens, A., Faraday Discussions, 1998(109): p. 463-474.

66. Barnun, A., Dror, J., Kochavi, E., and Laufer, D., Physical Review B, 1987. **35**(5): p. 2427-2435.

67. Bar-Nun, A. and Laufer, D., Icarus, 2003. **161**(1): p. 157-163.

68. Notesco, G., Bar-Nun, A., and Owen, T., Icarus, 2003. **162**(1): p. 183-189.

69. Notesco, G. and Bar-Nun, A., Icarus, 2000. **148**(2): p. 456-463.

70. Blake, D., Allamandola, L., Sandford, S., Hudgins, D., and Freund, F., Science, 1991. **254**(5031): p. 548-551.

71. Allamandola, L.J., Sandford, S.A., and Valero, G.J., Icarus, 1988. **76**(2): p. 225-252.

72. Sandford, S.A. and Allamandola, L.J., Astrophysical Journal, 1993. **417**(2): p. 815-825.

73. Sandford, S.A., Allamandola, L.J., Tielens, A., and Valero, G.J., Astrophysical Journal, 1988. **329**(1): p. 498-510.

74. Collings, M.P., Anderson, M.A., Chen, R., Dever, J.W., Viti, S., Williams, D.A., and McCoustra, M.R.S., Monthly Notices of the Royal Astronomical Society, 2004. **354**(4): p. 1133-1140.

75. Tielens, A., Hagen, W., and Greenberg, J.M., Journal of Physical Chemistry, 1983. **87**(21): p. 4220-4229.

76. Hagen, W., Tielens, A., and Greenberg, J.M., Chemical Physics, 1981. **56**(3): p. 367-379.

77. Jenniskens, P. and Blake, D.F., Science, 1994. **265**(5173): p. 753-756.

78. Allamandola, L.J., Sandford, S.A., Tielens, A., and Herbst, T.M., Astrophysical Journal, 1992. **399**(1): p. 134-146.

79. Dartois, E., Schutte, W., Geballe, T.R., Demyk, K., Ehrenfreund, P., and d'Hendecourt, L., Astronomy and Astrophysics, 1999. **342**(2): p. L32-L35.

80. Pontoppidan, K.M., Dartois, E., van Dishoeck, E.F., Thi, W.F., and d'Hendecourt, L., Astronomy & Astrophysics, 2003. **404**(1): p. L17-L20.

81. Skinner, C.J., Tielens, A., Barlow, M.J., and Justtanont, K., Astrophysical Journal, 1992. **399**(1): p. L79-L82.

82. Ehrenfreund, P., Dartois, E., Demyk, K., and d'Hendecourt, L., Astronomy and Astrophysics, 1998. **339**(1): p. L17-L20.

83. Millar, T.J., Macdonald, G.H., and Habing, R.J., Monthly Notices of the Royal Astronomical Society, 1995. **273**(1): p. 25-29.

84. Turner, B.E., Astrophysical Journal Supplement Series, 1991. **76**(2): p. 617-686.

Chapter 2 Experimental

The extreme conditions of the interstellar medium (ISM) that were described in the previous chapter cannot easily be replicated in the laboratory. However the current experimental setup, utilising an Ultrahigh Vacuum (UHV) system with liquid nitrogen cooled manipulator, enables the experiments described in this thesis to be carried out at exceptionally low pressures and low temperatures. The base pressure for the apparatus is 2×10^{-10} mbar, which is only a few orders of magnitude higher than that of the ISM. The base temperature used in the experiments described here is 95 K which, although considered high for an astrochemical model, continues to have relevance for systems that show elevated grain temperatures. In addition, previous studies of the molecules included in this thesis have demonstrated that the species only desorb when the temperature exceeds 100 K [1]. Dust grains within the dense clouds are believed to have temperatures of around 10 K but they do undergo heating processes due to localised shocks [2] or when present in the vicinity of newly formed stars or hot cores [3].

This chapter will describe the nature of the UHV apparatus and sample mounting used throughout the experiments discussed in this thesis and will summarise the techniques used.

2.1 The Ultra-high Vacuum Apparatus

The system used is shown in *Figure 2.1* and *Figure 2.2*. It comprises a UHV chamber with a liquid nitrogen cooled manipulator. The chamber has two experimental levels between which the sample can be moved by the action of the differentially pumped manipulator (Omniax Translator, MX series, Vacuum Generators, UK). A high precision leak valve is attached to the chamber and is used to controllably backfill the apparatus with gases for adsorption experiments. This leak valve is attached to a stainless steel manifold which in turn is connected to 4 separate gas lines, allowing the successive dosing of several gases into the chamber.

The upper experimental level contains an Ar ion gun (Physical Electronics Inc.) and low energy electron diffraction (LEED) optics (ErLEED-100A, Specs GmbH) that are used for metal sample cleaning and characterisation respectively. Also on this level is a quadrupole mass spectrometer (QMS) (HAL 201, Hiden Analytical Ltd.) used for residual gas analysis and for the temperature programmed desorption (TPD) experiments and an ion gauge for pressure measurement down to UHV.

The lower chamber level is used exclusively for reflection absorption infrared spectroscopy (RAIRS). There are two differentially pumped KBr windows situated on opposite sides of the chamber which allow the passage of the infrared beam from the fourier transform infrared (FTIR) spectrometer and two sets of externally mounted infrared optics.

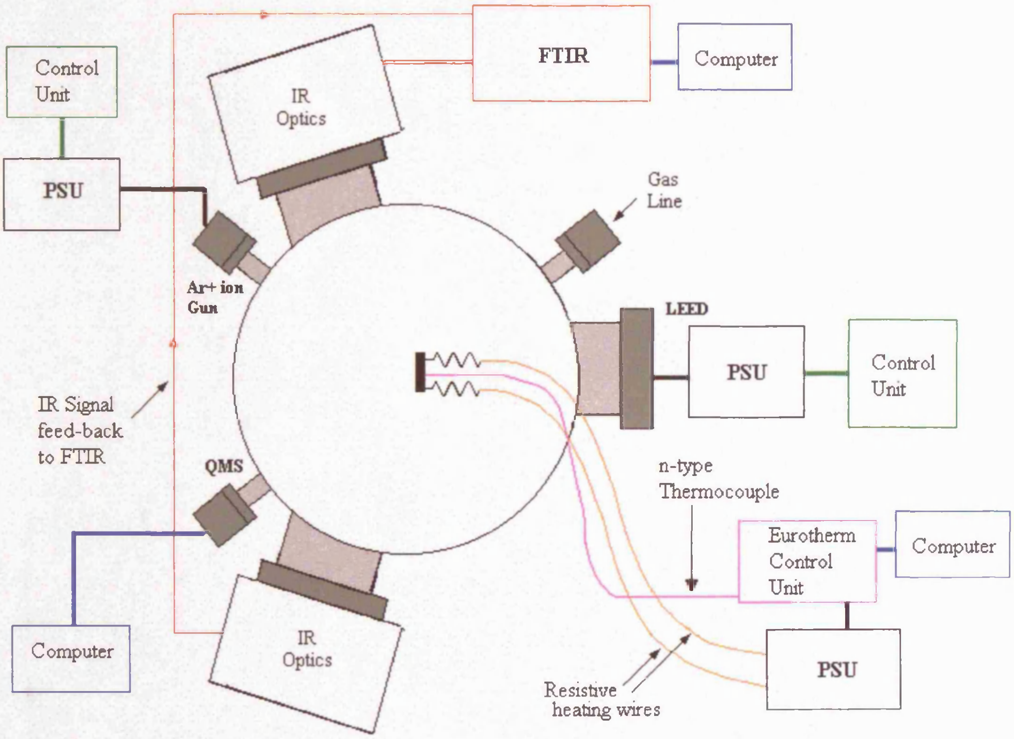

Figure 2.1 Schematic diagram of the experimental apparatus used for the experiments outlined in this thesis [4]. Where PSU is the power supply unit.

The main experimental chamber is connected to the vacuum pumps via a T-section at the base of the chamber as visible in the photograph shown in *Figure 2.2*. High vacuum is achieved by use of a water cooled 145 l s^{-1} turbo-molecular pump (TMP) (Turbovac 151, Leybold Ltd), backed by a 5 m^3 hr^{-1} rotary pump (Trivac D5E, Leybold). To reach UHV, the chamber is baked for a minimum of 24 hours and systematically degassed before optimum pressure can be achieved by the use of a combined ion pump and titanium sublimation pump (TSP) (Captorr ion pump & Boostivac TSP, Physical Electronics). The gas manifold is evacuated with an air cooled 55 l s^{-1} TMP (Turbovac 50, Leybold), backed by a 2.5 m^3 hr^{-1} rotary pump (Trivac D5E, Leybold).

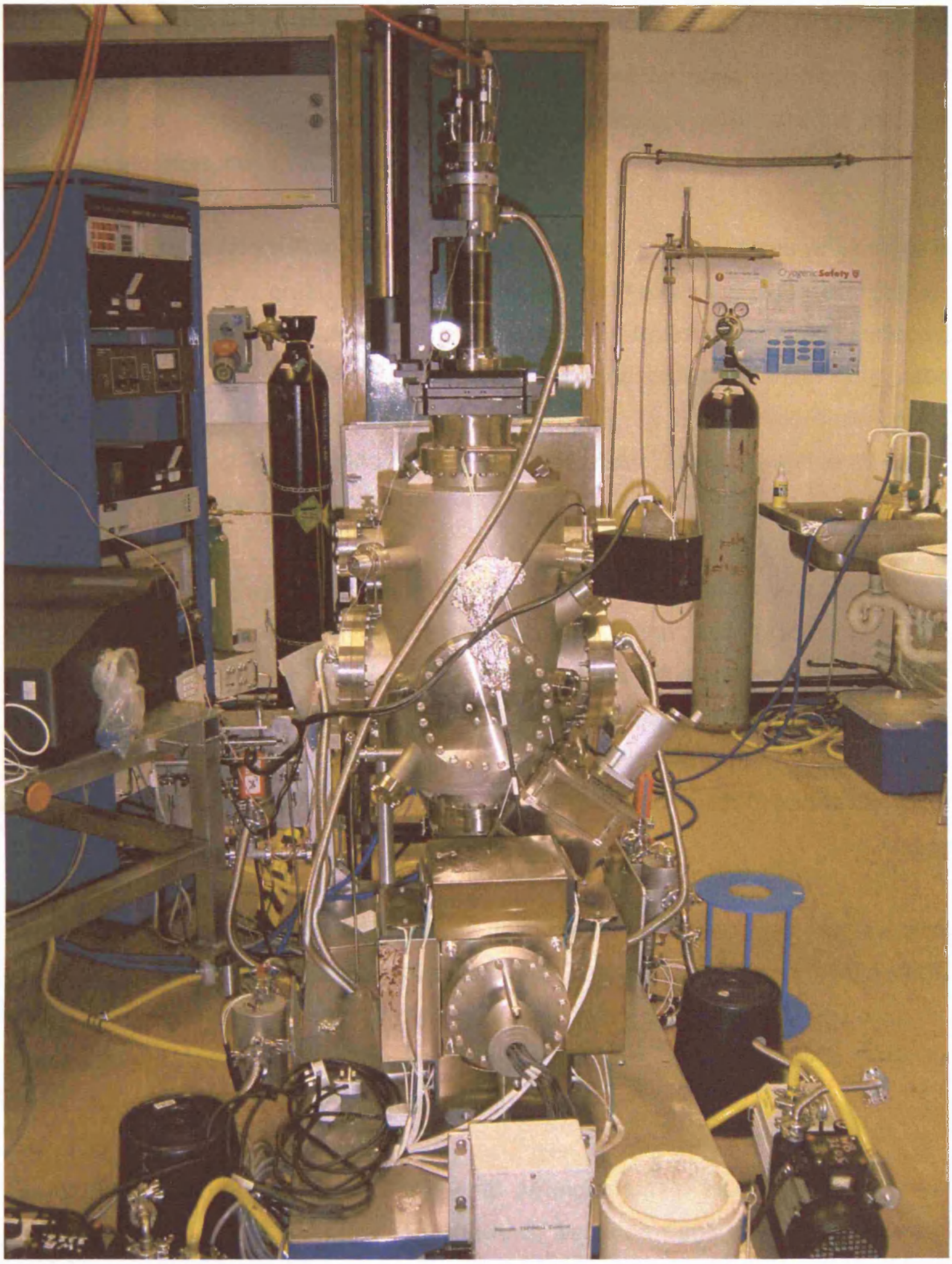

Figure 2.2 Photograph of the experimental apparatus used for the experiments described in this thesis. The external RAIRS optics boxes have been removed.

2.2 The Sample - Highly Oriented Pyrolytic Graphite (HOPG)

The proposed models for dust grains are characterised by huge variations in their properties and composition. Typical models include silicates, carbonaceous material and molecular ices, often with a mix of all three [5, 6].

It is not possible to conclusively model surface chemistry on dust grains while there is no definitive model of a grain. It is therefore necessary to extend experimental studies to a number of different systems which are suitable analogues of dust grain surfaces. Other groups are already working on adsorption and desorption of water dominated ices that have formed on amorphous gold surfaces [1, 7]. The studies described in this thesis will be of ices formed on a graphitic surface, using a sample of highly oriented pyrolytic graphite, HOPG.

HOPG may seem an unlikely model as it is ordered, but its simplicity is a benefit as it enables certain fundamental characteristics of adsorption and desorption of the molecules concerned to be revealed without having the confusion imposed by surface defects. In addition the HOPG surface has been well mapped by theoreticians and so will also enable direct comparison between the experimental results and theoretical calculations. Graphite also obeys the metal surface selection rule [8] and is therefore an ideal substrate for RAIRS experiments.

The HOPG (Goodfellow Ltd, UK) samples used measure 20 mm x 10 mm x 2 mm. HOPG consists of layers of carbon atoms arranged in a honeycomb structure, a single layer of which is demonstrated in *Figure 2.3*. In this figure, the corner of each hexagon represents a carbon atom, and the unit cell is highlighted in red along with its lattice constant, a, which is 2.46 Å, and angle, γ of 60 °.

Figure 2.4 demonstrates the 3-dimensional arrangement of HOPG as each layer stacks on top of the other layers. The distance between each layer is 3.35 Å and clearly demonstrates that the bonding between each layer is considerably weaker than the carbon-carbon bonds within the layer. This characteristic of graphite explains a number of its properties such as electrical conductivity and its ability to act as a lubricant. It also explains why the "scotch tape" method is effective in ensuring a clean surface prior to experimentation [9]. In this method, a piece of sticking tape is applied across the sample surface and then removed to cleave the graphite and reveal a fresh surface.

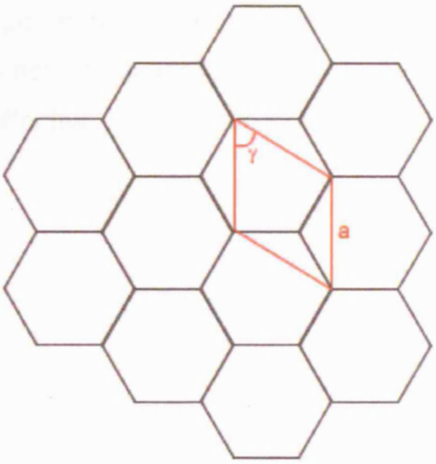

Figure 2.3 Diagram showing the honeycomb structure of HOPG, indicating the unit cell and lattice constant, a [10].

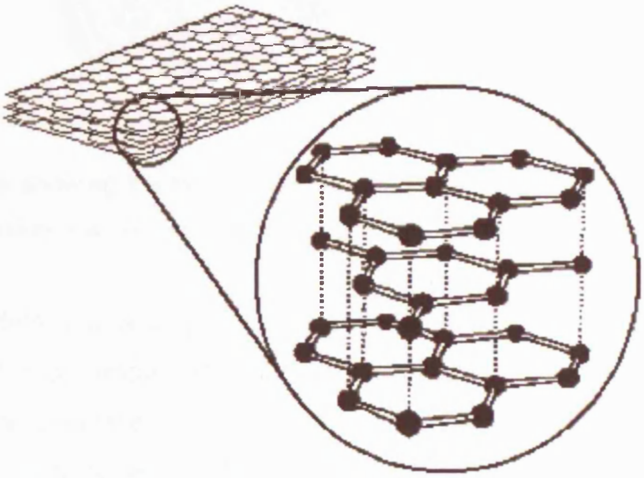

Figure 2.4 A diagram showing the layered structure of HOPG (from: **http://www.chem.wisc.edu/~newtrad/currRef/BDGTopic/BDGtext/BDGGraph.html**)

2.2.1 Sample Mounting

The HOPG sample is mounted on the base of the centrally located liquid nitrogen cooled manipulator. The manipulator can move through all three directions, x, y and z and can be rotated through 360°, which enables the precision positioning of the sample which is essential for both RAIRS and TPD experiments.

In order to clean the sample between experiments it must be annealed to 500 K and then cooled rapidly to experimental temperatures < 100 K. This combined requirement of heating and cooling is not a technically trivial task, but the current mounting system has proved to be very effective. A prototype of the tension wire mounting system is shown in *Figure 2.5.*

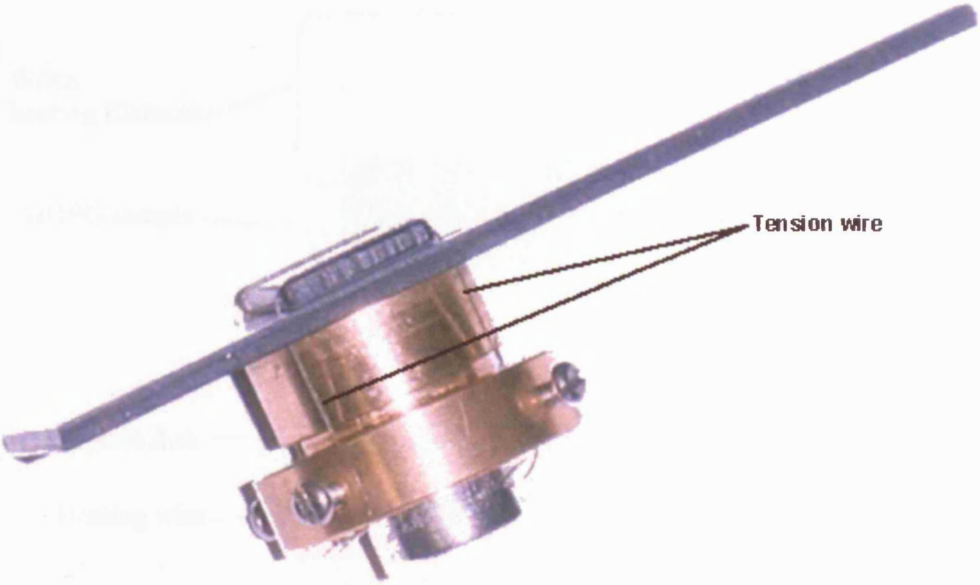

Figure 2.5 Prototype showing the HOPG sample attached to the sapphire block by means of tensioning wire. Tension is achieved by expansion of the copper block mechanism.

The mounting system has been previously described in detail [10] and is illustrated in *Figure 2.6.* The HOPG sample rests upon a back plate of Tantalum foil and both are held tightly onto the sapphire plate by the use of tension wires. Good thermal contact is required at all junctions within the mounting system to ensure adequate thermal conductivity between the heat exchanger at the base of the manipulator and the sample.

The sample is resistively heated using Tungsten/Rhenium (W75/Re25) heating wires which are mounted in tight grooves behind the sample and spot welded to the Tantalum foil back plate. The temperature is measured by an N-type thermocouple which is also spot welded to the Tantalum back plate. The mounting of the heating system is illustrated in *Figure 2.7.*

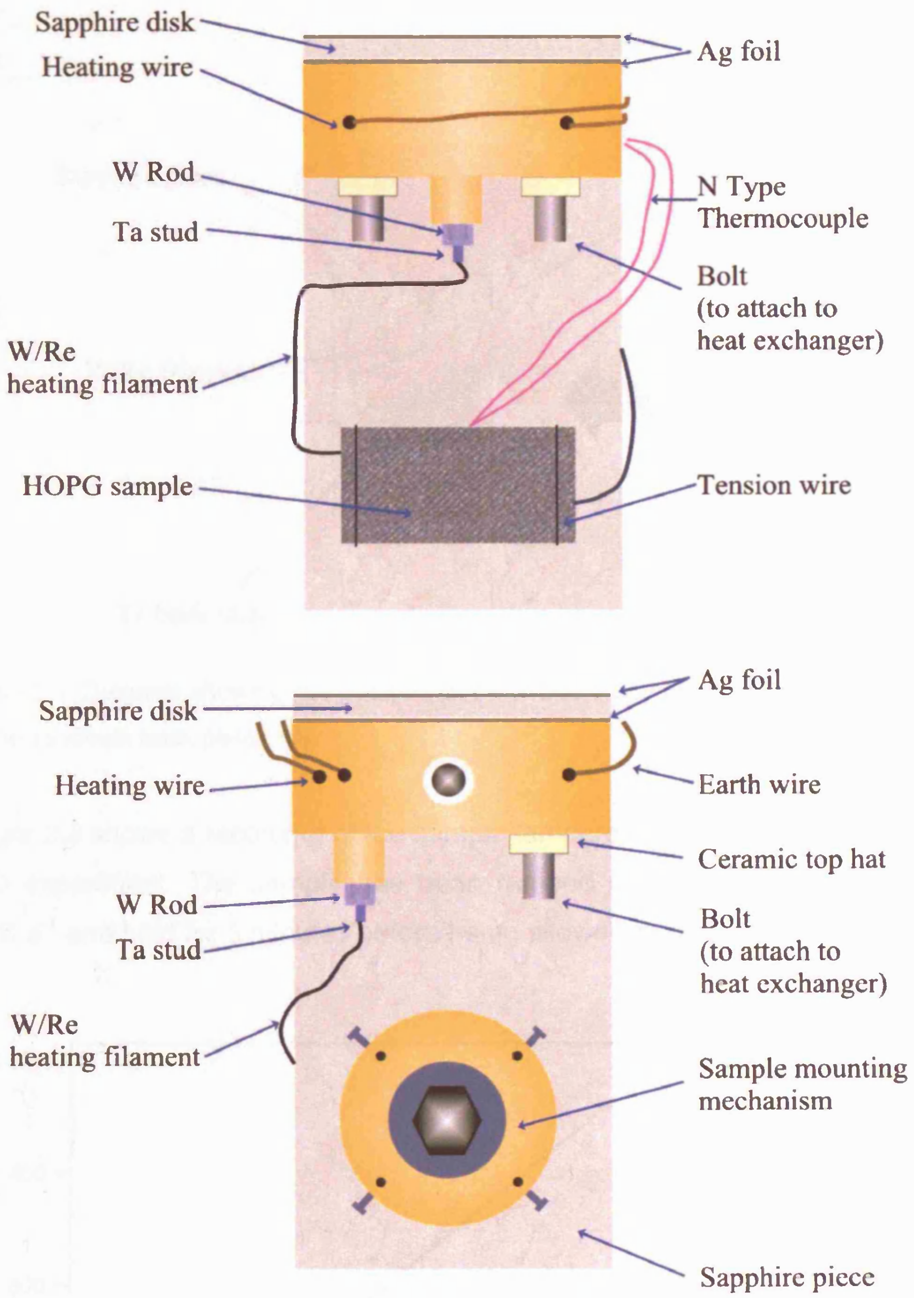

Figure 2.6 Diagram showing the layout of the sample mount attached to the heat exchanger. The sample is held in place by a pair of tension wires. The top diagram shows the front of the sample and the bottom diagram shows the rear of the sample [10].

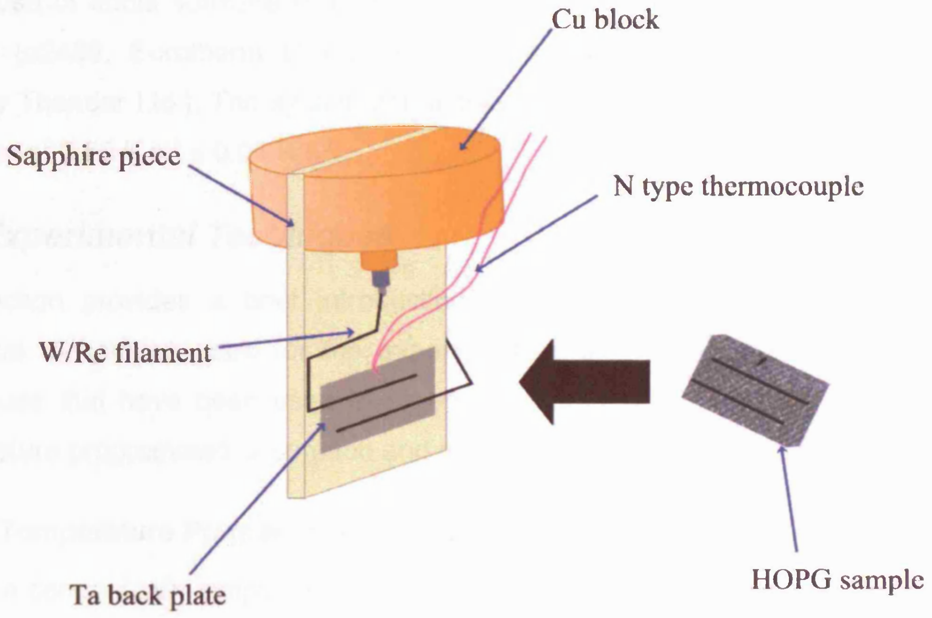

Figure 2.7 Diagram showing the position of the W/Re filaments and the N-type thermocouple on the tantalum back plate [10].

Figure 2.8 shows a recording of the sample temperature as it is controlled for a typical TPD experiment. The sample has been ramped up to 500 K at a heating rate of 0.5 K s^{-1} and held for 3 minutes before being allowed to cool back to 97 K.

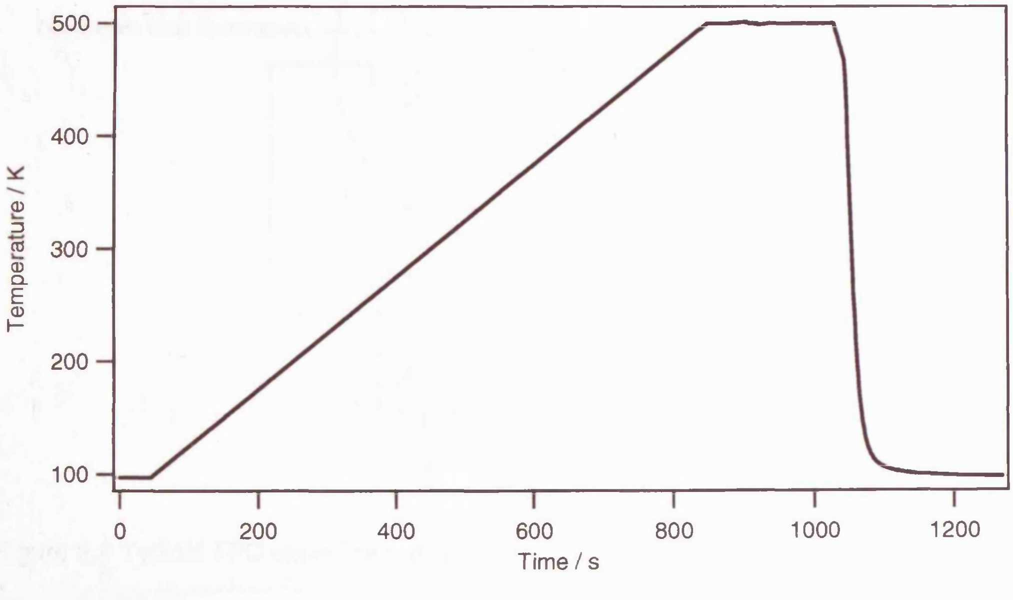

Figure 2.8 Chart showing the variation of temperature with time for a typical experimental heating process. In this case the sample has been ramped to 500 K at a heating rate of 0.5 K s^{-1} and held for 3 minutes before cooling back down to 97 K.

Heating for both the experimentation and annealing processes is controlled remotely by the use of Itools software (Eurotherm Ltd.) and a Eurotherm temperature control module (e2408, Eurotherm Ltd) powered by a Xantrex 30-70 power supply unit (Thurlby Thander Ltd.). The system can achieve a linear heating rate with a recorded accuracy of 0.50 K s^{-1} ± 0.01 K s^{-1}.

2.3 Experimental Techniques

The section provides a brief introduction to the theory behind the two surface analytical techniques used for the experiments presented in this thesis. The two techniques that have been used to probe the nature of the surface adsorbate are temperature programmed desorption and reflection absorption infrared spectroscopy.

2.3.1 Temperature Programmed Desorption (TPD)

TPD is a conceptually simple procedure. The sample is exposed to gas by backfilling the chamber to the required pressure for a predetermined time (1 Langmuir = 1s @ 1 x 10^{-6} mbar), and then heated in a linear manner while mass-selectively detecting the resulting rise in pressure by use of a quadrupole mass spectrometer. The sample temperature is also recorded simultaneously. The process is illustrated in *Figure 2.9.*

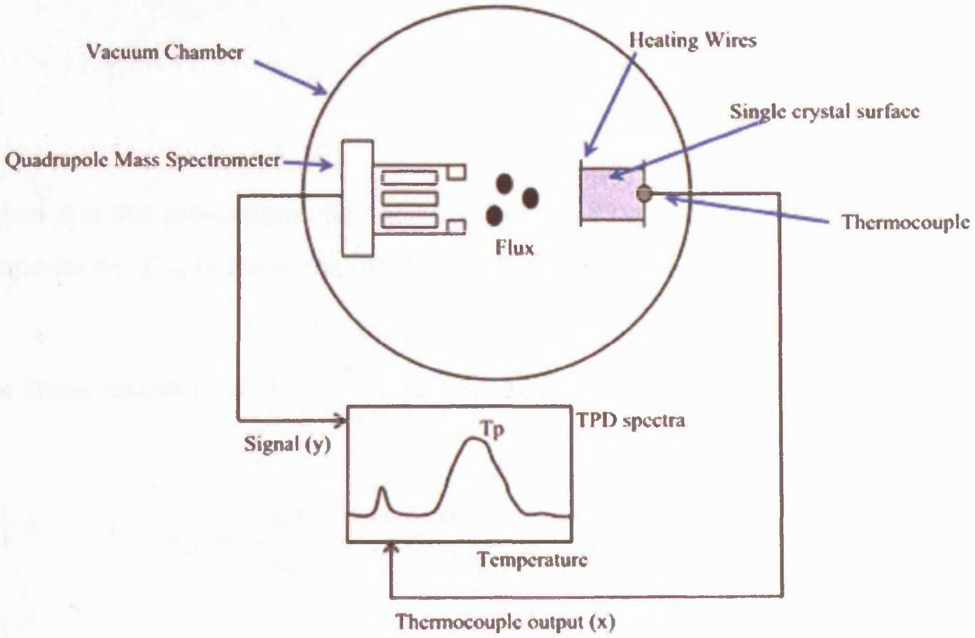

Figure 2.9 Typical TPD experimental set up [11].

TPD can be technically difficult as there are a number of constraints that will affect the accuracy of the spectra. The following list outlines the experimental requirements in a system designed for TPD:

- the sample must be heated in a linear manner
- temperature gradients must not exist across the sample
- the measured temperature must be an accurate representation of the temperature of the sample surface
- only gases desorbing from the surface should be analysed
- rapid pumping rate
- heating rate needs to be high enough to exclude equilibrium systems

A typical TPD spectrum is recorded as the intensity of desorption against temperature and can give an immediate qualitative "feel" of the nature of the surface interactions. It is used to highlight the number of species present, the nature of the surface interaction, the amount of product adsorbed and any reaction products present. True quantitative analysis of the data, revealing heats of adsorption and other kinetic information, is complex and will be discussed in the next chapter.

In TPD, the rate of desorption, r_{des} from the surface is described by the Polanyi-Wigner *Equation 2.1*

$$r_{des} = -\frac{\partial \theta}{\partial t} = A\,\theta^{n} \exp\left(-\frac{E_{des}}{RT}\right) \qquad \text{Equation 2.1}$$

where A is the pre-exponential factor for a kinetic process of order n, T is the surface temperature, E_{des} is the enthalpy of desorption, t is time and θ is coverage.

The linear heating rate β, or $\frac{\partial T}{\partial t}$, can be related to the rate of desorption as follows:

$$r_{des} = -\frac{\partial \theta}{\partial t} = -\frac{\partial T}{\partial t} \times \frac{\partial \theta}{\partial T} \qquad \text{Equation 2.2}$$

Substituting the linear heating ramp into *Equation 2.1* leads to *Equation 2.3*

$$-\frac{\partial \theta}{\partial T} = \frac{\partial t}{\partial T} A\theta^{n} \exp\left(-\frac{E_{des}}{RT}\right) \qquad \text{or}$$

$$-\frac{\partial\theta}{\partial T}=\frac{A\theta^{n}}{\beta}\exp\left(-\frac{E_{des}}{RT}\right)$$ Equation 2.3

The intensity of the desorption signal at a given temperature *I(T)* is proportional to the rate of change of surface coverage with temperature, so *Equation 1.3* can be re-written as:

$$I(T)\propto\frac{A\theta^{n}}{\beta}\exp\left(-\frac{E_{des}}{RT}\right)$$ Equation 2.4

I(T) is at a maximum when $\frac{\partial I}{\partial T}=0$, hence substituting *T* for T_p and differentiating *Equation 2.4* and equating to zero leads to the important *Equation 2.5:*

$$\frac{E_{des}}{RT_p^2}=\frac{nA}{\beta}\theta^{n-1}\exp\left(-\frac{E_{des}}{RT_p}\right)$$ Equation 2.5

For first-order desorption, characteristic of chemisorbed molecular monolayers where the molecule desorbs straight from the surface,

$$\frac{E_{des}}{RT_p{}^2}=\frac{A}{\beta}\exp\left(-\frac{E_{des}}{RT_p}\right)$$ Equation 2.6

For second-order desorption, characteristic of atomic adsorbates which recombine on desorption,

$$\frac{E_{des}}{RT_p{}^2}=\frac{2A\theta}{\beta}\exp\left(-\frac{E_{des}}{RT_p}\right)$$ Equation 2.7

Equations 2.6 and *2.7* show that first-order desorption is independent of initial coverage, while in second-order desorption the peak temperature shifts to lower temperatures as the initial coverage increases, assuming *A* and E_{des} are coverage independent.

Zero order is characteristic of physisorbed multilayers, where desorption is not dependant on coverage and does not technically lead to a peak. Substituting $n = 0$ into *Equation 2.1* indicates that the rate of desorption is a constant with respect to coverage.

2.3.2 Principles of Reflection Absorption Infrared Spectroscopy (RAIRS)

RAIRS is a vibrational technique for non-invasively probing the nature of adsorbates on a reflective surface. It uses an FTIR spectrometer in the reflection mode, as transmission experiments are not viable for opaque surfaces.

When infrared radiation is reflected from a plane surface, the light loses intensity at frequencies matching vibrations either within the adsorbed surface molecule or between the molecule and the surface. Comparison of the reflected beam from a clean surface (background) with the beam focussed through an adsorbate, offers information on the frequencies of vibrations present in the adsorbate [12].

There are two vibrational modes of interest for the surface scientist, those formed as a result of the interaction between the adsorbate and the surface and those within the adsorbed molecule itself. The metal to adsorbate vibrations, or librations, typically occur in the range 200-800 cm^{-1}, whereas the vibrations of functional groups within adsorbed molecules occur above 800 cm^{-1} [12]. The RAIRS set up used here, with a mercury cadmium telluride (MCT) detector, has a low end cut off of approximately 700 cm^{-1}, therefore the vibrations probed are restricted to those within the adsorbed molecule.

Experimentally, a modulated beam of infrared light from the Fourier Transform interferometer is focussed through a KBr window onto the sample surface at an angle of 75°, reflected through another KBr window and then focussed into a LN_2 cooled MCT detector as shown in *Figure 2.10.* KBr windows are chosen as they are transparent to infrared radiation. The entire path of the beam is purged in order to minimise absorption due to atmospheric molecules, in particular water and CO_2.

Energy is extracted from the incident radiation beam due to the excitation of surface vibrations within the adsorbate and represents an interaction between the radiation and the vibrating dipole. The absorption can be greatly enhanced at grazing angles of incidence as can be seen by a simple study of the electric fields involved.

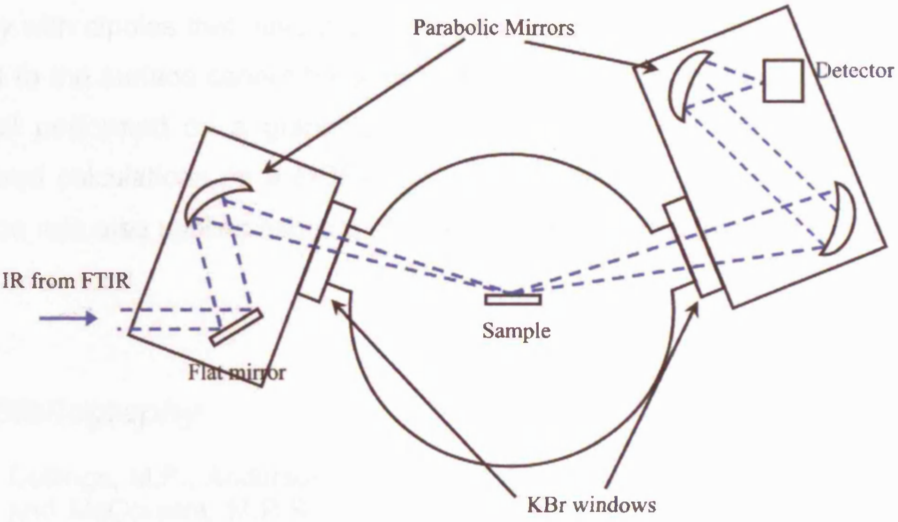

Figure 2.10 Optical arrangement for the FT-RAIRS experiments described in this thesis [12].

Figure 2.11 shows the reflection of incident radiation split into its s (perpendicular) and p (parallel) components. For reflection at a metal surface, at all angles of incidence the phase of the s component is reversed (by 180°) on reflection and therefore the vector sum is close to zero. This means that no IR light is available to interact with dipoles parallel to the surface and hence vibrations parallel to the surface cannot be observed with the RAIRS technique. P polarised light, however, undergoes a phase change dependent on the angle of incidence and its vector sum therefore varies with incidence angle up to a maximum approaching grazing angles [13].

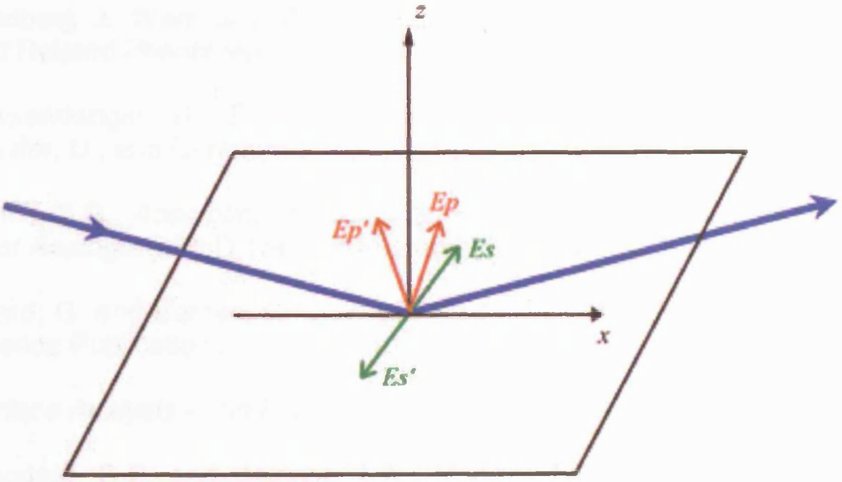

Figure 2.11 A diagram showing the electric fields associated with incident and reflected radiation at metal surfaces [12].

The metal surface selection rule states that the p component can therefore interact strongly with dipoles that have a component perpendicular to the surface but dipoles parallel to the surface cannot be observed. The experiments described in this thesis were all performed on a graphitic surface, however, Heidberg and Warskulat [8] performed calculations on a HOPG surface and determined that the metal surface selection rule also applies although the optimal angle of incidence is 73° as opposed to 88° for a metal.

2.4 Bibliography

1. Collings, M.P., Anderson, M.A., Chen, R., Dever, J.W., Viti, S., Williams, D.A., and McCoustra, M.R.S., Monthly Notices of the Royal Astronomical Society, 2004. **354**(4): p. 1133-1140.
2. Evans, A., *The Dusty Universe*. Series in Space Science and Technology. 1993: Ellis Horwood.
3. Whittet, D.C.B., *Dust in the Galactic Environment*. Series in Astronomy and Astrophysics. 2003: Institute of Physics Publishing.
4. Mukerji, R., *Studies of adsorption and reaction on the stepped Pt{211} surface.* PhD Thesis, Department of Chemistry, 2003, UCL.
5. Draine, B.T., Annual Review of Astronomy and Astrophysics, 2003. **41**: p. 241-89.
6. Greenberg, J.M., Surface Science, 2002. **500**(1-3): p. 793-822.
7. Collings, M.P., Dever, J.W., Fraser, H.J., and McCoustra, M.R.S., Astrophysics and Space Science, 2003. **285**(3-4): p. 633-659.
8. Heidberg, J., Warskulat, M., and Folman, M., Journal of Electron Spectroscopy and Related Phenomena, 1990. **54**: p. 961-970.
9. Wiesendanger, R., Eng, L., Hidber, H.R., Oelhafen, P., Rosenthaler, L., Staufer, U., and Guntherodt, H.J., Surface Science, 1987. **189**: p. 24-28.
10. Bolina, A.S., *Adsorption of Astrochemically Relevant Molecules on Interstellar Dust Analogues.* PhD Thesis, Department of Chemistry, 2005, UCL.
11. Attard, G. and Barnes, C., *Surfaces*. Oxford Chemistry Primers. 1998: Oxford Science Publications.
12. *Surface Analysis - The Principal Techniques*, ed. J.C. Vickerman. 1997: Wiley.
13. Woodruff, D.P. and Delchar, T.A., *Modern Techniques in Surface Science*. Cambridge Solid State Science Series. 1986: Cambridge University Press.

Chapter 3 TPD Studies of the Adsorption and Desorption of Layered Films of Methanol and Water Sequentially Adsorbed on Graphite.

3.1 Introduction

Methanol is one of the most abundant molecular species to have been observed in the interstellar medium, ISM [1]. There is a spatial variation in its distribution, with the fractional abundance relative to H_2 varying from $\approx 3 \times 10^{-9}$ in the cool dark cloud regions [2, 3] and increasing to $\approx 10^{-6}$ in the warm regions of hot cores and high mass protostars [4, 5].

Gas phase formation of methanol is predicted to follow a radiative association reaction between a methyl radical and water to form protonated methanol, which then forms methanol by dissociative association with an electron [1]. This route does not explain the total gas phase abundance and it is therefore necessary to consider the possible formation of methanol on the surface of cold grains [1, 6]. Watanabe et al have conducted a number of studies that demonstrate that methanol can indeed form on the surface of cold grains through the successive hydrogenation of CO molecules within a H_2O:CO mixed ice [7-9].

As predicted, methanol is typically observed within water rich ices and, where present, is often the most abundant molecule after water [10, 11]. Its abundance ratio in the grain mantles is predicted to vary between 0.05 and 0.5 relative to water [10, 12]. This large variation in predicted abundance could be due to segregation within the ice along the observational line of sight or could arise from an incorrect assignment of one of the spectral bands [12]. It is generally considered that the lower abundance estimates are likely to be more accurate [12].

Given the close association of methanol with water in the ISM, a detailed understanding of the desorption of methanol from the surface of icy grains is vital to enable accurate modelling of regions such as hot cores and to explain the observed gas phase abundances [13]. Studies have already been completed on the desorption of pure methanol and pure water from the bare surface of the graphitic dust grain analogue HOPG [14, 15], but combining pure ice studies does not necessarily give reliable results when modelling the behaviour of mixed ices. This chapter will discuss the adsorption and desorption of methanol from a binary layered system consisting of methanol deposited on top of amorphous solid water, ASW.

ASW has aroused much interest in the astrochemical field as it undergoes structural transitions that alter its porosity and surface area and can result in the trapping of certain volatile species [16-19]. Many studies have been completed on mixed methanol and water ices that have been codeposited onto a substrate and these will be discussed further in Chapters 5 and 6 [11, 20-25]. In contrast, binary layered systems have not been considered in such great detail.

As discussed in the introduction, in 1986 Bar Nun and co-workers [17] published a study that highlighted the ability of amorphous solid water to trap argon. They believed that water was able to trap argon within a complex they described as a a clathrate hydrate. Clathrate hydrates are crystalline regions of water ice that enclose or encage small amounts of a guest molecule within the structure [20]. The nature of the guest molecule has been debated, with groups such as Collings et al [25] suggesting that methanol is too large to form a clathrate. However, Blake et al [20, 26, 27] have shown experimentally that methanol can indeed form a clathrate structure, albeit a slightly distorted version classified as a Type II clathrate hydrate. Further studies of the clathrate hydrates will be discussed in more detail later.

Ayotte et al [18] extended the study of Bar Nun [17] by considering the behaviour of Ar, N_2, O_2, CO and CH_4 deposited both on top of and underneath ASW. They observed the trapping of the gaseous species within the water layer but were not able to distinguish between molecules trapped in surface pores and those within clathrate structures.

Souda and co workers [28, 29] completed very convincing studies of methanol and water layers and have articulated some of the latest thoughts on how layered structures of methanol and water intermix. They studied methanol bound to layers of heavy water and observed thermally induced isotope scrambling by the use of temperature programmed time of flight secondary ion mass spectrometry [29]. The group found that the two layers completely intermix above the glass transition temperature of water [28]. The glass transition represents the temperature at which a substance becomes a viscous liquid, and for water this occurs at 136 K [28, 30].

In contrast to studies of mixed ice systems, layered studies of water and methanol are quite limited. In this work, detailed TPD studies of methanol adsorbed on differing thicknesses of pre-existing layers of water ice will be reported. In all cases the underlying substrate is HOPG and the results complement previous work carried out for pure methanol adsorbed on HOPG [14] and pure water adsorbed on HOPG [15], and have important implications for future astrochemical models.

3.2 Methodology

Experiments were performed in an ultra-high vacuum (UHV) chamber, described in Chapter 2. The chamber has a base pressure of 2 x 10 $^{-10}$ mbar. The HOPG sample has been described previously along with the "scotch tape" method of cleaning [15].

All TPD experiments were performed at a heating rate of 0.50 K s^{-1} ± 0.01 K s^{-1}. The temperature was monitored with an N-type thermocouple mounted in a groove behind the face of the HOPG sample. Heating was achieved by the use of two resistive heating elements, again mounted in grooves behind the sample and the steady heating rate was maintained by a Eurotherm temperature control unit. Spectra for masses 31, 32 and 18 were recorded simultaneously with a Hiden Analytical HAL201 quadrupole mass spectrometer. The methanol cracking pattern was monitored during experiments and the mass 31 to 32 ratio remained constant throughout, showing that dissociative surface chemistry was not a feature of the reported experiments. Mass 31 is the major fragment detected by the mass spectrometer for methanol and is reported in preference to mass 32 throughout. The sample was cleaned between experiments by annealing at 500 K for 3 minutes.

Ices were grown in situ by exposing the cold HOPG surface, held at $\approx$ 97 K, to a stream of gas by back filling the chamber through a high precision leak valve. The exposures were measured in Langmuir (L), where 1 L = 10^{-6} mbar s and were recorded during dosing by the mass spectrometer, to enable the relative doses of the two species to be determined. The chamber pressure was allowed to recover to $\approx$ 9 x 10^{-10} mbar before TPD spectra were recorded. The chemicals used during the experiments were distilled, de-ionised water and methanol (CH_3OH – 99.9% - Aristar – BDH). The purity of the dosed species was confirmed by monitoring the mass spectrometer during dosing.

3.3 TPD Results and Discussion

In the first series of experiments, increasing doses of methanol were exposed to an existing film of water ice to form a layered ice structure. The ice samples studied are summarised in *Table 3.1.*

Table 3.1 Summary of the layered ice structures and exposures used in the experiments described here. Also included, for comparison, are data for the pure ice systems.

	H_2O / L	CH_3OH / L
Pure H_2O^a	0.1 - 200	-
Pure CH_3OH	-	2 - 300
CH_3OH/H_2O	2	3 - 300
CH_3OH/H_2O	10	3 - 300
CH_3OH/H_2O	50	3 - 300

[a] data previously reported by Bolina et al [15].

The mixed ice notation previously described by Bisschop et al [31] has been adopted, so that CH_3OH/H_2O ice indicates that the methanol species appears on top of the water with a layered morphology.

3.3.1 Pure Ice Systems

In recent publications, the desorption characteristics of pure water and pure methanol on a HOPG surface were reported along with the calculated desorption orders and desorption energies for these systems [14, 15]. In order to allow comparisons to be made with the results from the layered systems, the features of the pure ice systems are reproduced in *Figures 3.1a, b, c* and *d.* The figure shows TPD spectra for increasing exposures of pure water and methanol, deposited on a HOPG sample at 97 K. *Figure 3.1a* shows TPD spectra following low exposures of pure water onto HOPG [15][§]. The following peak assignments were made: Peak A is assigned to the desorption of water molecules from 2-dimensional islands and Peak B is assigned to multilayer desorption from 3-dimensional islands. At higher exposures, as shown in *Figure 3.1b*, Peak B' represents the combination of peaks of A and B, and is assigned to the desorption of multilayer water.

[§] The pure water spectra shown in Figure 3.1 were obtained with a different sample mounting compared to the data discussed in this thesis. Since this data has been taken, it has been determined that there was a small systematic error in the thermocouple reading for the previous experiments. Therefore, in order to compare the previous results [15] with the data in this thesis, a systematic offset in the previous temperature readings has been introduced and all spectra displayed in Figure 3.1 are offset by -9 K. This small temperature offset does not affect the values of the kinetic parameters, previously determined for water [15].

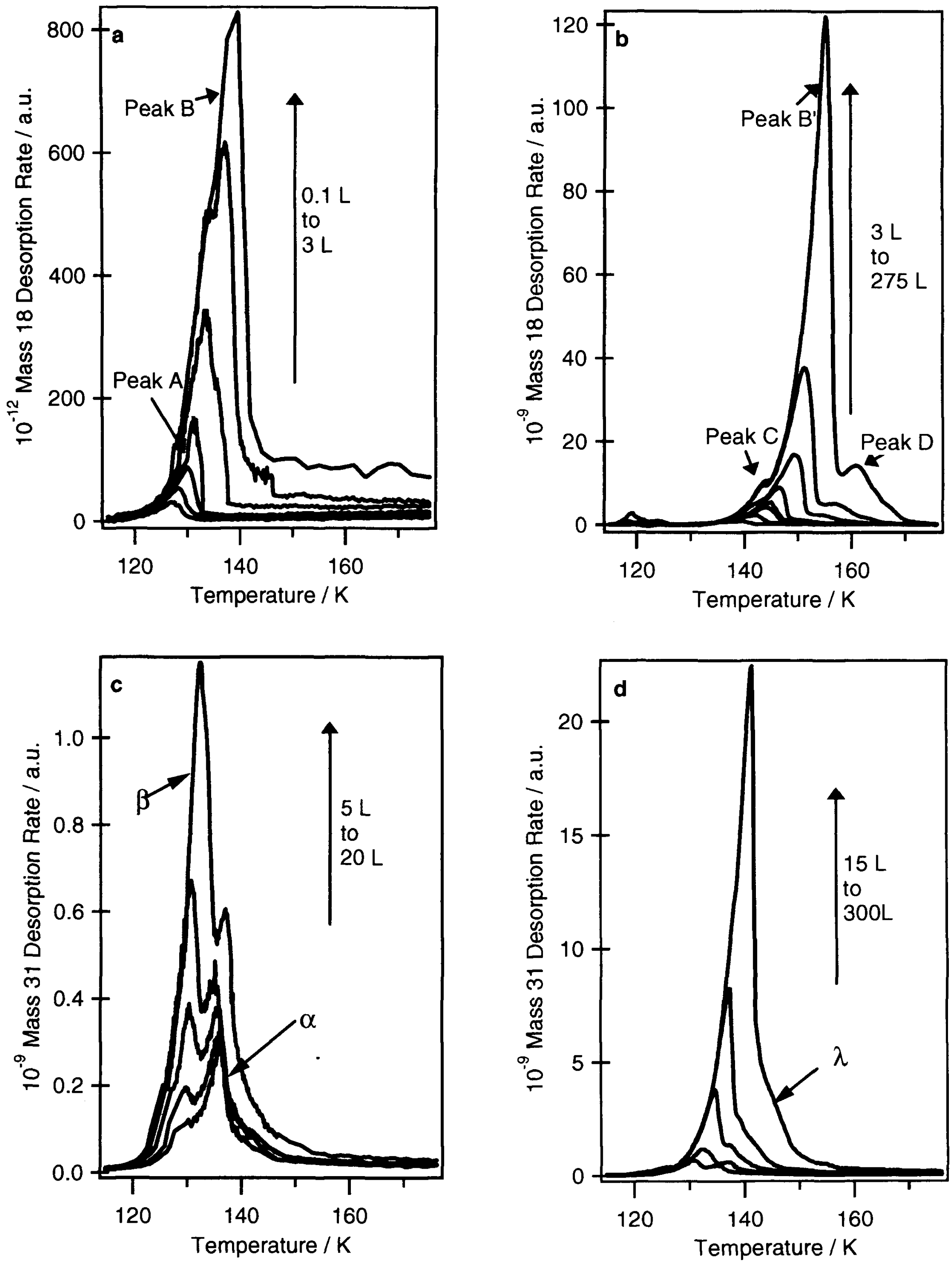

Figure 3.1 TPD spectra for increasing exposures of pure ices deposited on a HOPG surface at 97 K. (a) H_2O exposures of 0.1, 0.2, 0.3, 0.4, 1, 2 and 3 L [15]§, (b) H_2O exposures of 3, 7, 10, 15, 20, 50, 100 and 275 L [15]§, (c) CH_3OH exposures of 5, 7, 10, 15 and 20 L, and (d) CH_3OH exposures of 15, 20, 50, 100 and 300 L.

Peak C and Peak D are both assigned to phase changes within the water ice. The low temperature bump, labelled Peak C, at ≈ 146 K represents the conversion of water in its amorphous phase to crystalline ice, CI. The phase transition is accompanied by a change in the vapour pressure of the ice and hence a change in the desorption rate which gives rise to the bump in the spectra. The higher temperature phase transition, at ≈ 162 K, has been assigned to the CI to hexagonal ice, HI transition [15]. In both phase transitions the bump only shows for the high exposure layers. With the thinner layers, the transition occurs before desorption takes place and so is not visible.

The interaction of pure methanol with a graphite surface has also been studied previously [14] and the assignments for the spectra shown in *Figure 3.1c* and *3.1d* are consistent with the earlier report. Peak α is assigned to the monolayer feature which saturates following ≈ 5 L exposure, Peak β is the multilayer desorption feature and the high temperature bump, labelled λ, is thought to be due to the desorption of crystalline multilayer methanol that forms during the TPD heating process.

3.3.2 Sequential Dosing

Within this study, three separate adsorbate systems were examined in order to explore the ice desorption features as a function of the underlying water multilayer thickness. Previous studies of pure H_2O adsorption on HOPG, using the same experimental system, have reported the formation of three dimensional islands, and therefore multilayer ice formation, following a water exposure of between 1 and 2 L [15]. As a result, water exposures of 2 L, 10 L and 50 L, corresponding to thin, medium and thick multilayers of water ice respectively, were investigated. These will be described as CH_3OH/H_2O(2 L), CH_3OH/H_2O(10 L) and CH_3OH/H_2O(50 L), where the figure in brackets represents the exposure used to create the underlying water ice in the layered system.

Water ice is known to exist in a number of different phases with its precise morphology depending on deposition conditions [32, 33]. Previous studies have shown that water ice grows in the ASW phase at deposition temperatures below 135 K. ASW is therefore the dominant phase of the pre-existing water layers described in this work. The water layers were deposited at 97 K and the phase was confirmed by the fingerprint OH ratio in the RAIR spectra [15].

3.3.3 Water Desorption

Desorption traces for masses 31, 32 and 18 were recorded simultaneously, but as the mass spectrometer has different sensitivities for methanol and water, the spectra are plotted separately for clarity. Mass 18, water, TPD spectra are reported in *Figure 3.2*, which shows desorption of the water sub-layer for all three systems. In each chart the same amount of water has been adsorbed; 2 L for *Figure 3.2a*, 10 L for *Figure 3.2b* and 50 L for *Figure 3.2c*. However, the thickness of the overlaying methanol layer is increasing in each case and the individual traces are colour coded to indicate this increase.

With the thinnest sub-layer of water ice, in the CH_3OH/H_2O(2 L) system shown in *Figure 3.2a*, a single, consistent and reproducible water peak is recorded at 139 K for all methanol exposures ≤ 50 L.

In TPD, the area under the peak gives a measure of the amount of desorbing species. Within experimental error the integrated peak area for the 2 L exposure of water, normalised for variations in dose, remains relatively constant as expected, see *Figure 3.3*. However, as the methanol overlayer exposure increases to 100 L the water peak broadens and shows a second peak at 150 K. By 300 L the water trace now shows a very sharp peak at 140 K, with a shoulder at 143 K and a smaller peak at ≈ 152 K. With the latter two exposures of methanol, it is found that the integrated area under the water trace has increased significantly as shown in *Figure 3.3*. The sharp peak coincides with the maximum desorption rate of methanol, also recorded at 140 K.

Figure 3.2b shows water desorption traces for the CH_3OH/H_2O(10 L) system. With low exposures of methanol overlaying the water, a single peak at 144 K is recorded. As the methanol exposure increases, the water peak shows a shift up in temperature, (see the inset in *Figure 3.2b*), and by 300 L of methanol the water peak temperature is 155 K. The bump appearing at 144 K in the water trace for the layered system covered by a 300 L methanol exposure has not proved reproducible and can be ignored. As for the desorption of the water from the CH_3OH/H_2O (2 L) system, the peaks also show a broadening as the methanol exposure increases, although the normalised integrated area for the mass 18 peak remains relatively constant, as shown in *Figure 3.4*.

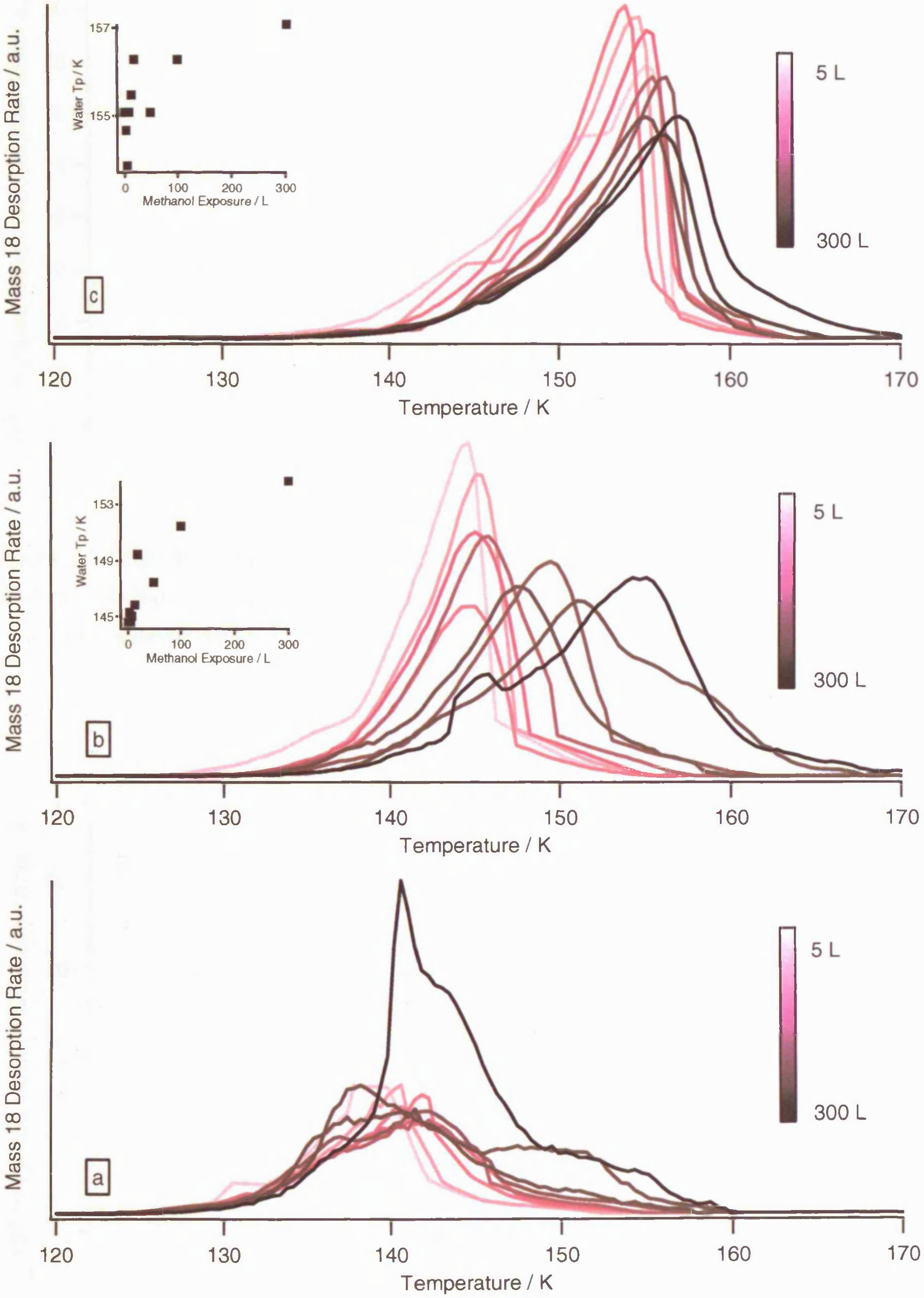

Figure 3.2 TPD traces showing the desorption of water from CH_3OH/H_2O layered structures adsorbed on HOPG at 97 K. The amount of methanol overlaying the water ice increases through the exposures of 3 L, 5 L, 7 L, 10 L, 15 L, 20 L, 50 L, 100 L and 300 L. a) 2 L exposure of H_2O ice, b) 10 L exposure of H_2O ice and c) 50 L exposure of H_2O ice on a HOPG surface at 97 K. The insets in charts b and c represent the water peak temperature, *Tp* as a function of methanol overlayer coverage.

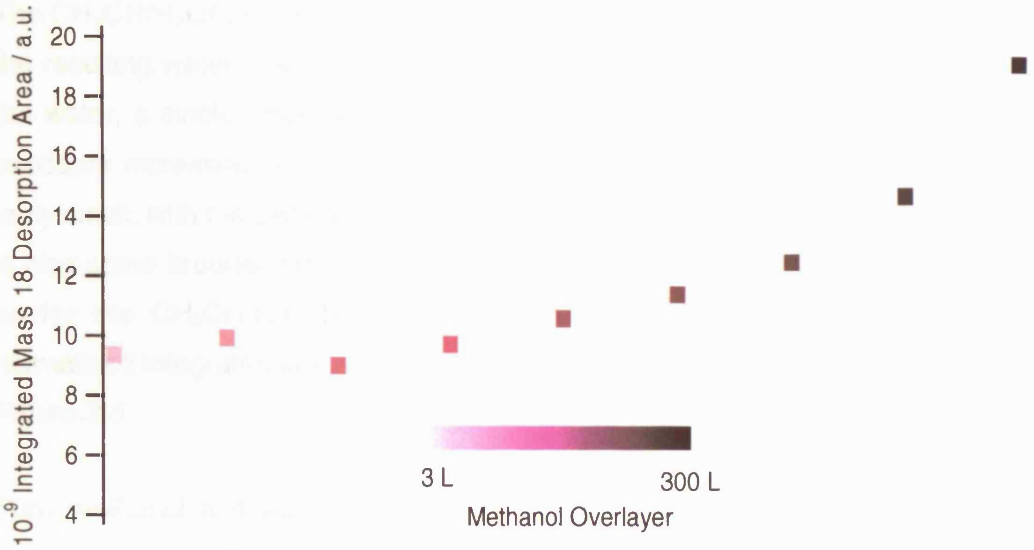

Figure 3.3 Chart showing the variation in the integrated area under the 2 L water TPD curve produced for the CH_3OH/H_2O(2 L) layered ice as the exposure, and hence thickness, of the methanol overlayer increases.

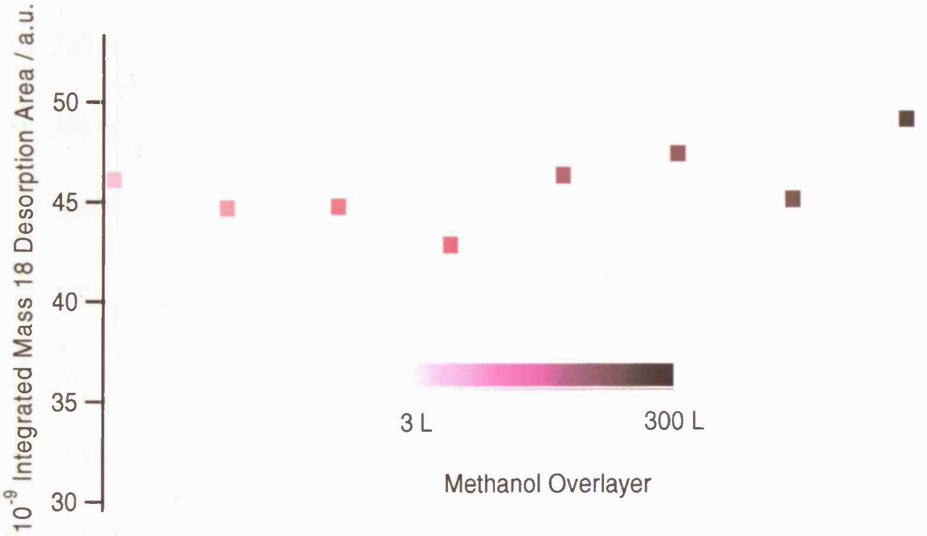

Figure 3.4 Chart showing the variation in the integrated area under the 10 L mass 18 TPD curve produced for the CH_3OH/H_2O(10 L) layered ice as the exposure, and hence thickness, of the methanol overlayer increases.

The CH_3OH/H_2O(50 L) system also shows a very similar trend, and *Figure 3.2c* shows the resulting water desorption traces. Again at low exposures of methanol overlaying the water, a single peak is recorded which shifts up in temperature as the methanol exposure increases (see the inset in *Figure 3.2c*). The shift in peak temperature is fairly small, with the peak starting at 154 K and moving to a maximum of 157 K. There is also some broadening but, as with the temperature shift, this is not as pronounced as for the CH_3OH/H_2O(10 L) system. As for the CH_3OH/H_2O(10 L) system the normalised integrated areas for the 50 L of water ice remain fairly constant, as seen in *Figure 3.5*.

Pure methanol and water multilayer desorption are both characterised by fractional order processes [14, 15, 34-36] and, as a result, desorption temperatures are expected to increase with coverage. Within each system considered, the water exposure remains constant and so it would be expected that the peak temperature of the water desorption would also remain constant. Referring back to *Figure 3.2*, it can be seen that the water desorption temperature appears to remain constant for the CH_3OH/H_2O(2 L) system, but clearly shifts to higher temperatures as the methanol exposure increases in both the CH_3OH/H_2O(10 L) and CH_3OH/H_2O(50 L) systems.

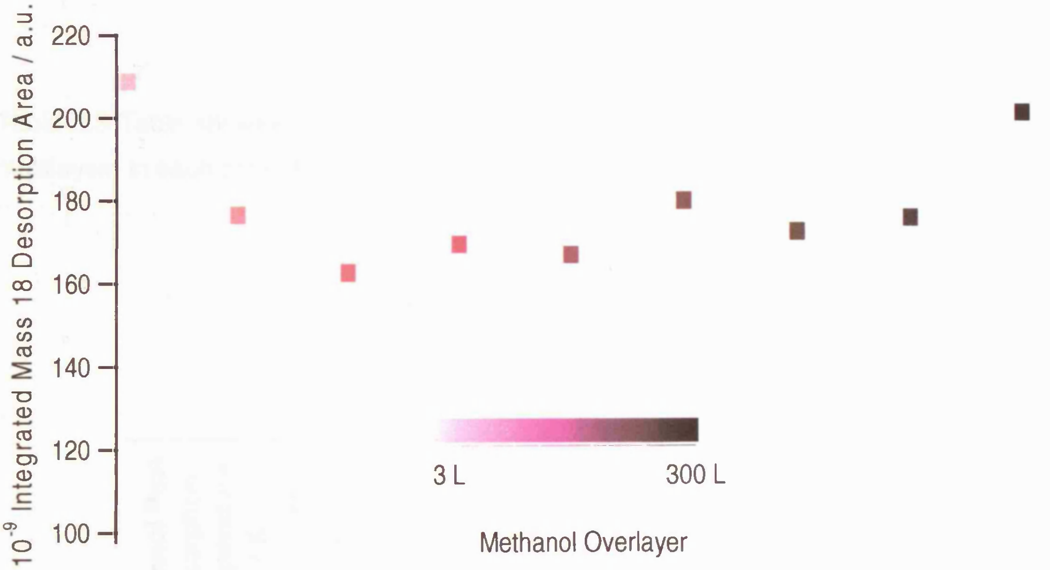

Figure 3.5 Chart showing the variation in the integrated area under the 50 L mass 18 TPD curve produced for the CH_3OH/H_2O(50 L) layered ice as the exposure, and hence thickness, of the methanol overlayer increases.

This broadening and shifting of the water peaks in the layered systems can be understood by considering the interplay between the relative coverages of water and methanol and their individual desorption temperatures. The peak desorption temperatures for water (and those for methanol) are shown in *Tables 3.2* and *3.3*. Note that, in each case, the temperature shown is for the maximal rate of desorption (i.e. the peak temperature) and not the point at which all of the adsorbate has been released. The data for methanol is included at this point to aid the discussion, but will be considered in more detail later in the chapter.

Table 3.2 Table showing the water peak desorption temperatures for pure water and water in each of the three CH_3OH/H_2O layered systems adsorbed on HOPG. These figures are plotted in the inset to Figure 3.2.

	System		**Methanol Exposure**									
		Pure H_2O	**3 L**	**5 L**	**7 L**	**10 L**	**15 L**	**20 L**	**50 L**	**100 L**	**300 L**
Water Peak Desorption Temperature / K	**CH_3OH/H_2O(2 L)**	140	138	141	142	142	142	142	141		141
	CH_3OH/H_2O(10 L)	144	144	145	145	145	146	149	148	151	155
	CH_3OH/H_2O(50 L)	153	155	154	154	155	156	156	155	156	157

Table 3.3 Table showing the peak desorption temperatures for pure methanol and methanol multilayers in each of the three CH_3OH/H_2O layered systems.

	System	**Methanol Exposure**					
		10 L	**15 L**	**20 L**	**50 L**	**100 L**	**300 L**
	Pure Methanol	132	132	133	135	137	142
Methanol Peak Desorption Temperature / K	**CH_3OH/H_2O(2 L)**	-	-	131	133	135	141
	CH_3OH/H_2O(10 L)	-	-	-	135	139	143
	CH_3OH/H_2O(50 L)	-	-	136	138	146 & 150	153

It appears that water desorption is inhibited by large overlayers of methanol, which act to hold the water in place. This results in a broadening of the water desorption peak and an increasing water peak temperature with increasing thickness of the methanol overlayer, see insets in *Figure 3.2*. Due to the sequential nature of the dosing, the water cannot desorb until the retaining methanol has also desorbed. Hence, in cases where the methanol desorption occurs around, or beyond, the pure water desorption temperature, a delay will occur, resulting in a broadening of the spectra and a higher peak temperature.

It is clear from *Figure 3.2* that the water desorption shows different features in the CH_3OH/H_2O(2 L) system, compared to the remaining two systems. At low exposures of methanol the water desorption peak remains approximately constant but as the methanol exposure increases beyond 100 L the peak shape, integrated area (see *Figure 3.3*) and behaviour changes dramatically. With a sublayer of only 2 L the water is held in place beyond its “natural” or pure desorption temperature, in this case 140 K. Hence, by the time the retaining methanol has desorbed at 141 K the water explodes from the surface at a rate that exceeds the pumping speed of the vacuum chamber. This explains why the apparent water coverage increases for the 2 L system and why the peak is so sharp.

For the 10 L sublayer, the pure desorption temperature of water (144 K) is only slightly higher than that of the highest exposures of methanol (143 K). Competition between the two processes will result in a broadening and delay of the water desorption, but does not lead to the explosive desorption seen for the CH_3OH/H_2O(2 L) system. With the 50 L water sublayer there are much less obvious effects on the water desorption as the methanol overlayer thickness increases, the shift in temperature is less and the broadening is slight. The pure desorption temperature of 50 L of water is $\approx$ 153 K, which is 10 K higher than the recorded peak temperature of 142 K for 300 L of methanol in the pure system. Hence, in this case the water now desorbs at its “natural” temperature and is relatively unaffected by the presence of the methanol overlayer.

3.3.4 Methanol Desorption

CH_3OH TPD spectra following low exposures of methanol on 2 L, 10 L and 50 L of water adsorbed on HOPG at 97 K are shown in *Figures 3.6, 3.8 and 3.10* respectively. CH_3OH TPD spectra following high exposures of methanol on the same water layers are shown in *Figures 3.7, 3.9 and 3.11* respectively.

In the case of methanol desorption from the thinnest (2 L) layer of water, shown in *Figures 3.6 and 3.7*, the methanol TPD spectra are comprised of two peaks. At the lowest exposures, a single peak is visible at 134 K. As the exposure is increased, this peak shifts up in temperature to 136 K and appears to saturate between 7 and 10 L. A second peak is visible at lower temperatures from 7 L onwards.

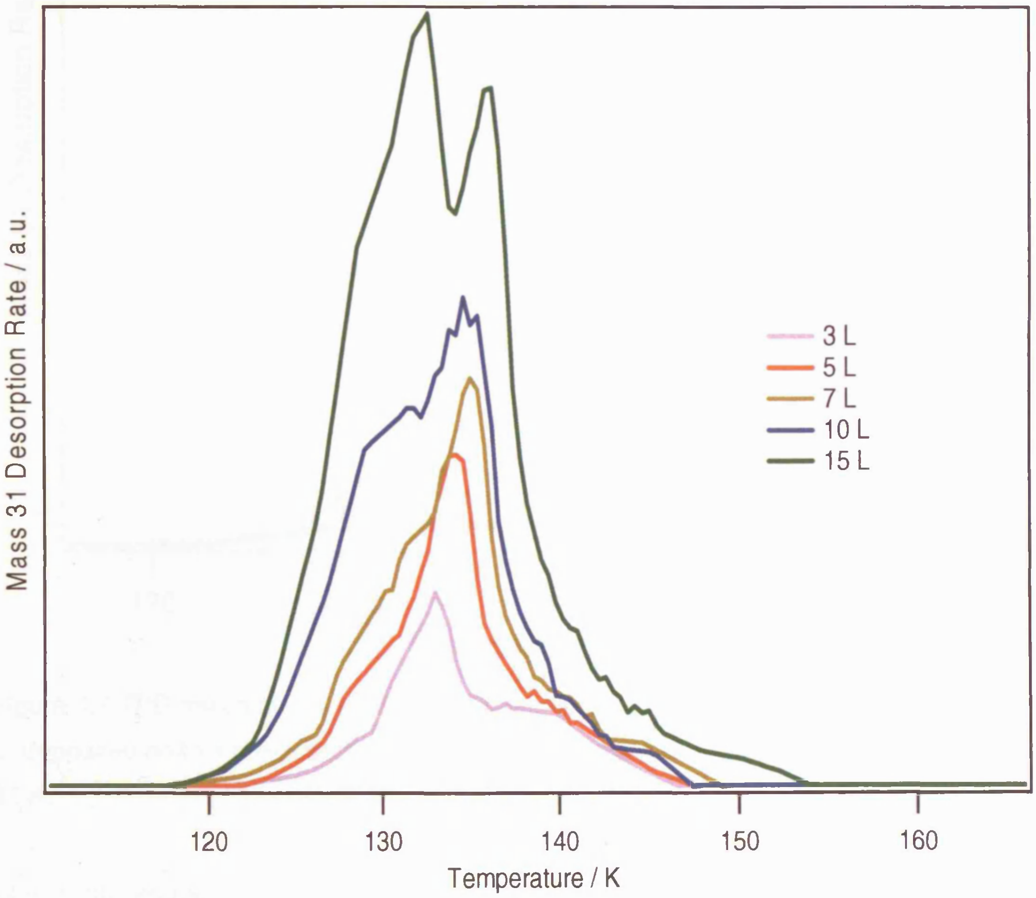

Figure 3.6 Methanol TPD traces following low exposures of methanol (3, 5, 7, 10, and 15 L) deposited on to a pre-adsorbed layer of water ice (2 L exposure) on a HOPG surface at 97 K.

As the methanol exposure is increased beyond 15 L (see *Figure 3.7*), the low temperature peak shifts up in temperature and grows to dominate the spectrum. The peak does not saturate and following a 300 L exposure of methanol the maximal peak desorption occurs at ≈ 140 K.

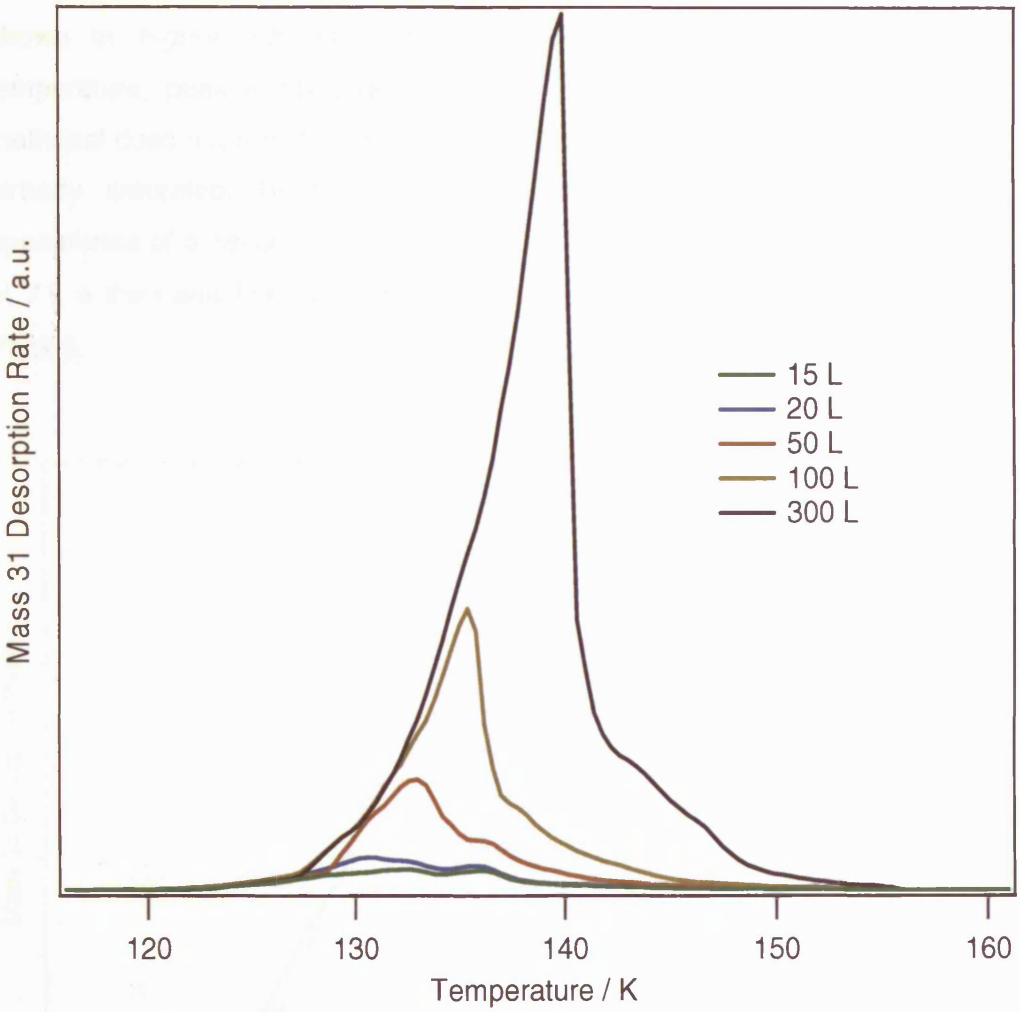

Figure 3.7 TPD traces of intermediate to high exposures of methanol (15, 20, 50, 100 and 300 L) deposited on to a pre-adsorbed multilayer of water ice (2 L exposure) on a HOPG surface at 97 K.

With both peaks observed in the TPD spectra of methanol deposited onto a 2 L layer of water ice, the temperatures, shape and behaviour coincide with the two peaks seen in the spectra for pure methanol adsorbed on the HOPG surface, shown in *Figures 3.1c and d*. The high temperature, saturating, peak is therefore assigned to the desorption of monolayer methanol and the lower temperature, dominant, peak is assigned to the desorption of multilayer methanol.

TPD spectra for the desorption of methanol deposited on the thicker layers (10 and 50 L) of water ice are complex, with three desorption features visible, and will be considered individually.

A series of TPD spectra for increasing exposures of methanol on 10 L of water ice are shown in *Figure 3.8*. At methanol exposures below 5 L only a single, high temperature, peak is observable at 145 K, labelled α. Increasing the exposure of methanol does not result in an increase in intensity of this peak, showing that this has already saturated. However, increasing the methanol exposure leads to the appearance of a second, lower temperature, peak at 133 K, labelled β. At exposures of 7 L a third and final peak, labelled λ, appears as a low temperature shoulder on Peak β.

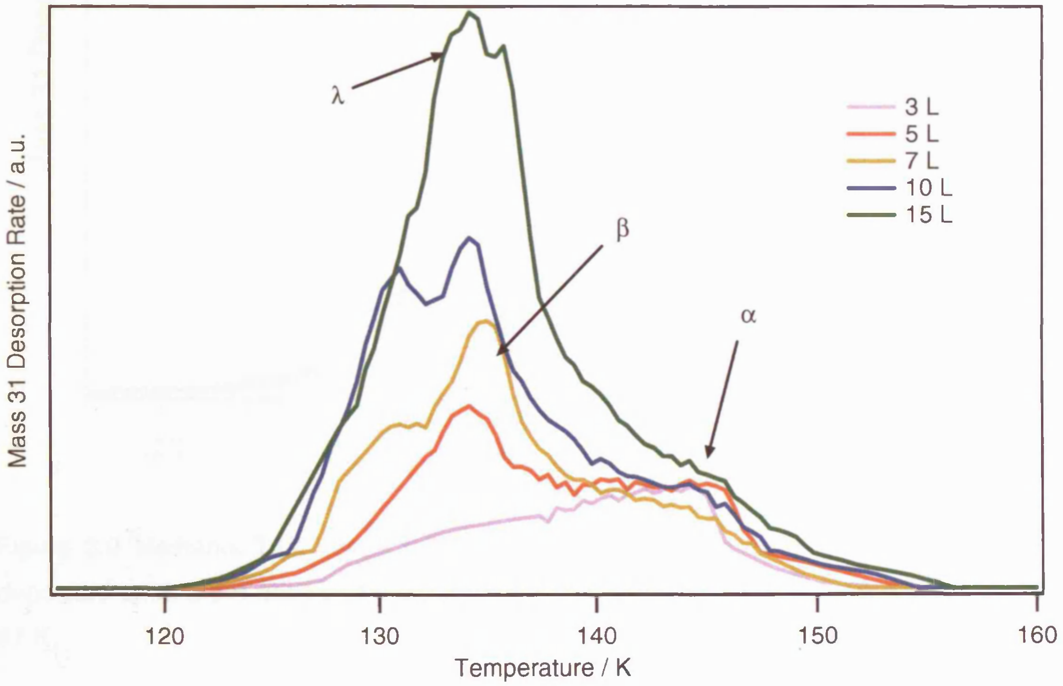

Figure 3.8 Methanol TPD traces following increasing exposures of methanol deposited on to a pre-adsorbed multilayer of water ice (10 L exposure) on a HOPG surface at 97 K.

Increasing the methanol exposure beyond 7 L (*Figure 3.9*), shows that Peak λ begins to dominate the spectrum, and by 50 L Peak α and Peak β can no longer be distinguished. The resulting combined peak shifts up in desorption temperature as the exposure is further increased. This peak does not saturate and by 300 L the maximal desorption temperature has reached 143 K, (*Figure 3.9*). From 50 L upwards a high temperature shoulder is also apparent and this has been labelled δ.

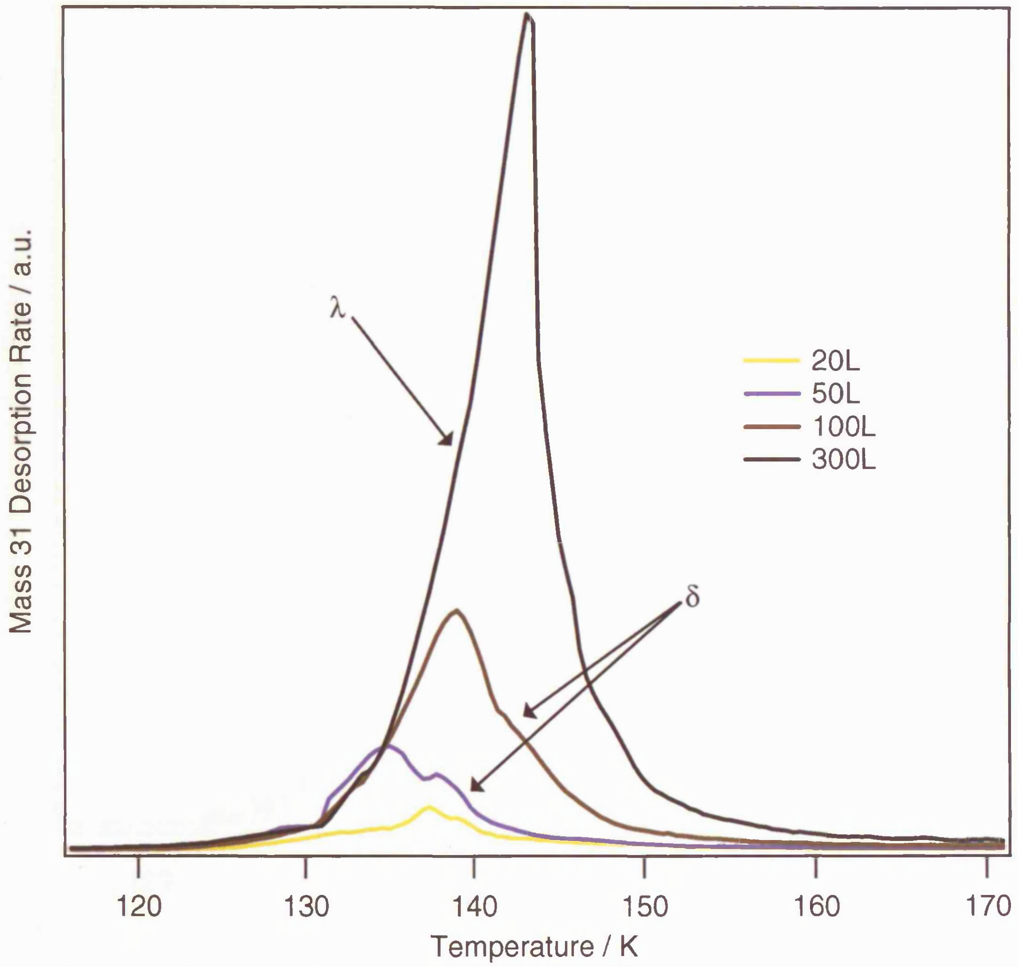

Figure 3.9 Methanol TPD traces following increasing exposures of methanol up to 300 L, deposited on to a pre-adsorbed multilayer of water ice (10 L exposure) on a HOPG surface at 97 K.

Spectra for increasing exposures of methanol on 50 L of water ice are shown in *Figure 3.10*. At methanol exposures below 5 L a broad desorption trace is observed between 124 K and 160 K. Within this broad feature is a single, high temperature, peak at 153 K, labelled α. Increasing the exposure of methanol up to 10 L does not result in an increase in intensity of the α peak indicating that it has already saturated. Instead the lower temperature part of the broad desorption trace increases in intensity but still does not form a defined peak. At exposures of 15 L two additional peaks can now be resolved, a low temperature peak labelled λ, a shoulder labelled β, and a mid-temperature peak at 145 K which is not labelled.

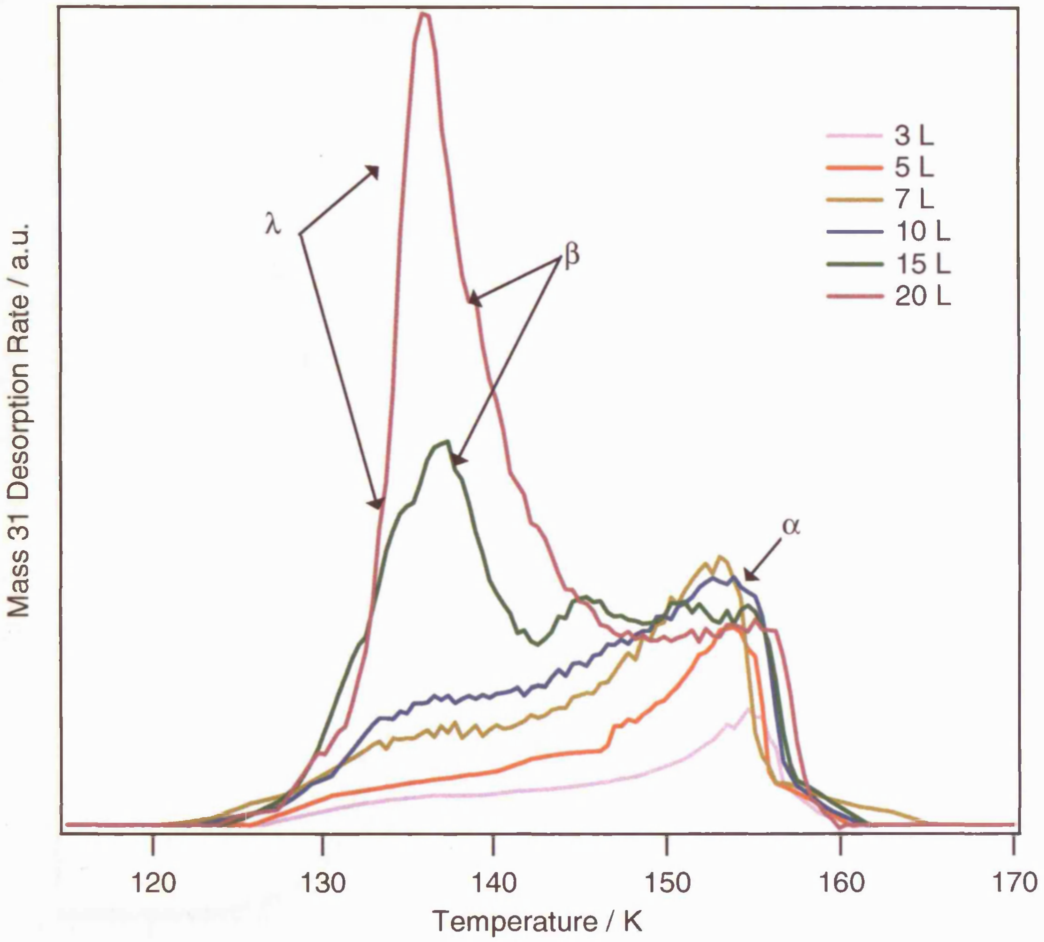

Figure 3.10 Methanol TPD traces following increasing exposures of methanol deposited on to a pre-adsorbed multilayer of water ice (50 L exposure) on a HOPG surface at 97 K.

Increasing the methanol exposure beyond 15 L, results in the λ peak growing in intensity and dominating the spectra, as seen in *Figure 3.11*. Following a methanol dose of 100 L the λ peak splits into two clearly defined peaks of similar intensity. The low temperature peak at 137 K is thought to be a continuation of λ and the high temperature peak at 142 K is labelled τ. By 300 L the λ peak has again grown to dominate the spectra but the τ feature is still visible as a small, but defined, peak at 146 K. Potential assignments of these features will be discussed in the next section.

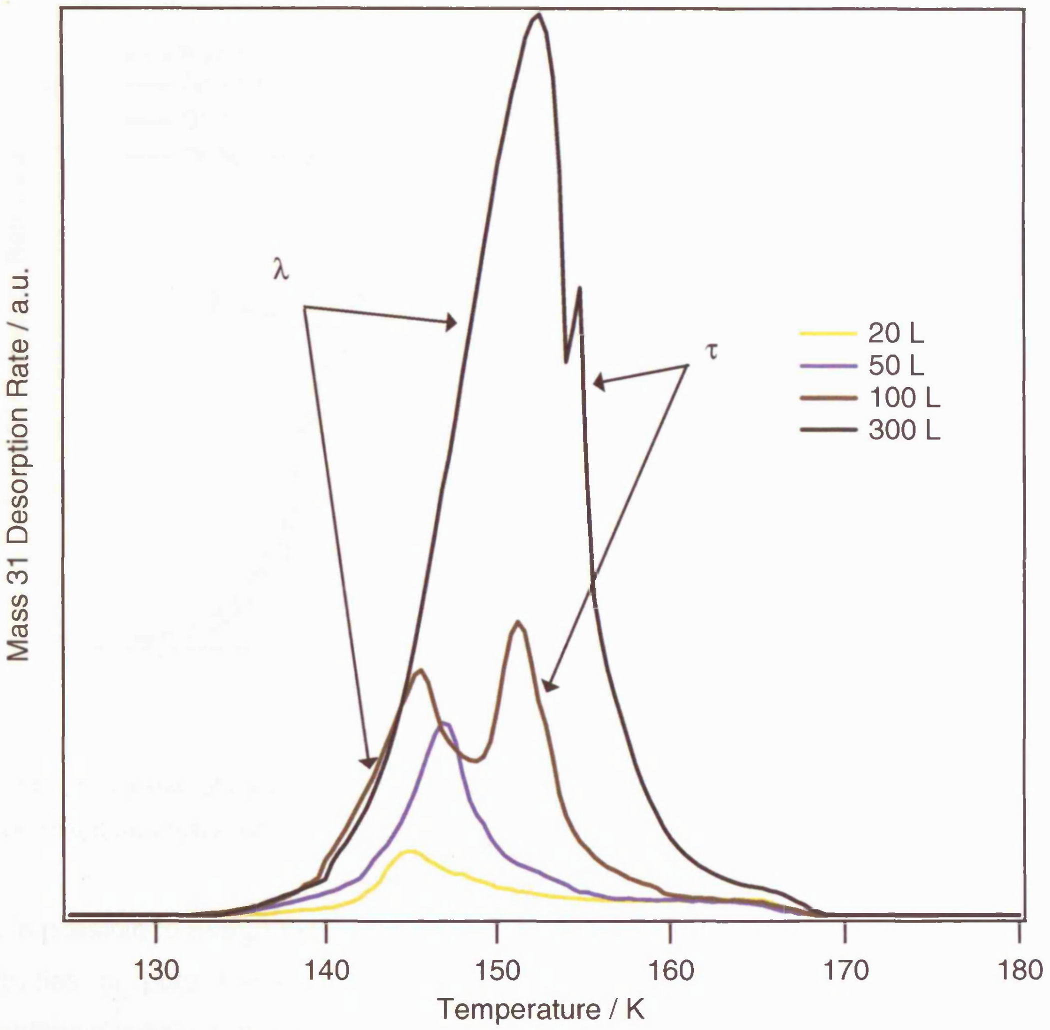

Figure 3.11 Methanol TPD traces following increasing exposures of methanol (up to 300 L) deposited on to a pre-adsorbed multilayer of water ice (50 L exposure) on a HOPG surface at 97 K.

3.3.5 Assignment of the Methanol Peaks

A comparison of low exposure methanol TPD spectra following methanol dosing on to differing thicknesses of water sublayer is shown in *Figure 3.12*. The same 3 peaks labelled α, β and λ are observed in all the spectra, and follow the same sequence of appearance with α appearing first, already saturated. The β peak is the next to appear and, following increasing exposures, the λ peak appears as a low temperature shoulder that then grows to dominate the entire spectrum. The peak labelled δ, which is visible in the methanol trace when the exposure is ≥ 50 L, and shown in *Figure 3.9*, only appears in the ices grown on 10 L of water and is thought to be different to the more defined high temperature peak labelled τ, visible in the high exposure ices grown on 50 L of water.

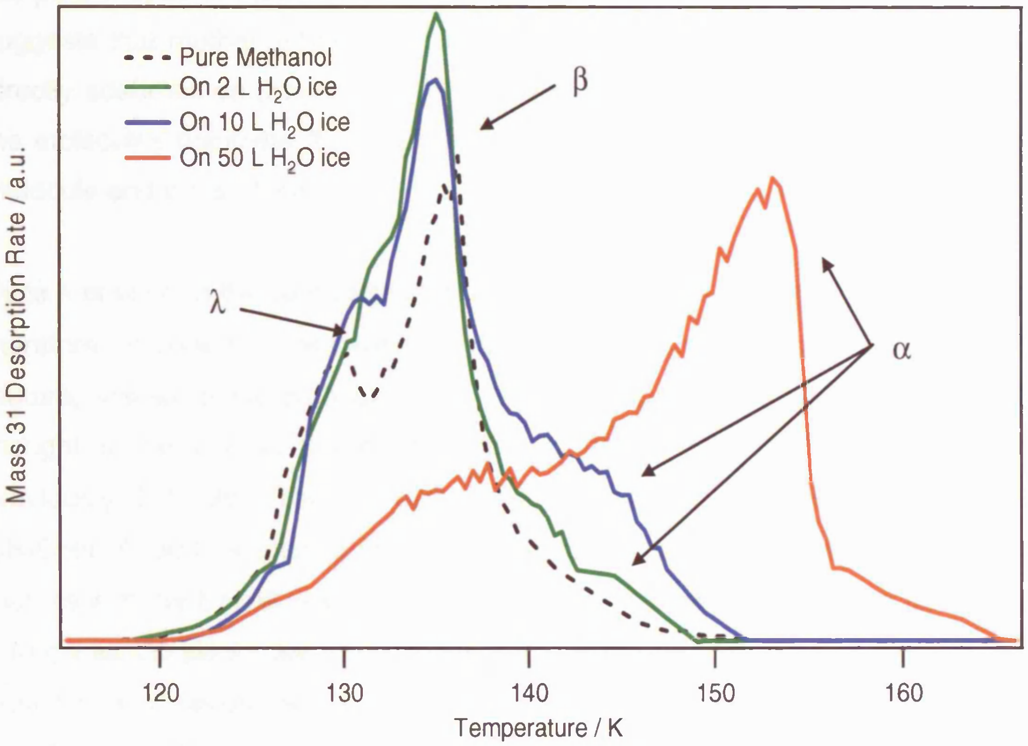

Figure 3.12 Desorption of 7 L exposures of methanol deposited on to differing thicknesses of a pre-adsorbed multilayer of H_2O ice on a HOPG surface at 97 K.

It is possible to assign the β and λ desorption peaks by comparison with previous TPD studies of pure methanol adsorbed on graphite [14]. Studies have shown that methanol initially forms a monolayer on the surface of graphite, and as exposures are increased the multilayer forms. Two peaks were described for multilayer methanol formation - one was assigned to the standard amorphous multilayer and the other to the formation of crystalline methanol formed during the heating process. This peak was only visible when exposures exceeded 50 L [14].

Peak β observed in *Figure 3.12* is therefore assigned to desorption of methanol from the monolayer. It is not possible to distinguish between monolayer formation on the water surface and monolayer formation on the graphite surface as only a single peak is observed in both cases. This is also found to be the case for the RAIR spectra discussed in the next chapter as these do not enable the monolayers of methanol on HOPG and water to be distinguished from one another. Water does not wet the graphite surface, instead it has a tendency to form clumps or islands [37]. The result of this is that, following a 2 L exposure of water (and possibly even at 10 L), there will be bare patches of graphite present. Hence it is likely that methanol initially adsorbs both on the graphite surface and on the water islands. *Figure 3.12* shows how similar the pure methanol monolayer feature is to that formed in the layered systems. This suggests that methanol bound to water has a similar adsorption energy to methanol directly adsorbed on graphite. It is likely that this is because the interactions between the molecules dominate the binding energy rather than the interactions between the molecule and the surface.

Peak λ is seen at the same temperature for the both the pure and layered ices and is therefore assigned to desorption from within the multilayers of methanol. The δ feature, visible in the high exposure spectra of CH_3OH/H_2O(10 L) (*Figure 3.9*), is thought to be due to the crystallisation of bulk methanol and has been noted previously [14, 38]. The τ peak visible in the high exposure spectra of the CH_3OH/H_2O(50 L) system (*Figure 3.11*) cannot be definitively assigned. It is possible that, as with the δ peak, it is also a bulk methanol crystallisation feature but this seems unlikely as the peaks are too well-defined for this to be the case. It may be better to view this as a second wave of methanol desorption from within the bulk of the water ice. The τ peak occurs at the same temperature as the second phase transition of water, and the associated structural rearrangement may lead to the release of further methanol molecules trapped within the bulk of the water ice. A similar peak is seen for the desorption of methanol from codeposited CH_3OH/H_2O ice systems as discussed in Chapter 5. In *Figure 5.9* for example, a high temperature methanol TPD peak is seen which coincides with the conversion of crystalline ice to hexagonal ice. On the basis of this peak assignment, the observation of τ peak in the methanol TPD spectra for the CH_3OH/H_2O(50 L) system, suggests that mixing of the water and methanol layers occurs on heating.

By observing the water desorption along with the methanol desorption, see *Figure 3.13*, it is seen that the β feature shares its leading desorption edge with that of water, suggesting that it desorbs as the water first begins to sublime. This is consistent with the assignment of this peak to the desorption of monolayer methanol that is adsorbed on the water ice. Peak α, on the other hand, desorbs with the bulk of the water ice. Its sharp trailing edge coincides with the trailing edge of the corresponding water feature. Peak α is a new feature that has not previously been noted in any of the pure methanol studies. It is clearly a co-desorption peak which represents the desorption of methanol that is very closely associated with the bulk of the water ice. It shows a desorption typical of trapped molecules and may represent methanol encaged within clathrate structures [18, 25, 39]. The observation of this trapped methanol feature provides further evidence for the mixing of the water and methanol ice layers when heating occurs.

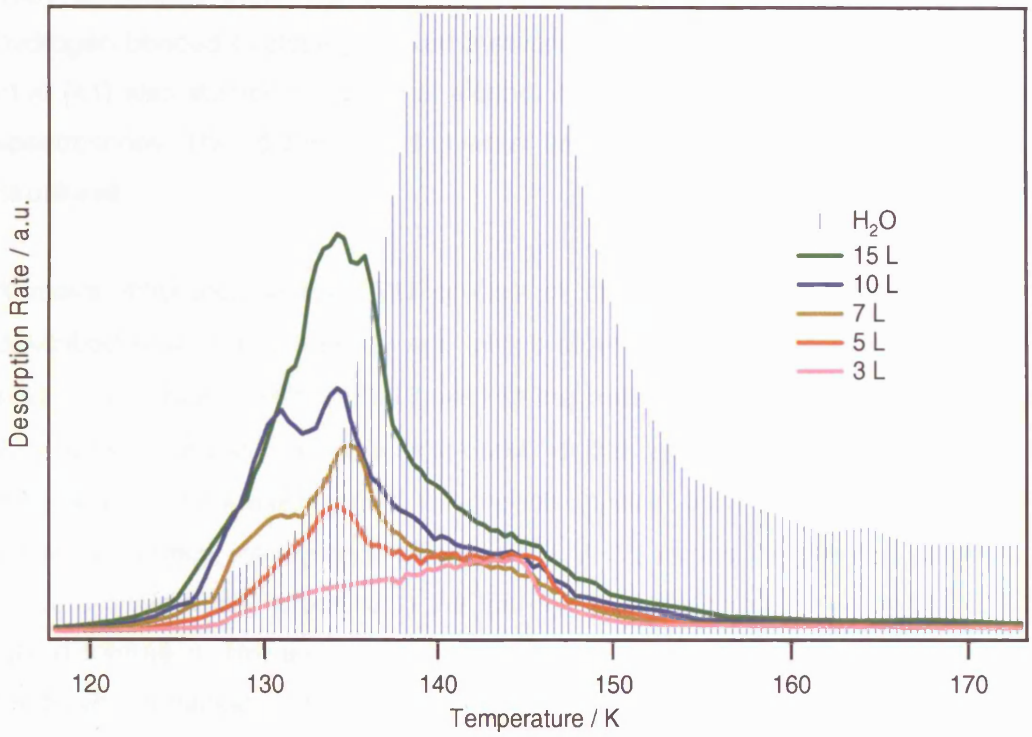

Figure 3.13 TPD traces of methanol deposited on a pre-adsorbed layer of H_2O ice (10 L) on a HOPG surface at 97 K. The water desorption trace is shown (shaded) for comparison.

Notesco and Bar-Nun [17, 22], and Blake et al [20] have all reported similar trapping behaviour with mixed methanol and water ices and have proposed the formation of type II clathrate hydrates to explain the tendency of methanol to remain on the surface until the water has sublimed. As discussed earlier clathrate hydrates are hydrogen bonded water cages that trap small amounts of a guest molecule within the structure. With large molecules such as methanol, a type II clathrate will typically form and the ideal ratio of water:guest molecule will be 17:1 [20, 26]. Blake et al performed transmission electron microscopy and selected area electron diffraction to characterise condensed ice mixtures of H_2O:CH_3OH (2:1). They found evidence for the formation of the clathrate hydrate structure from around 130 K, when molecular intermixing occurs [28]. They also noted that excess methanol, over and above the 6% required to saturate the clathrate structure, would segregate and form pure crystalline boundaries [20].

The clathrate hydrate model is not universally accepted, clathrates typically form under high pressure conditions and it is debatable whether they will form in the low pressure regions of the ISM. Dixit et al [40] performed a neutron diffraction isotopic substitution study of solutions of methanol and water to explore the unexpectedly low entropy of the mix when compared to the predicted behaviour of an ideal solution. They concluded that incomplete mixing of strings or clusters of water molecules hydrogen bonded to closely packed methanol groups is a more accurate model. Guo et al [41] also studied solutions of alcohol and water mixtures, using X-ray emission spectroscopy. They determined that water bridges the chains of methanol to form ring structures.

A major difference in the TPD spectra of the three different adsorbate systems described here is the intensity and temperature of the saturated α peak. The peak area of α increases with the thickness of the water sublayer. With the thinnest layer, 2 L exposure of water, the α peak is barely visible, appearing only as a slight bump on the base line. However, by 50 L the α peak appears as a prominent sharp peak with an almost vertical trailing edge (*Figure 3.12*). A 2 L exposure of water ice will result in some 3-dimensional structure to the ice layer, as water has a tendency to grow by island formation. However, following a 50 L exposure there has been considerable multilayer formation. This greater volume of bulk water ice leads to an increased volume of the trapped or co-desorption feature α. *Figure 3.12* also shows that the peak temperature of the α feature increases as the thickness of the underlying water increases. This shift is actually a function of the desorption temperature of the underlying water. As water has a near zero order desorption [15, 42], the peak temperature will increase as the exposure increases from 10 L through to 50 L. The trapped α feature, held within the bulk of the water ice, is therefore retained on the surface to higher temperatures as a result.

In order to confirm the assignment of Peak α to a trapped feature, a series of TPD experiments were performed with methanol deposited on a sub-layer of crystalline ice. Crystalline ice is considerably less porous than its amorphous counterpart [17] and will therefore have fewer surface pores and pathways available for the entrapment of methanol. The crystalline ice layer was formed by adsorbing water on an HOPG surface held at an elevated temperature of 145 K. The phase of the ice was confirmed by RAIR spectra (see Chapter 4), which demonstrated the characteristic OH vibrational fingerprint of crystalline ice [15, 43, 44]. The surface was then cooled back down to base temperature (97 K), before being exposed to methanol.

Figure 3.14 compares the desorption features of methanol adsorbed on crystalline and amorphous water ice equivalent to the CH_3OH/H_2O(10 L) system. The sticking probability is reduced at the higher temperature required to form crystalline ice, and hence the exposure was increased to attain a comparable thickness of the crystalline and amorphous water ice layers (as determined by the integrated peak areas).

Adsorption of methanol on crystalline ice results in a less intense co-desorption feature, Peak α and monolayer feature, Peak β. The multilayer feature, Peak λ, is also observed earlier on the crystalline ice surface. Crystallisation of ice seals off surface pores, thereby reducing the surface area for the monolayer and cutting off diffusion pathways for the methanol to enter into the bulk of the ice. As the monolayer peak now saturates earlier, multilayer growth is noted at lower coverages. The existence of a small, although much reduced, co-desorption peak may be explained by the incomplete crystallisation of such a thick water layer as described in earlier work on the system [45]. In addition Notesco and Bar-Nun reported that, following codeposition of methanol with water, methanol would still trap when the ice was formed at temperatures as high as 160 K suggesting that a small amount of trapping may still take place in the crystalline phase [22].

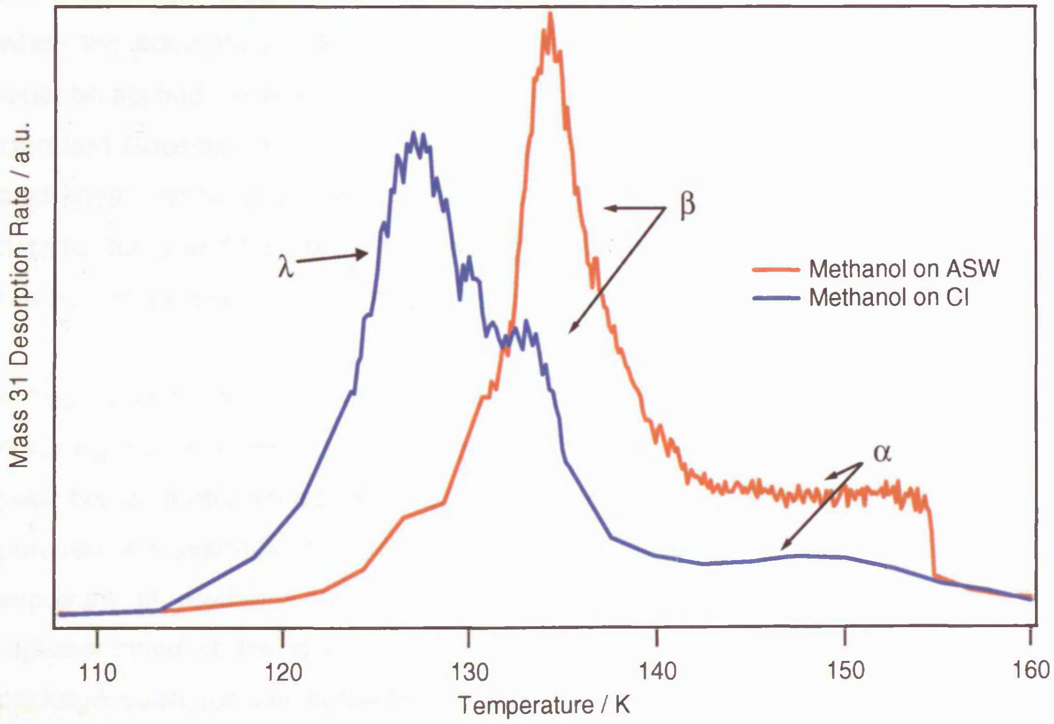

Figure 3.14 Desorption of 15 L of methanol deposited on a pre-adsorbed layer of amorphous solid water (ASW - shown in red) and crystalline water (CI - shown in blue) on a HOPG surface at 97 K. In each case the layers of water ice were of a comparable thickness, 10 L.

Although the TPD results presented here do not enable the precise nature of the water-methanol interaction to be determined at the molecular level, they are sufficient to allow the confident assignment of Peak α as a bulk trapping feature. This trapping is either due to the formation of a clathrate hydrate structure or due to the simple containment of methanol in water ice pores.

3.4 Quantitative Analysis of TPD Spectra

A quantitative approach will not be used to study the water desorption behaviour as the shifting temperature with increasing thickness of the methanol overlayer is an artificial, rather than a kinetic, feature. However, it is possible to analyse the methanol spectra, and a detailed study reveals insights into the kinetics by allowing the determination of desorption orders, desorption energies and pre-exponential factors.

Most of the analysis discussed in this section is performed on the experimental data following base line correction to remove the residual gas signal present at the beginning and end of each experiment. In some cases it has proved necessary to separate out the peaks attributable to individual surface species, particularly when determining the relative abundances of each surface species. Where peak fitting was performed, the best match of both peak shape and area was achieved by using the basic Lorentzian shape to model the α and β peaks. This approach will be rationalised when the desorption orders are calculated later in section 3.4.3. However, caution must be applied to the λ multilayer peak, as it is not accurately modelled by any of the standard Gaussian, Lorentzian or Voigt peak shapes available within standard fitting packages. Hence, the multilayer peak has been modelled by subtracting the peak fit data for the α and β peaks. The resulting λ peak is then the residual and ensures that the sum of the peak fit data is equal to the overall experimental data.

It has proved possible to fit the three previously defined peaks for TPD spectra resulting from the deposition of methanol on either 2 L of water or 10 L of water, but peak fits for methanol adsorbed on 50 L of water are ambiguous and have not been pursued. An example of the peak fit for the TPD spectrum that results from a 10 L exposure of methanol on 10 L of water ice is shown in *Figure 3.15*. This is representative of the quality of the remaining peak fits used in this section. The package used for the correction, fitting and analysis of the spectra is IGOR Pro (Version 5.04), Wavemetrics, Inc with the SpXZeigR package.

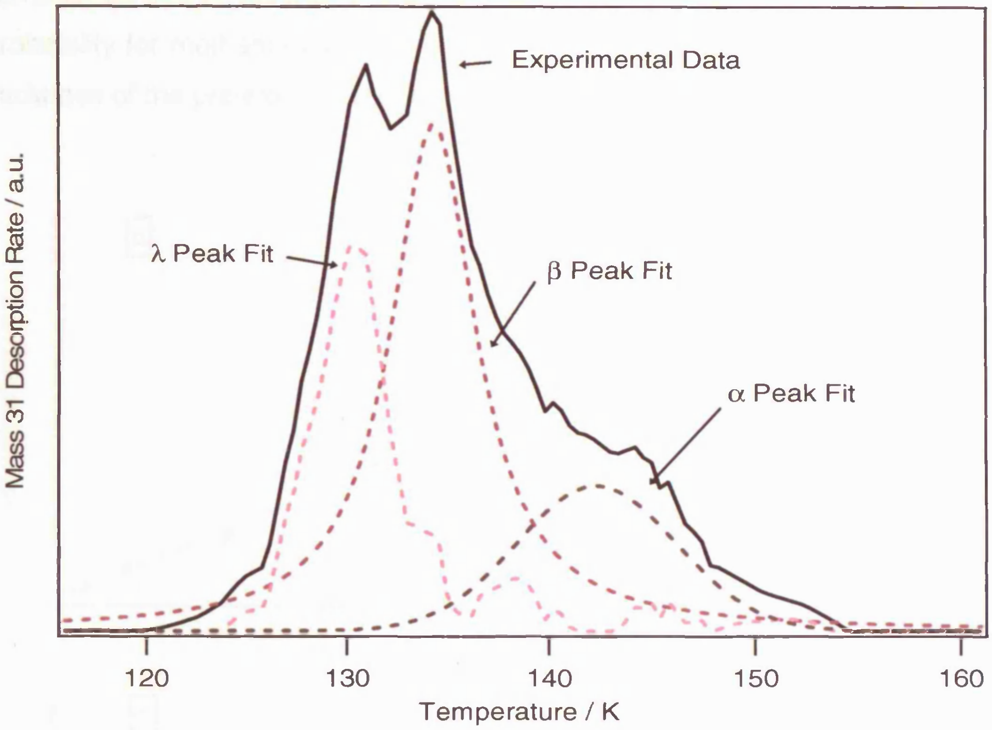

Figure 3.15 Deconvolution of a complex methanol TPD desorption trace into the component α, β and λ peaks. The experimental trace is for a 10 L exposure of methanol on a pre-adsorbed multilayer of H_2O ice (10 L exposure) adsorbed on HOPG at 97 K.

3.4.1 Uptake and Sticking Probability

With the experimental setup described earlier, it is not possible to determine the absolute coverage of adsorbate on the HOPG sample. However, the intensity of the mass spectrometer signal is proportional to the rate of change of coverage of the adsorbate with time, and so the integrated area under each TPD spectrum gives the relative coverage of the species concerned.

During each dose, the mass spectrometer was set to record the intensity and duration of the exposure. Relative exposure was then determined by integrating the area under these dose curves. Uptake curves were then plotted for the adsorption of methanol on each of the three water systems at 97 K. *Figure 3.16* shows the total uptake of methanol adsorbed on a) 2 L H_2O, b) 10 L H_2O and c) 50 L H_2O, adsorbed on HOPG, each as a function of increasing exposure of methanol.

It is clear from *Figure 3.16* that for each of the three systems, methanol uptake is linear. This indicates that there is a constant sticking probability for methanol adsorbed on a water ice surface. In addition, the gradients of the best fit lines are the same for all three systems, at 0.0200 ± 0.0015 which confirms that the actual sticking probability for methanol exposed to water ice at 97 K is the same, regardless of the thickness of the pre-existing water ice layer.

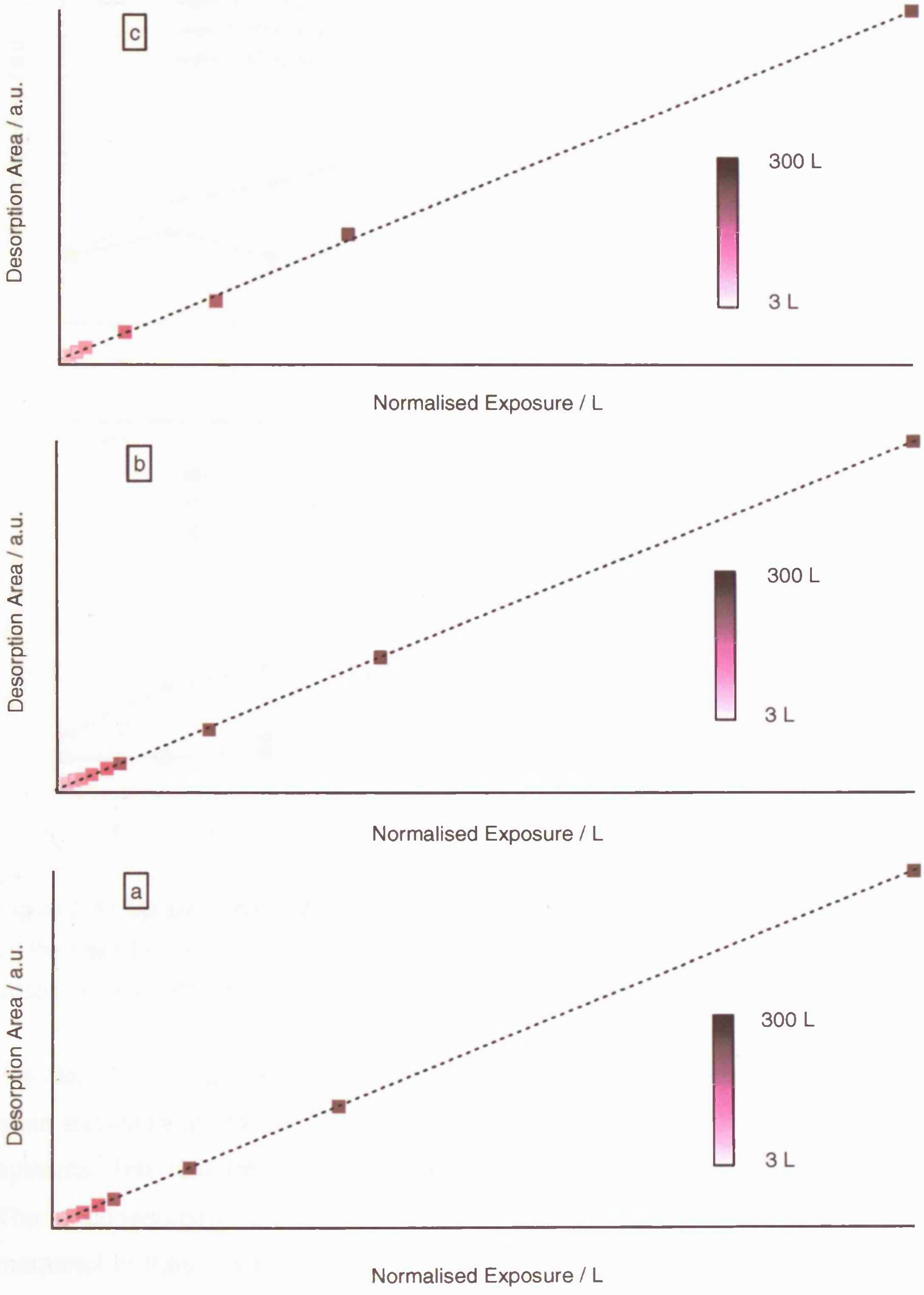

Figure 3.16 Uptake curves showing, as a function of increasing methanol exposure, the total integrated area of the TPD curves obtained for methanol adsorbed on a) 2 L of H_2O ice, b) 10 L of H_2O ice and c) 50 L of H_2O ice. All exposures were performed at 97 K with an underlying substrate of HOPG.

Uptake curves can also be plotted for individual adsorbate species present on the surface following deconvolution of the overlapping TPD peaks, see *Figure 3.17*.

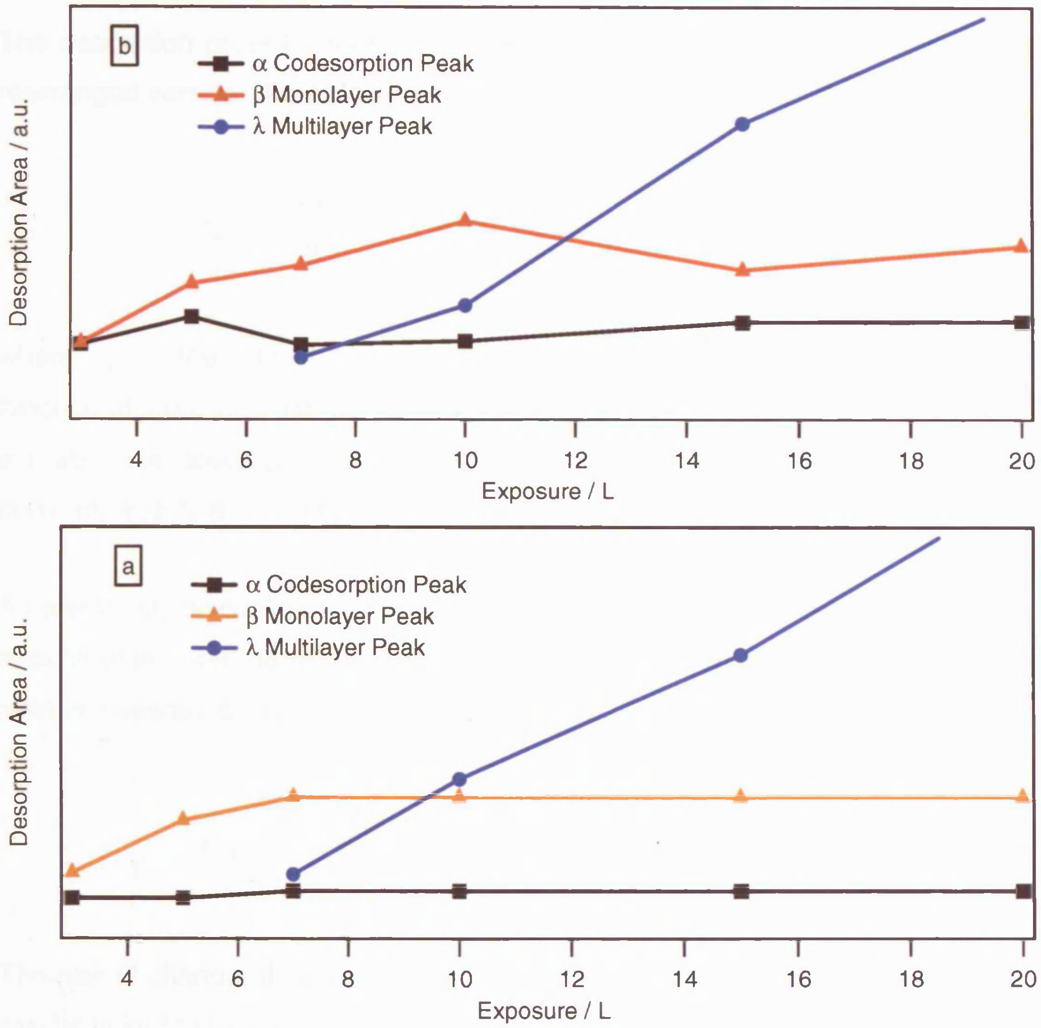

Figure 3.17 Uptake curves, showing the integrated area of the deconvoluted peaks that make up the fitted TPD spectra for methanol deposited on a) 2 L of water ice and b) 10 L of water ice adsorbed on HOPG at 97 K.

It is clear from *Figure 3.17* that the integrated area of the β monolayer peak saturates at an exposure approaching 7 L for both the CH_3OH/H_2O(2 L) and CH_3OH/H_2O(10 L) systems. This reaffirms the assignment of Peak β to desorption from the monolayer. The α codesorption feature appears to be saturated from the initial exposure of methanol in these two systems. However, the integrated area that gives rise to this saturated peak is higher when methanol is deposited on 10 L of water ice than on 2 L of water ice as there is more bulk volume available for trapping. In both systems the λ peak increases almost linearly with exposure and does not saturate. This is in complete agreement with the assignment of this peak to the desorption of multilayer methanol. As expected, the multilayer feature is not observed until both the codesorption and monolayer features have saturated.

3.4.2 Desorption Orders

The desorption order for methanol adsorbed on water ice can be calculated using a rearranged version of the Polanyi-Wigner equation (*Equation 3.1*) [46]:

$$r_{des} = -\frac{\partial \theta}{\partial t} = v_n \theta^n \exp\left[\frac{-E_{des}}{RT_s}\right] \qquad \text{Equation 3.1}$$

where r_{des} is the rate of desorption, which is the rate of change of coverage as a function of time, v_n is the pre-exponential factor of the desorption process order n, θ is the absolute coverage, E_{des} is the activation energy for desorption, R is the gas constant and T_s is the temperature of the surface.

As previously discussed, it is not possible to measure the absolute coverage in these experiments, and hence the Polanyi-Wigner equation is modified to incorporate relative coverages, θ_{rel}:

$$r_{des} = -\frac{\partial \theta_{rel}}{\partial t} = v_n \theta_{rel}{}^n \exp\left[\frac{-E_{des}}{RT_s}\right] \qquad \text{Equation 3.2}$$

The rate of change of coverage (and therefore relative coverage) with respect to time, can be linked to temperature, through the heating rate β:

$$\frac{\partial \theta_{rel}}{\partial t} = \frac{\partial \theta_{rel}}{\partial T}\frac{\partial T}{\partial t} = \frac{\partial \theta_{rel}}{\partial T}\beta \qquad \text{Equation 3.3}$$

As the heating rate β, is constant, *Equation 3.3* now becomes:

$$\frac{\partial \theta_{rel}}{\partial t} \propto \frac{\partial \theta_{rel}}{\partial T} \qquad \text{Equation 3.4}$$

As discussed in Chapter 2, in TPD experiments the intensity of the mass spectrometer signal *I(T)* is proportional to the rate of change of coverage with respect to temperature:

$$I(T) \propto \frac{\partial \theta_{rel}}{\partial T} \qquad \text{Equation 3.5}$$

This proportionality enables us to modify the Polanyi-Wigner equation to give:

$$I(T) \propto \nu_n \theta_{rel}{}^n \exp\left[\frac{-E_{des}}{RT_s}\right] \qquad \text{Equation 3.6}$$

and by rearranging and taking logarithms, *Equation 3.7* is produced:

$$\ln[I(T)] \propto n \ln\theta_{rel} + \ln\nu_n - \frac{E_{des}}{RT_s} \qquad \text{Equation 3.7}$$

Equation 3.7 shows that a plot of $ln[I(T)]$ versus $ln[\theta_{rel}]$ at a fixed temperature T_x, will yield a straight line with gradient *n*, which is the order of desorption [47]. It has been assumed that neither the desorption energy, E_{des} or the pre-exponential factor, ν_n vary with coverage or temperature. The validity of these assumptions will be discussed later.

Ideally an order plot should be performed for each separate adsorbate species however this is not possible when the peaks are so heavily overlapping as in the TPD spectra recorded here. An order plot of $ln[I(T)]$ versus $ln[\theta_{rel}]$ at a fixed temperature T_x of 131 K is shown in *Figure 3.18* for methanol adsorption on a pre-existing layer of water ice (2 L exposure) at 97 K. The chart is split into two sections with clearly defined gradients. These sections correspond to methanol exposures of 3 L - 15 L and exposures of 15 L - 300 L, i.e. within the monolayer and multilayer regimes.

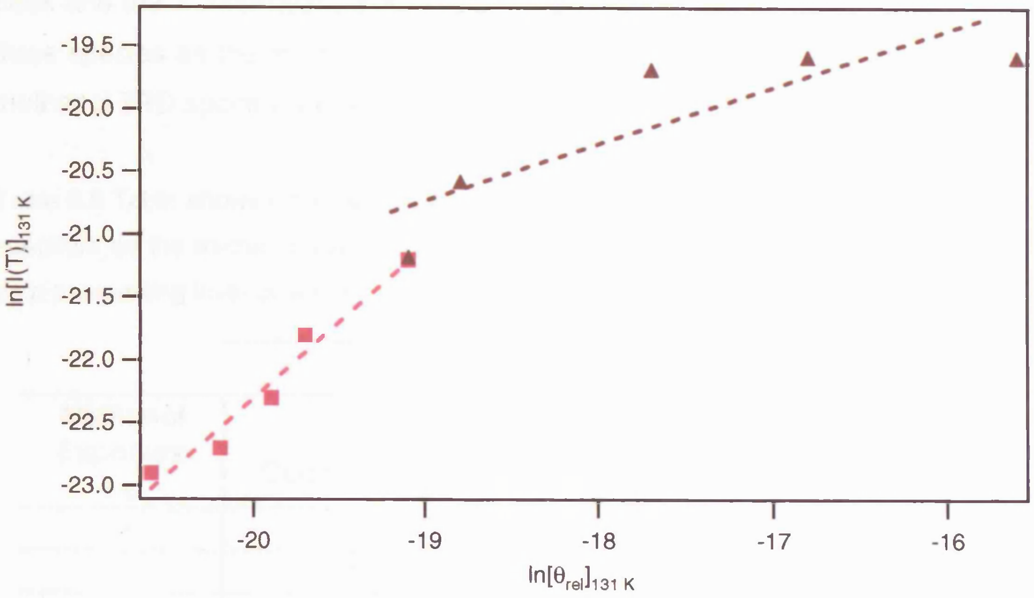

Figure 3.18 An order plot of ln[I(T)]$_{Tx}$ against ln[θ_{rel}]$_{Tx}$ for a fixed temperature T_x of 131 K for increasing exposures of methanol on a pre-existing layer of water ice (2 L) adsorbed on HOPG at 97 K. Square symbols represent exposures from 3-15 L and the triangles represent exposures from 15- 300 L.

This process is repeated for a range of fixed temperatures and desorption orders obtained from the gradients are shown in *Table 3.4* for each exposure range.

Table 3.4 Table showing calculated desorption orders for methanol deposited on a pre-existing layer of water ice (2 L) at 97 K.

	Desorption Order	
T_x / K	**Low Methanol Exposures 3 - 15 L**	**High Methanol Exposures 15 - 300 L**
127.74	1.55	0.17
128.54	1.54	0.28
128.94	1.54	0.32
129.75	1.41	0.35
130.95	1.12	0.42
131.76	1.54	0.32
133.37	1.41	0.35

When interpreting the gradients in *Table 3.4* it is important to consider the contribution made by the individual desorbing species. For example, the gradient for exposures between 3 and 15 L will be composed of the α codesorption peak, the β monolayer peak and the λ multilayer peak. *Table 3.5* shows the percentage contributions of the three species as the methanol coverage increases, determined by deconvoluting the methanol TPD spectra with a peak fitting package as previously described.

Table 3.5 Table showing the % contribution made by each individual species to the total TPD spectrum as the methanol exposure increases. The system shown is for methanol deposited on a pre-existing layer of water ice (2 L) at 97 K.

	% Contribution to Total Spectrum		
Methanol Exposure / L	**α Codesorption**	**β Monolayer**	**λ Multilayer**
3	35%	65%	-
5	22%	78%	-
7	17%	59%	24%
10	12%	41%	47%
15	8%	30%	62%
20	6%	22%	72%
50	2%	7%	91%
100	1%	3%	96%
300	0%	1%	99%

From *Table 3.5* it is clear that by far the largest contribution to the high exposure spectra (15-300 L) comes from the λ multilayer peak. Therefore, multilayers of methanol on 2 L of water ice have a desorption order of 0.32 ± 0.15. Thick multilayers would typically show zero order desorption kinetics, where the desorption rate is independent of the surface coverage [48], however fractional order processes have previously been observed for the desorption of pure methanol [14]. Fractional order desorption is characteristic of hydrogen bonded systems [14, 35, 36]. The figure reported here for methanol multilayers deposited on the surface of water ice is the same, within confidence limits, as the 0.35 ± 0.21 reported for pure methanol adsorbed on HOPG [14]. This is to be expected as the bulk methanol formed in physisorbed multilayers is shielded from any interactions at the surface, and hence it is irrelevant which surface adsorption takes place on.

Within the lower exposure range, the dominant species present on the surface are the α codesorption peak and the β monolayer peak. Therefore the gradient of 1.44 ± 0.31 represents the average desorption order of these two features. This average figure is not very useful, so the process of determining the desorption order was repeated. The contribution of the α codesorption peak, determined by peak fitting analysis, was removed from the data prior to calculating the order. The results are detailed in *Table 3.6* and show that the β monolayer peak has a desorption order of 1.24 ± 0.14. This is slightly higher than for a pure first order process and is indicative of lateral interactions with neighbouring molecules, in this case via hydrogen bonding. The figure is also remarkably similar to the figure reported for the pure methanol monolayer on a graphitic HOPG surface at 1.23 ± 0.14 [14], which suggests that the process of binding to the water ice layer is very similar to the binding to HOPG, as already discussed.

Table 3.6 Table showing the calculated desorption orders for low exposures of methanol deposited on a pre-existing layer of water ice (2 L) adsorbed on HOPG at 97 K. The contribution from the α codesorption peak has been subtracted.

	Desorption Order
T_x / K	**Low Methanol Exposures 3 - 15 L**
126.13	1.15
127.34	1.33
127.74	1.30
128.54	1.22
128.94	1.22

Having determined the order for the monolayer peak, it is now possible to use the relative abundances in *Table 3.5* to calculate the desorption order for the α codesorption peak. Taking the average ratio of the monolayer peak to the codesorption peak in the low exposure range to be 70:30, the desorption order for the codesorption peak is calculated to be 1.91 ± 0.33. Second order desorption suggests dissociative chemisorption, which is known not to occur. This value of the desorption order therefore indicates that there are very strong lateral interactions involved, which is expected given the assignment of this feature as a trapped species.

This whole process was repeated for the CH_3OH/H_2O(10 L) system and an example order plot for T_x = 131 K is shown in *Figure 3.19*.

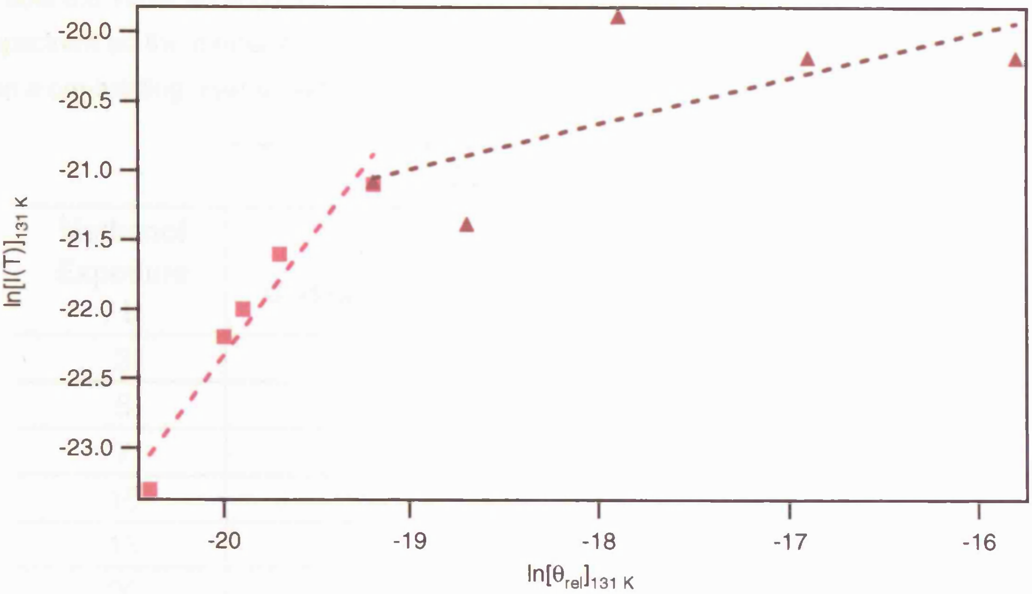

Figure 3.19 An order plot of ln[I(T)]$_{Tx}$ against ln[θ_{rel}]$_{Tx}$ for a fixed temperature T_x of 131 K for increasing exposures of methanol on a pre-existing layer of water ice (10 L).

A summary of the calculated desorption orders for the system at different fixed temperatures is shown in *Table 3.7*. As with the CH_3OH/H_2O(2 L) system, the largest contribution to the high exposure (15 – 300 L) gradient comes from the λ multilayer peak, see *Table 3.8*. Therefore, multilayers of methanol adsorbed on 10 L of water ice can be assumed to have a desorption order of 0.23 ± 0.22. This is lower than the stated figure for the CH_3OH/H_2O(2 L) system but still within confidence limits of both this and the work on pure methanol adsorbed on HOPG [14].

Table 3.7 Table showing calculated desorption orders for methanol deposited on a pre-existing layer of water ice (10 L) at 97 K.

	Desorption Order	
T_x / K	**Low Methanol Exposures 3 - 15 L**	**High Methanol Exposures 15 - 300 L**
126.53	2.16	0.13
127.34	2.04	0.10
131.76	1.61	0.19
132.16	1.64	0.24
133.37	1.83	0.32
134.57	1.95	0.38

Table 3.8 Table showing the % contribution made by each individual species to the total TPD spectrum as the methanol exposure increases. The system shown is for methanol deposited on a pre-existing layer of water ice (10 L) at 97 K.

	% Contribution to Total Spectrum		
Methanol Exposure / L	**α Codesorption**	**β Monolayer**	**λ Multilayer**
3	50%	50%	-
5	42%	58%	-
7	25%	55%	20%
10	19%	52%	29%
15	17%	27%	56%
20	13%	25%	62%
50	6%	11%	84%
100	2%	5%	93%
300	1%	3%	96%

The low exposure gradient also has contributions from both the codesorption and monolayer peak, and results in an average desorption order of 1.87 ± 0.42. To assign an order to each species individually, the order plot was again constructed with the codesorption contribution subtracted, as previously described. This results in the figures detailed in *Table 3.9* and corresponds to a desorption order for the monolayer of 1.15 ± 0.18. This is slightly lower than the monolayer figure quoted for the 2 L system but there is considerable overlap within the error range.

The desorption order for the codesorption peak can now be calculated. Taking the average ratio of the monolayer peak to the codesorption peak in the low exposure range to be 55:45, the desorption order for the codesorption peak is calculated to be 2.75 ± 0.45. This is an extremely high value for a desorption order and is likely to be an indication that the trapping of methanol within the bulk water layer is not adequately modelled by a kinetic process and that this form of analysis is not appropriate for this constrained feature.

Table 3.9 Table showing calculated desorption orders for low exposures of methanol deposited on a pre-existing layer of water ice (10 L) at 97 K. The contribution from the α codesorption peak has been subtracted.

	Desorption Order
T_x / K	**Low Methanol Exposures 3 - 15 L**
128.14	1.26
129.35	1.15
130.15	1.15
131.76	1.10
132.16	1.09
133.37	1.15
134.57	1.16

In summary, *Table 3.10* shows the desorption orders that have been calculated for the sequential layered systems of methanol deposited on 2 L of pre-existing amorphous solid water and methanol deposited on 10 L of pre-existing amorphous solid water.

Table 3.10 Summary of the desorption orders calculated for each peak observed in the TPD spectra of the following two systems, CH_3OH/H_2O(2 L) and CH_3OH/H_2O(10 L). Errors are displayed to 2 standard deviations.

	CH_3OH/H_2O(2 L)	**CH_3OH/H_2O(10 L)**
α **Codesorption**	1.90 ± 0.34	2.75 ± 0.13
β **Monolayer**	1.24 ± 0.14	1.15 ± 0.18
λ **Multilayer**	0.32 ± 0.15	0.23 ± 0.22

3.4.3 Desorption Energy

It is also possible to determine desorption energies for the multilayer of methanol in both the CH_3OH/H_2O(2 L) system and the CH_3OH/H_2O(10 L) system by analysis involving further manipulation of the Polanyi-Wigner equation. An Arrhenius type analysis proposed by Parker et al [49] has been used for this data.

Starting with *Equation 3.1*,

$$r_{des} = -\frac{\partial \theta}{\partial t} = v_n \theta^n \exp\left[\frac{-E_{des}}{RT_s}\right] \qquad \text{Equation 3.1}$$

taking logarithms of both sides gives:

$$\ln\left(-\frac{\partial \theta}{\partial t}\right) = \ln(v_n) + n \ln \theta \; - \frac{E_{des}}{RT_s} \qquad \text{Equation 3.8}$$

Rearrangement gives:

$$\ln\left(-\frac{\partial \theta}{\partial t}\right) - n \ln \theta \; = \ln v_n - \frac{E_{des}}{RT_s} \qquad \text{Equation 3.9}$$

Use of relative coverages rather than absolute coverages results in the following proportionality expression:

$$\ln I(T) - n \ln \theta_{rel} \propto \ln v_n - \frac{E_{des}}{RT_s} \qquad \text{Equation 3.10}$$

This shows that a plot of $\ln I(T) - n \ln \theta_{rel}$ versus $1/T$ will yield a straight line with the slope $-E_{des}/R$, provided that the pre-exponential factor does not vary with coverage. If the correct value of n is chosen, the gradient will be linear. This form of plot was designed by Parker et al [49], to determine both the desorption energy and the order of the process. Orders were confirmed by testing for linearity as the plot moves beyond the peak temperature, but tests undertaken here have shown that this has only proved to be effective for continuous or simulated data and so the method will be used to determine E_{des} and not desorption order.

An average figure for the entire process, comprising all three surface species, can be extracted from analysis of the whole spectra but to determine accurate desorption energies for each individual species requires the use of the peak fitted data. It is not appropriate to continue this detailed analysis on the peak fit results for the α codesorption peak or the β monolayer peak. Even at the low coverages studied here, both peaks are present simultaneously and overlap strongly. The peaks are also saturated, or near to saturated, from even the early exposures. These factors mean that the confidence in the peak fits for modelling both the shape and the area of the underlying feature is not great enough to proceed. Pisani, Rabino and Ricca [50] issued a warning that was later reiterated by King [51], regarding the ambiguities involved in fitting overlapping desorption peaks, demonstrating very clearly that models based on very different kinetic parameters cannot be separated on the basis of fit alone.

In contrast, the λ multilayer feature is by far the most dominant peak in the spectra as the exposure extends beyond 20 L. As the shape and area of the combined codesorption and monolayer trace can be confidently isolated, and hence subtracted, from the overall TPD trace to leave the multilayer fitted data, analysis will be performed on this feature.

Figure 3.20 shows plots of $ln\ I(T) - n\ ln\ \theta_{rel}$ against $1/T$ for the fitted multilayer methanol plots obtained from the 20 L, 50 L, 100 L and 300 L spectra from the CH_3OH/H_2O(2 L) system. The spectra following these methanol exposures were chosen, as the multilayer peak accounts for at least 70 % of the total desorption in all of these cases. The order of desorption n, has been fixed at 0.32, the average value determined in the previous section.

There is an error associated with the uncertainty in the choice of the desorption order. For the CH_3OH/H_2O(2 L) system, the calculated desorption order for the multilayer methanol species is 0.32 ± 0.15 (all errors in the text are quoted to 2 standard deviations unless stated otherwise). By taking into account the error in the order of desorption, the plots shown in *Figure 3.20* can be repeated to determine an upper and a lower limit for the value of the gradient $-E_{des} / R$. The upper and lower gradient limits for the CH_3OH/H_2O(2 L) system, are shown in *Table 3.11*.

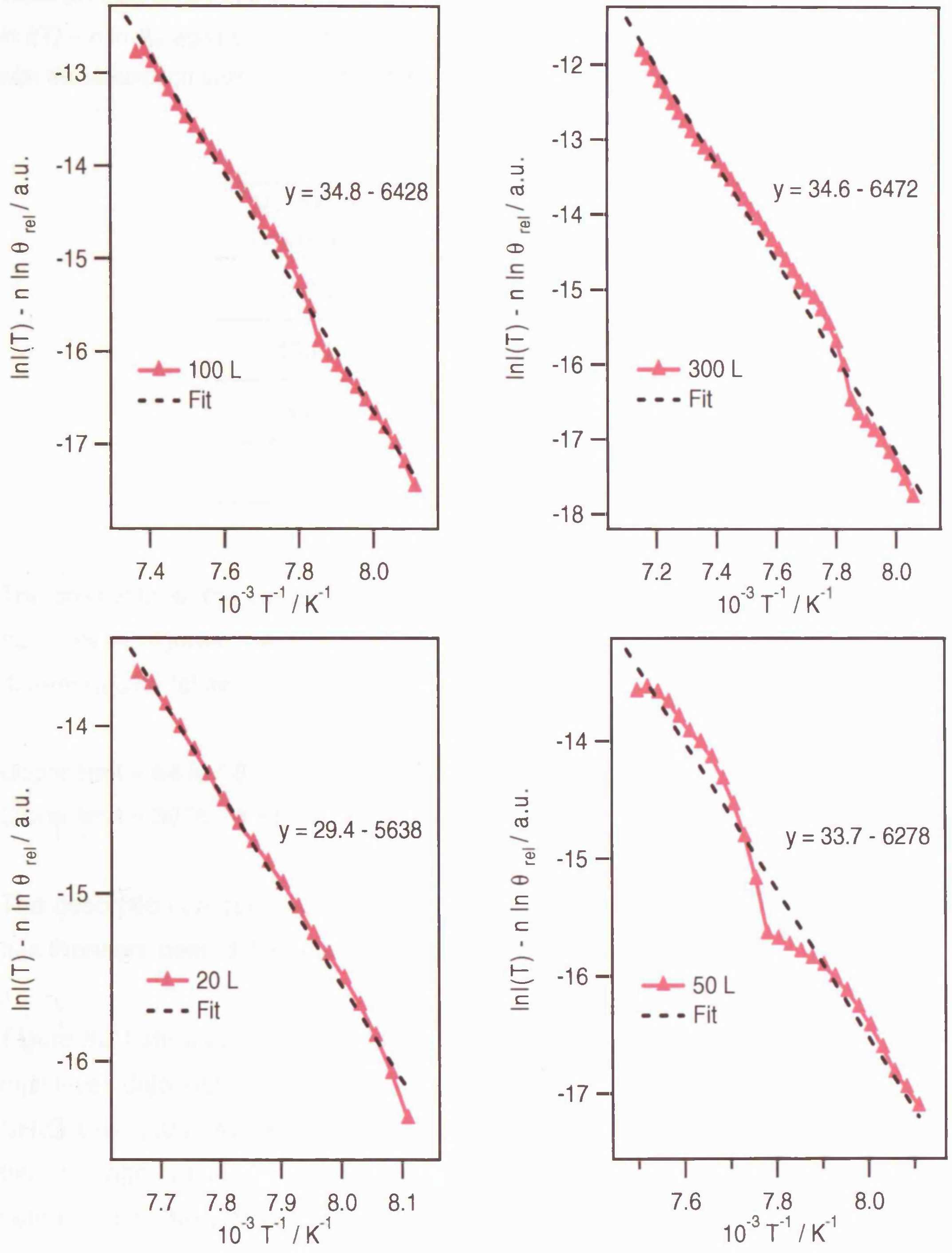

Figure 3.20 Plot of *ln I(T) – n ln* θ_{rel} against *1/T* for the multilayer fitted data for 20 L, 50 L, 100 L and 300 L exposures of methanol deposited on an existing layer of water ice (2 L). The order of desorption, *n* has been fixed at 0.32.

Table 3.11 Summary of the upper and lower limits to the gradient $-E_{des} / R$, acquired by plotting *ln I(T) – n ln* θ_{rel} against *1/T*, for the CH_3OH/H_2O(2 L) system. The lower limit was determined with the desorption order *n* = 0.17 and the upper value was obtained with n = 0.47.

	Gradient	
Methanol Overlayer	**Lower Limit**	**Upper Limit**
300 L	- 6297	- 6647
100 L	- 6226	- 6631
50 L	- 6073	- 6482
20 L	- 5316	- 5961

The gradients for the exposures of 20 L, 50 L, 100 L and 300 L can be averaged, and from these figures the range of values for the desorption energy, E_{des} can be determined as follows:

Upper limit = 6430 * 8.314 = 53461 J mol^{-1}
Lower limit = 5978 * 8.314 = 49701 J mol^{-1}

The desorption energy, E_{des} for the multilayer feature of the CH_3OH/H_2O(2 L) system has therefore been determined to be 52 kJ mol^{-1} ± 2 kJ mol^{-1}.

Figure 3.21 shows similar plots of *ln I(T) – n ln* θ_{rel} against *1/T* for the fitted methanol multilayer data obtained from the 20 L, 50 L, 100 L and 300 L spectra from the CH_3OH/H_2O(10 L) system. The order of desorption *n*, has been fixed at 0.23, which is the average value for multilayer desorption in the CH_3OH/H_2O(10 L) system, determined in the previous section.

The range analysis is repeated to take into account the uncertainty associated with the choice of the desorption order. For the CH_3OH/H_2O(10 L) system, the calculated desorption order for the multilayer methanol species is 0.23 ± 0.22 (2 S.D.). *Table 3.12* shows the upper and lower limits for the value of the gradient $-E_{des} / R$, for the CH_3OH/H_2O(10 L) system.

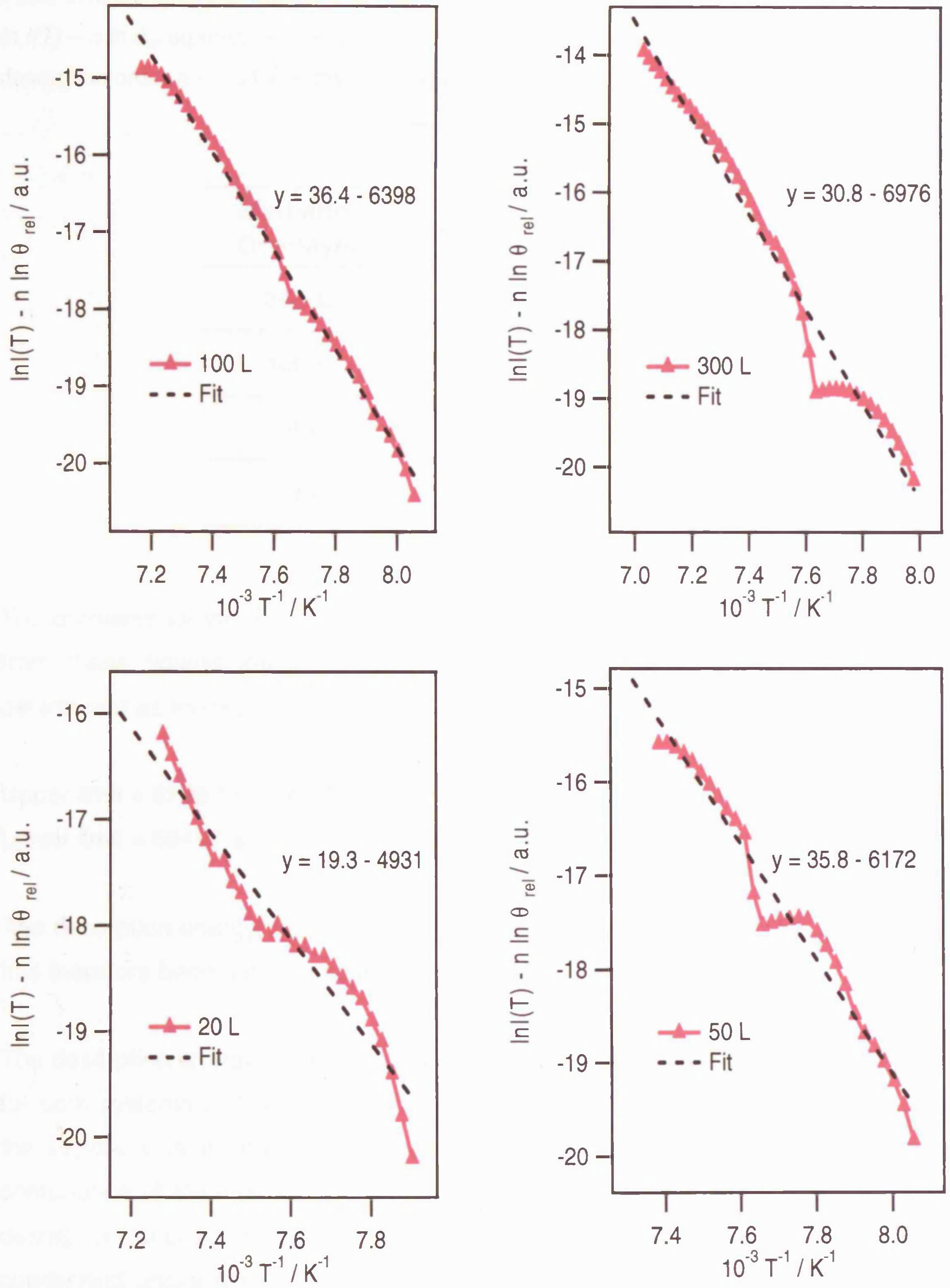

Figure 3.21 Plot of *ln I(T) – n ln* θ_{rel} against *1/T* for the multilayer fitted data for 20 L, 50 L, 100 L and 300 L exposures of methanol deposited on an existing layer of water ice (10 L). The order of desorption, *n* has been fixed at 0.23.

Table 3.12 Summary of the upper and lower limits to the gradient $-E_{des} / R$, acquired by plotting $\ln I(T) - n \ln \theta_{rel}$ against $1/T$, for the CH_3OH/H_2O(10 L) system. Lower limit determined with the desorption order $n = 0.01$ and the upper value with $n = 0.45$.

Methanol Overlayer	Gradient Lower Limit	Gradient Upper Limit
300 L	- 6838	- 7113
100 L	-6235	-6560
50 L	- 5969	- 6374
20 L	- 4737	- 5124

The gradients for the exposures of 20 L, 50 L, 100 L and 300 L can be averaged, and from these figures the range of values for the desorption energy, E_{des} can be determined as follows:

Upper limit = 6293 * 8.314 = 52318 J mol^{-1}
Lower limit = 5945 * 8.314 = 49425 J mol^{-1}

The desorption energy, E_{des} for the multilayer feature of the CH_3OH/H_2O(10 L) system has therefore been determined to be 51 kJ mol^{-1} ± 2 kJ mol^{-1}.

The desorption energy values for exposures of 20 L, 50 L, 100 L and 300 L are shown for both systems in *Figure 3.22*. The values appear to converge in both systems as the exposure is increased. The increased exposure corresponds to an increased contribution of the multilayer in each system. It is, of course, to be expected that the desorption energy should be the same in each system as the multilayer is a condensed phase where the nature of the surface should be irrelevant. The average value for the CH_3OH/H_2O(2 L) system is 52 ± 2 kJ mol^{-1}, and that for the CH_3OH/H_2O(10 L) system is 51 ± 2 kJ mol^{-1}.

In both systems, the desorption energy reported here is slightly higher than that previously recorded for pure methanol multilayers on a HOPG surface, where Bolina et al quoted a figure of ≈ 40 kJ mol^{-1} [14]. These observed differences are likely to be due to the refined technique that has been applied to fitting the data obtained here. In this study a minimal approach was taken by fitting the monolayer and trapped peaks, with the smallest contribution to the overall spectra, and then subtracting these from the experimental data to achieve a fit for the multilayer with the least opportunity for error. The technique used by Bolina [14, 45] involved creating Lorentzian fits for the individual multilayer peaks. As pointed out [14] this did not give ideal results as the shared leading edges were lost when the peak fits were stacked.

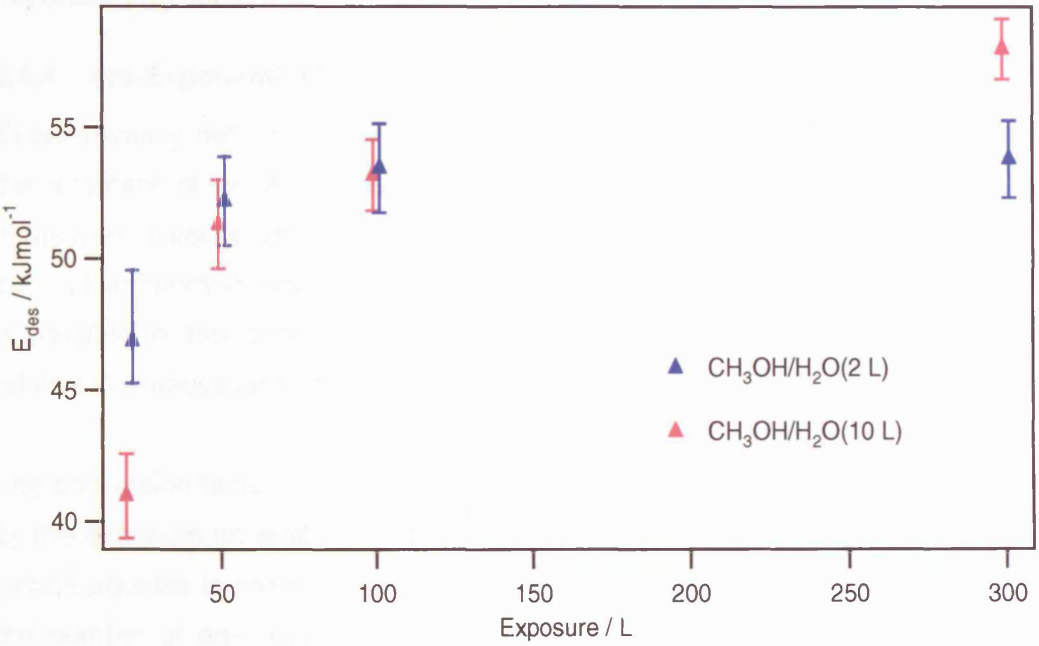

Figure 3.22 Chart showing the values and ranges for E_{des} calculated for the exposures of 20 L, 50 L, 100 L and 300 L in both the CH_3OH/H_2O(2 L) system and the CH_3OH/H_2O(10 L) system.

The values obtained here are in reasonable agreement with other calculations of the desorption energy of methanol multilayers available in the literature. Christmann and Demuth completed a study of methanol adsorbed on Pd(100) and recorded desorption energy values of 37.7 kJ mol^{-1} for the first physisorbed layer and 30.1 kJ mol^{-1} for the later condensed phase [34, 52]. Nishimura et al [35] completed a TPD study on the Al_2O_3(0001) substrate and determined the multilayer desorption energy of methanol to be 46 ± 2 kJ mol^{-1}. The values calculated in this study for the multilayer methanol desorption energies of methanol deposited on differing thicknesses of water ice are comparable with the results of Nishimura et al [35], but are slightly higher than those reported by Christmann and Demuth [34, 52] and the previous study of methanol on HOPG [14].

Further analysis was carried out on TPD spectra recorded for pure methanol adsorbed on to a HOPG substrate using the refined fitting technique described in this study, in an attempt to determine if the variation in recorded desorption energies was a result of the different surface. By completing exactly the same analysis as described in the previous sections, the desorption energy for multilayers of pure methanol adsorbed on HOPG was also determined to be 51 ± 2 kJ mol^{-1}. This confirms that, as expected, the desorption energy for multilayers of methanol is the same regardless of the underlying substrate.

3.4.4 Pre-Exponential Factor

Experimentally determined pre-exponential factors would typically be obtained from the intercept of an Arrhenius plot [47], provided that absolute coverages can be measured. Throughout the experiments reported here, absolute coverages have not been experimentally determined. However, using a technique devised by Bolina [14] it is possible to determine a conversion, or scaling, factor that can be used to convert relative coverages and intensities into actual coverage values.

The conversion factor is calculated by dividing the number of adsorbates per unit area by the exposure (in arbitrary units), required to form one monolayer of the adsorbate, (which equates to the saturation point of the monolayer peak). Bolina [14] calculated the number of adsorbates per unit area for both water and methanol on a HOPG surface by treating each molecule as a perfect sphere. The values obtained are shown in *Table 3.13.*

Table 3.13 Estimate of the number of adsorbates present per unit area of the HOPG surface. Taken from Bolina [45].

	Adsorbates per Unit Area
Water	3.71×10^{18} molec m^{-2}
Methanol	3.66×10^{18} molec m^{-2}

Figure 3.17 shows that, in both the CH_3OH/H_2O(2 L) and CH_3OH/H_2O(10 L) systems, the monolayer peak saturates following an exposure of 7 L. The integrated area for each 7 L exposure of methanol, and the associated conversion factor, is shown in *Table 3.14.* As shown earlier, the uptake of methanol remains constant as the exposure increases, so this conversion factor can then be applied to mass spectrometer intensities enabling absolute coverage values to be determined. The

conversion factor is higher for the methanol adsorbed on 10 L of water ice. This is probably due to the amorphous nature of the water, which results in variations in surface area which will impact on the conversion factor value and therefore on the accuracy of the pre-exponential factor calculation.

Table 3.14 Estimated values for the saturated area of the methanol monolayer peak in the CH_3OH/H_2O(2 L) and CH_3OH/H_2O(10 L) systems, along with the associated conversion factors.

	Monolayer Saturation Area / a.u.	**Conversion Factor**
CH_3OH/H_2O(2 L)	3.2×10^{-9}	1.14×10^{27}
CH_3OH/H_2O(10 L)	3.7×10^{-9}	9.89×10^{26}

All relative coverage values of methanol have been scaled by the relevant conversion factor in *Table 3.14* to give estimated absolute coverage values, enabling the calculation of the pre-exponential factor for methanol multilayers deposited on a pre-existing layer of water ice. Rearrangement of *Equation 3.1* gives an expression for the pre-exponential factor υ_n.

$$v_n = \frac{I(T)}{\theta^n \exp\left[\frac{-E_{des}}{RT_s}\right]} \qquad \text{Equation 3.11}$$

where *I(T)* is the scaled signal from the mass spectrometer, θ is the absolute coverage derived from the scaled intensity, *n* is the order of desorption calculated in the previous section, and E_{des} is the desorption energy also calculated earlier.

Equation 3.11 is used to determine the pre-exponential value at every data point and an average is taken for each exposure trace. *Table 3.15* shows the effect of increasing the exposure of methanol on the calculated pre-exponential factor for the two systems, CH_3OH/H_2O(2 L) and CH_3OH/H_2O(10 L). As observed for methanol adsorption directly onto HOPG [14], no exposure dependence has been detected for either system, which confirms the earlier assumption that the pre-exponential factor is not a function of coverage.

Table 3.15 Table showing the effect of altering the methanol exposure on the calculated pre-exponential factor for multilayer methanol desorption from a pre-existing layer of water ice adsorbed on HOPG.

	Pre-exponential Factor[a] / molecules m^{-2} s^{-1}	
Exposure / Langmuir	**CH_3OH/H_2O(2 L)**	**CH_3OH/H_2O(10 L)**
10	1.5×10^{22}	1.5×10^{25}
15	2.1×10^{22}	1.3×10^{25}
20	2.7×10^{22}	8.5×10^{24}
50	1.2×10^{22}	3.5×10^{25}
100	1.3×10^{22}	2.7×10^{25}
300	1.2×10^{22}	2.7×10^{25}
Average	1.7×10^{22}	2.1×10^{25}

[a] The units for the pre-exponential factor are those expected for zero order desorption, despite the observation of a fractional desorption order.

A number of variables affect the accuracy of this estimated pre-exponential factor and these include the accuracy of the conversion factor, the calculated order of the desorption process, *n*, and the energy of desorption, E_{des}. Bolina [14] showed that the the value of the conversion factor actually has the least impact on the accuracy of the pre-exponential factor and does not contribute greatly to the propagation of errors. The errors associated with the calculated desorption energy and the desorption order, make the biggest impact on the calculated value of the pre-exponential factor. *Tables 3.16* and *3.17* show how the value of the pre-exponential factor varies as a result of altering the desorption energy and desorption order respectively. The largest source of error in the determination of the pre-exponential factor for each system originates from the uncertainty in the desorption order, which in turn arises from the complex nature of the overlapping peaks in the TPD spectra.

The final figures for the pre-exponential factor of desorption of multilayers of methanol from a pre-existing layer of water ice are found to be $1.7 \times 10^{22 \pm 4}$ molecule m^{-2} s^{-1} for the CH_3OH/H_2O(2 L) system and $2.1 \times 10^{25 \pm 5}$ molecule m^{-2} s^{-1} for the CH_3OH/H_2O(10 L) system. There is significant overlap between these two values and the early figure of $6.1 \times 10^{25 \pm 3}$ molecule m^{-2} s^{-1}, reported for pure methanol multilayers deposited on HOPG [14], and hence, within experimental error, these values are the same.

Table 3.16 Table showing the effect of altering the desorption energy on the calculated pre-exponential factor for multilayer methanol desorption from a pre-existing layer of water ice adsorbed on HOPG. The desorption energy has been varied by 2 standard deviations about the mean for each system.

	Pre-exponential Factor[a] / molecules m^{-2} s^{-1}	
Desorption Energy / kJ mol^{-1}	**CH_3OH/H_2O(2 L)**	**CH_3OH/H_2O(10 L)**
49	-	4.0×10^{24}
50	3.0×10^{21}	-
51	-	**2.1×10^{25}**
52	**1.7×10^{22}**	-
53	-	1.1×10^{26}
54	9.3×10^{22}	-

Table 3.17 Table showing the effect of altering the desorption order on the calculated pre-exponential factor for multilayer methanol desorption from a pre-existing layer of water ice adsorbed on HOPG. The desorption order has been varied by 1 standard deviation about the mean for each system.

	Pre-exponential Factor[a] / molecules m^{-2} s^{-1}	
Desorption Order	**CH_3OH/H_2O(2 L)**	**CH_3OH/H_2O(10 L)**
0.12	-	2.5×10^{30}
0.24	8.0×10^{25}	-
0.23	-	**2.1×10^{25}**
0.32	**1.7×10^{22}**	-
0.34	-	1.8×10^{20}
0.4	3.6×10^{18}	-

3.5 Conclusions

This TPD study has considered the adsorption of methanol directly onto the surface of a layer of amorphous solid water. Three different systems were considered based on the thickness of the underlying water layer.

The resulting TPD spectra for water demonstrated that the desorption of water was inhibited by the overlying layer of methanol. As the exposure of methanol was increased, the water peaks became broader and their desorption temperatures shifted up due to the competition between the desorption of each species.

Methanol TPD traces showed evidence for the monolayer and multilayer features that were observed previously in the study of pure methanol on HOPG [14]. The low exposure spectra also included an additional, high temperature, peak that can be described as a trapped feature. This trapped feature was observed to desorb along with the bulk of the water ice and its peak area increased as the thickness of the underlying water increased. When methanol deposition occurred on the surface of crystalline water ice, the trapped feature saturated at a lower exposure of methanol, confirming the assignment of this peak to methanol molecules trapped within the bulk pores of the amorphous water ice structure.

The exact nature of this trapped feature is unclear, but it is possible that it is due to the formation of a methanol-water clathrate hydrate structure [20]. There is clear evidence for the thermally induced migration of methanol into the bulk water ice, but without further structural analysis it is impossible to say whether the complex formed is actually a clathrate hydrate or some other structure. This is counter to the suggestions of some research groups [25] who have suggested that large molecules such as methanol will not diffuse in the ice, especially in the relatively low porous ice formed at 97 K. However, this observation is in agreement with Souda [28] who worked on amorphous methanol and heavy-water films and found evidence for the intermixing of the two species at the glass transition phase.

Figure 3.23 presents a proposed model describing the processing that occurs in the layered ice as it is heated. As methanol is exposed to a pre-existing layer of ASW, some of the methanol molecules lodge in the surface micro-pores of the water [17] before the monolayer and multilayers are formed. Heating the layered ice between 125 K and 133 K results in the desorption of the multilayer methanol. Beyond 133 K there is an increased mobility of the water molecules as the temperature associated with the transformation of amorphous water into the crystalline phase is approached [17]. This results in closure of a number of holes in the water surface and effectively traps the methanol molecules. Further heating sees the desorption of the methanol monolayer along with a small amount of the water ice. At ≈ 145 K the water ice has completely crystallised and permanently sealed off the pores, entrapping the methanol deep within the ice structure. The remaining methanol is not released until the bulk of the water ice has desorbed.

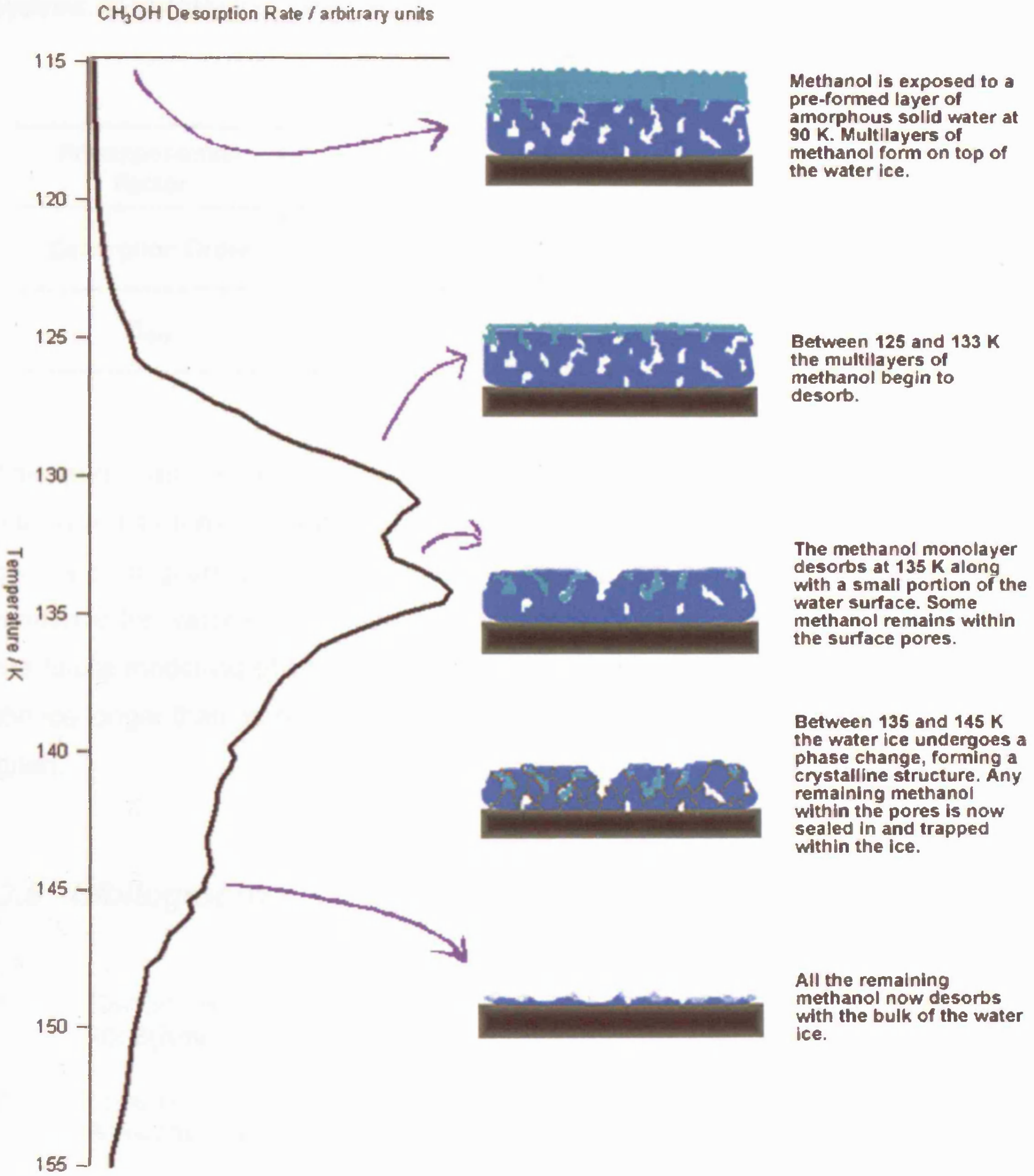

Methanol is exposed to a pre-formed layer of amorphous solid water at 90 K. Multilayers of methanol form on top of the water ice.

Between 125 and 133 K the multilayers of methanol begin to desorb.

The methanol monolayer desorbs at 135 K along with a small portion of the water surface. Some methanol remains within the surface pores.

Between 135 and 145 K the water ice undergoes a phase change, forming a crystalline structure. Any remaining methanol within the pores is now sealed in and trapped within the ice.

All the remaining methanol now desorbs with the bulk of the water ice.

Figure 3.23 Model of proposed behaviour of the layered methanol and water system adsorbed on HOPG, during the TPD process.

Quantitative analysis was completed for methanol multilayers in both the CH_3OH/H_2O(2 L) and the CH_3OH/H_2O(10 L) system. This gave the values shown in *Table 3.18*, all of which are identical within error limits to those calculated for methanol multilayers deposited directly onto the HOPG surface. It can therefore be concluded that as expected, the desorption of methanol multilayers is the same regardless of the underlying substrate.

Table 3.18 Kinetic parameters determined for methanol multilayers in the following two systems, CH_3OH/H_2O(2 L) and CH_3OH/H_2O(10 L).

	CH_3OH/H_2O(2 L)	**CH_3OH/H_2O(10 L)**
Pre-exponential Factor	$1.7 \times 10^{22 \pm 4}$ molecule m^{-2} s^{-1}	$2.1 \times 10^{25 \pm 5}$ molecule m^{-2} s^{-1}
Desorption Order	0.32 ± 0.15	0.23 ± 0.22
E_{des}	52 ± 2 kJ mol^{-1}	51 ± 2 kJ mol^{-1}

This study has confirmed that binary layered systems of water and methanol become intermixed as they are heated above 100 K and that amorphous water ices deposited onto a dust grain analogue surface can trap molecules as large as methanol. The tendency for water to constrain the methanol molecules will have consequences for the future modelling of interstellar gas phase abundances, as methanol is held within the ice longer than proposed by the sublimation temperatures of methanol from a bare grain.

3.6 Bibliography

1. Garrod, R., Park, I.H., Caselli, P., and Herbst, E., Faraday Discussions, 2006(Advance Article): p. 1-12.
2. Friberg, P., Madden, S.C., Hjalmarson, A., and Irvine, W.M., Astronomy and Astrophysics, 1988. **195**(1-2): p. 281-289.
3. Smith, I.W.M., Herbst, E., and Chang, Q., Monthly Notices of the Royal Astronomical Society, 2004. **350**(1): p. 323-330.
4. Menten, K.M., Walmsley, C.M., Henkel, C., and Wilson, T.L., Astronomy and Astrophysics, 1988. **198**(1-2): p. 253-266.
5. van der Tak, F.F.S., van Dishoeck, E.F., and Caselli, P., Astronomy and Astrophysics, 2000. **361**(1): p. 327-339.
6. Charnley, S.B., Kress, M.E., Tielens, A., and Millar, T.J., Astrophysical Journal, 1995. **448**(1): p. 232-239.
7. Watanabe, N. and Kouchi, A., Astrophysical Journal, 2002. **571**: p. l173-l176.

8. Watanabe, N., Nagaoka, A., Shiraki, T., and Kouchi, A., Astrophysical Journal, 2004. **616**(1): p. 638-642.

9. Watanabe, N., Shiraki, T., and Kouchi, A., Astrophysical Journal, 2003. **588**(2): p. L121-L124.

10. Sandford, S.A., Meteoritics & Planetary Science, 1996. **31**(4): p. 449-476.

11. Sandford, S.A. and Allamandola, L.J., Astrophysical Journal, 1993. **417**: p. 815.

12. Skinner, C.J., Tielens, A., Barlow, M.J., and Justtanont, K., Astrophysical Journal, 1992. **399**(1): p. L79-L82.

13. Viti, S., Collings, M.P., Dever, J.W., McCoustra, M.R.S., and Williams, D.A., Monthly Notices of the Royal Astronomical Society, 2004. **354**(4): p. 1141-1145.

14. Bolina, A.S., Wolff, A.J., and Brown, W.A., Journal of Chemical Physics, 2005. **122**(4): p. art. no.-044713.

15. Bolina, A.S., Wolff, A.J., and Brown, W.A., Journal of Physical Chemistry B, 2005. **109**: p. 16836-16845.

16. Jenniskens, P. and Blake, D.F., Science, 1994. **265**(5173): p. 753-756.

17. Barnun, A., Dror, J., Kochavi, E., and Laufer, D., Physical Review B, 1987. **35**(5): p. 2427-2435.

18. Ayotte, P., Smith, R.S., Stevenson, K.P., Dohnalek, Z., Kimmel, G.A., and Kay, B.D., Journal of Geophysical Research-Planets, 2001. **106**(E12): p. 33387-33392.

19. Barnun, A., Kleinfeld, I., and Kochavi, E., Physical Review B, 1988. **38**(11): p. 7749-7754.

20. Blake, D., Allamandola, L., Sandford, S., Hudgins, D., and Freund, F., Science, 1991. **254**(5031): p. 548-551.

21. Notesco, G. and Bar-Nun, A., Icarus, 2000. **148**(2): p. 456-463.

22. Notesco, G. and BarNun, A., Icarus, 1997. **126**(2): p. 336-341.

23. Ehrenfreund, P., Kerkhof, O., Schutte, W.A., Boogert, A.C.A., Gerakines, P.A., Dartois, E., d'Hendecourt, L., Tielens, A., van Dishoeck, E.F., and Whittet, D.C.B., Astronomy and Astrophysics, 1999. **350**(1): p. 240-253.

24. Allamandola, L.J., Sandford, S.A., and Valero, G.J., Icarus, 1988. **76**: p. 225.

25. Collings, M.P., Anderson, M.A., Chen, R., Dever, J.W., Viti, S., Williams, D.A., and McCoustra, M.R.S., Monthly Notices of the Royal Astronomical Society, 2004. **354**(4): p. 1133-1140.

26. Blake, D.F., Allamandola, L., Freund, F., Sandford, S., and Hudgins, D., IAU Symposia, 1992(150): p. 437-438.

27. Blake, D.F., Allamandola, L.J., Sandford, S., and Freund, F., Meteoritics, 1991. **26**(4): p. 319-320.

28. Souda, R., Physical Review Letters, 2004. **93**(23): p. art. no.-235502.

29. Souda, R., Kawanowa, H., Kondo, M., and Gotoh, Y., Journal of Chemical Physics, 2003. **119**(12): p. 6194-6200.

30. Smith, R.S. and Kay, B.D., Nature, 1999. **398**(6730): p. 788-791.

31. Bisschop, S.E., Fraser, H.J., Oberg, K.I., van Dishoeck, E.F., and Schlemmer, S., Astronomy & Astrophysics, 2006. **449**(3): p. 1297-U257.

32. Stevenson, K.P., Kimmel, G.A., Dohnalek, Z., Smith, R.S., and Kay, B.D., Science, 1999. **283**(5407): p. 1505-1507.

33. Mayer, E. and Pletzer, R., Nature, 1986. **319**: p. 298.

34. Christmann, K. and Demuth, J.E., Journal of Chemical Physics, 1982. **76**(12): p. 6308-6317.

35. Nishimura, S.Y., Gibbons, R.F., and Tro, N.J., Journal of Physical Chemistry B, 1998. **102**(35): p. 6831-6834.

36. Wu, M., Truoung, C.M., and Goodman, D.W., Journal of Physical Chemistry, 1993. **97**: p. 9425-9433.

37. Lofgren, P., Ahlstrom, P., Lausma, J., Kasemo, B., and Chakarov, D., Langmuir, 2003. **19**(2): p. 265-274.

38. Pratt, S.J., Escott, D.K., and King, D.A., Journal of Chemical Physics, 2003. **119**(20): p. 10867-10878.

39. Collings, M.P., Dever, J.W., Fraser, H.J., McCoustra, M.R.S., and Williams, D.A., Astrophysical Journal, 2003. **583**(2): p. 1058-1062.

40. Dixit, S., Crain, J., Poon, W.C.K., Finney, J.L., and Soper, A.K., Nature, 2002. **416**(6883): p. 829-832.

41. Guo, J.H., Luo, Y., Augustsson, A., Kashtanov, S., Rubensson, J.E., Shuh, D.K., Agren, H., and Nordgren, J., Physical Review Letters, 2003. **91**(15).

42. Chakarov, D.V., Osterlund, L., and Kasemo, B., Vacuum, 1995. **46**(8-10): p. 1109-1112.

43. Hagen, W., Tielens, A., and Greenberg, J.M., Chemical Physics, 1981. **56**(3): p. 367-379.

44. Maldoni, M.M., Smith, R.G., Robinson, G., and Rookyard, V.L., Monthly Notices of the Royal Astronomical Society, 1998. **298**(1): p. 251-258.

45. Bolina, A.S., *Adsorption of Astrochemically Relevant Molecules on Interstellar Dust Analogues.* PhD Thesis, Department of Chemistry, 2005, UCL.

46. Kolasinski, K.W., *Surface Science: Foundations of Catalysis and Nanoscience.* 2002: John Wiley and Sons Ltd.

47. Dejong, A.M. and Niemantsverdriet, J.W., Surface Science, 1990. **233**(3): p. 355-365.

48. Attard, H. and Barnes, C., *Surfaces*. Oxford Chemistry Primers. Vol. 59. 2001: Oxford University Press.

49. Parker, D.H., Jones, M.E., and Koel, B.E., Surface Science, 1990. **233**(1-2): p. 65-74.

50. Pisani, C., Rabino, G., and Ricca, F., Surface Science, 1974. **41**(1): p. 277-292.

51. King, D.A., Surface Science, 1975. **47**(1): p. 384-402.

52. Christmann, K. and Demuth, J.E., Journal of Chemical Physics, 1982. **76**(12): p. 6318-6327.

Chapter 4 RAIRS Studies of the Adsorption and Desorption of Layered Films of Methanol and Water Sequentially Adsorbed on Graphite.

4.1 Introduction

As discussed in the previous chapter, methanol is an important interstellar molecule and is typically observed as a dilute component of water rich ices [1, 2]. This chapter forms part of a comprehensive study that aims to provide a detailed understanding of the desorption of methanol from the surface of icy grains. Studies have already been completed on the desorption of pure methanol and pure water from the bare surface of the graphitic dust grain analogue HOPG [3, 4] and the previous chapter outlined the TPD results obtained for the study of the adsorption and desorption of methanol from a layer of amorphous solid water, ASW. This chapter will detail an infrared study of the binary layered system with methanol deposited on top of ASW.

Most astronomical spectra of ices contain a prominent feature at around 3250 cm^{-1} which is attributed to the presence of water, and is usually referred to as the 3 μm band [5-7]. The specific shape of the observed bands are rarely well matched with laboratory spectra of pure water ices and it has been proposed that the breadth of the band, and the specific peak positions, can only be modelled adequately by more complex laboratory mixtures [7]. Infrared studies are particularly useful in characterising the observed interstellar ices. Tielens and co-workers [6] completed an infrared study of solid water ice mixed with a number of different species, including methanol, in an attempt to match observed spectral features in the 3 μm region. The group indicated that dilution with methanol considerably altered the infrared spectrum and they attributed a low frequency band observed on the 3250 cm^{-1} feature to the presence of CH stretching vibrations in methanol.

There have been a number of infra-red studies of mixed methanol and water ices [6, 8, 9], sometimes with additional species such as carbon monoxide and ammonia within the mix [10, 11]. Although these previous studies have been based on intimate mixtures, rather than the discrete layered structures that will be described in this chapter, their work has emphasised the importance of conducting detailed infrared studies of complex water dominated ices. It is only by producing detailed laboratory spectra of controlled ices that astronomers can hope to provide direct information on the composition of interstellar dust grain mantles. There is some suggestion in the literature that polar ice mantles may undergo some molecular segregation [12] and even studies on clathrate hydrates have indicated that methanol will begin to auto-associate when it is present in high enough concentrations relative to water [13]. These studies support the requirement of studying layered ice systems and so this chapter will describe the first detailed infrared study of binary layers of water and methanol.

4.2 Methodology

Experiments were performed in an ultra-high vacuum (UHV) chamber, described in Chapter 2. The chamber has a base pressure of 2×10^{-10} mbar. The HOPG sample has been described previously along with the "scotch tape" method of cleaning [4].

Ices were grown in situ by exposing the cold HOPG surface, held at ≈ 97 K, to a stream of gas by back filling the chamber through a high precision leak valve. The exposures were measured in Langmuir (L), where $1\ \mathrm{L} = 10^{-6}$ mbar s, and were recorded during dosing by the mass spectrometer, to gain an accurate measure of the exposure of the two species and to confirm purity. The chemicals used during the experiments were distilled, de-ionised water and methanol (CH_3OH – 99.9% - Aristar – BDH).

All RAIR spectra were recorded using a Mattson instruments Fourier transform infrared spectrometer coupled to a mercury cadmium telluride (MCT) detector. The spectra were recorded with a resolution of 4 cm^{-1} following 256 scans. During the annealing and desorption sequence, the sample was held at the set temperature for 3 minutes and then cooled to the base temperature before performing the scan. Between experiments the sample was annealed to 500 K and held for three minutes to remove all adsorbates from the surface.

4.3 RAIRS Results and Discussion

4.3.1 Adsorption of pure water

In these experiments, increasing doses of methanol were exposed to an existing film of water ice to form a layered structure. Three different thicknesses of water ice, equivalent to 2 L, 10 L and 50 L exposures, were considered. The ice samples studied were summarised in the previous chapter (see *Table 3.1*). The same notation has been used to describe these layered ices, such that $CH_3OH/H_2O(2\ L)$ represents a layered ice with methanol on top of a pre-existing layer (2 L exposure) of water ice.

The initial layer of water ice was deposited onto an HOPG sample held at 97 K. This temperature is well below the glass transition temperature for water and the ice formed is therefore expected to be in its amorphous phase [14]. The phase of the water can be confirmed by comparing the OH stretching region of the pure water RAIR spectra (see *Figure 4.1*) with previous studies that have documented the infrared crystalline/amorphous fingerprint [4, 15, 16]. *Figure 4.1* shows that, following an exposure of 50 L of water, the major peak is centred at 3392 cm^{-1} with a low frequency shoulder at 3324 cm^{-1}. The low frequency shoulder has an amplitude approximately 90% of that of the main 3392 cm^{-1} peak, which is characteristic of the amorphous state. In contrast, crystalline ice would be expected to show approximately equal amplitudes for both the 3392 cm^{-1} and 3324 cm^{-1} feature [4].

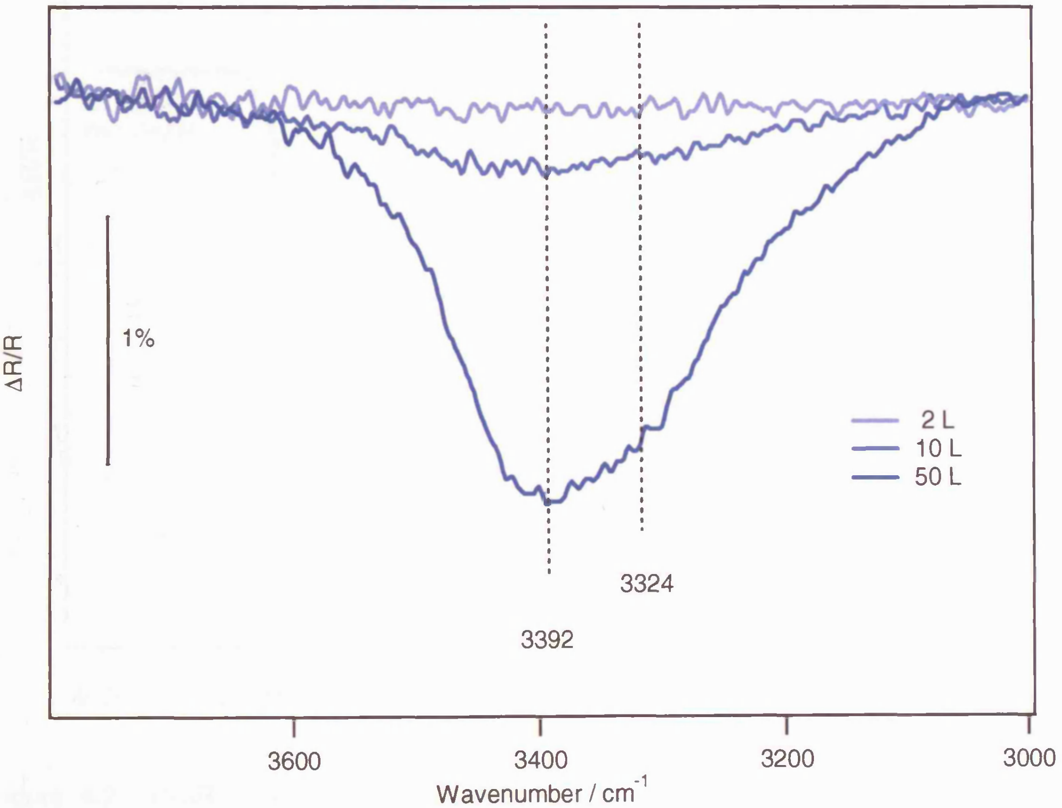

Figure 4.1 RAIR spectra recorded between 3000 cm^{-1} and 3800 cm^{-1}, showing the OH stretching region for the three exposures of pure water ice (2 L, 10 L and 50 L) adsorbed on HOPG at 97 K.

4.3.2 Adsorption of methanol on water

Figure 4.2 shows RAIR spectra of the CH_3OH/H_2O(50 L) system following adsorption of increasing exposures of methanol on the 50 L exposure of water ice. The initial pure water trace is also shown. The water and methanol were deposited at 97 K and all scans were taken prior to any heating. The spectra show the clear transition from the water dominated features of the ice to the methanol dominated features as the methanol exposure increases to 300 L. For comparison, pure water spectra and pure methanol spectra are shown in *Figure 4.3* and *Figure 4.4* respectively.

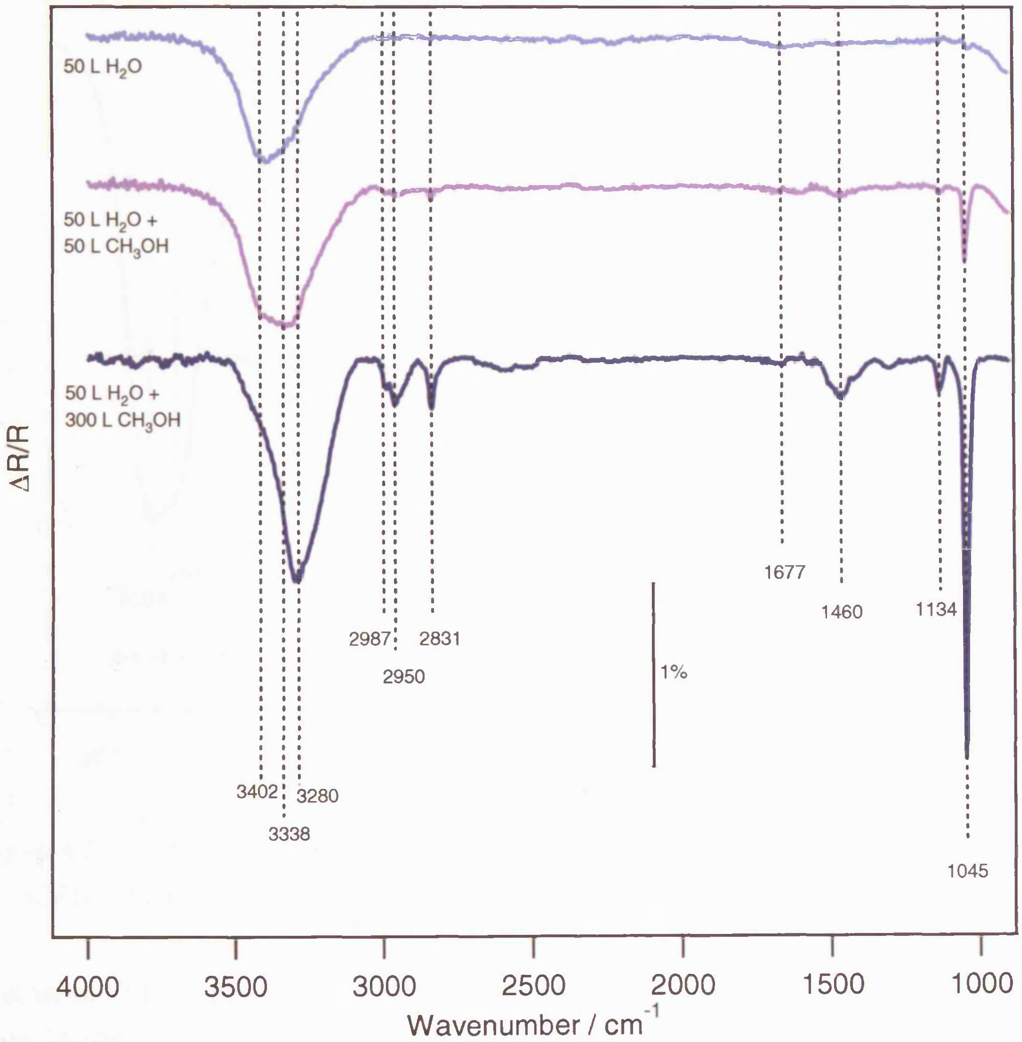

Figure 4.2 RAIR spectra showing the growth of the layered ice formed by depositing increasing amounts of methanol on a pre-existing 50 L layer of water, all deposited on HOPG at 97 K.

The bands observed in *Figure 4.2* can be confidently assigned by comparison with previous studies of both water [4, 17, 18] and methanol [3] studied in isolation on the HOPG surface. Water typically shows a broad band between 3100 cm^{-1} and

3600 cm^{-1} with defined shoulders at 3400 cm^{-1} and 3320 cm^{-1} which are assigned to the OH stretching modes. The HOH scissors mode has also been reported at 1677 cm^{-1}. The assigned water features are summarised in *Figure 4.3,* which shows the RAIR spectra for pure water adsorbed on HOPG. The small feature at 2237 cm^{-1} is likely to be a combination band of the scissors and librational modes, and was previously reported in a study of ice growth on a polycrystalline surface [19]. Spectra of annealed water ice showing the changes in the OH stretching region, characteristic of crystalline water ice, are shown in a later chapter (*Figure 6.8*).

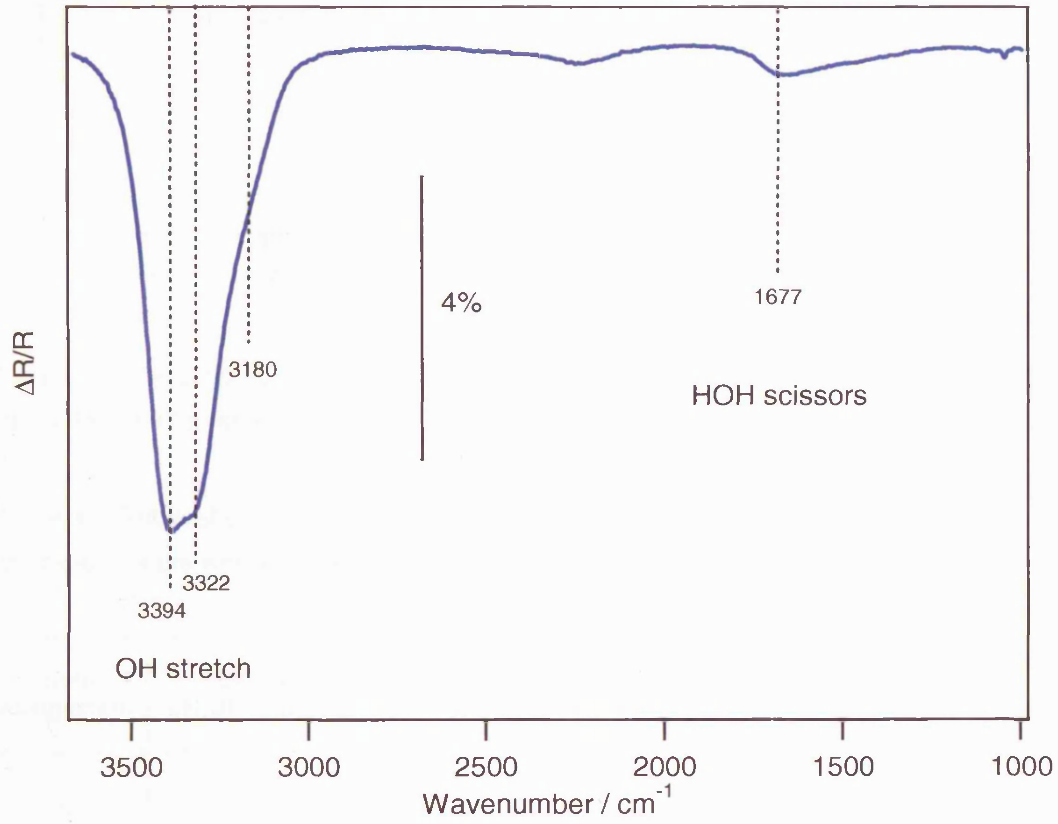

Figure 4.3 The 3600-1000 cm^{-1} RAIR spectrum for a 300 L exposure of pure water adsorbed on HOPG at 97 K, showing vibrational assignments.

Methanol has a more complex spectral fingerprint, but has been well characterised on both HOPG [3] and on metal surfaces [20]. *Figure 4.4* shows a summary of the methanol assignments for the RAIR spectra of a pure methanol ice adsorbed on HOPG. The typical spectra observed when pure methanol is annealed to increasing temperatures will be shown later (*Figure 4.15*). *Table 4.1* summarises the assignments for the layered ice investigated in this study, along with the previously reported vibrational bands for pure methanol multilayers adsorbed on HOPG [3], Pd [20] and in an Ar matrix [21]. The assignments for crystalline methanol have also been included for comparison [3, 22].

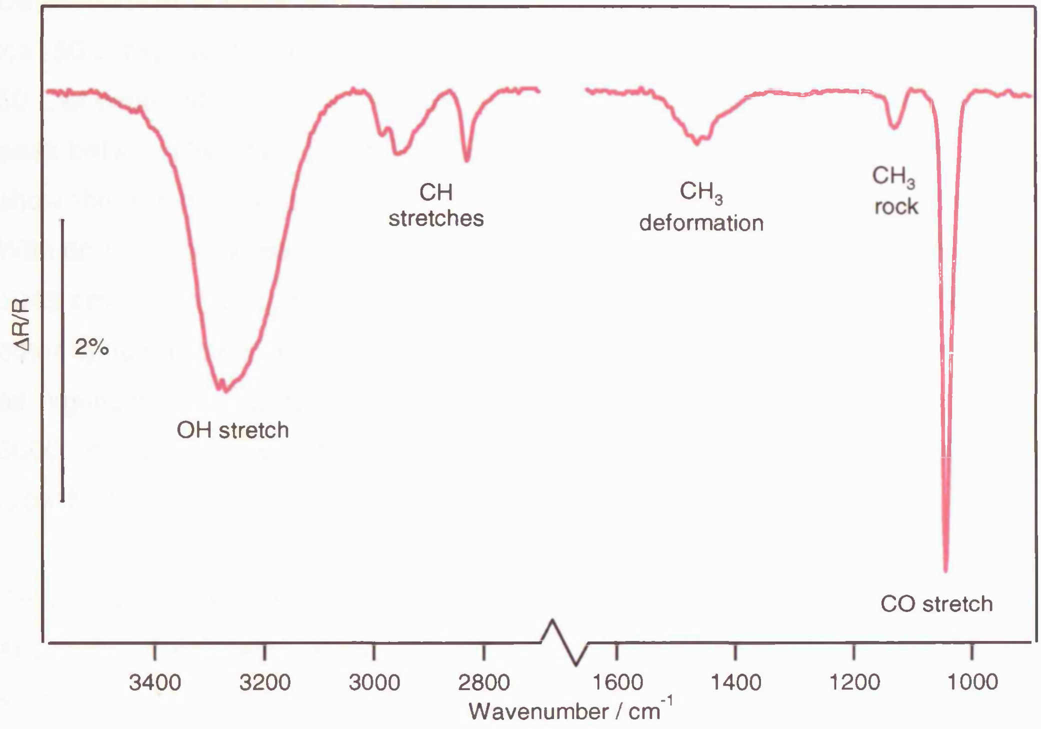

Figure 4.4 The 3600-900 cm^{-1} RAIR spectrum for a 300 L exposure of pure methanol adsorbed on HOPG at 97 K, showing vibrational assignments.

Table 4.1 Table showing the assignment of vibrational bands of high exposures of methanol exposed to a pre-existing layer of water ice, adsorbed on HOPG at 97 K.

Band Assignment	**Layered CH_3OH/H_2O(50 L)**	**Multilayer CH_3OH (HOPG) [3]**	**Multilayer CH_3OH (Pd) [20]**	**CH_3OH in an Argon matrix [21]**	**Crystalline α phase [20]**
υ(OH)	3402*				
	3323		3301	3667	3284
	3280	3260	3193		3187
υa(CH_3)	2987	2983	2987	3006	2982
	2950	2956	2959	2962	2955
					2912
υs(CH_3)	2831	2833	2832	2848	2829
δs(CH_3)	1460	1468	1473	1466	1458
ρ(CH_3)	1134	1132	1144	1145	1256
				1077	1162
					1142
υ(CO)	1045	1045	1028	1034	1046
				1028	1029

* The 3402 cm^{-1} feature present in the layered system is attributed to the υ(OH) stretch from the H_2O molecule.

Detailed RAIR spectra for the adsorption of methanol on an underlying layer of water ice (50 L exposure) are shown in *Figure 4.5*. The initial trace, following adsorption of 50 L of water, shows the previously described features of pure water, namely a broad peak between 3050 cm^{-1} and 3600 cm^{-1} assigned to the OH stretch. The other traces show the effect of depositing increasing amounts of methanol on top of the water ice. With an initial 3 L exposure of methanol an additional peak appears in the spectrum at 1045 cm^{-1}. Increasing the exposure beyond 7 L results in the appearance of several other spectral features at 1132 cm^{-1}, 1460 cm^{-1}, 2831 cm^{-1}, 2950 cm^{-1} and 2987 cm^{-1} as highlighted in *Figure 4.5*. The shape of the broad OH feature between 3050 and 3600 cm^{-1} noticeably changes when the methanol exposure exceeds 20 L, with the growth of a new band centred on 3280 cm^{-1}.

During the adsorption of methanol onto the existing layer of water, increasing the exposure of methanol leads to an increasing intensity of all bands visible in the spectrum. None of the bands appear to saturate, nor do they undergo frequency shifts. These two features are indicative of the formation of physisorbed multilayers. If the complex OH stretching region, which receives contributions from both the methanol and water present in the ice, is ignored all of the methanol-only bands have the same vibrational frequencies as those previously recorded for physisorbed methanol multilayers on the HOPG surface [3]. This is in agreement with the TPD data discussed in the previous chapter, where it was also impossible to distinguish between methanol molecules adsorbed directly on HOPG from those adsorbed on the water layer.

Figure 4.6 shows the variation of the integrated peak area as the methanol exposure increases, for the three most intense methanol-only peaks in the layered spectrum. The methanol exposures have been normalised by integrating each dose area and plotting on a relative scale. This chart confirms that there is a linear uptake as the methanol exposure increases. This suggests that the sticking probability remains constant as the exposure increases. This is in agreement with the results of the TPD data presented in Chapter 3. The lack of a gradient change between low and high exposures suggests that the tendency for methanol to bind to the water surface is the same as its tendency to bind to other methanol molecules. This was also noted in the previous TPD chapter, as it was not possible to distinguish separate monolayer peaks for the adsorption of methanol on graphite and the monolayer on the water surface.

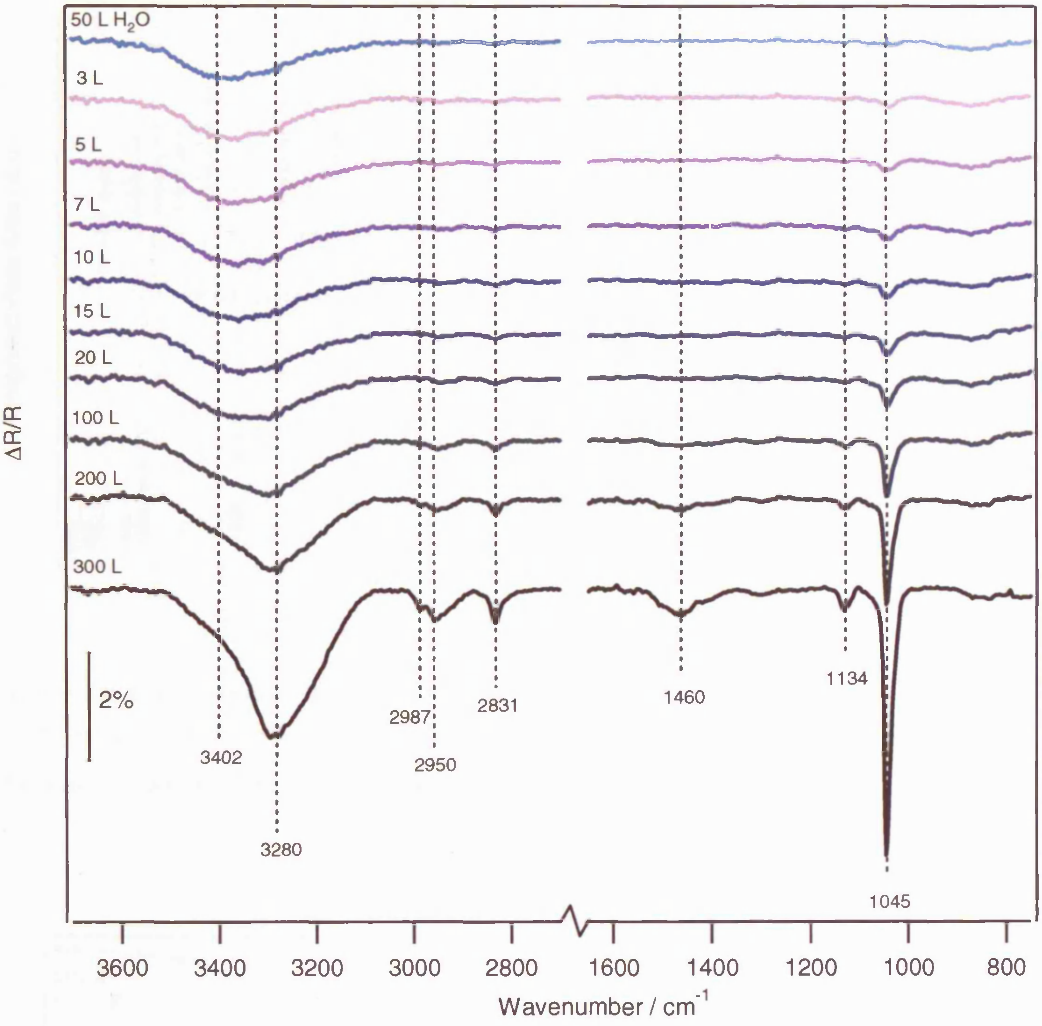

Figure 4.5 The 3600-750 cm^{-1} RAIR spectrum showing the full adsorption sequence for increasing exposures of pure methanol on a pre-existing layer of water ice (50 L) adsorbed on HOPG at 97 K.

Unsurprisingly, the same vibrational features are observed regardless of the underlying water thickness. *Figure 4.7* shows the final 300 L exposure of methanol in all three systems, CH_3OH/H_2O(2 L), CH_3OH/H_2O(10 L) and CH_3OH/H_2O(50 L). The only difference observed is a change in the shape of the OH peak, with the CH_3OH/H_2O(50 L) system showing a broader feature, with a more pronounced high frequency shoulder corresponding to the greater input from the water.

At low coverages, where the interaction of the adsorbed molecules with the surface can be observed, there are no observable differences in the RAIR spectra across the three systems. This is in agreement with the TPD uptake curves which are identical for the three systems, and confirms that the adsorption of methanol on water cannot be distinguished from adsorption of methanol on HOPG.

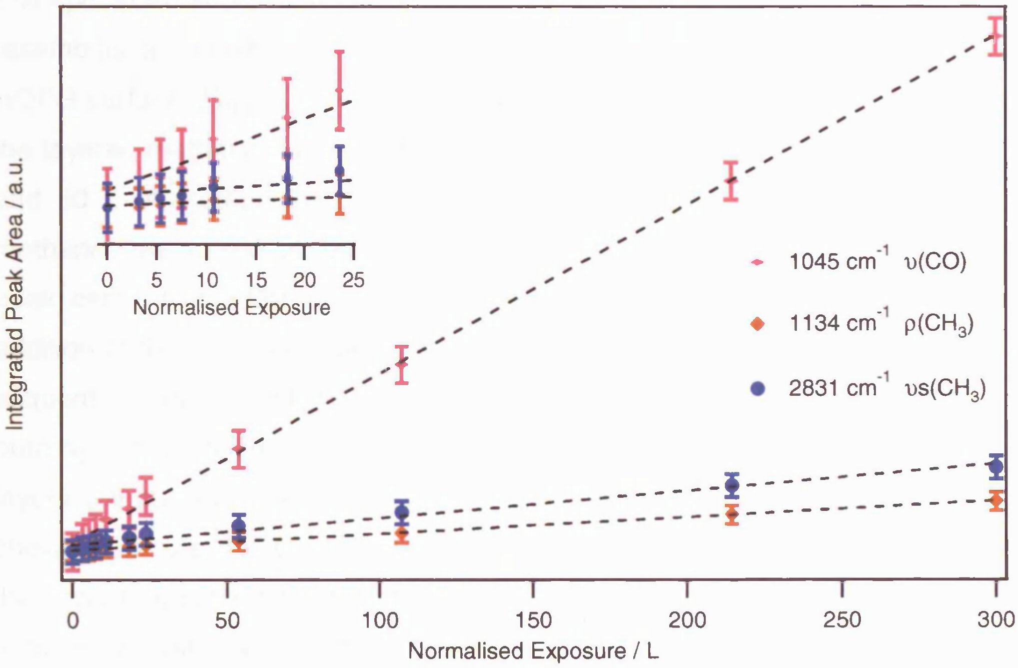

Figure 4.6 Chart showing the integrated peak area for the methanol bands at 1045 cm^{-1}, 1134 cm^{-1} and 2831 cm^{-1} as a function of increasing methanol exposure on a pre-existing layer of water ice (50 L). The inset focuses on the low exposure region.

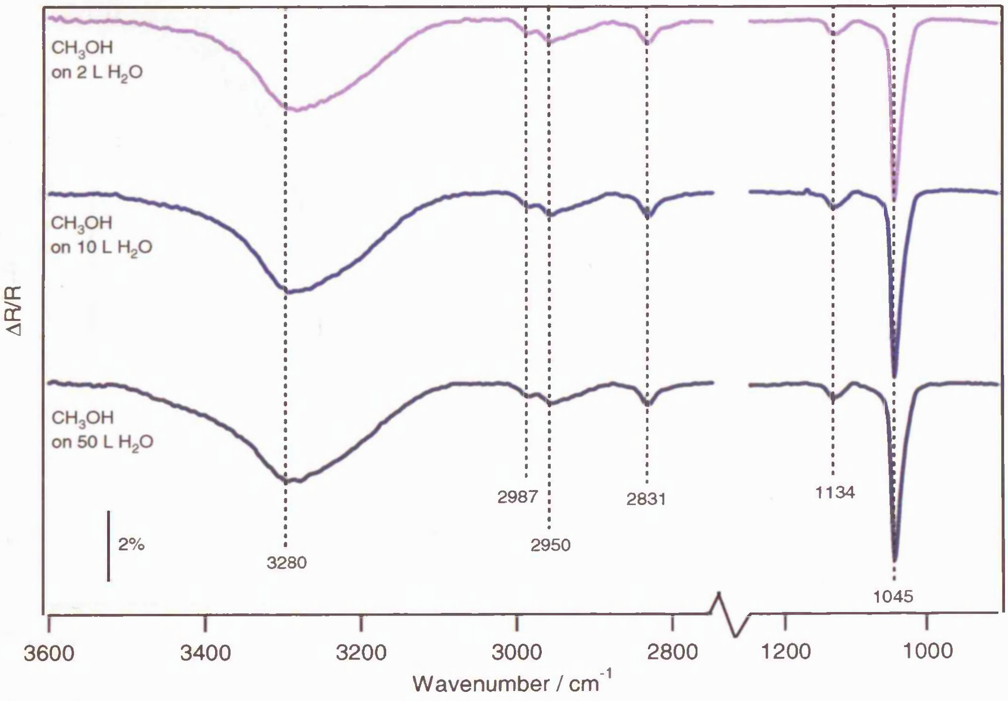

Figure 4.7 The 3600-900 cm^{-1} RAIR spectrum showing the highest exposure of methanol (300 L) deposited on each of the underlying thicknesses of water (2 L, 10 L and 50 L) adsorbed on HOPG at 97 K.

The spectrum recorded in the OH stretching region between 3600 cm^{-1} and 2600 cm^{-1} resembles a combination of that recorded for pure water and pure methanol on a HOPG surface. *Figure 4.8* compares the OH region for pure methanol, pure water and the layered methanol-water system formed by the sequential addition of 50 L of water and 50 L of methanol. Pure water has a broad peak centred at 3390 cm^{-1}, pure methanol has a peak at 3260 cm^{-1} and the methanol-water layer reported here has a peak centred at 3330 cm^{-1}. The layered ice trace is well modelled by the simple addition of the pure water and pure methanol spectra (*Figure 4.8*). This suggests that sequential exposure of methanol and water has caused little perturbation from the pure systems and that, unsurprisingly, the two species have effectively remained as layers without any mixing. This assumption is further supported by the pure spectra shown in *Figure 4.2* and the assignments shown in *Table 4.1*. These both show that the band frequencies seen in the layered systems correspond directly to those found in the pure systems [3, 4]. Note that the TPD spectra reported in the previous chapter showed evidence for mixing between the methanol and water layers. However, the RAIR spectra presented here show conclusively that this mixing only occurs as a result of the heating process.

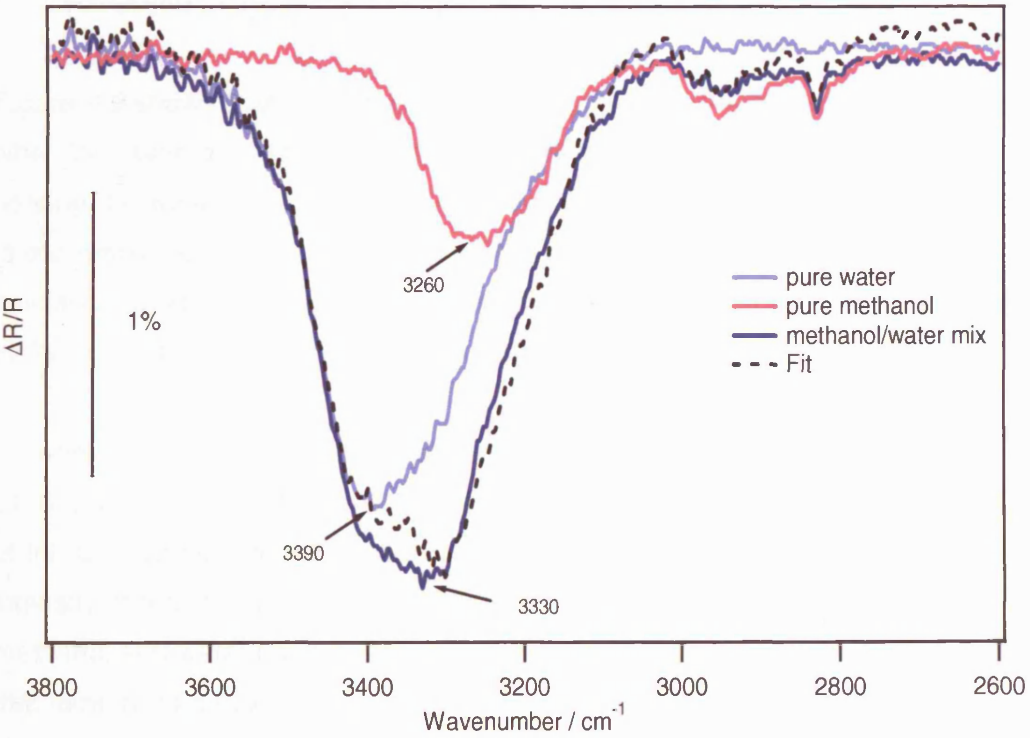

Figure 4.8 RAIR spectra for pure water, pure methanol and the 50 L methanol on 50 L exposure of water ice, deposited on HOPG at 97 K. The region between 3800 cm^{-1} and 2600 cm^{-1} is plotted and the combined peak generated by addition of the pure methanol and pure water peaks is shown as a dotted line.

4.3.3 Annealing the layered ice

Following adsorption, desorption and annealing behaviour was studied for all three ice systems by annealing the layered surface to increasing temperatures. While the methanol exposure remained at or below 50 L, altering the thickness of the underlying water layer resulted in little observable difference between the RAIR spectra recorded after annealing the surface. However, differences were observed when thicker methanol layers adsorbed on top of an underlying water layer were annealed. The CH_3OH/H_2O(50 L) system has been chosen to illustrate the desorption behaviour as the quality of the spectra are better for the thicker ice systems. The thickness of the overlaying methanol was also adjusted prior to annealing and data for 10 L, 20 L, 50 L and 300 L exposures of methanol were recorded. Very few differences were found between the lower three exposures and so data for the 50 L exposure of methanol will be used to describe the situation for all methanol exposures at or below 50 L. The 300 L CH_3OH/H_2O(50 L) system will be described separately.

A series of spectra focussing on the OH stretching region, resulting from annealing the layered ice, are shown in *Figure 4.9*. The spectra focussing on the CO region of the same system will be shown later. The ices shown in the figures are from the CH_3OH/H_2O(50 L) system with an exposure of 50 L of methanol on top of the water.

Figure 4.9 shows that there is little change to the spectra in the OH stretching region, when the layered ice is annealed to temperatures between 97 K and 135 K. However, heating the water-methanol ice layer beyond this point results in a significant change to the visible peaks. By 145 K, the broad peak centred at 3361 cm^{-1} has increased in amplitude and appears to split, with two peaks observable at 3361 cm^{-1} and 3236 cm^{-1}, labelled Peak X and Peak Y respectively.

On annealing to 155 K Peak Y increases in intensity and a low frequency shoulder at 3150 cm^{-1} becomes apparent. Heating beyond 155 K shows a rapid loss in intensity of the CH_3 vibrational modes shown at 2943 cm^{-1} and 2830 cm^{-1} along with a loss of intensity of the OH stretching vibrations, indicating considerable desorption of both the methanol and water multilayers. By 180 K the CH_3 modes are no longer visible and all that remains is a slight peak at 3236 cm^{-1}.

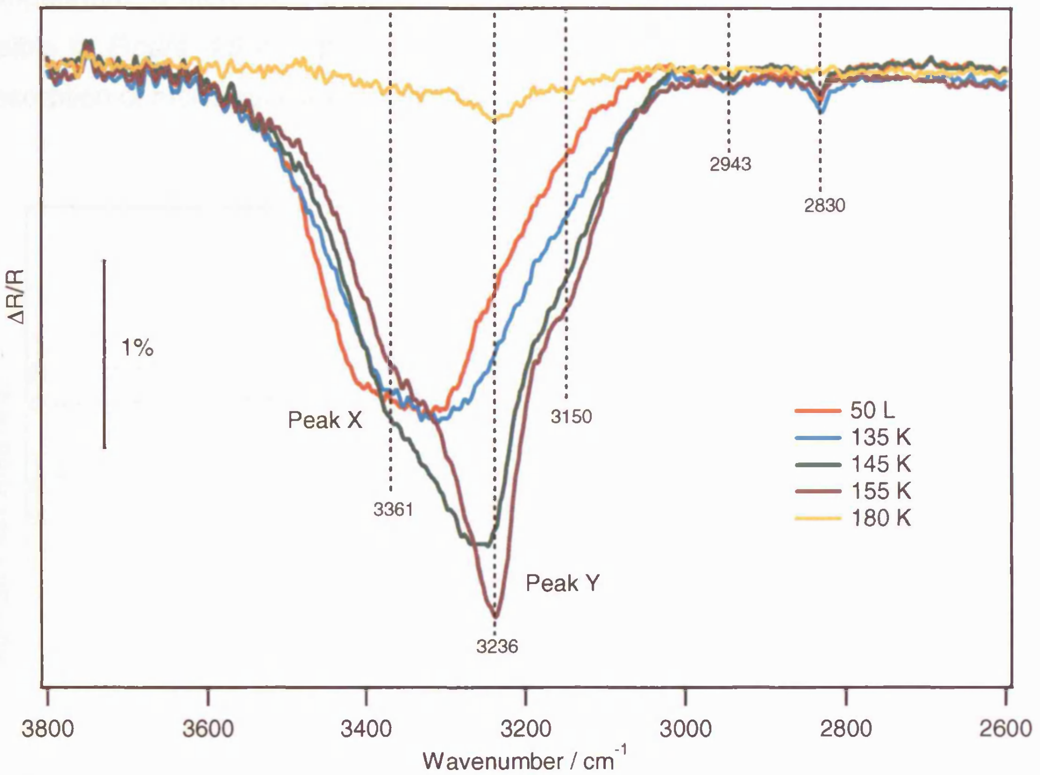

Figure 4.9 RAIR spectra recorded between 3800 cm^{-1} and 2600 cm^{-1} showing the sequential heating of the layered ice formed by depositing 50 L of methanol on a pre-existing 50 L layer of water, all deposited on HOPG at 97 K.

The feature at 3236 cm^{-1} that is remaining on the surface even after heating to 180 K has not previously been reported for either the pure methanol or pure water systems and it was initially considered to be a possible indicator of the trapped feature that was recorded at high temperatures in the TPD experiments. However, further detailed tests of pure water desorption from the HOPG surface indicated that, after high temperature annealing, the final peak visible in the spectra before complete desorption was at 3236 cm^{-1}. The final peak visible in *Figure 4.9* is therefore a pure water component.

Figure 4.10 shows the variation in integrated peak area with increasing annealing temperature for the three most dominant methanol peaks in the high frequency region of the CH_3OH/H_20(50 L) system, displayed in *Figure 4.9*. The total spectral area has also been included. The increase in total area that occurs around 145 K represents the crystallisation of water and it is characterised by a sharpening of the OH stretching bands. This sharpening occurs on a back drop of declining intensity for all remaining bands. The chart also shows that all of the methanol bands have disappeared by around 170 K, but the OH stretch and the total spectral area is not clear until the temperature is increased beyond 180 K. This confirms that the 3236 cm^{-1} feature visible in *Figure 4.9* is a pure water component, and probably represents the final desorption of monolayer water remaining on the HOPG surface.

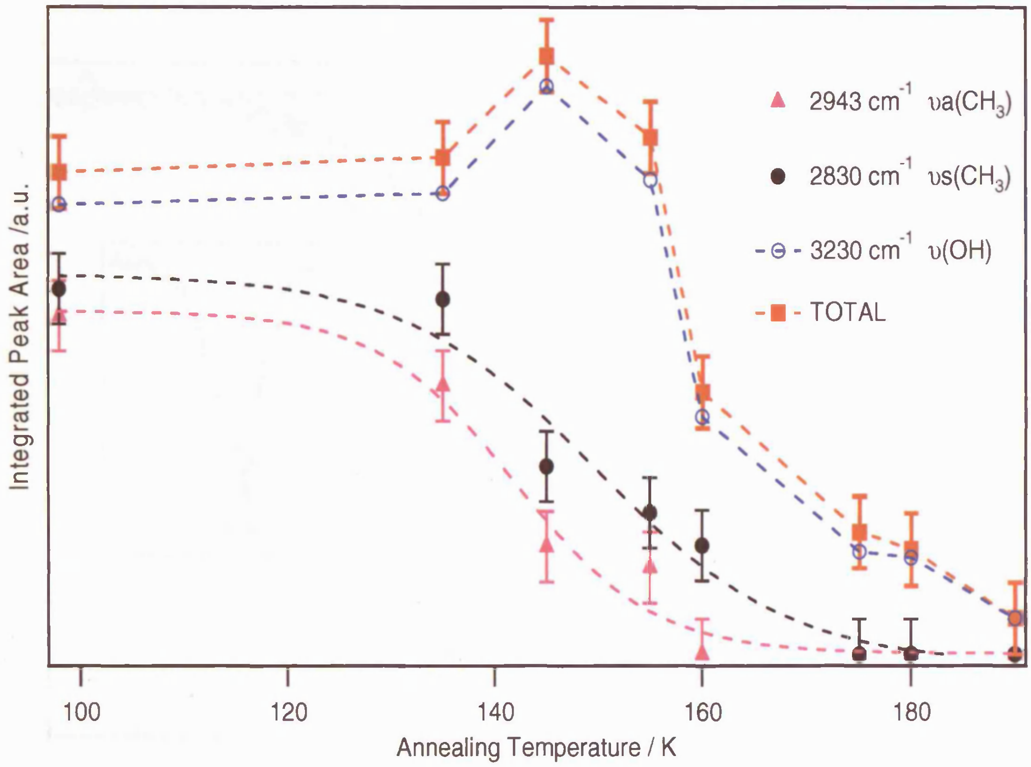

Figure 4.10 Chart showing the integrated peak area for selected bands in the layered CH_3OH/H_20(50 L) system with a 50 L exposure of methanol as a function of annealing temperature. The integrated area for the entire spectrum is also displayed but has been scaled to fit, as has the υ(OH) feature.

An attempt to model the 3000-3600 cm^{-1} region formed by annealing the CH_3OH/H_20(50 L) system with 50 L overlayer of methanol to 155 K is shown in *Figure 4.11*. The figure shows a model fit achieved by the addition of the pure methanol and pure water traces following heating to 141 K and 150 K respectively. Both traces have been scaled to achieve the combined fit. The model shows generally a very good fit to the shape of the recorded spectrum, but the layered feature shows a redshift of approximately 50 cm^{-1} compared to the combination fit. The inset in *Figure 4.11* shows the modelled fit offset by 50 cm^{-1} to confirm the quality of the model. The infrared spectrum resulting from methanol annealed to 141 K was used in the model, rather than the required temperature of 155 K, as pure methanol adsorbed on a HOPG sample will have almost completely desorbed by 155 K [3]. This clearly indicates that the methanol is being retained on the surface longer when dosed on top of water ice compared to when deposited directly on to the HOPG surface. As further confirmation of this, the fit in *Figure 4.11* clearly indicates that a component of methanol is still present at this elevated temperature, which is in agreement with the TPD evidence for the trapping of methanol within the bulk of the water ice.

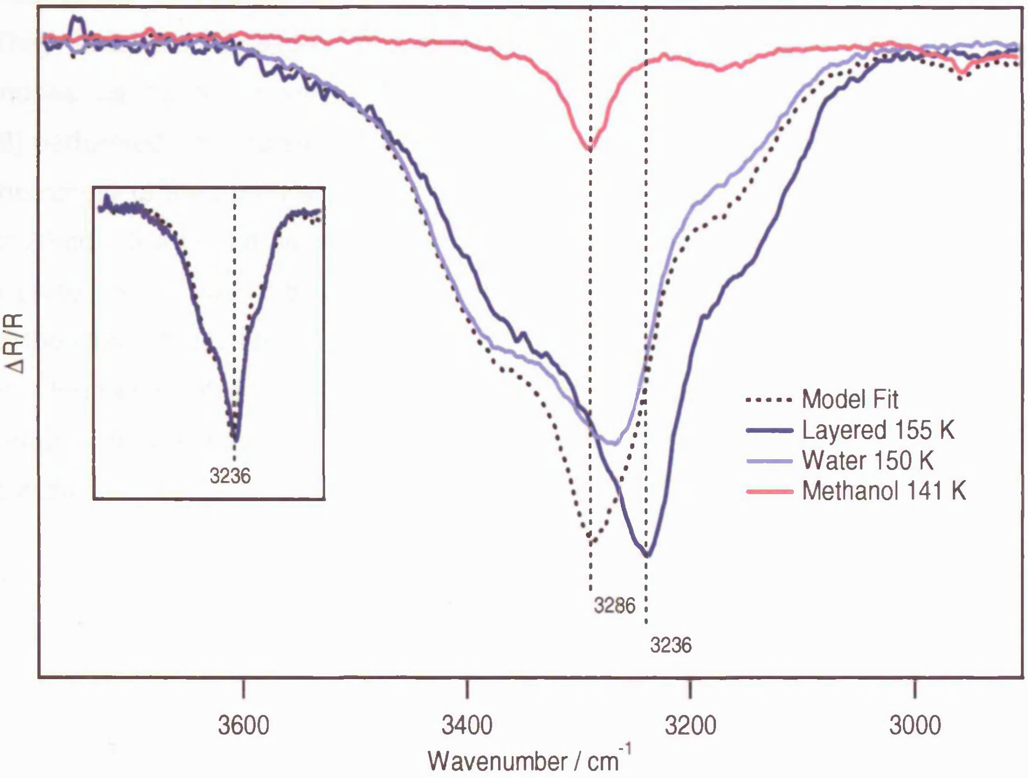

Figure 4.11 RAIR traces for pure water annealed to 150 K, pure methanol annealed to 141 K and 50 L methanol on 50 L of water ice annealed to 155 K, deposited on HOPG at 97 K. The region between 3800 cm^{-1} and 2600 cm^{-1} is plotted, and the combined peak generated by addition of the pure methanol and pure water peaks is shown as a dotted line. The inset shows the combined model fit shifted down by 50 cm^{-1} to show the overlap with the recorded trace for the layered system.

The downshift in frequency from that expected for a direct combination of the two individual species also indicates that the methanol and water are interacting with each other, as does the increased desorption temperature for methanol. This was not observed during the adsorption sequence shown in *Figure 4.8* and is therefore a direct result of the heating process, which results in intermixing of the water and methanol. The mixing of the two species was also reported in Chapter 3, the additional evidence from the RAIRS study confirms that the mixing occurs as a result of the TPD heating process. This proposed mixing mechanism is supported by the experimental work completed by Souda [23] on layers of water and heavy methanol.

Souda reported the complete intermixing of binary ice films as the temperature was raised to 136 K, which represents the glass transition of water.

The downshift in the OH stretch is also an indication of a hydrogen bonded complex that is formed after the methanol and water have intermixed. Strong hydrogen bonds weaken the O-H bonds and therefore lower the frequency of the stretching vibrations. They would also be expected to increase the frequency of the librational and bending modes, as these are both inhibited by hydrogen bonding [6]. Bakkas and co-workers [8] performed infrared studies of matrix isolated $CH_3OH:H_2O$ complexes, to determine the nature of the hydrogen bonding between the two species. They recorded redshifts of 20 cm^{-1} from the methanol monomer spectra when the methanol molecule acted as a proton donor, see *Figure 4.12.* Hence the observed 50 cm^{-1} downshift in frequency of the CH_3OH/H_2O OH infrared band after annealing (*Figure 4.11*) can be attributed to the formation of a $CH_3OH:H_2O$ complex. As already discussed in the previous chapter, further structural studies are required to determine the exact nature of the complex.

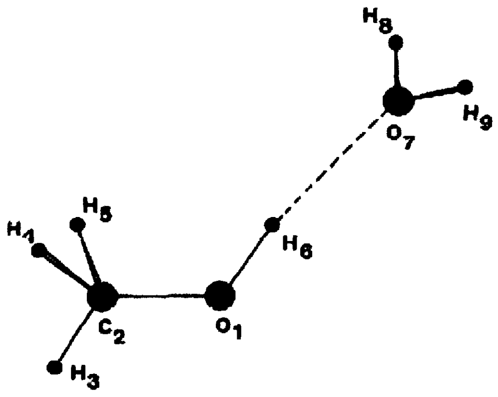

Figure 4.12 Structure for the methanol:water complex proposed by Bakkas et al [8] where the methanol molecule is acting as a proton donor and the water molecule is the proton acceptor.

Figure 4.13 shows a close up of the region between 980 cm^{-1} and 1150 cm^{-1} for a series of spectra that result from the annealing of the CH_3OH/H_2O(50 L) system with a 50 L exposure of methanol. Heating results in a decrease in intensity of the CO stretch at 1044 cm^{-1} and a small downshift in frequency, with increasing annealing temperature. Immediately after heating, a shoulder appears at 1013 cm^{-1} which has not previously been noted in the pure methanol system. In contrast to the pure methanol system, the υ(CO) stretch at 1044 cm^{-1} does not obviously split but it is possible that the feature at 1013 cm^{-1} indicates the start of methanol crystallisation.

The shift in frequency of the 1044 cm^{-1} feature is strongly suggestive of crystallisation, but on the other hand there is an absence of the associated frequency shift in the ρ(CH_3), 1130 cm^{-1}, feature. Results from the pure methanol study indicated that temperature induced crystallisation of methanol was coverage dependent and that crystallisation was not noted below 50 L [3]. It seems likely that the 50 L exposure in this study is just approaching the coverage required for conclusive crystallisation of methanol to be observed.

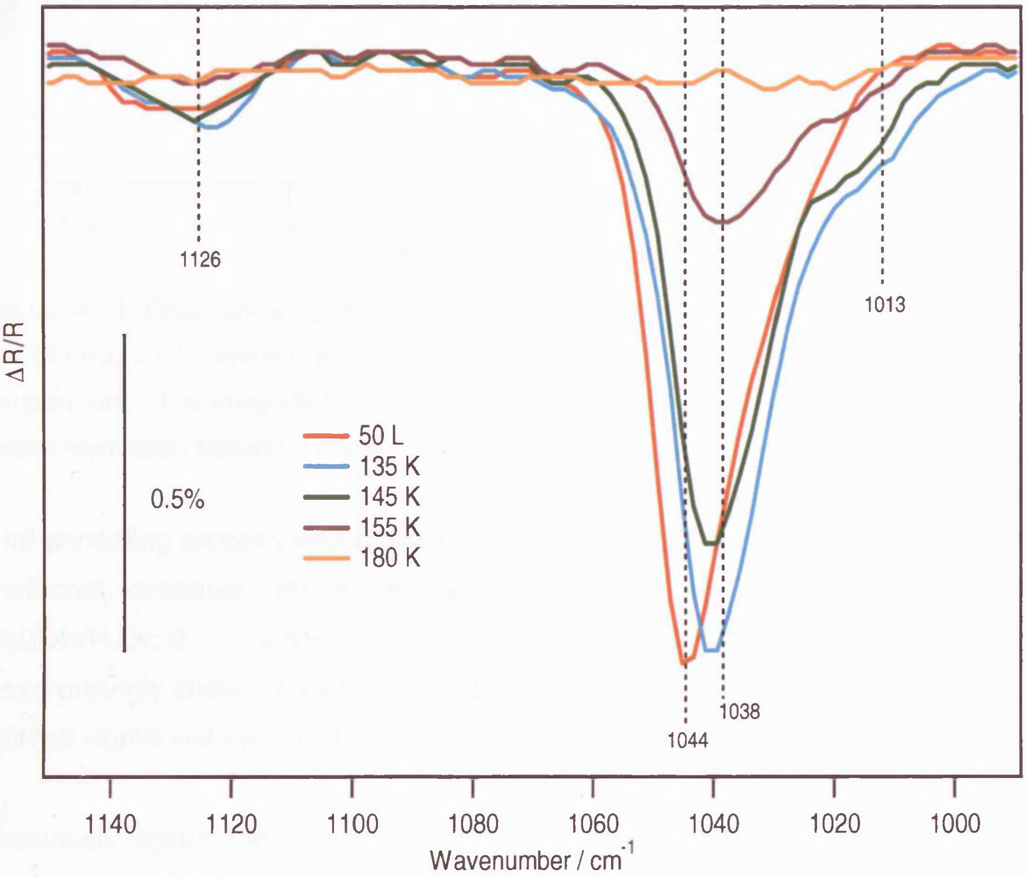

Figure 4.13 RAIR spectra between 1150 cm^{-1} and 980 cm^{-1} showing the sequential heating of the layered ice formed by depositing 50 L of methanol on a pre-existing 50 L layer of water, all deposited on HOPG at 97 K.

Figure 4.14 shows the integrated peak areas as a function of annealing temperature for the low frequency bands illustrated in *Figure 4.13.* By 180 K, all of the low frequency methanol features have disappeared but, as previously noted, there is a component of the total spectrum still persisting until 190 K. This component is attributable to the OH stretch from the residual water and can be seen clearly in *Figure 4.10.*

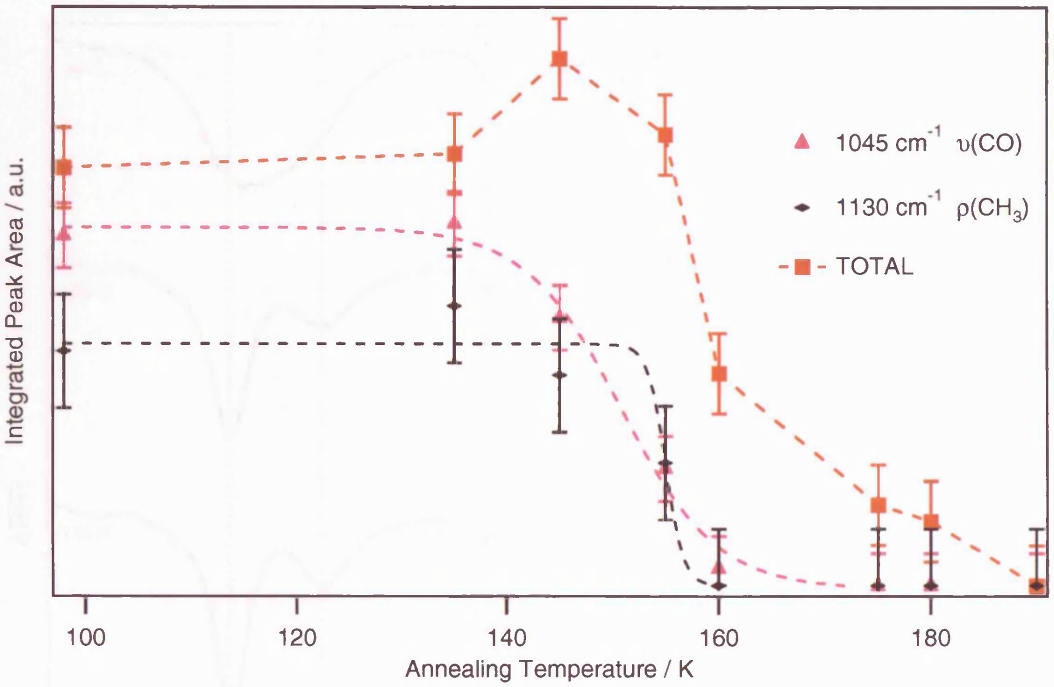

Figure 4.14 Chart showing the integrated peak area for selected bands in the layered CH_3OH/H_20(50 L) system with a 50 L exposure of methanol, as a function of annealing temperature. The integrated area for the entire spectrum (TOTAL) is also displayed and all traces have been scaled for clarity.

The annealing process was repeated for each of the three ice systems with a thicker methanol overlayer, formed by an exposure of 300 L of methanol. Only the CH_3OH/H_2O(50 L) system will be illustrated, as the resulting RAIR spectra unsurprisingly show the same behaviour regardless of the underlying water thickness, with all vibrational frequencies coincident.

Previously reported spectra for the desorption of pure methanol from a HOPG surface are shown in *Figure 4.15* [3], to demonstrate the well documented changes expected as a physisorbed methanol layer is heated. The υ(CO) stretch at 1045 cm^{-1} splits immediately on heating and can be resolved into two lower frequency peaks at 1038 and 1028 cm^{-1}. The broad υ(OH) stretch also splits into two bands at 3292 and 3188 cm^{-1}.

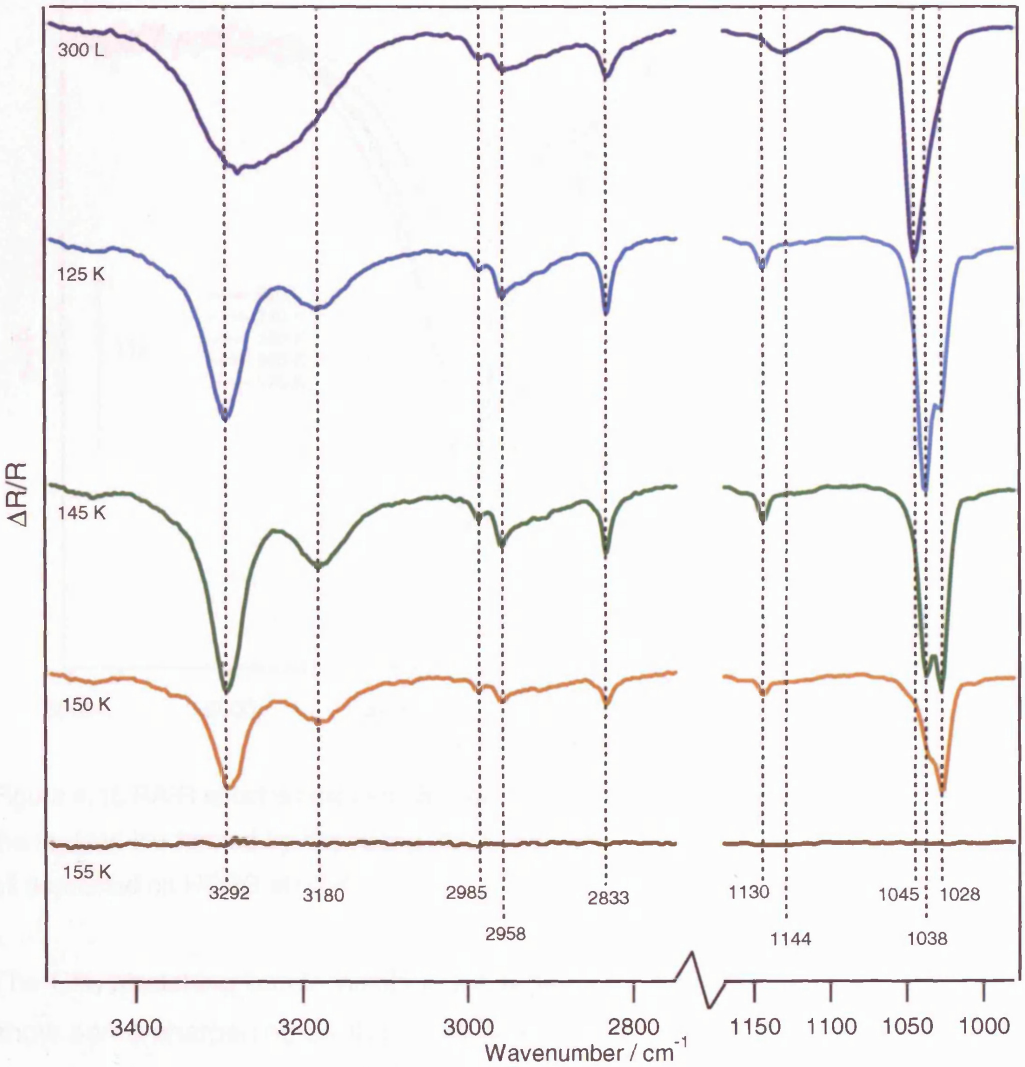

Figure 4.15 RAIR spectra between 3500 cm^{-1} and 900 cm^{-1} showing the sequential heating of a 300 L exposure of pure methanol, deposited on HOPG at 97 K [3].

Figure 4.16 shows a close up of the 3800 cm^{-1} to 2600 cm^{-1} region resulting from the heating of the layered system. Upon heating to 140 K, although the broad feature at 3296 cm^{-1} maintains the same intensity, it splits revealing a low amplitude shoulder at 3155 cm^{-1}. Pure methanol (see *Figure 4.15*) shows the same behaviour on heating, although the splitting is more pronounced, with a clear low frequency peak at 3180 cm^{-1}. This splitting has been attributed to the ordering of the methanol multilayer following the conversion to crystalline methanol [3]. It is proposed that the methanol present in the layered system also undergoes crystallisation, as evidenced by the splitting, but coordination to the water molecules results in the down shift in frequency.

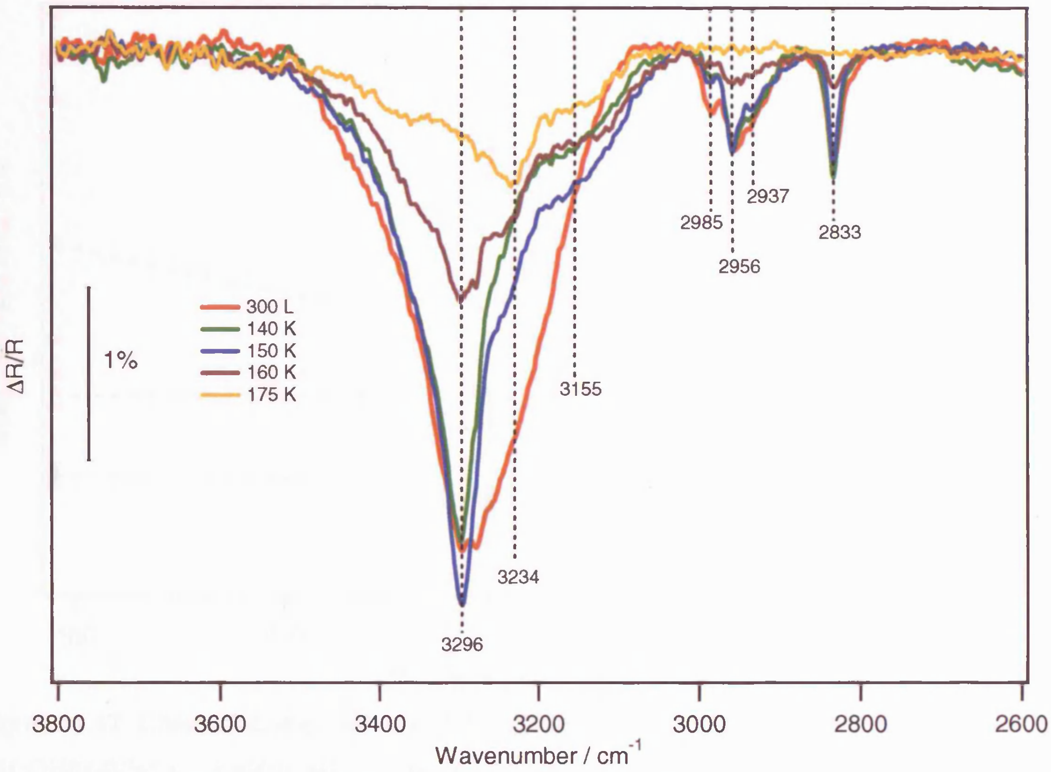

Figure 4.16 RAIR spectra between 3800 cm^{-1} and 2600 cm^{-1} showing the sequential heating of the layered ice formed by depositing 300 L of methanol on a pre-existing 50 L layer of water, all deposited on HOPG at 97 K.

The CH_3 stretching bands visible in the region between 2985 cm^{-1} and 2833 cm^{-1} also show some sharpening as the ice is heated to 140 K but there is significant loss in intensity after annealing to 160 K and the peaks are completely absent by 175 K.

Figure 4.17 shows the variation in integrated peak area with increasing annealing temperature for the three most dominant methanol peaks in the high frequency region of the CH_3OH/H_20(50 L) system, following a 300 L exposure of methanol as displayed in *Figure 4.16.* The total spectral area has also been included. There is an increase in the area of the OH stretching band around 145 K which indicates the crystallisation of water. However, the total spectral area does not demonstrate this increase at 145 K, as it does in the system with only a 50 L overlayer of methanol, and this is due to the rapidly declining methanol features which mask the impact of the υ(OH) sharpening. As expected, the chart also shows that all the methanol bands have disappeared by around 170 K, but the OH stretch area and the total spectral area is not zero until 190 K.

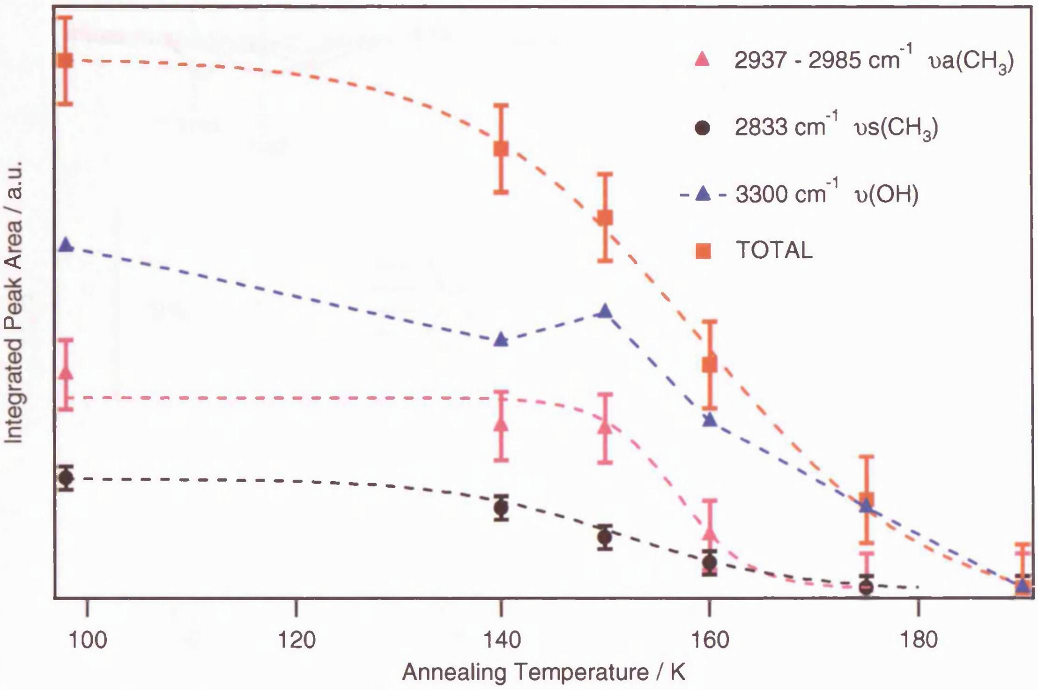

Figure 4.17 Chart showing the integrated peak area for selected bands in the layered CH_3OH/H_20(50 L) system with a 300 L exposure of methanol as a function of annealing temperature. The integrated area for the entire spectrum is also displayed but has been scaled to fit, as has the υ(OH) feature.

Figure 4.18 shows a close up of the 1170 cm^{-1} to 950 cm^{-1} region resulting from the heating of the CH_3OH/H_2O(50 L) layered system, with the 300 L exposure of methanol. Immediately upon heating, the sharp υ(CO) band at 1045 cm^{-1} splits into a doublet with peaks at 1039 cm^{-1} and 1028 cm^{-1}. This is in agreement with the previous study of pure methanol multilayers on a HOPG sample, where the two bands were assigned to the υ(CO) vibrations of crystalline methanol [3]. Further agreement is noted by the shifting and sharpening of the ρ(CH_3) vibration from 1132 cm^{-1} to 1144 cm^{-1}, again attributable to the formation of crystalline methanol.

Figure 4.19 shows the decline in the intensity of the two dominant bands present in the spectra of *Figure 4.18* as a function of annealing temperature. All vibrational bands have disappeared from the spectra after annealing to 175 K apart from the previously noted 3234 cm^{-1} feature (see *Figure 4.16*). This peak has been assigned to the monolayer of water on HOPG. Pure methanol multilayers are expected to show complete desorption by ≈ 165K [3], the fact that methanol vibrations are still recorded up to 175 K confirms that methanol is being retained in the bulk of the water ice.

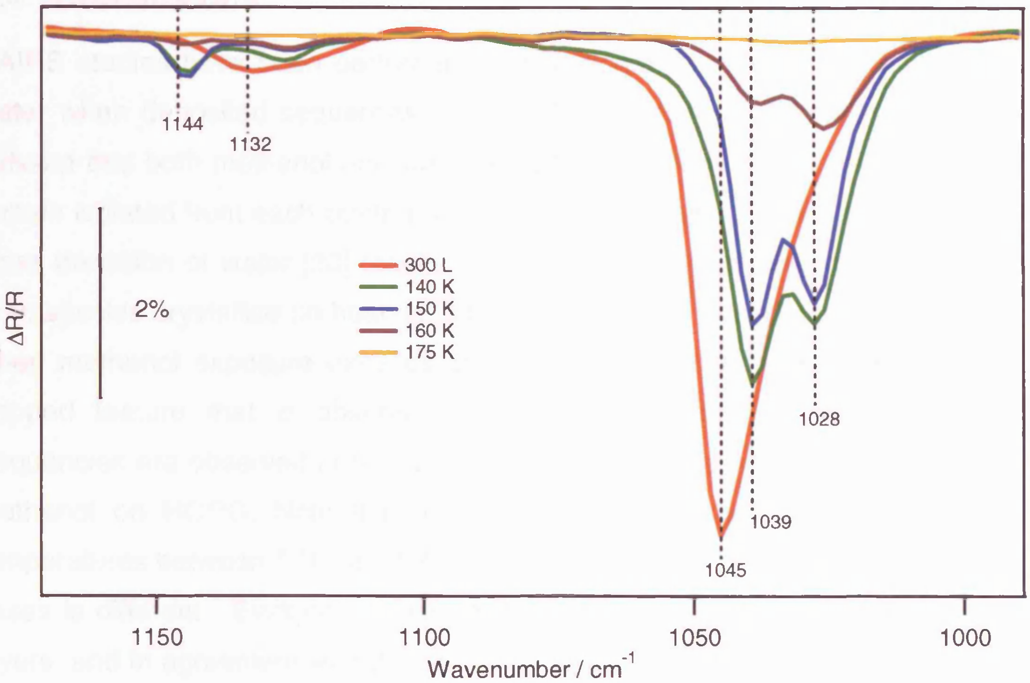

Figure 4.18 RAIR spectra between 1170 cm^{-1} and 950 cm^{-1} showing the sequential heating of the layered ice formed by depositing 300 L of methanol on a pre-existing 50 L of water, all deposited on HOPG at 97 K.

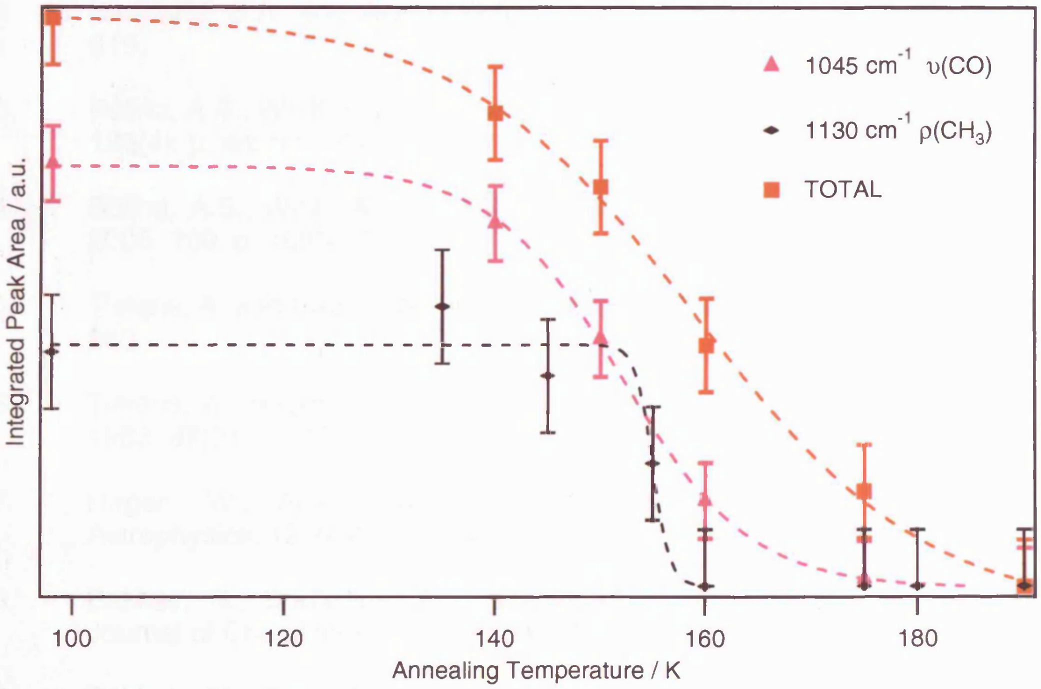

Figure 4.19 Chart showing the integrated peak area for selected bands in the layered CH_3OH/H_20(50 L) system with a 300 L exposure of methanol as a function of annealing temperature. The integrated area for the entire spectrum is also displayed but has been scaled to fit, as has the υ(OH) feature.

4.4 Conclusions

RAIRS studies have been performed to investigate the interaction of methanol and water when deposited sequentially on a HOPG surface at 97 K. The RAIR spectra indicate that both methanol and water adsorb molecularly in a physisorbed state and remain isolated from each other in a layered morphology. Heating the ices above the glass transition of water [23] results in the mixing of the methanol and water layers. Both species crystallise on heating, although methanol crystallisation is only apparent when methanol exposure exceeds 50 L. The RAIR spectra show evidence for the trapped feature that is observed in the TPD spectra, as methanol vibrational frequencies are observed at temperatures above the sublimation temperature of pure methanol on HOPG. Note that it is not possible to directly compare desorption temperatures between TPD and RAIRS experiments as the heating process in the two cases is different. Evidence is also observed for temperature induced mixing of the layers, and in agreement with the TPD data in the previous chapter, provides support for the trapping mechanism.

4.5 Bibliography

1. Sandford, S.A., Meteoritics & Planetary Science, 1996. **31**(4): p. 449-476.
2. Sandford, S.A. and Allamandola, L.J., Astrophysical Journal, 1993. **417**: p. 815.
3. Bolina, A.S., Wolff, A.J., and Brown, W.A., Journal of Chemical Physics, 2005. **122**(4): p. art. no.-044713.
4. Bolina, A.S., Wolff, A.J., and Brown, W.A., Journal of Physical Chemistry B, 2005. **109**: p. 16836-16845.
5. Tielens, A. and Hagen, W., Astronomy and Astrophysics, 1982. **114**(2): p. 245-260.
6. Tielens, A., Hagen, W., and Greenberg, J.M., Journal of Physical Chemistry, 1983. **87**(21): p. 4220-4229.
7. Hagen, W., Allamandola, L.J., and Greenberg, J.M., Astronomy and Astrophysics, 1980. **87**(1-2): p. L3-L6.
8. Bakkas, N., Bouteiller, Y., Loutellier, A., Perchard, J.P., and Racine, S., Journal of Chemical Physics, 1993. **99**(5): p. 3335-3342.
9. Bakkas, N., Bouteiller, Y., Loutellier, A., Perchard, J.P., and Racine, S., Chemical Physics Letters, 1995. **232**(1-2): p. 90-98.
10. Ehrenfreund, P., Kerkhof, O., Schutte, W.A., Boogert, A.C.A., Gerakines, P.A., Dartois, E., d'Hendecourt, L., Tielens, A., van Dishoeck, E.F., and Whittet, D.C.B., Astronomy and Astrophysics, 1999. **350**(1): p. 240-253.

11. Allamandola, L.J., Sandford, S.A., and Valero, G.J., Icarus, 1988. **76**: p. 225.

12. Ehrenfreund, P., Dartois, E., Demyk, K., and d'Hendecourt, L., Astronomy and Astrophysics, 1998. **339**(1): p. L17-L20.

13. Blake, D., Allamandola, L., Sandford, S., Hudgins, D., and Freund, F., Science, 1991. **254**(5031): p. 548-551.

14. Stevenson, K.P., Kimmel, G.A., Dohnalek, Z., Smith, R.S., and Kay, B.D., Science, 1999. **283**(5407): p. 1505-1507.

15. Bensebaa, F. and Ellis, T.H., Progress in Surface Science, 1995. **50**(1-4): p. 173-185.

16. Grecea, M.L., Backus, E.H.G., Riedmuller, B., Eichler, A., Kleyn, A.W., and Bonn, M., Journal of Physical Chemistry B, 2004. **108**(33): p. 12575-12582.

17. Phelps, R.B., Kesmodel, L.L., and Kelley, R.J., Surface Science, 1995. **340**(1-2): p. 134-140.

18. Chakarov, D.V., Osterlund, L., and Kasemo, B., Vacuum, 1995. **46**(8-10): p. 1109-1112.

19. Mitlin, S. and Leung, K.T., Journal of Physical Chemistry B, 2002. **106**(24): p. 6234-6247.

20. Pratt, S.J., Escott, D.K., and King, D.A., Journal of Chemical Physics, 2003. **119**(20): p. 10867-10878.

21. Serrallach, A., Meyer, R., and Gunthard, H.H., Journal of Molecular Spectroscopy, 1974. **52**: p. 94.

22. Falk, M. and Whalley, E., Journal of Chemical Physics, 1961. **34**(5): p. 1554.

23. Souda, R., Physical Review Letters, 2004. **93**(23): p. art. no.-235502.

Chapter 5 TPD Studies of the Adsorption and Desorption of Mixed Films of Methanol and Water Codeposited on Graphite.

5.1 Introduction

In the previous chapters, studies of the adsorption and desorption of methanol from a binary layered system, consisting of methanol deposited on top of amorphous solid water, ASW, were discussed. In interstellar molecular ices, methanol is often the most abundant component within water rich ices [1, 2]. It has an abundance predicted to vary between 5% and 50% relative to water [1, 3, 4], although the lower abundance estimates are thought to be more reliable. Both water and other hydrogenated species such as methanol are thought to form on the surface of grains, by a mixture of freeze out and by sequential hydrogenation reactions [5]. As a result, it is generally considered that studies of codeposited mixtures form a more astrochemically relevant model of an icy mantle than studies of layered systems.

Studies of water rich mixed ices, where methanol is the major constituent after water, are plentiful in the astrochemical literature [2, 6-11]. In 1991, Blake et al published an important paper that highlighted the formation of clathrate hydrates in mixed methanol and water ices [6]. They performed X-ray diffraction studies that demonstrated the formation of type II clathrate hydrates, with excess methanol (> 7%) segregating to form crystalline grain boundaries. This process holds implications for cometary ices, and indeed interstellar molecular ices, as clathrates act as a reservoir for volatile gases, trapping them within the ice beyond their usual sublimation temperature.

In 1997, Notesco and Bar-Nun published a study of the trapping of methanol in water ices [7], which was an extension of earlier work focussing on the ability of amorphous water to trap molecules [12, 13]. In TPD spectra, they observed methanol release over three ranges: a) ≈ 160 K during the decomposition of the clathrate hydrate, b) ≈ 165 K during the transformation of the amorphous and cubic ice into hexagonal ice, and c) when the water ice itself evaporated. They also varied the deposition temperature between 60 K and 160 K and found that the amount of trapping decreased exponentially with temperature, in line with the decreasing porosity of the water ice, which crystallises around 135 K.

Collings et al [9] performed a recent survey of the thermal desorption of 16 astronomically relevant molecules from water ices, deposited on an amorphous gold substrate. They studied layered and codeposited mixtures, and observed four different zones of desorption across the 16 molecules. These zones were: 1) monolayer desorption from the surface of the water ice, 2) multilayer desorption, 3) volcano desorption as trapped molecules are released during the crystallisation of water ice, and 4) codesorption, where trapped molecules are released along with the water. They grouped each molecule according to their shared desorption characteristics. Water-like species showed a single codesorption peak coincident with the release of water, CO-like species showed volcano, codesorption, monolayer and multilayer features, and intermediate species demonstrated volcano and codesorption features along with a monolayer peak for small molecules. Methanol was assigned to the water-like category, as only a codesorption peak was observed when methanol and water were codeposited on the gold surface.

This chapter will outline the first detailed results obtained from a TPD study of mixed water:methanol ices, of varying composition, formed by codepositing water and methanol vapour onto an HOPG sample, held at 97 K. Results from this chapter have recently been published as a comparison with the studies of Collings et al [9], with a view to determining the role of the grain surface when interpreting TPD results for astrochemical models [14].

5.2 Methodology

Experiments were performed in an ultra-high vacuum (UHV) chamber, described in Chapter 2. The chamber has a base pressure of 2×10^{-10} mbar. The HOPG sample has been described previously along with the "scotch tape" method of cleaning [15].

As with all of the experiments discussed in this thesis, the ices were grown in situ by exposing the HOPG surface, held at ≈ 97 K, to a stream of gas by back filling the chamber at a constant dosing pressure. Exposures were measured in Langmuir (L), where $1 \text{ L} = 10^{-6}$ mbar s. The dosing gas is the vapour formed from a mixture of water and methanol, held in a glass bulb. The composition of the vapour was measured during the dosing process by recording a mass spectrum. The chamber pressure was allowed to recover to $\approx 9 \times 10^{-10}$ mbar before TPD spectra were recorded. The chemicals used during the experiments were distilled, de-ionised water and methanol (CH_3OH – 99.9% - Aristar – BDH). The purity of the dosed species was confirmed by monitoring the mass spectrometer signal during dosing.

All TPD experiments were performed at a heating rate of 0.50 K s^{-1} ± 0.01 K s^{-1}. Temperature and heating control were identical to the previous TPD experiments and were described in the experimental section of Chapter 3.

Mass 31 is the major fragment detected by the mass spectrometer for methanol and is reported in preference to the other fragments. As mentioned in previous chapters, spectra for masses 31, 32 and 18 were recorded simultaneously, but as the ratios of each fragment remain constant throughout the experiment, dissociative processes can be ignored.

The sample was cleaned between experiments by annealing to 500 K for 3 minutes.

5.3 Results and Discussion

In these experiments, water and methanol were codeposited onto a graphite surface by exposing the HOPG sample to the vapour from a vessel containing a 25% mix of methanol in water. Although the composition of the dosing mixture remained constant throughout the experiment, there was a noticeable fluctuation in the gas phase composition of the vapour, as measured by the mass spectrometer. The relative proportions of the two components of the mix have been determined by integrating the areas under each mass spectrum trace, recorded during the dosing process. *Table 5.1* shows the variation in the composition of the dosing vapour recorded for one experiment. The differing composition of the dosing vapour is reflected in the composition of the resulting ice formed

Table 5.1 Proportion of methanol in the mixed water:methanol dosing vapour.

EXPOSURE	**3 L**	**5 L**	**7 L**	**10 L**	**15 L**	**50 L**	**100 L**	**300 L**
Methanol Vapour Composition	4%	12%	10%	14%	14%	10%	4%	19%

Table 5.2 shows the proportion of methanol in the mixed water:methanol ice formed on the HOPG surface. TPD spectra were found to be consistent for all ice mixtures, where the methanol composition relative to water varied between 7 and 17%. The average composition of the mixed ices discussed in this chapter is 9% methanol in water. The actual composition of the ice will be highlighted in the text where an extreme value alters the expected behaviour of the TPD trace.

Table 5.2 Proportion of methanol in the mixed water:methanol ice, formed on HOPG at 97 K.

EXPOSURE	3 L	5 L	7 L	10 L	15 L	20 L	50 L	100 L	300 L
Methanol Ice Composition	2%	7%	8%	9%	10%	11%	10%	4%	17%

5.3.1 TPD results from the water:methanol mix

The desorption traces for both water and methanol were recorded simultaneously during the experiment, but they are displayed separately for clarity. Each trace shown in the TPD spectra represents an increasing thickness of the mixed ice layer formed. Using the estimate derived by Bolina [16], where there are 5.3×10^{17} water molecules on the HOPG surface following a 1 L exposure and the estimate by Collings et al [9] that 9.5×10^{21} molecules m^{-2} represents a 0.3 μm thick ice, it is estimated that the mixed ice thickness varies from ≈ 5×10^{-5} to 5×10^{-3} μm as the exposure increases from 3 L to 300 L.

5.3.1.1 Water Desorption

TPD spectra for water desorption from the mixed water:methanol ice are shown in *Figure 5.1* and *Figure 5.2*. At low exposures, there is one, clear, peak present in each trace. At 5 L this peak appears at ≈ 142 K, but the peak temperature increases with exposure and by 50 L the peak temperature is ≈ 151 K. As the exposure increases beyond 20 L a second feature appears at high temperatures (seen at ≈ 156 K for the 50 L exposure and 163 K for the 300 L exposure). In the higher exposure spectra, shown in *Figure 5.2*, an additional low temperature feature is also visible as a bump on the leading edge of the main peak, at ≈ 145 K.

The three water peaks in *Figure 5.2*, can be confidently assigned by comparison to the TPD spectra of pure water deposited on an HOPG surface, which were reproduced in *Figure 3.1* [15]. The pure water spectra are identical to the water spectra obtained from the mixed water:methanol ice, which indicates that, at least with the low methanol concentrations considered, methanol does not influence water desorption. This is in contrast to the sequentially deposited systems discussed in Chapter 3, where the methanol overlayer was shown to delay water desorption slightly. The main peak is a non-saturating feature that has shared leading edges and an increasing peak temperature as the exposure increases. This is assigned to the desorption of multilayers of water. The low temperature bump, is attributed to a change in the desorption rate as the water ice undergoes a phase transition from amorphous to crystalline ice. The small high temperature peak, is assigned to a further phase transition, where crystalline ice converts to hexagonal ice.

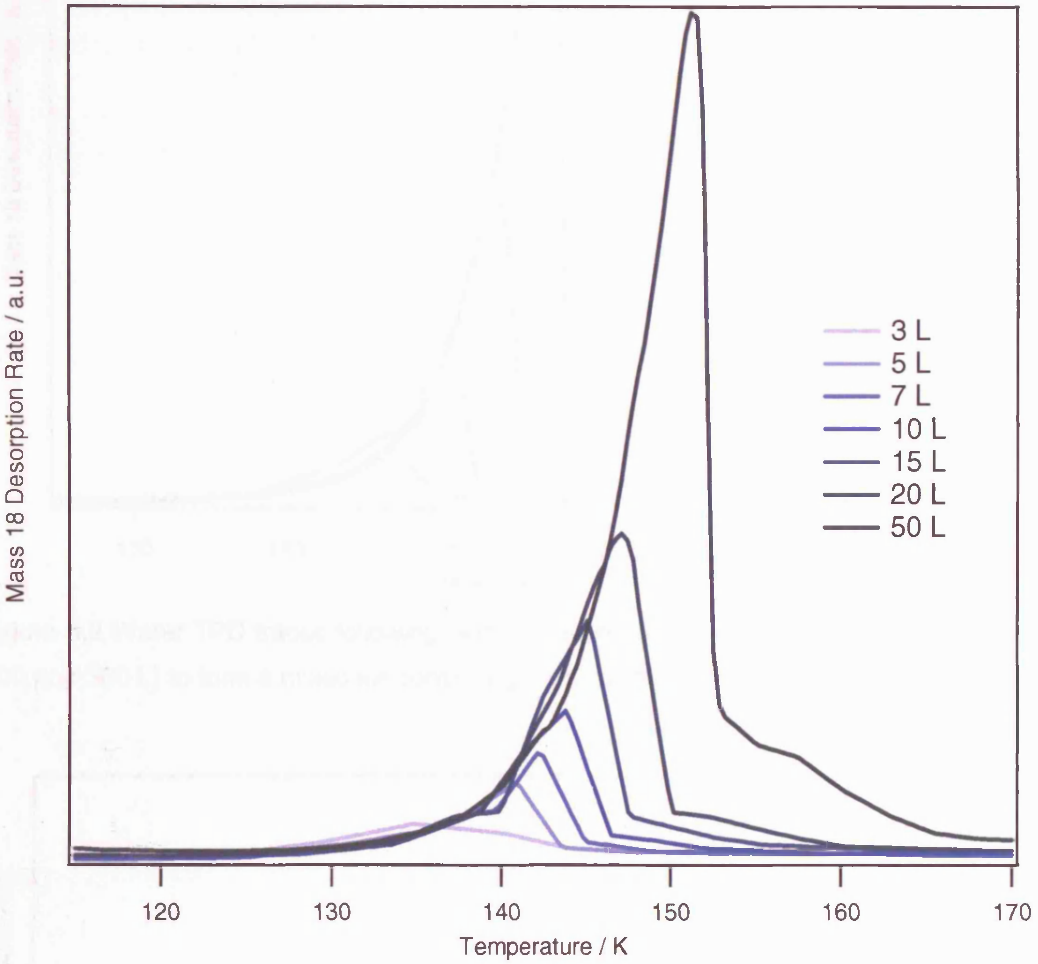

Figure 5.1 Water TPD traces following low exposures of the water:methanol mixture (3, 5, 7, 10, 15, 20 and 50 L) to form a mixed ice containing ≈ 9% methanol on an HOPG surface at 97 K.

Figure 5.3 shows the total uptake of water as a function of increasing exposure of the water:methanol mix. The plot is produced by integrating the areas under the water TPD spectra and the mass spectrum traces recorded during the dose. The dose areas have been normalised to show the exposure on a relative scale. The uptake curve shows a linear relationship between desorption area and exposure, which indicates that there is a constant sticking probability for water within the water:methanol mix, when deposited on HOPG at 97 K.

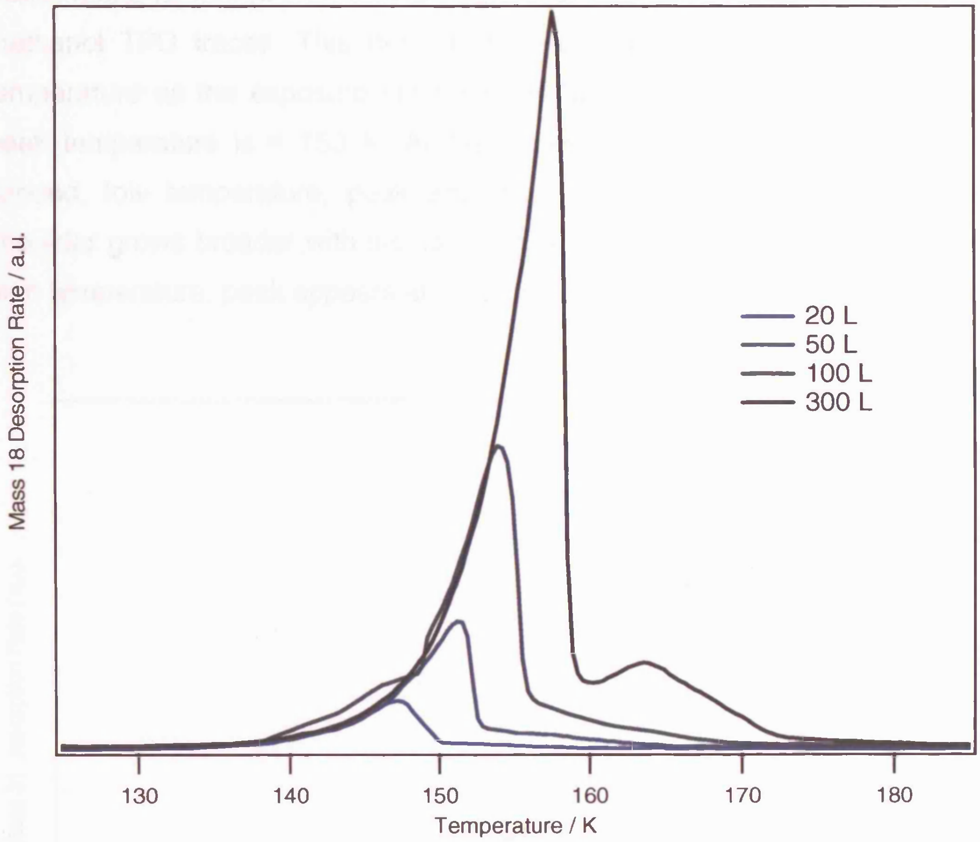

Figure 5.2 Water TPD traces following high exposures of the water:methanol mixture (20, 50, 100 and 300 L) to form a mixed ice containing ≈ 9% methanol on an HOPG surface at 97 K.

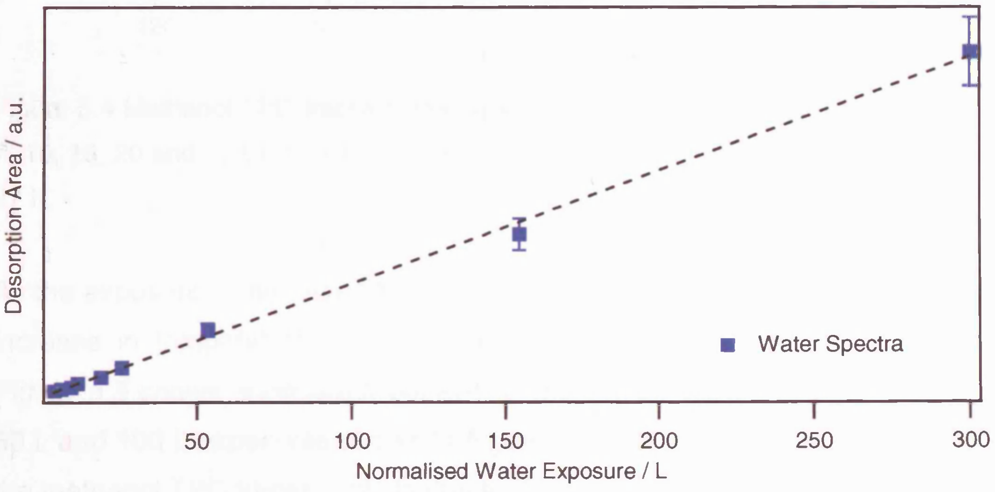

Figure 5.3 Total integrated area of the water TPD curves plotted as a function of increasing exposure of the water:methanol mix (≈ 9% methanol), on to the HOPG sample at 97 K.

5.3.1.2 Methanol Desorption

Figure 5.4 shows methanol TPD spectra for low exposures (≤ 50 L) of the water:methanol mix. It shows that, following the lowest exposures of the water:methanol mix (≤ 7 L), only a single desorption peak is observed in the resulting methanol TPD traces. This desorption peak appears at ≈ 141 K but shifts up in temperature as the exposure increases. Following a 50 L exposure of the mix, the peak temperature is ≈ 150 K. At exposures ≥ 10 L of the water:methanol mix, a second, low temperature, peak appears as a shoulder on the main peak. This shoulder grows broader with increasing exposure of the water:methanol mix. A third, high temperature, peak appears at ≈ 154 K as the exposure reaches 50 L.

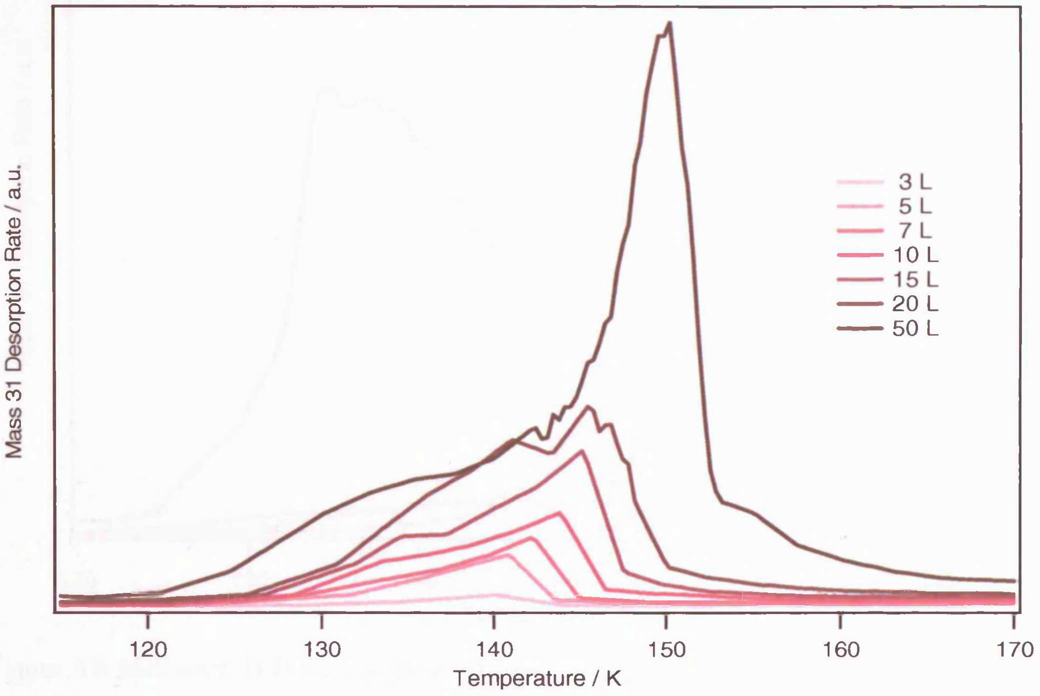

Figure 5.4 Methanol TPD traces following low exposures of the water:methanol mixture (3, 5, 7, 10, 15, 20 and 50 L) to form a mixed ice containing ≈ 9% methanol on an HOPG surface at 97 K.

As the exposure is increased beyond 50 L, see *Figure 5.5*, the main peak continues to increase in temperature and sharpens considerably. The 100 L exposure peak in *Figure 5.5* shows anomalous behaviour and will discussed in more detail later. The 50 L and 100 L exposures shown in *Figure 5.5* give rise to similar integrated areas for the methanol TPD traces. This is due to the anomalously low methanol composition in the 100 L dose (≈ 4% methanol in water, see *Table 5.2*). Despite representing the same exposure of methanol, following the 100 L exposure of the mix the methanol is retained on the surface for an extra 5 K compared to the ice formed following a 50 L exposure. The higher desorption temperature for the 100 L exposure is in line with the higher desorption temperature of the larger amount of water ice. This clearly demonstrates that water controls the desorption behaviour of methanol, as noted previously by Collings et al [9] and discussed in more detail below. The methanol TPD peak observed for the 300 L exposure of the methanol:water mix is unusual. It is a very broad and irregular feature, whose desorption commences at 124 K, along with all the other exposures, but culminates in a very sharp peak at ≈ 158 K.

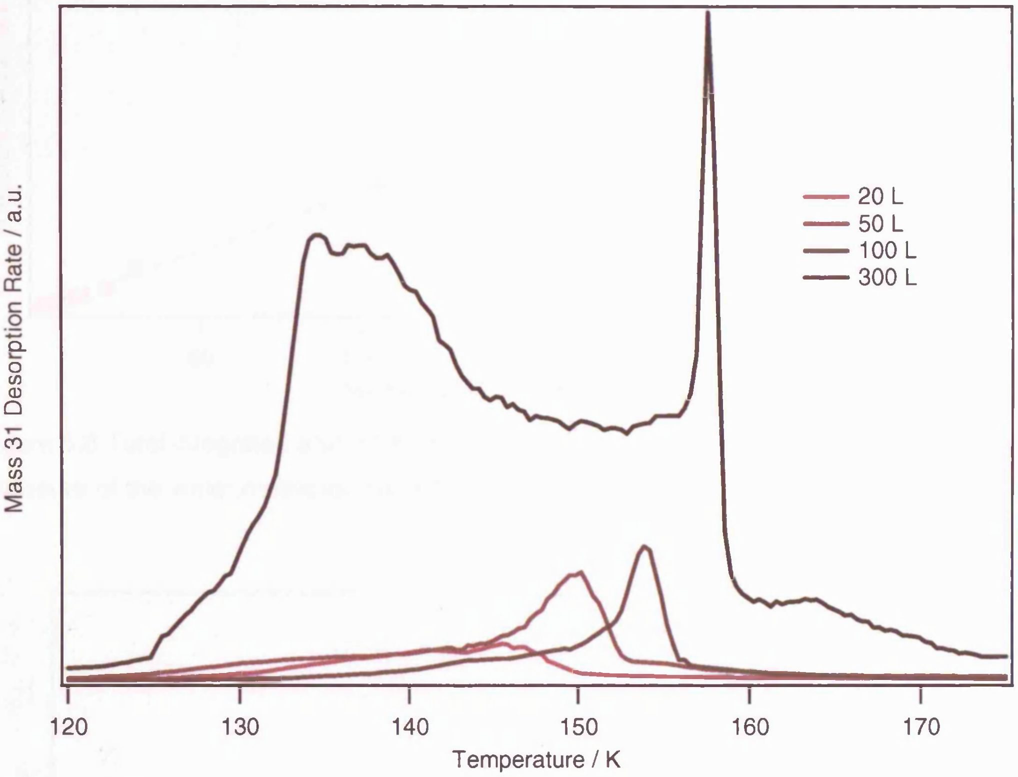

Figure 5.5 Methanol TPD traces following high exposures of the water:methanol mixture (20, 50, 100 and 300 L) to form a mixed ice containing ≈ 9% methanol on an HOPG surface at 97 K.

Figure 5.6 shows that the total uptake of methanol as a function of increasing exposure of the water:methanol mix follows a linear trend, as did the uptake curve for water. The plot is produced by integrating the areas under the methanol TPD spectra and the mass spectrum traces for methanol, recorded during the dose. The exposure is normalised to show the doses on a relative scale.

With increasing exposure the low temperature feature, seen in *Figure 5.5,* broadens to span the temperature range from approximately 124 K to 154 K. This low temperature feature demonstrates unusual behaviour at high ice thicknesses. *Figure 5.7* shows two traces acquired on different days, following a 300 L exposure of the water:methanol mix. Although the methanol composition varies slightly between the two doses, the figure clearly illustrates that the main peak at ≈ 158 K coincides precisely, while the low temperature feature reproduces the overall character, i.e. its breadth and irregular peak shape. The origin of this broad feature will be discussed later in the chapter.

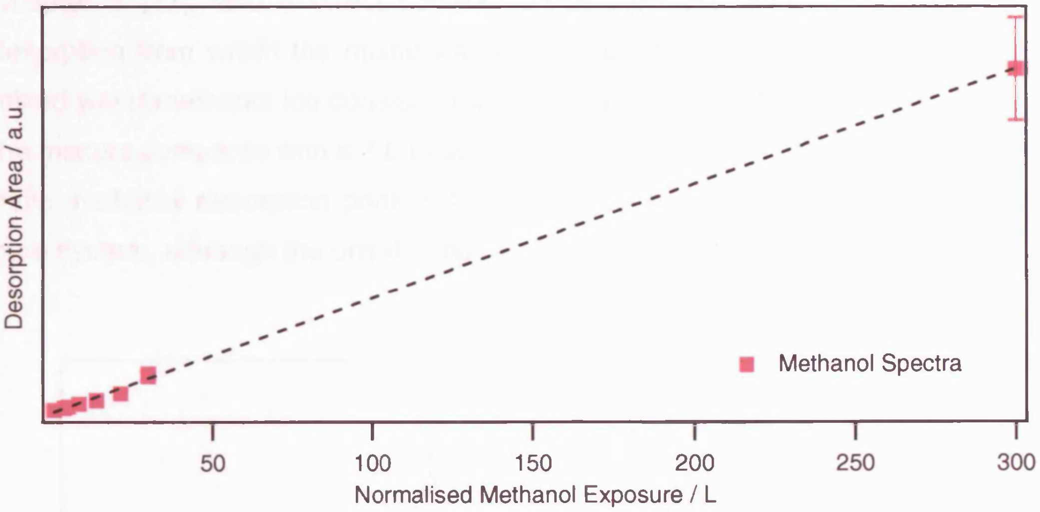

Figure 5.6 Total integrated area of the methanol TPD curves plotted as a function of increasing exposure of the water:methanol mix (≈ 9% methanol), on to the HOPG sample at 97 K.

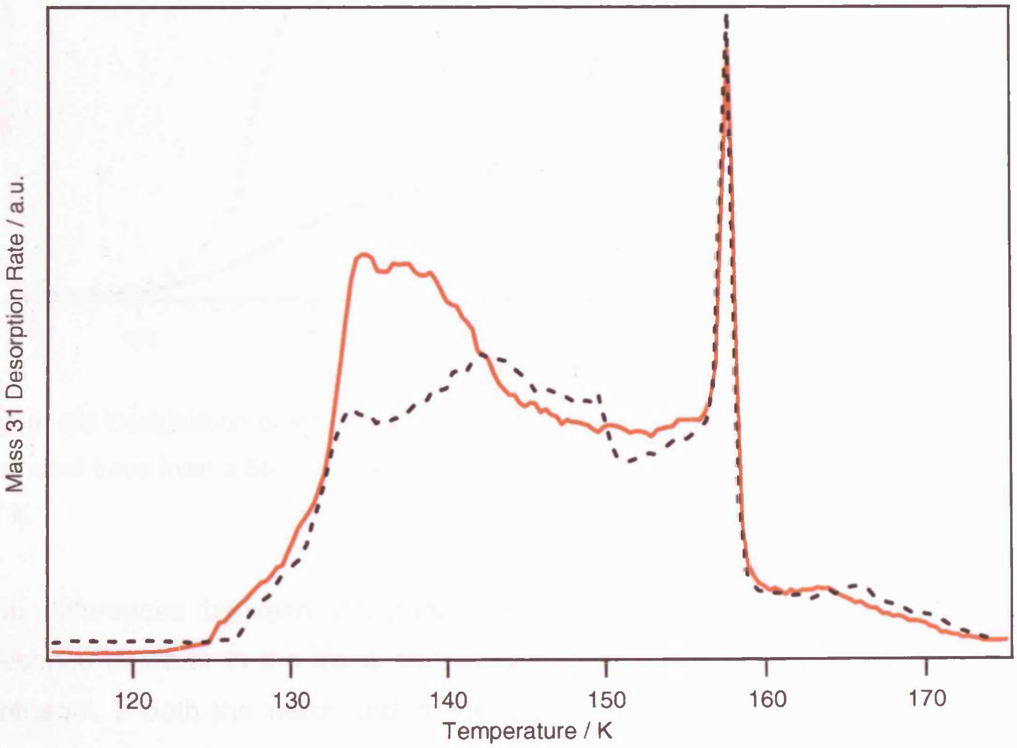

Figure 5.7 Two methanol TPD traces, showing the variation observed in the peak shapes for the same 300 L exposure of the water:methanol mixture, resulting in an ice containing ≈ 9% methanol.

In contrast to the water spectra, methanol desorption from the mixed ice shows a marked deviation from the behaviour observed for pure methanol deposited directly onto a HOPG surface. The pure methanol spectra were reproduced in *Figure 3.1* of Chapter 3 [17], and a direct comparison of the pure spectra with the methanol desorption from within the mixed water:methanol ice is shown in *Figure 5.8*. As the mixed water:methanol ice consists of approximately 9% methanol, a 50 L exposure of the mixture compares with a 7 L exposure of pure methanol. *Figure 5.8* shows that the main methanol desorption peak in the mixed ice appears ≈ 15 K higher than in the pure system, although the onset of desorption begins at the same point, ≈ 122 K.

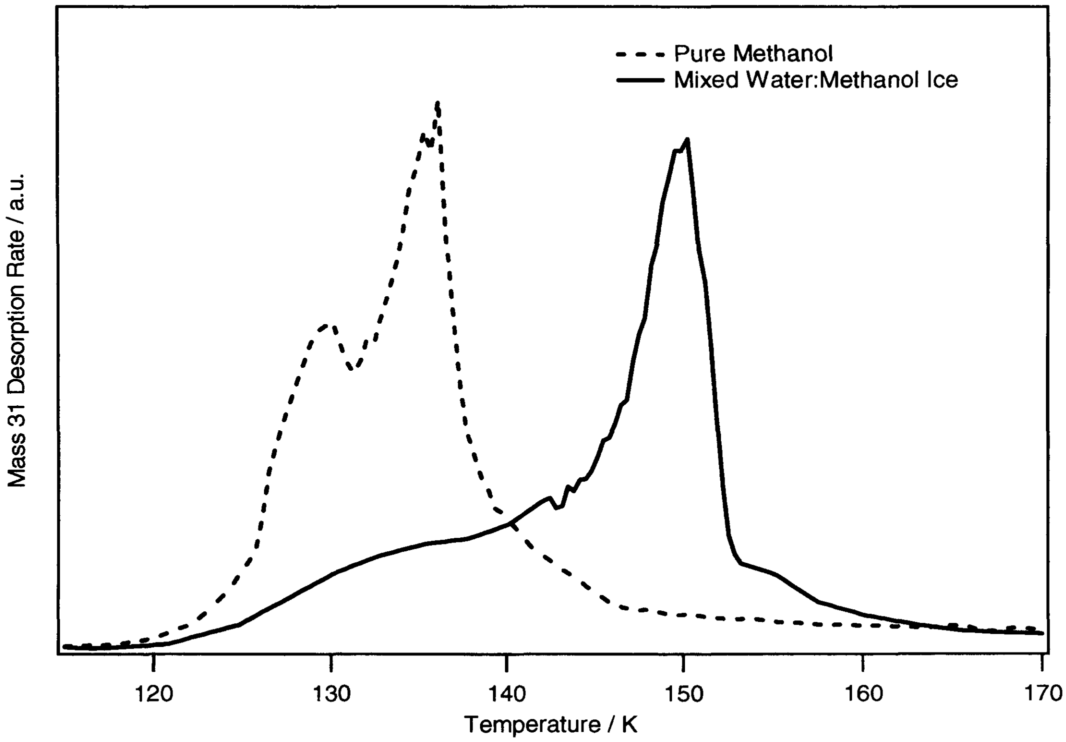

Figure 5.8 Comparison of the 7 L TPD trace for pure methanol deposited on HOPG with the methanol trace from a 50 L exposure of the mixed water:methanol ice adsorbed on HOPG at 97 K.

The differences between the pure and the mixed ice spectra suggest that the presence of water in the ice is strongly influencing the desorption characteristics of methanol. If both the water and methanol desorption traces are viewed together, it becomes clear that the main desorption peak for methanol coincides with the desorption peak for water in the mixed ice. *Figure 5.9* shows superimposed methanol and water TPD traces obtained from the 20 L, 50 L, 100 L and 300 L exposures of the water:methanol mix, adsorbed onto the HOPG surface. The water spectra have been plotted on a larger scale to improve clarity.

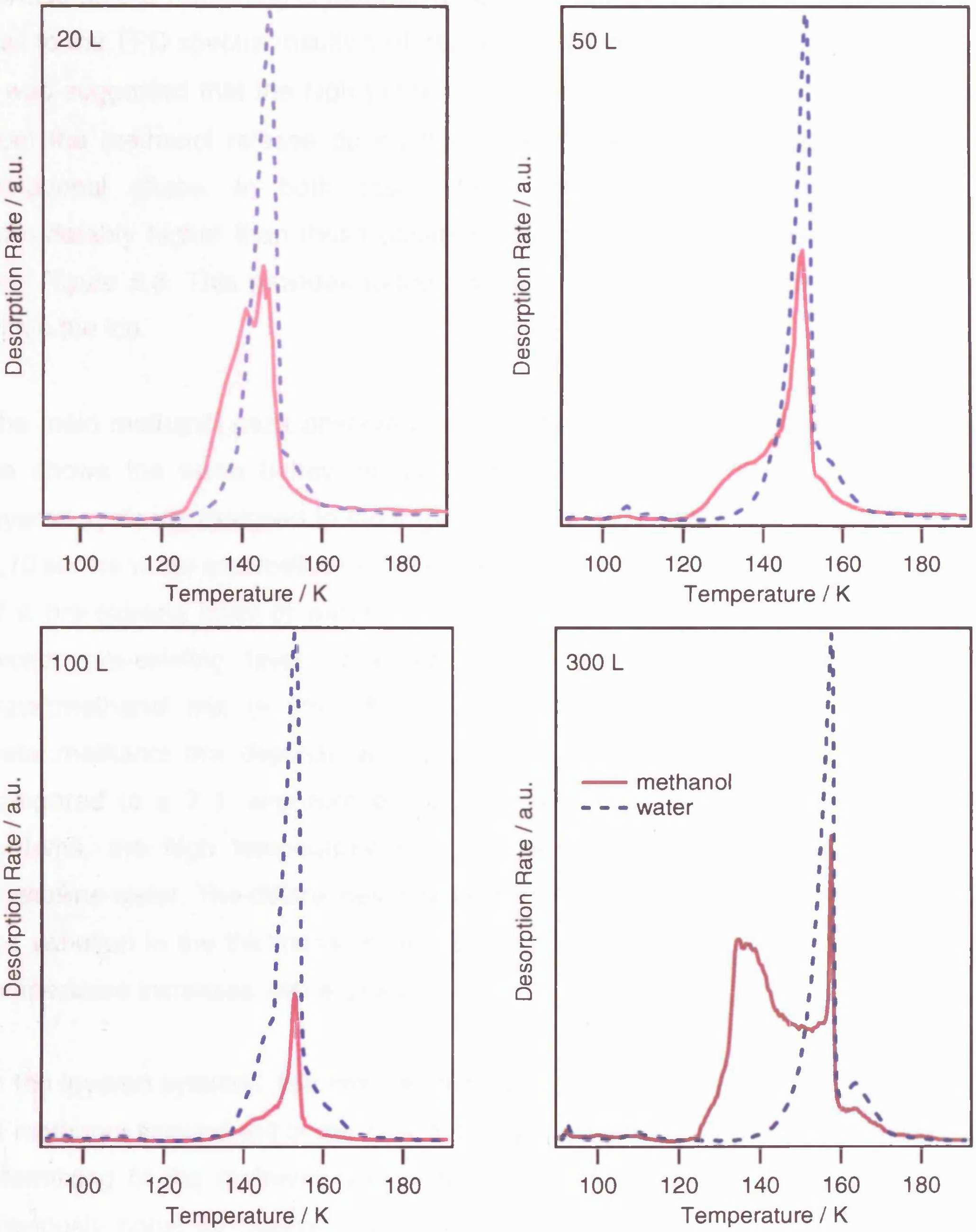

Figure 5.9 TPD traces showing both the methanol and water desorption, following high exposures of the water:methanol mixture (20, 50, 100 and 300 L) to form a mixed ice containing ≈ 9% methanol on an HOPG surface at 97 K. In each case, the water traces have been plotted on a larger scale (1:40), reducing the peak height.

It is clear that the main methanol peak desorbs along with the crystalline multilayers of water in a so called codesorption feature. It is also apparent in the 300 L exposure spectrum, displayed in *Figure 5.9*, that the high temperature methanol peak, ≈ 165 K, coincides with the high temperature water peak assigned to the conversion of crystalline ice to hexagonal ice. Therefore there is still some methanol present on the surface as the remaining crystalline water converts to hexagonal ice. This compares well to the TPD spectra resulting of the methanol/water layered systems, in Chapter 3 it was suggested that the high temperature, τ peak observed in *Figure 3.11* resulted from the methanol release during the transformation of crystalline water ice to its hexagonal phase. In both cases, the methanol desorption temperatures are considerably higher than those observed for pure methanol deposited onto HOPG, see *Figure 5.8*. This provides further evidence that water is retaining the methanol within the ice.

The main methanol peak observed in the TPD spectra of the mixed water:methanol ice shows the same behaviour as the high temperature feature observed in the layered systems, assigned to the trapped feature, and discussed in Chapter 3. *Figure 5.10* shows water and methanol TPD spectra for a) a 7 L exposure of methanol on top of a pre-existing layer of water (10 L), b) a 7 L exposure of methanol on top of a thicker pre-existing layer of water (50 L), and c) a 50 L exposure of the water:methanol mix (≈ 9%). As previously mentioned, a 50 L exposure of the water:methanol mix deposits an equivalent amount of methanol on to the surface compared to a 7 L exposure of pure methanol. In both the layered and mixed systems, the high temperature methanol peak coincides with the desorption of crystalline water. The differences in peak temperatures seen in *Figure 5.10* are due to the variation in the thickness of the water ice in each case, as the water desorption temperature increases with exposure.

In the layered systems, this high temperature feature was assigned to the desorption of methanol trapped within the bulk of the water layer, and provided evidence for the intermixing of the methanol and water layers during the TPD heating process as previously noted by Souda et al [18]. This peak, unlike that observed in the binary layered systems, does not saturate in the mixed ice spectra, as the volume of water available for trapping is constantly increasing with exposure. If experiments were conducted at lower temperatures, it is expected that this peak would be larger for both the mixed and layered systems as the water would exist with a more porous ice structure.

The two high temperature methanol peaks observed in the mixed water:methanol ices are therefore assigned to codesorption features, which represent methanol that is trapped within the bulk of the water ice, possibly in a clathrate hydrate structure [6].

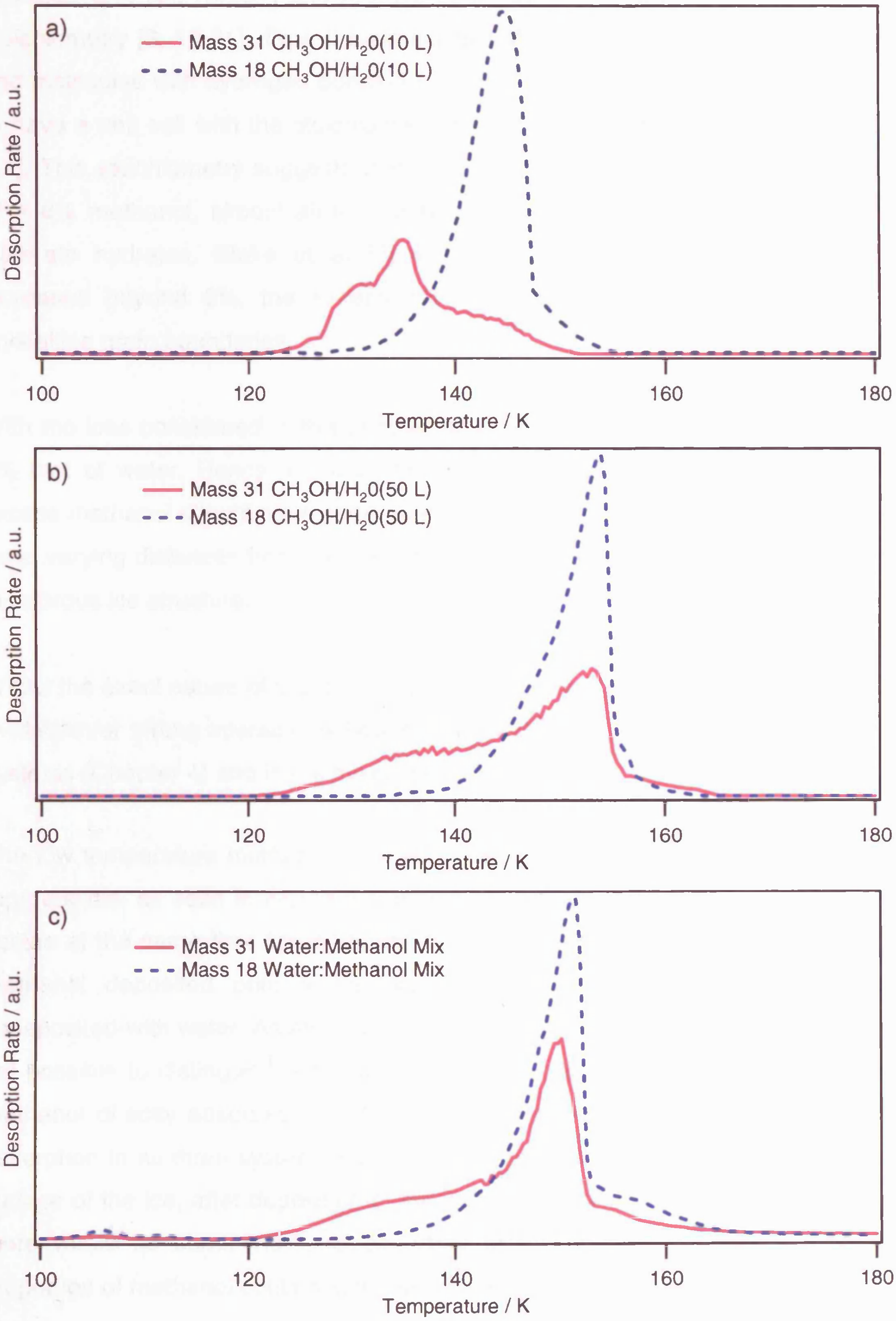

Figure 5.10 TPD spectra showing both water and methanol desorption for a) 7 L exposure of methanol onto a 10 L pre-existing water layer, b) 7 L exposure of methanol onto a 50 L pre-existing water layer and c) 50 L exposure of the water:methanol mix (≈ 9%). In each case the water desorption is shown on a larger scale 1:4 for a) and b) and 1:40 for c).

A number of previous studies have been carried out on the nature of clathrate hydrates, and two types, I and II, have been identified based on their structure and stoichiometry [6, 19-21]. Type II clathrate hydrates are known to form between water and molecules with hydrogen bonding potential, such as methanol, and are predicted to have a unit cell with the stoichiometry 8Y:136H_2O, where Y is the guest molecule [21]. This stoichiometry suggests that, in a dilute water:methanol mixture, comprised of ≈ 6% methanol, almost all the methanol would be available for inclusion within clathrate hydrates. Blake et al [6] suggested that if the methanol composition increases beyond 6%, the excess will be expected to segregate out and form crystalline grain boundaries.

With the ices considered in this chapter, the methanol composition was on average, 9% that of water. Hence any clathrate hydrate structures would be saturated, and excess methanol should have segregated. These segregated regions of methanol will be at varying distances from the ice surface and possibly held in open networks within the porous ice structure.

Whilst the exact nature of the trapped methanol peak is unknown, RAIR spectra show evidence for strong interactions between the water and methanol both in the layered systems (Chapter 4) and in the mixed ices (Chapter 6).

The low temperature methanol peak is harder to assign as its shape is not perfectly reproducible, as seen in *Figure 5.7*. However, it is noted that the onset of desorption occurs at the same time for methanol deposited directly onto the HOPG surface, for methanol deposited onto a pre-existing layer of water ice and for methanol codeposited with water. As already noted for the layered methanol/water systems, it is not possible to distinguish between methanol adsorbed on the water ice surface and methanol directly adsorbed on HOPG. Hence the observation of a similar onset of desorption in all three systems suggests that there is some methanol present on the surface of the ice, after deposition of the water:methanol mix. It is to be expected that there would be some methanol adsorbed on the water ice surface, however the proportion of methanol contained in this low temperature peak is quite considerable.

An attempt has been made to determine the relative proportions of methanol within this low temperature feature and that within the two codesorption features, by fitting the individual peaks. *Figure 5.11* shows an example of the fit used to determine the area attributable to the codesorption feature. This fit is then subtracted from the total peak area to give an area for the low temperature feature. The fit was obtained by a manual process of scaling the water desorption feature until the leading edges matched with the main methanol desorption peak. As a result there will be some error in this fit, estimated at ≈ 10%.

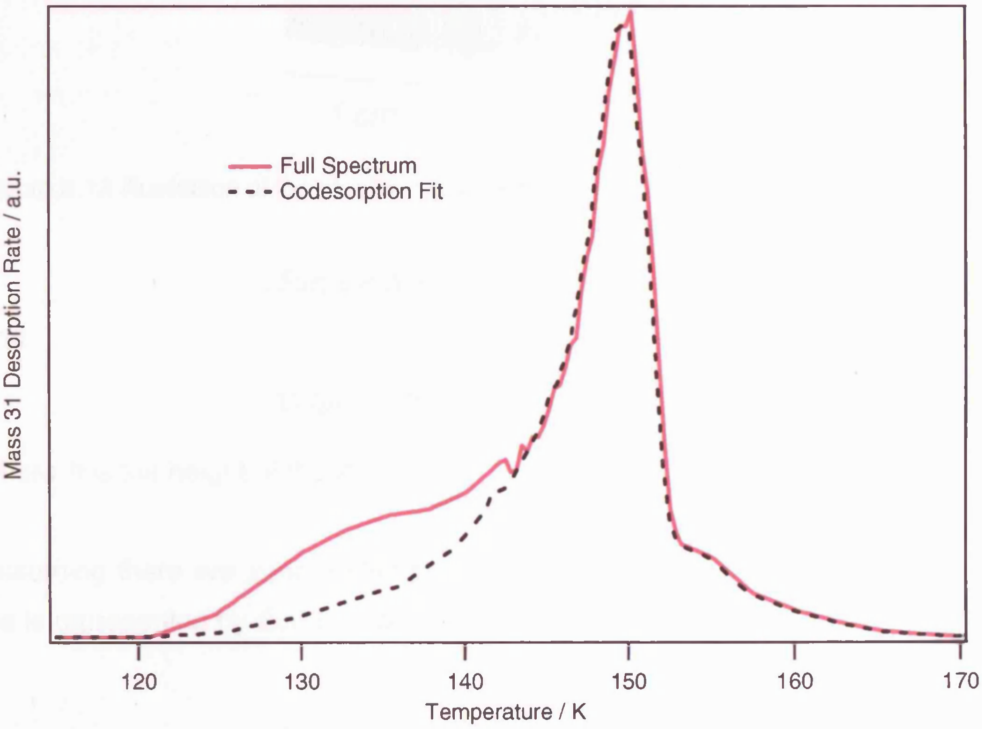

Figure 5.11 Chart showing the proposed fit of the codesorption feature observed in the methanol desorption spectra following a 50 L exposure of the water:methanol mix (≈ 9%) on to HOPG at 97 K.

As the area under a TPD curve is proportional to the number of desorbing molecules, it would be useful to attempt to determine a relationship between the number of molecules expected on the surface of the water ice and those within the bulk, as a function of increasing ice thickness.

Assuming a perfectly smooth surface and ordered growth of the ice on the 2 cm x 1 cm HOPG sample, illustrated in *Figure 5.12*, the total surface area (in cm^2) and volume (in cm^3) can be described by *Equation 5.1* and *Equation 5.2* respectively. Water ice formed at 97 K does not have a smooth surface. It is a highly porous, amorphous, structure [22]. However, this assumption is appropriate for determining a simple relationship between the number of surface molecules and bulk molecules.

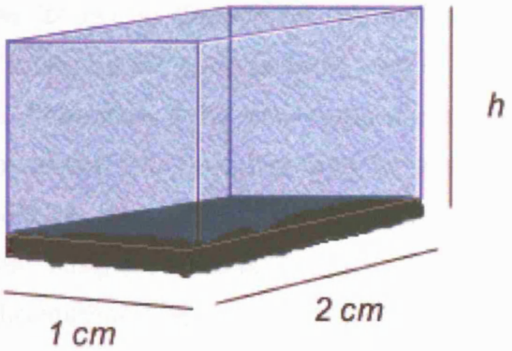

Figure 5.12 Illustration of the idealised geometry of the mixed water:methanol ice structure.

$$\mathit{Surface\ Area} = 2 + 6h \text{ cm}^2 \qquad \text{Equation 5.1}$$

and

$$\mathit{Volume} = 2h \text{ cm}^3 \qquad \text{Equation 5.2}$$

where *h* is the height of the ice.

Assuming there are *x* molecules per cm^3, the number of molecules in the bulk of the ice is represented by *Equation 5.3:*

$$\mathit{Molecules\ in\ bulk\ ice} = 2hx \qquad \text{Equation 5.3}$$

and the number of molecules on the 5 surfaces of the ice is represented by *Equation 5.4:*

$$\mathit{Molecules\ on\ surface} = (2 + 6h)xy \qquad \text{Equation 5.4}$$

where *y* is the thickness of the ice molecules in cm.

Therefore, the ratio between the number of surface molecules and those in the bulk is represented by *Equation 5.5:*

$$\frac{\mathit{Surface\ Molecules}}{\mathit{Bulk\ Molecules}} = \left(\frac{1}{h} + 3\right)y \qquad \text{Equation 5.5}$$

Hence, although there is a linear increase in the surface area as exposure, and therefore as *h,* increases (shown in *Equation 5.1*) there is actually a decrease in the proportion of molecules found on the surface compared to those in the bulk as the ice film thickness increases. Therefore, if the low temperature peak was purely a feature of surface methanol desorption the ratio between its area and that of the bulk, or codesorption, peak would be expected to decrease with increasing ice thickness. *Figure 5.13* shows the integrated peak areas for the codesorption and low temperature feature in the methanol spectra, as a function of the overall spectral area. It shows that the contribution from both features remains approximately constant, with the low temperature feature consistently accounting for ≈ 17% of the total methanol desorption trace. This constant proportion indicates that there must be an additional contribution beyond the expected surface methanol that gives rise to this low temperature feature. It seems likely, given the early onset of methanol desorption in this low temperature feature followed by a broad and slightly erratic feature between 135 K and 150 K, that this peak represents both the desorption of surface methanol and the release of bulk methanol during the crystallisation of the water ice, which occurs between these temperatures [23, 24].

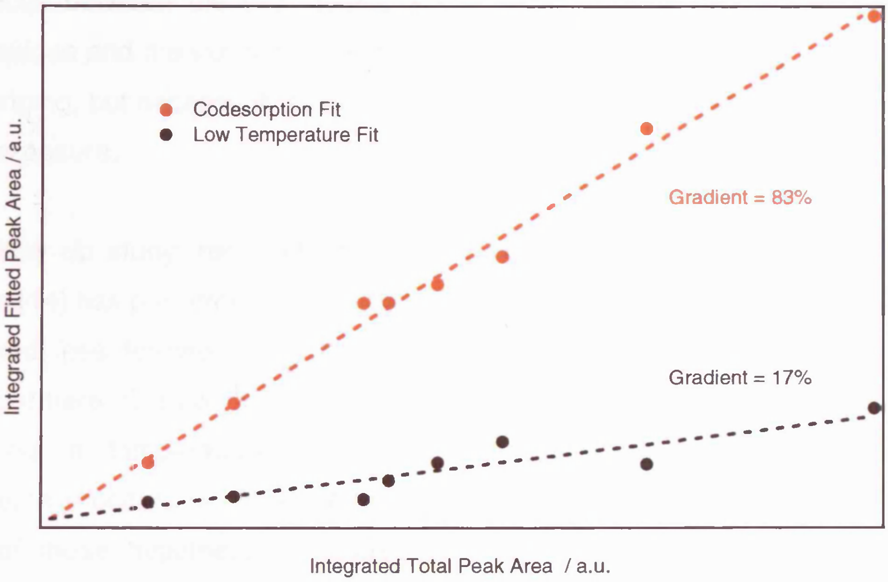

Figure 5.13 Chart showing the integrated methanol peak areas for the fitted low temperature feature and the fitted codesorption feature as a function of the total methanol spectral area. The overall mixed ice composition varied between 5% and 13% methanol in water.

It is likely that the so called bulk methanol is segregated within the mixed ice to form areas of pure methanol ice. Segregation of methanol at concentrations > 6% has been suggested by Blake et al [6]. If some of the methanol desorbing in the low temperature feature comes from the bulk of the ice, then this methanol clearly needs to find a route out of the ice when heating occurs. It has previously been proposed that channels form in the ice as the water structure crystallises, and that these allow the percolation, and subsequent release, of trapped molecules [13, 25]. This could be tested experimentally by dosing water on top of a pre-existing layer of methanol and looking for desorption of methanol before the bulk of the water desorbs. The release of such molecules through this process has historically been termed volcano desorption [9, 26]. The low temperature feature observed in the methanol TPD of the mixed water:methanol ice, is therefore assigned to a combined "Surface & Volcano" feature.

In their studies of the desorption of astrophysically relevant molecules from mixed water ices, Collings et al [9] classified methanol as a water-like species, which shows a single codesorption peak, coincident with water desorption. The spectra discussed in this chapter clearly demonstrate the presence of both a volcano and a codesorption peak. Hence, following on from their categorisation, it might be more appropriate to assign methanol to the intermediate category, where species typically show both volcano and codesorption features, but not a monolayer peak. The observed differences between the two studies are possibly related to the differences in ice compositions and the variation in exposures considered. Collings et al [9] performed a wide ranging, but necessarily brief, study and restricted the methanol experiments to a single exposure.

In a follow up study, reported as a comment within a Faraday Discussions paper, Collings [14] has performed a more comprehensive study of methanol desorption from the mixed ices formed on a gold surface and has found similar results to those presented here. Collings believes, however, that the low temperature feature actually represents a temperature induced phase separation of the methanol, which coincidentally occurs at the same temperature as water crystallisation. To determine which of these hypotheses is correct it would be necessary to repeat the TPD experiments using a range of different heating rates. This would test the link between the two competing processes and assumptions to be drawn about the kinetics of the lower temperature methanol release. Kouchi et al [25] demonstrated that the water crystallisation process approximates a first order process and therefore, if the methanol release was shown to result from a volcano process during the crystallisation of water, it would also be expected to demonstrate first order desorption kinetics.

5.3.1.3 Summary of TPD Findings

During codeposition of the water and methanol vapour onto the cold HOPG surface, a mixed ice is formed. Some of the methanol will be present on the surface of the ice, although the majority of the surface will be comprised of water molecules. The remaining methanol will be in the bulk of the ice, possibly trapped within the pores of the predominantly water ice, and some will be trapped in hydrogen bonded cages or clathrates. Some of the methanol may also segregate to form areas of pure methanol.

As the mixed ice is heated, the first methanol to desorb is the weakly bound molecules on the ice surface. Further heating, beyond the glass transition temperature of water, results in significant reordering of the ice structure and causes channels to open and close, allowing the percolation of methanol molecules towards the surface [26]. Some of these molecules escape, and appear as part of the "Surface & Volcano" feature, before crystallisation of the water ice is complete and the remaining channels become permanently sealed. This escape mechanism is expected to be somewhat irregular, and based on the proportion of methanol that segregates from a saturated clathrate structure, along with the nature of the heat induced structural changes in the ice. This may explain why this feature alters from experiment to experiment.

Any methanol still left within the bulk of the ice will either be part of the segregated methanol that was held too deeply to find a pathway of escape or will be trapped within a clathrate type structure. Either way, this methanol will now only desorb along with the water, and will appear in the TPD spectra as the codesorption feature.

5.4 Bibliography

1. Sandford, S.A., Meteoritics & Planetary Science, 1996. **31**(4): p. 449-476.
2. Sandford, S.A. and Allamandola, L.J., Astrophysical Journal, 1993. **417**: p. 815.
3. Skinner, C.J., Tielens, A., Barlow, M.J., and Justtanont, K., Astrophysical Journal, 1992. **399**(1): p. L79-L82.
4. Allamandola, L.J., Sandford, S.A., and Valero, G.J., Icarus, 1988. **76**(2): p. 225-252.
5. Allamandola, L.J., Bernstein, M.P., Sandford, S.A., and Walker, R.L., Space Science Reviews, 1999. **90**(1-2): p. 219-232.
6. Blake, D., Allamandola, L., Sandford, S., Hudgins, D., and Freund, F., Science, 1991. **254**(5031): p. 548-551.
7. Notesco, G. and BarNun, A., Icarus, 1997. **126**(2): p. 336-341.

8. Notesco, G. and Bar-Nun, A., Icarus, 2000. **148**(2): p. 456-463.

9. Collings, M.P., Anderson, M.A., Chen, R., Dever, J.W., Viti, S., Williams, D.A., and McCoustra, M.R.S., Monthly Notices of the Royal Astronomical Society, 2004. **354**(4): p. 1133-1140.

10. Allamandola, L.J., Sandford, S.A., and Valero, G.J., Icarus, 1988. **76**: p. 225.

11. Ehrenfreund, P., Kerkhof, O., Schutte, W.A., Boogert, A.C.A., Gerakines, P.A., Dartois, E., d'Hendecourt, L., Tielens, A., van Dishoeck, E.F., and Whittet, D.C.B., Astronomy and Astrophysics, 1999. **350**(1): p. 240-253.

12. Barnun, A., Dror, J., Kochavi, E., and Laufer, D., Physical Review B, 1987. **35**(5): p. 2427-2435.

13. Barnun, A., Kleinfeld, I., and Kochavi, E., Physical Review B, 1988. **38**(11): p. 7749-7754.

14. Brown, W.A., Viti, S., Wolff, A.J., and Bolina, A.S., Faraday Discussions, 2006 in press.

15. Bolina, A.S., Wolff, A.J., and Brown, W.A., Journal of Physical Chemistry B, 2005. **109**: p. 16836-16845.

16. Bolina, A.S., *Adsorption of Astrochemically Relevant Molecules on Interstellar Dust Analogues.* PhD Thesis, Department of Chemistry, 2005, UCL.

17. Bolina, A.S., Wolff, A.J., and Brown, W.A., Journal of Chemical Physics, 2005. **122**(4): p. art. no.-044713.

18. Souda, R., Physical Review Letters, 2004. **93**(23): p. art. no.-235502.

19. Bertie, J.E. and Jacobs, S.M., Journal of Chemical Physics, 1978. **69**(9): p. 4105-4113.

20. Boutron, P. and Kaufmann, A., Journal of Chemical Physics, 1978. **68**(11): p. 5032-5041.

21. Mak, T.C.W. and McMullan, R.K., Journal of Chemical Physics, 1965. **42**(8): p. 2732-2737.

22. Mayer, E. and Pletzer, R., Nature, 1986. **319**: p. 298.

23. Hallbrucker, A., Mayer, E., and Johari, G.P., Journal of Physical Chemistry, 1989. **93**(12): p. 4986-4990.

24. Jenniskens, P. and Blake, D.F., Science, 1994. **265**(5173): p. 753-756.

25. Kouchi, A., Yamamoto, T., Kozasa, T., Kuroda, T., and Greenberg, J.M., Astronomy and Astrophysics, 1994. **290**(3): p. 1009-1018.

26. Laufer, D., Kochavi, E., and Barnun, A., Physical Review B, 1987. **36**(17): p. 9219-9227.

Chapter 6 RAIRS Studies of the Adsorption and Desorption of Mixed Films of Methanol and Water Codeposited on Graphite.

6.1 *Introduction*

The previous chapter presented a detailed TPD study of mixed water:methanol ices, of varying composition, formed by codepositing water and methanol vapour onto an HOPG sample held at 97 K. Due to the proposed mechanism of formation of methanol, via sequential surface hydrogenation reactions [1], codeposition studies are generally considered to be the most astrochemically relevant method of studying mixed molecular ices. This chapter will describe the results of a complementary RAIRS study of mixed water:methanol ices. This is the first UHV RAIRS study of mixed water:methanol ices deposited onto a graphitic surface.

Earlier studies of mixed water:methanol ices, discussed in the previous chapter, have identified the ability of water to trap methanol within hydrogen bonded cages, called clathrate hydrates [2, 3]. The TPD results discussed in Chapter 5 provide evidence that at least some of the methanol from the mixture is trapped within the bulk of the water ice, and held beyond the natural desorption temperature for methanol.

A number of previous infrared studies have concentrated on methanol and water dimers [4-7], with fewer studies of binary water and methanol mixtures that have a direct relevance to cometary and interstellar ices [8, 9]. Bakkas et al performed infrared studies of methanol and water dimers, isolated in both a nitrogen [5] and an argon matrix [6]. They concluded that the frequency of the $\upsilon(CO)$ mode is indicative of the role methanol plays in the hydrogen bond with water. When methanol acts as a proton donor (see *Figure 4.12*), as it does in the nitrogen matrix, the $\upsilon(CO)$ mode is blueshifted from the pure monomer frequency and when it acts a proton acceptor, as in the argon matrix, there is a corresponding shift to the red.

Buck and Huisken [7] performed infrared studies and molecular depletion spectroscopy on methanol and water clusters of various sizes. When methanol was considered in isolation, they reported splitting of the $\upsilon(CO)$ band with distinct peaks at 1026.5 cm^{-1} and 1051.6 cm^{-1}, which they believe correspond to the proton-acceptor band and the proton-donor band respectively. Methanol and water dimers demonstrated a single peak, corresponding to methanol acting solely as a proton-acceptor [10]. When methanol was studied as part of a large water cluster [7], their results suggested that methanol acts as both acceptor and donator, which is conducive with the formation of a cyclic structure.

Allamandola, Sandford and Valero completed a detailed infrared study of a number of interstellar ice analogues, which included binary mixes of methanol and water, alongside more complex multicomponent mixes [8]. The methanol and water mixes were studied before and after ultraviolet irradiation in order to mimic photochemical evolution occurring in interstellar ices. In a later study, Sandford and Allamandola [9] performed an infrared study of the thermal evolution of ices containing methanol, water and ammonia, to determine their surface binding energies.

6.2 Methodology

Experiments were performed in an ultra-high vacuum (UHV) chamber, described in Chapter 2. The chamber has a base pressure of 2×10^{-10} mbar. The HOPG sample has been described previously along with the "scotch tape" method of cleaning [11].

The ices were grown in situ by exposing the HOPG surface, held at $\approx$ 97 K, to a stream of gas by back filling the chamber at a constant dosing pressure, with the exposures measured in Langmuir (L). The dosing gas is the vapour formed from a mixture of water and methanol, held in a glass bulb. The composition of the vapour was measured during the dosing process by recording a mass spectrum and comparing the ratios of both components after correcting for relative sensitivities. The chamber pressure was allowed to recover to $\approx 9 \times 10^{-10}$ mbar before RAIR spectra were recorded. The chemicals used during the experiments were distilled, de-ionised water and methanol (CH_3OH – 99.9% - Aristar – BDH). The purity of the dosed species was confirmed by monitoring the mass spectrometer during dosing.

All RAIR spectra were recorded using a Mattson instruments Fourier transform infrared spectrometer coupled to a mercury cadmium telluride (MCT) detector. The spectra were recorded with a resolution of 4 cm^{-1} following 256 scans. During the annealing and desorption sequence, the sample was held at the set temperature for 3 minutes and then cooled to the base temperature before performing the scan. Between experiments the sample was annealed to 500 K and held for three minutes to remove all contaminants from the surface.

6.3 Results and Discussion

In the experiments that follow, an intimate mix of methanol and water was deposited onto a HOPG surface, and the behaviour of the resultant ice was studied by the use of RAIRS. The sample was exposed to vapour from a vessel containing a mix of methanol:water and the exact composition of the vapour was determined by monitoring the dose with the mass spectrometer. Three separate ices were considered, differing in the proportion of methanol within the dosing mix. The vapour for Mix A is 11% methanol, Mix B is 16% methanol and Mix C is 60% methanol. If the sticking probability of both species are presumed to be both high and equal then this should translate to an equivalent composition in the ice. However, earlier TPD results for the methanol and water mix, discussed in Chapter 5, suggest that the methanol composition in the ice will be slightly lower than that in the vapour.

6.3.1.1 Adsorption of the Methanol and Water Mix

Figure 6.1 shows RAIR spectra for the H_2O:CH_3OH system following a 300 L exposure of the water and methanol mix B, the vapour of which contains approximately 16% methanol.

All the bands visible at high exposures of the mix can be confidently assigned by comparison with the spectra obtained from pure water and methanol deposited individually on to an HOPG surface [11, 12]. A pure water spectrum was reproduced, along with assignments, in *Figure 4.3* and the pure methanol spectrum is shown in *Figure 4.4*. The spectrum in *Figure 6.1* is dominated by a large band between 3000 and 3600 cm^{-1}, with defined shoulders at 3377 and 3325 cm^{-1}. This is assigned to the OH stretching modes, present in both the individual water and methanol spectra. The combination band from the scissor (bending) and librational modes of water is seen at 2247 cm^{-1}, but the HOH scissors mode expected at 1677 cm^{-1} is masked by vibrations from gaseous water in the optical path. The smaller features observed in *Figure 6.1* are all attributable to the presence of methanol. The peak at 2831 cm^{-1} is due to the $\upsilon s(CH_3)$, 1128 cm^{-1} is the $\rho(CH_3)$. The bands at 1035 cm^{-1} and 1018 cm^{-1} are $\upsilon(CO)$ features. In the pure methanol study [12] and in the sequentially dosed system discussed in Chapter 4 the $\upsilon(CO)$ band was recorded as a singlet that split on heating, The methanol features are not well defined at this scale due to the dilution in water, but will be discussed in more detail later.

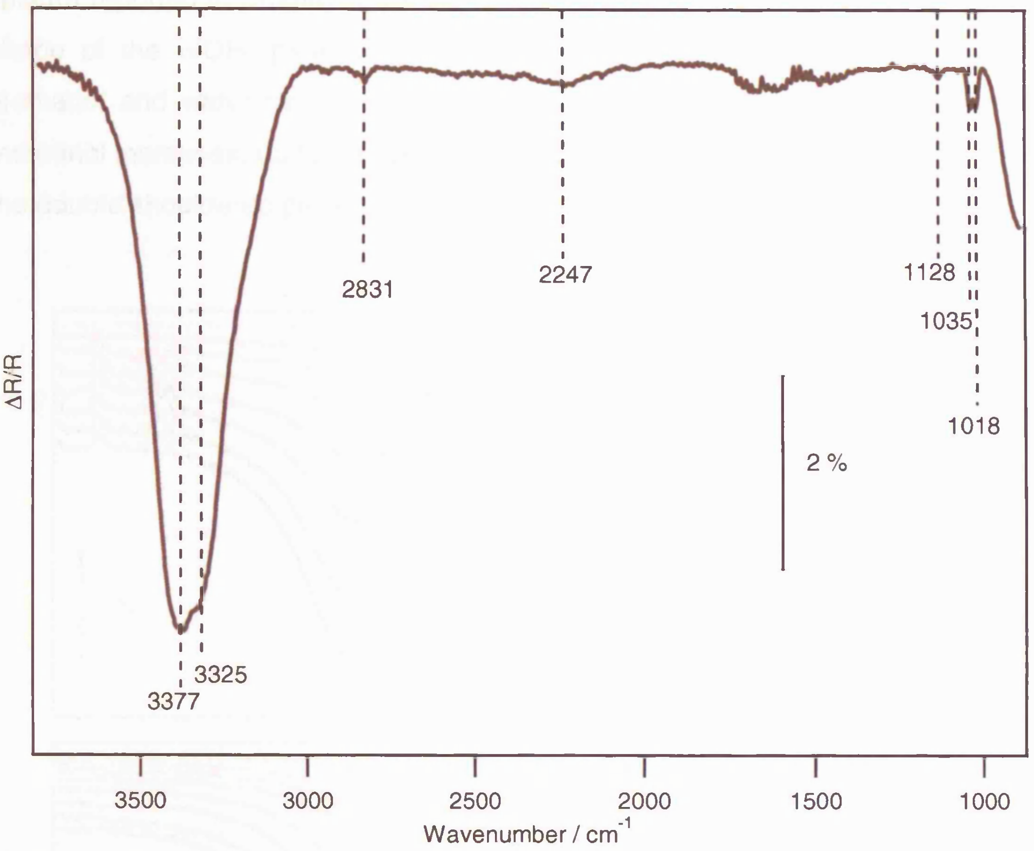

Figure 6.1 RAIR spectra showing the vibrational frequencies present, following a 300 L exposure of the water:methanol mix B, deposited on HOPG at 97 K. Mix B comprises ≈ 16% methanol in the vapour.

Figure 6.2 shows the full adsorption spectra in the region between 3800 cm^{-1} and 2500 cm^{-1} for all three water:methanol mixes studied. The features are very similar across all three mixes, with a broad υ(OH) feature appearing at around 5 L and the υs(CH_3) at 2831 cm^{-1} appearing at exposures beyond 20 L. As the proportion of methanol increases, moving from Mix A through to Mix C, the peak at 2831 cm^{-1} becomes more intense. This is to be expected as it is a methanol only vibration and therefore increases in line with the methanol composition.

The broad OH stretch receives contributions from both methanol and water which explains the subtle shape change as the proportion of methanol increases. In Mix A, the peak has two well defined shoulders at 3395 cm^{-1} and 3304 cm^{-1}, but in Mix C the shoulders are no longer apparent and the peak appears to be centred at 3350 cm^{-1}. The OH stretch seems to represent a simple addition of the spectral features from the pure water and methanol systems and does not provide any evidence for a direct interaction between the two species. This compares directly with the adsorption spectra reported in Chapter 4, for the methanol and water layered systems, where the shape of the υ(OH) peak could be explained by the simple addition of the pure methanol and water traces. *Figure 4.5* demonstrates that, as the contribution from methanol increases, up to a maximum exposure of 15 L, the υ(OH) band moves from the double shouldered peak to a single peak centred at ≈ 3350 cm^{-1}.

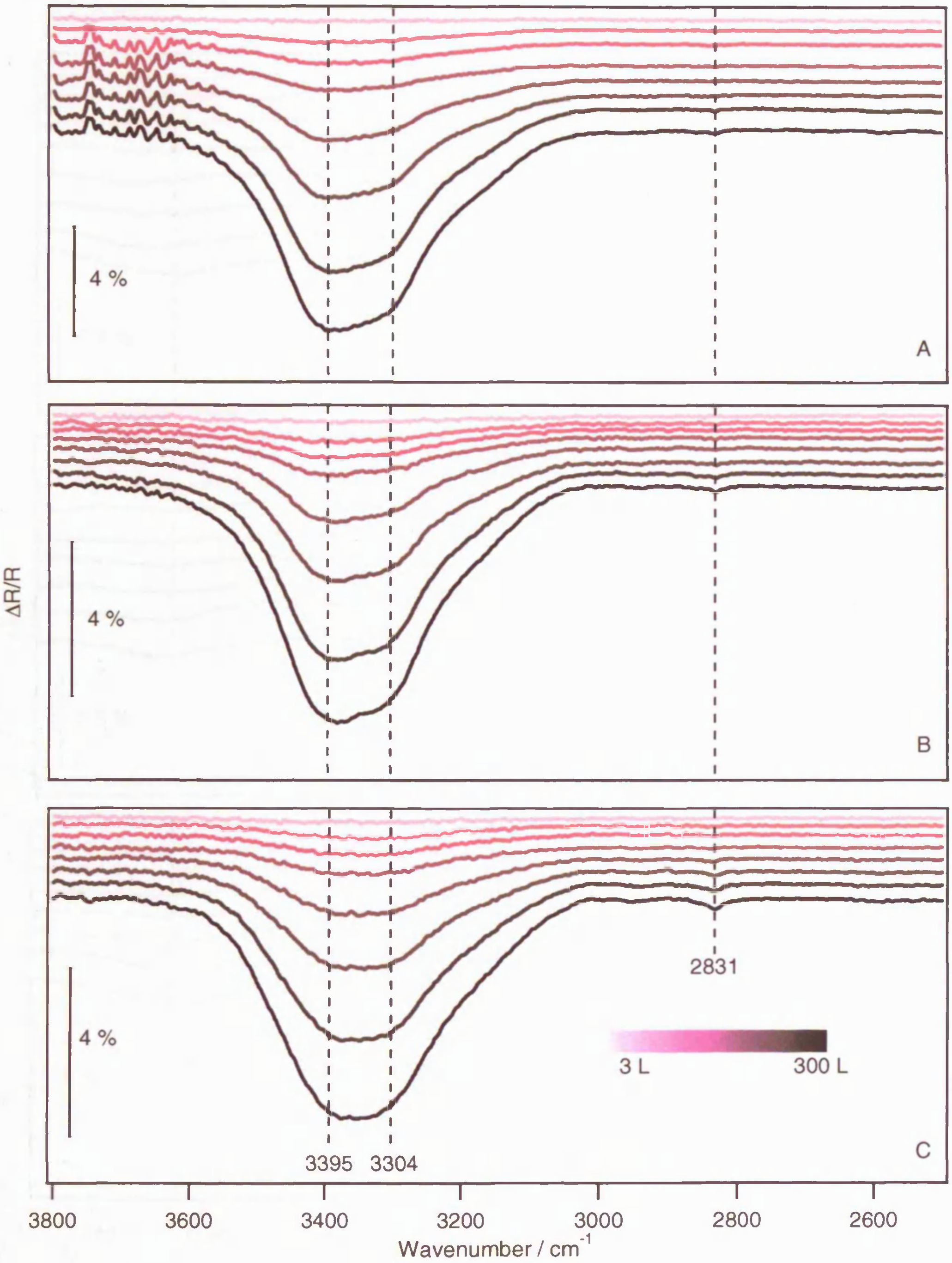

Figure 6.2 RAIR spectra recorded over the wavenumber range from 3800 to 2500 cm^{-1}, showing the full adsorption sequence for increasing exposures of the three different water:methanol mixes, A, B and C adsorbed on HOPG at 97 K.

Figure 6.3 shows the adsorption spectra for the three mixes, in the region between 1150 cm^{-1} and 950 cm^{-1}. Across all three mixes, the first peak to appear in the RAIR spectra is the feature at 1035 cm^{-1}, observed after a 7 L exposure. When the exposure is increased to 50 L, an additional peak is observed at 1018 cm^{-1}. It is only at very high exposures, > 100 L, that the feature at 1126 cm^{-1} can be observed. This is the $\rho(CH_3)$ vibration and must have only a weak vertical component.

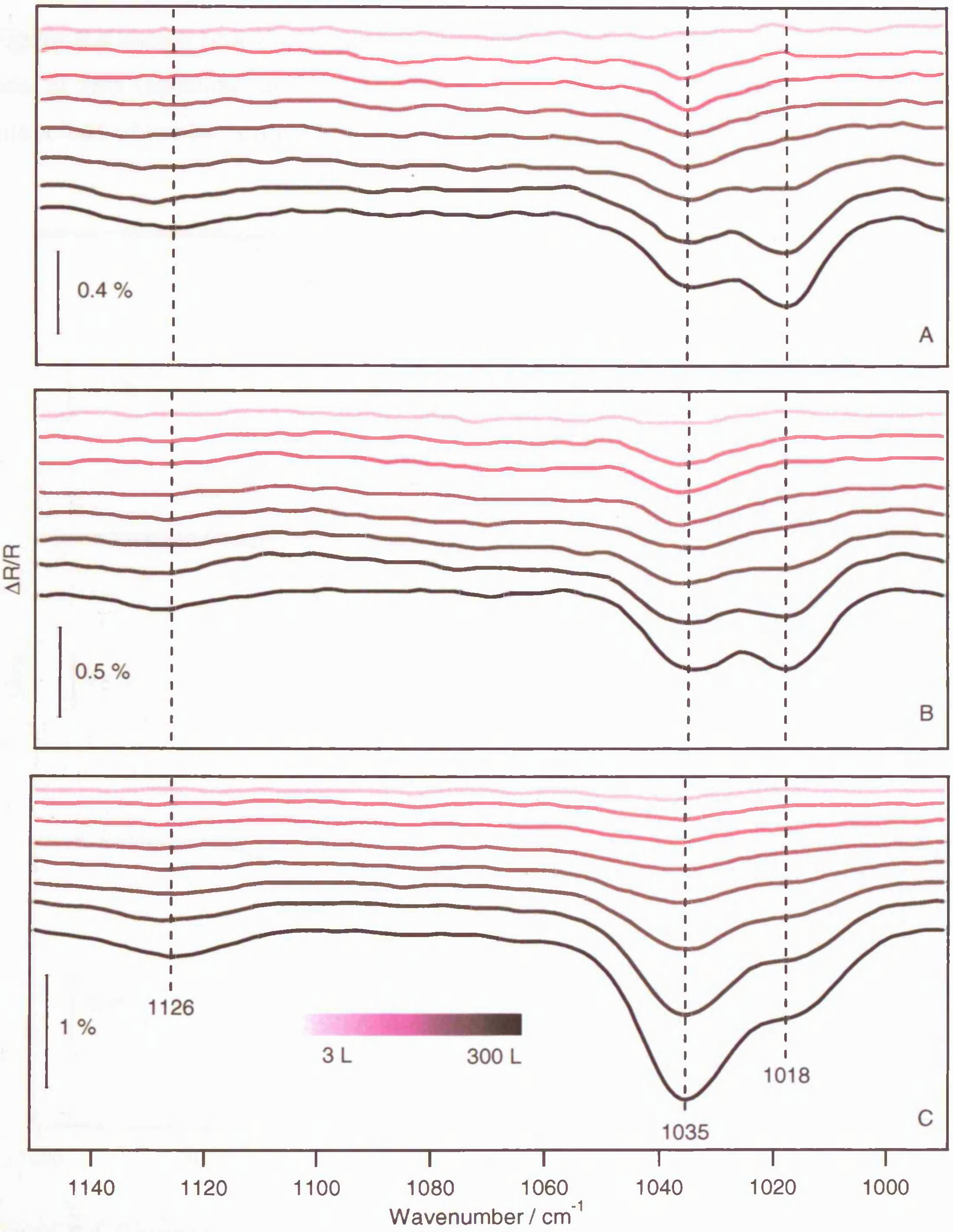

Figure 6.3 RAIR spectra recorded over the wavenumber range from 1150 to 950 cm^{-1}, showing the full adsorption sequence for increasing exposures of the three different water:methanol mixes, A, B and C adsorbed on HOPG at 97 K.

As expected, the intensities of all of these bands increase as the proportion of methanol in the mix increases, but the relative intensities of the 1035 cm^{-1} and 1018 cm^{-1} bands alter as the mix changes. For Mix A, at 11% methanol, the 1018 cm^{-1} feature is the most intense feature following a 300 L exposure. In Mix B, when the methanol composition has increased to 16%, the two features have an equal intensity and in Mix C, where the methanol composition is 60%, there has been a complete intensity inversion with the 1035 cm^{-1} feature being the most intense.

Figure 6.4 shows how the combined 1035 and 1018 cm^{-1} feature can be fitted with the use of two Gaussian curves. These fits have been used to determine the relative intensities of the two bands in each mix and the results are shown in *Table 6.1*.

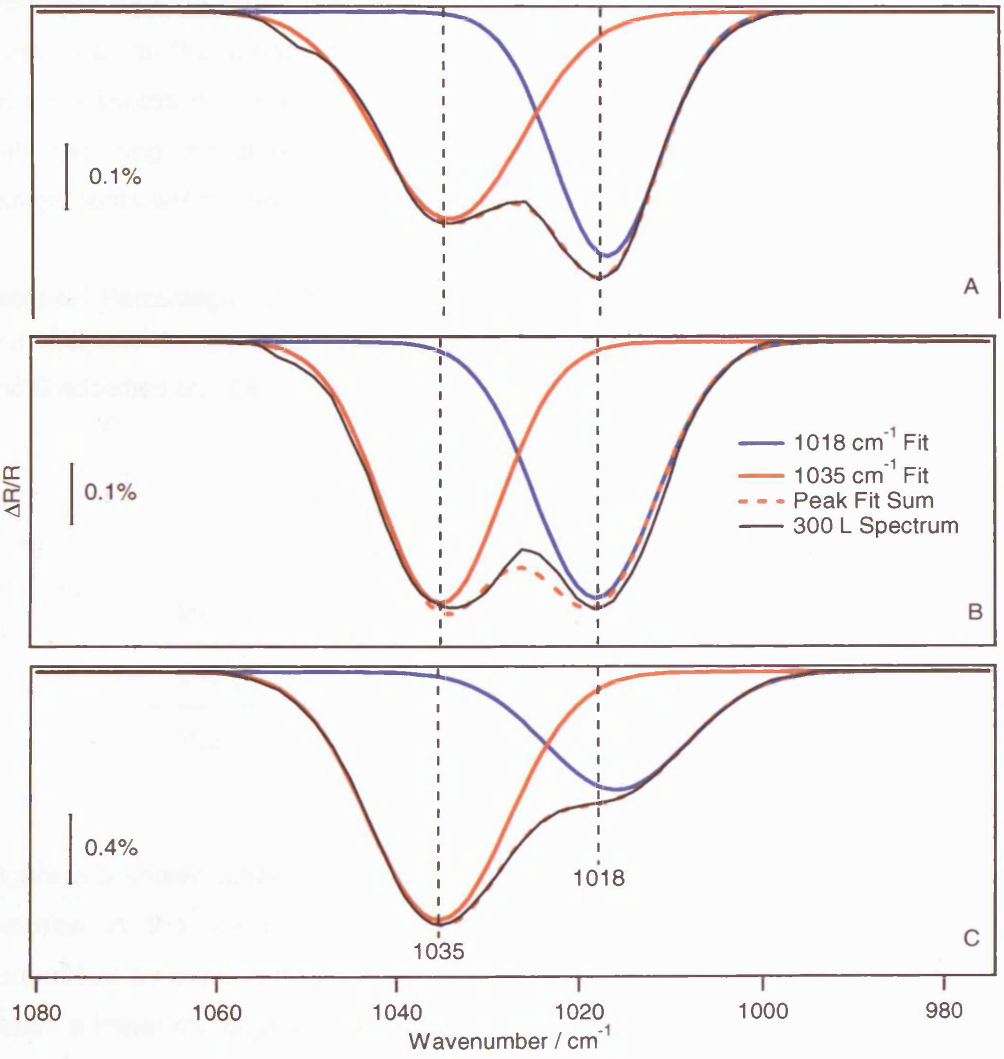

Figure 6.4 Gaussian fits for the combined 1035 cm^{-1} and 1018 cm^{-1} feature in the 300 L spectra of the three different water:methanol mixes, A, B and C adsorbed on HOPG at 97 K.

In both of the early studies of pure methanol adsorbed on HOPG [12] and methanol sequentially deposited onto a water surface, the υ(CO) band first appears as a singlet at 1045 cm^{-1}. After annealing either the pure or layered ices, provided the exposure is $\geq$ 50 L, this feature splits into two peaks at 1038 cm^{-1} and 1028 cm^{-1}, and there is an associated shift of the 1144 cm^{-1} feature to 1130 cm^{-1}. This splitting has been attributed to the crystallisation of multilayer methanol and occurs in both cases at $\approx$ 40 K. In the codeposited systems studied in this chapter, the CO feature appears as a doublet immediately upon adsorption. This is unlikely to be an indication of crystalline methanol, as at 97 K the temperature is too low and crystallisation has only previously been reported in thick multilayers [12]. Instead the two band frequencies are likely to represent methanol present in two spatially distinct environments. Referring back to the results of the TPD data discussed in Chapter 5, these could be methanol trapped within the bulk of the water ice and methanol that has segregated close to or on the surface of the ice. Alternatively the two bands could be originating from the proton donor and proton acceptor roles that Buck and Huisken [7] observed with the ring structure formed by methanol in large water clusters. Possible assignments will be discussed later in this chapter.

Table 6.1 Percentage contributions of the individual Gaussian fits for the combined 1035 cm^{-1} and 1018 cm^{-1} feature in the 300 L spectra of the three different water:methanol mixes, A, B and C adsorbed on HOPG at 97 K.

		Relative Peak Areas	
	% Methanol in Mix	**1018 cm^{-1}**	**1035 cm^{-1}**
Mix A	11%	46%	54%
Mix B	18%	50%	50%
Mix C	60%	33%	67%

Figure 6.5 shows uptake curves for the total spectra and for the four most dominant features in the water:methanol spectra for Mix B. The exposures have been normalised by integrating each dose area and plotting on a relative scale. The figure shows a linear increase in both individual and total peak areas as the exposure of the mix is increased, which suggests that the sticking probability remains constant and that there is no preferential orientation of the molecules.

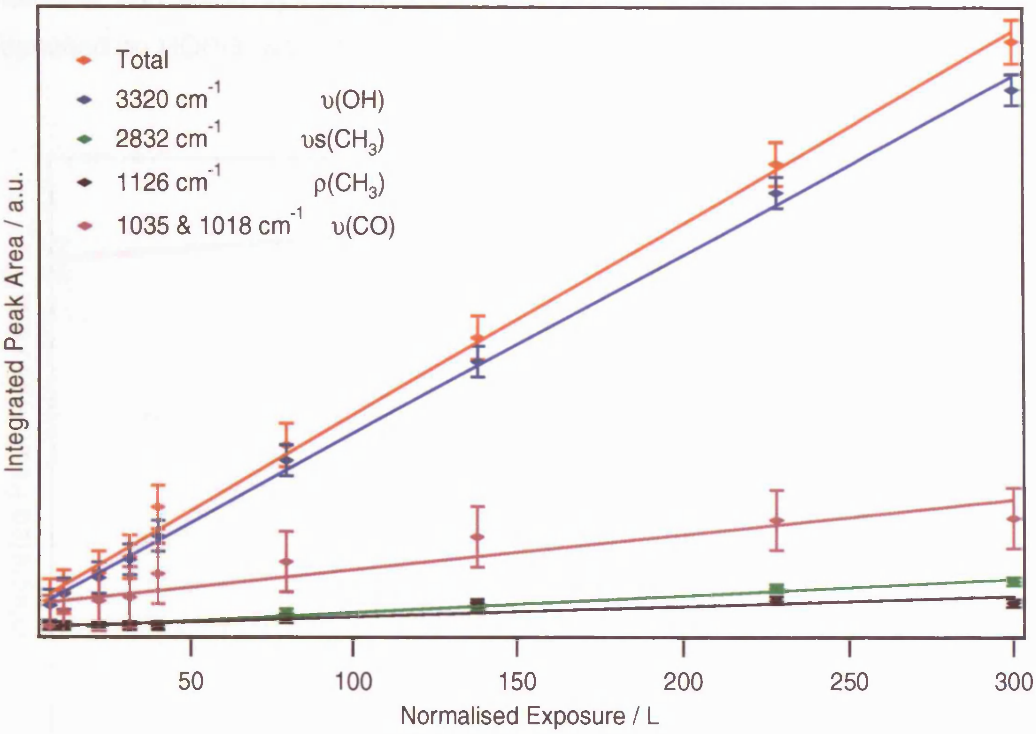

Figure 6.5 Chart showing the integrated peak areas for the total spectrum and the bands at 3320 cm^{-1}, 2832 cm^{-1}, 1126 cm^{-1} and the combined feature at 1035 & 1018 cm^{-1} as a function of increasing exposure of the water:methanol Mix B on HOPG at 97 K. The trace for the total spectra and 3320 cm^{-1} feature are plotted on a reduced scale.

Uptake curves for mixes A and C also show the same linear trend. This is in agreement with the observations from the TPD data shown in Chapter 5. Similar plots for the layered methanol and water systems were also shown to be linear, see *Figure 4.6*.

6.3.1.2 Annealing the Mixed Methanol and Water System

The desorption behaviour of the mixed water:methanol ice was studied by annealing the sample to increasing temperatures before cooling and performing RAIRS scans. Ices formed by the adsorption of the three different mixes of water:methanol (A, B and C) were studied in turn. *Figure 6.6* shows the integrated area of the 300 L water:methanol Mix B spectrum, recorded at temperatures between 97 K and 190 K. There is an increase in the total spectral area as the sample is heated to 145 K, which is attributed to the sharpening recorded in the υ(OH) band (see *Figure 6.7*) as the bulk water and methanol are heated beyond their glass transition temperatures [11-13]. Beyond 145 K, there is a rapid decrease in the total spectral area and desorption is complete by 190 K. This behaviour is identical to that observed when the layered methanol and water system was annealed (see *Figure 4.10*) and when pure water deposited on HOPG, was annealed [14].

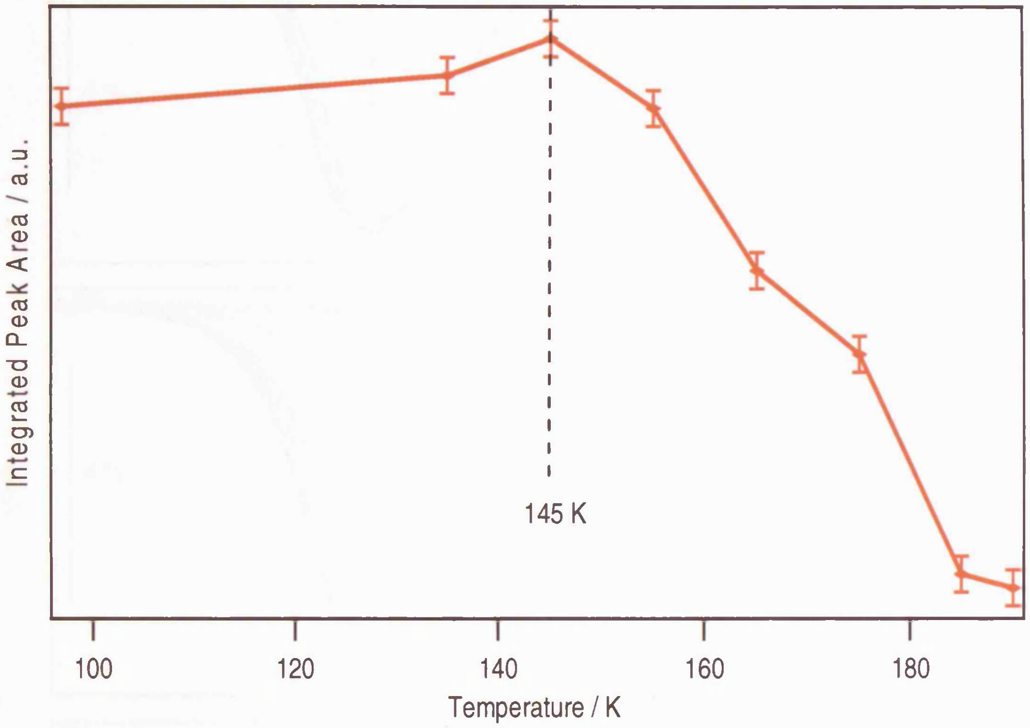

Figure 6.6 Chart showing the integrated peak areas for the total spectrum obtained following a 300 L exposure of the water:methanol Mix B, as a function of the annealing temperature.

There are a number of changes to the bands appearing in the spectra of the mixed ices during the heating process. *Figure 6.7* shows the spectra in the region between 3800 cm^{-1} and 2500 cm^{-1} for all three of the annealed water:methanol mixes studied. As the ice mix is heated between 135 K and 155 K there is a noticeable increase in the intensity of the broad υ(OH) feature recorded between 3700 cm^{-1} and 3000 cm^{-1}. The two shoulders, observed at 3395 cm^{-1} and 3304 cm^{-1} following the adsorption of 300 L of the water:methanol mix, demonstrate a sharpening and downshift to 3370 cm^{-1} and 3272 cm^{-1} respectively. A further shoulder becomes apparent at 3170 cm^{-1}. Heating beyond 155 K shows a rapid decline in all of the features and desorption is complete in this high frequency region by 185 K. The trend is the same across all three mixes, although Mix C, with the highest proportion of methanol (≈ 60%), shows a more dramatic, temperature induced, intensity increase in the υ(OH) region and the 3272 cm^{-1} peak is clearly the most dominant of the three peaks described. The low intensity peak at 2832 cm^{-1}, assigned to the $\upsilon s(CH_3)$, shows a gradual decline as the sample is heated, and disappears by 165 K.

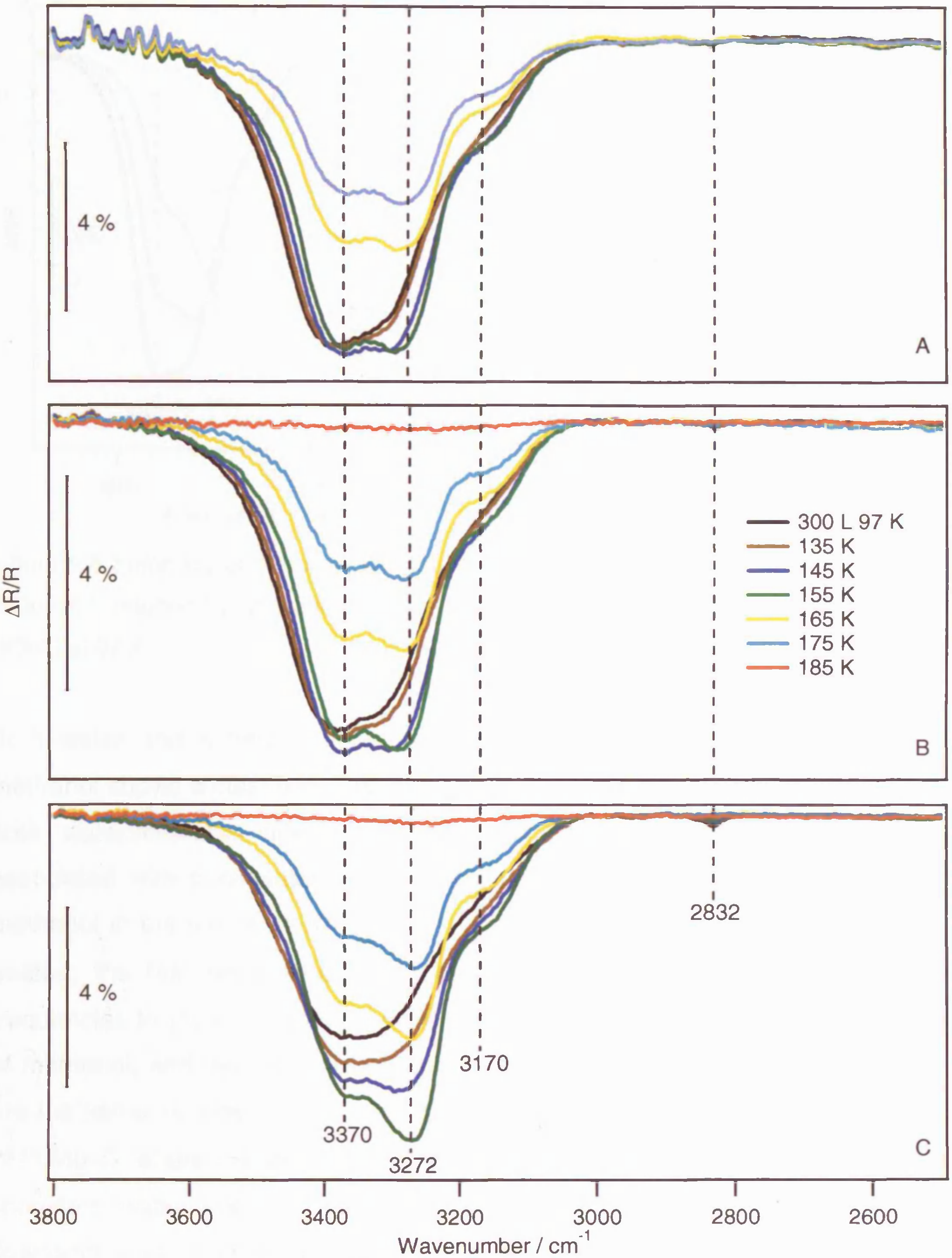

Figure 6.7 RAIR spectra recorded over the wavenumber range from 3800 to 2500 cm^{-1}, showing the sequential heating of the ice formed by depositing 300 L of the three different water:methanol mixes, A, B and C on HOPG at 97 K.

The heat induced changes seen in the υ(OH) region of the mixed spectra can be understood by comparison with the behaviour of the pure water and methanol systems. *Figure 6.8* illustrates the classic features observed in the RAIR spectra of both water and methanol as they crystallise during the annealing process [11, 12].

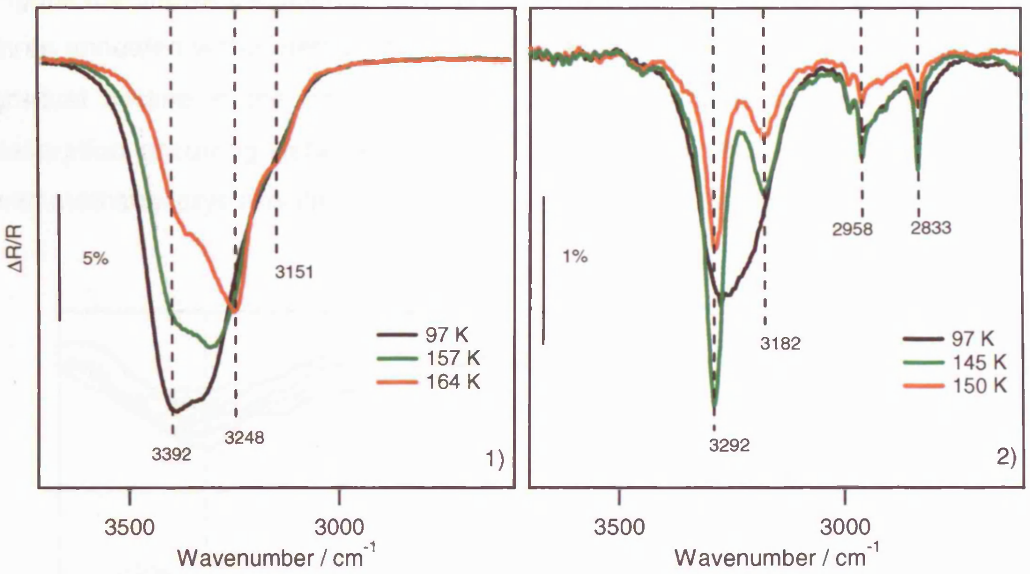

Figure 6.8 Summary of the observed spectral changes in the region between 3700 cm^{-1} and 2600 cm^{-1} induced by annealing ices of 1) pure water, 2) pure methanol, all deposited on HOPG at 97 K.

Both water and methanol show splitting of the υ(OH) band on heating but only methanol shows a clear intensity increase of the peak at 3292 cm^{-1}. Prior to annealing both water:methanol mixes A and B are dominated by the spectral features associated with pure water, which is perhaps to be expected as the proportion of methanol in the mix remains low, at 11% and 16% respectively. As the mixed ice is heated, the features in the υ(OH) region for mixes A and B show very similar frequencies to the pure water spectra, although slightly downshifted by the presence of methanol, and the ratio of the intensities of the high and low frequency shoulders are the same as those recorded for the transition to crystalline water ice [11, 15, 16]. With Mix C, where the methanol content is high ($\approx$ 60%), the frequencies of the υ(OH) shoulders visible when the water crystallises are downshifted by $\approx$ 20 cm^{-1}. A similar downshift was noted in the study of sequentially deposited water and methanol discussed in Chapter 4. This was attributed to a direct interaction between the water and the methanol, and provided evidence of the heat induced mixing of the two species, also reported by Souda et al [13]. An attempt was made to fit the mixed peak by combining the pure water and pure methanol peaks but this proved inconclusive, due to limited data for the pure systems at the relevant exposures. Performing the experiments with deuterated water would enable the frequencies of the methanol OH stretch to be determined as it would result in a shifting of the overlapping water spectra.

Figure 6.9 shows the spectra in the region between 1150 cm^{-1} and 950 cm^{-1} for the three annealed water:methanol mixes (A, B and C). Heating the mixed ice results in a gradual decline in the intensity of the ρ(CH_3) feature at 1127 cm^{-1} with complete desorption occurring between 165 K and 175 K. The frequency shifting associated with methanol crystallisation in the pure system [12] is not observed here.

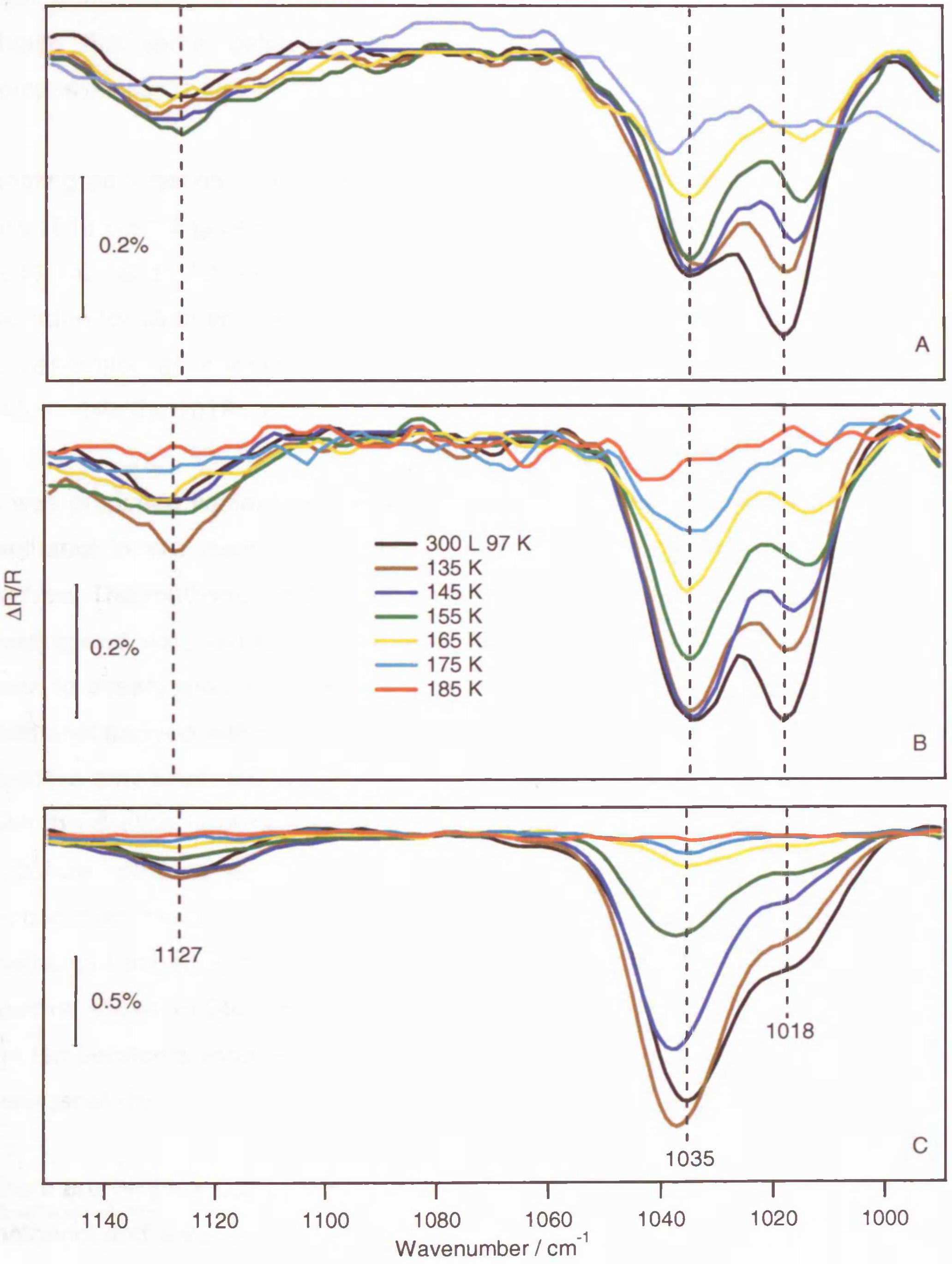

Figure 6.9 RAIR spectra recorded over the wavenumber range from 1150 to 950 cm^{-1}, showing the sequential heating of the ice formed by depositing 300 L of the three different water:methanol mixes, A, B and C on HOPG at 97 K.

It was noted earlier that the ρ(CH_3) feature is one of the last bands to appear in the adsorption spectra of the mixed ice, only appearing in the spectra after an exposure of at least 100 L. Increasing exposure in the mixed system represents only an increasing volume of the ice formed, it does not result in a change in composition of the ice, as it would in the layered systems considered earlier. As a result, the behaviour of the ρ(CH_3) band is more likely to be a result of it being only weakly infrared active rather than representing an orientation change as the exposure increases. This feature shows the same behaviour across all three mixes, regardless of methanol composition, although it is more intense in Mix C.

Heating also results in a decrease in the intensity of both of the peaks at 1035 cm^{-1} and 1018 cm^{-1}. *Figure 6.10* shows the areas for the Gaussian fits used to separate the 1018 cm^{-1} and 1035 cm^{-1} feature into individual peaks for Mix B (the same trend is recorded for all three mixes). It seems that the high frequency peak is more resistant to desorption as it maintains, or slightly increases, its intensity until approximately 145 K while the 1018 cm^{-1} feature starts to decline immediately.

It was proposed earlier that the two peaks at 1035 cm^{-1} and 1018 cm^{-1} represented methanol in two distinct environments, either in the bulk or segregated near the surface. The methanol contributing to the peak at 1018 cm^{-1} desorbs immediately on heating and so could be the methanol held near the surface of the ice, which was seen to desorb around 120 K in the TPD results. The 1035 cm^{-1} peak is likely to be methanol trapped within the bulk of the ice. The TPD results suggest that this species desorbs only when the water starts to desorb at around 140 K, which is consistent with the decline in peak area seen in *Figure 6.10*. There is still a component of the 1035 cm^{-1} peak remaining at temperatures as high as 175 K, which is considerably higher than the pure methanol desorption temperature and must be due to the methanol trapped within the bulk of the water ice. This compares well with the TPD spectra, shown in Chapter 5, which demonstrated that methanol was still desorbing at the temperatures associated with the phase transition of the water from crystalline to hexagonal ice.

There are very few comparable studies in the literature that present infrared spectra of methanol and water ices although Allamandola, Sandford and Valero present a single RAIR spectrum for a 2:1 H_2O:CH_3OH mix, in their study of the photochemical evolution from ice analogues [8]. The spectrum is shown for the mix prior to photolysis and, interestingly, the υ(CO) peak shows no sign of any splitting. A 2:1 mix of the components in the dosing flask will result in an ice with a very high proportion of methanol, considerably higher than the mixes presented in this chapter. *Figure 6.3* demonstrates that increasing the proportion of methanol in the mixture, results in a reduction in the contribution of the lower frequency band and so for very high methanol mixtures it may be expected that splitting would not be apparent.

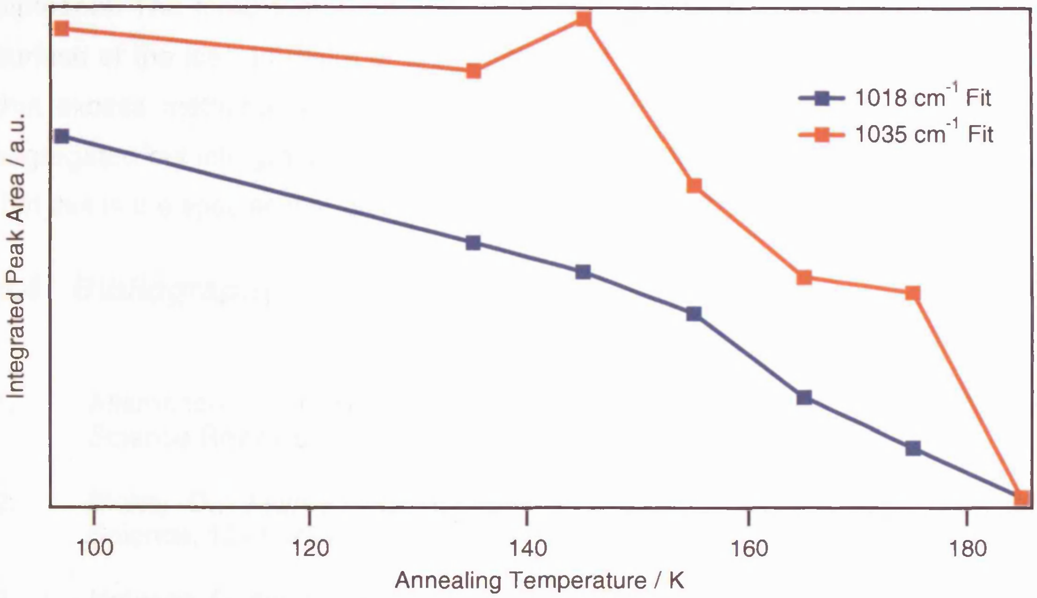

Figure 6.10 Chart showing the integrated areas for the fitted peaks at 1035 & 1018 cm^{-1}, following a 300 L exposure of the water:methanol Mix B, as a function of the annealing temperature.

To summarise, the RAIRS study of the mixed water:methanol ices has provided an interesting complement to the TPD studies reported in Chapter 5. The behaviour of the water within the mixed ice appears to be little changed from that expected for pure water. Desorption commences and is complete at the same temperature recorded for pure water deposited on HOPG [11]. The shape of the υ(OH) feature after heating is suggestive of the crystallisation of water occurring at around 145 K, as expected.

In contrast to the water desorption, the behaviour of the methanol is very much perturbed by the presence of the water in the ice. Pure methanol [12] and methanol deposited onto a layer of water ice shows characteristic features of crystallisation on heating. There is no evidence from either the RAIRS experiments discussed here, or the TPD presented in the previous chapter, that suggests that the methanol present in a mixed ice actually crystallises. In addition, the RAIR spectra provide evidence that methanol is being retained in the ice mixture to temperatures higher than its expected sublimation temperature, in agreement with TPD studies.

The observation of two peaks for the υ(CO) vibration, observed immediately upon adsorption, provides evidence that methanol is found in two different environments as the mixture is deposited onto the HOPG sample. The feature at 1035 cm^{-1} is likely to represent methanol within the bulk of the ice, possibly trapped within clathrate hydrate structures [2]. It is the most resistant feature, and only starts to desorb when the water desorbs, staying on the surface well beyond the expected desorption temperature of methanol. The feature at 1018 cm^{-1} is likely to represent methanol on, or near, the surface of the ice. In Blake et al's [2] study of type II clathrate hydrates, they found that excess methanol, beyond that which could be encaged in the clathrate, was segregated out into grain boundaries of nearly pure methanol and hence it is possible that this is the species that gives rise to the 1018 cm^{-1} CO stretch feature.

6.4 Bibliography

1. Allamandola, L.J., Bernstein, M.P., Sandford, S.A., and Walker, R.L., Space Science Reviews, 1999. **90**(1-2): p. 219-232.
2. Blake, D., Allamandola, L., Sandford, S., Hudgins, D., and Freund, F., Science, 1991. **254**(5031): p. 548-551.
3. Notesco, G. and BarNun, A., Icarus, 1997. **126**(2): p. 336-341.
4. Stockman, P.A., Blake, G.A., Lovas, F.J., and Suenram, R.D., Journal of Chemical Physics, 1997. **107**(10): p. 3782-3790.
5. Bakkas, N., Bouteiller, Y., Loutellier, A., Perchard, J.P., and Racine, S., Journal of Chemical Physics, 1993. **99**(5): p. 3335-3342.
6. Bakkas, N., Bouteiller, Y., Loutellier, A., Perchard, J.P., and Racine, S., Chemical Physics Letters, 1995. **232**(1-2): p. 90-98.
7. Buck, U. and Huisken, F., Chemical Reviews, 2000. **100**(11): p. 3863-3890.
8. Allamandola, L.J., Sandford, S.A., and Valero, G.J., Icarus, 1988. **76**: p. 225.
9. Sandford, S.A. and Allamandola, L.J., Astrophysical Journal, 1993. **417**: p. 815.
10. Huisken, F. and Stemmler, M., Chemical Physics Letters, 1991. **180**(4): p. 332-338.
11. Bolina, A.S., Wolff, A.J., and Brown, W.A., Journal of Physical Chemistry B, 2005. **109**: p. 16836-16845.
12. Bolina, A.S., Wolff, A.J., and Brown, W.A., Journal of Chemical Physics, 2005. **122**(4): p. art. no.-044713.
13. Souda, R., Physical Review Letters, 2004. **93**(23): p. art. no.-235502.

14. Bolina, A.S., *Adsorption of Astrochemically Relevant Molecules on Interstellar Dust Analogues.* PhD Thesis, Department of Chemistry, 2005, UCL.

15. Mitlin, S. and Leung, K.T., Journal of Physical Chemistry B, 2002. **106**(24): p. 6234-6247.

16. Bensebaa, F. and Ellis, T.H., Progress in Surface Science, 1995. **50**(1-4): p. 173-185.

Chapter 7 RAIRS Study of Ethanol Adsorbed on HOPG

7.1 Introduction

Ethanol has been detected in star-forming regions of the interstellar medium [1-3] and is of great interest to astronomers, not least because of its proposed involvement in chemical pathways leading to the formation of large, complex molecules [4, 5].

Abundance estimates relative to H_2 vary from $\approx 10^{-9}$ [2] to $\approx 10^{-6}$ [6], but even the lowest estimates are far in excess of those proposed solely by gas phase formation mechanisms [7, 8]. This leaves grain-surface chemistry as the only viable option to explain the formation of ethanol [4]. The gas phase abundance is then due to heating of the icy mantle which discharges its component molecules during sublimation [2, 9]. Model based predictions of the abundance of solid ethanol within the mantle vary between <1% - 5% relative to water [4, 10, 11].

A number of mechanisms have been proposed to explain the formation of ethanol on the grain surface, including H addition to C_2H_2 followed by oxidation of the resultant vinyl or ethyl radical [4, 12]. Alternatively ethanol could be formed by a number of radical-radical surface reactions between hydroxyl, methyl and methylene radicals [10]. Bernstein et al [13] have shown that ethanol can be produced in ultraviolet and thermally processed samples of mixed interstellar/cometary ice analogues. The ice samples studied contained H_2O, CH_3OH, CO and NH_3 in the ratios 100:50:10:10 respectively. They proposed a mechanism involving the addition of a methyl radical to the carbon of a C=O bond, for instance in formaldehyde, followed by addition of a hydrogen atom to produce ethanol, *Equation 7.1*.

$$CH_3\bullet + CH_2 = O \rightarrow CH_3CH_2O\bullet \xrightarrow{+H\bullet} CH_3CH_2OH \qquad \text{Equation 7.1}$$

In the gas phase, ethanol exists in two different conformations, anti and gauche, which differ in the orientation of the hydroxyl group relative to the methylene group, see *Figure 7.1* [14]. The two conformers have been isolated in microwave spectra of ethanol vapour [15], but there have been some disagreements regarding the relative stabilities of the two conformations. Perchard and Josien [16] stated that the gauche conformer was dominant, but Barnes and Hallam [17] claimed that the proportions were 2:1 in favour of the anti conformer, although this was based on suggestions from previous microwave studies. Dothe et al [18] used a combined experimental and ab-initio method, the scaled quantum mechanical force field method, and found remarkable agreement with the observational work carried out by Perchard and Josien. They determined that the anti and gauche conformers are almost degenerate with an energy difference of only 0.4 kJ mol^{-1} between them. They claim that the gauche conformer predominates, due to the absence in the experimental spectra of some distinct fundamental modes of the anti conformer such as 1150 cm^{-1} and 1430 cm^{-1}.

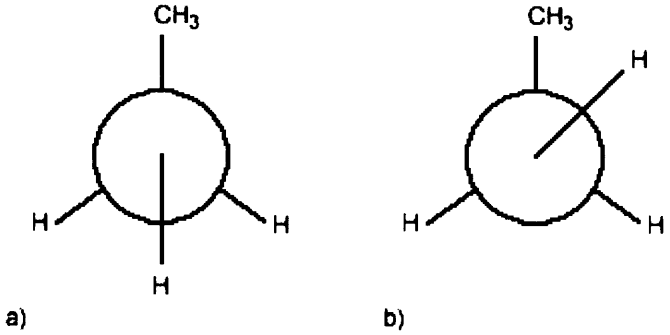

Figure 7.1 Illustration of the two stable conformers of gas phase ethanol, a) anti-CH_3CH_2OH and b) gauche-CH_3CH_2OH.

Anti-ethanol is in the C_s point group, which indicates that it has one symmetry element; the gauche conformation shows no symmetry. Both structures are expected to display 21 infrared active vibrations. The resulting infrared spectra are very complex with many overlapping peaks. Much spectroscopic work has been completed in an attempt to identify the fundamental modes of vibration of ethanol and this has focused on isotopic substitution and conformational analysis in a number of different environments, but still there is clearly some confusion in the assignments. *Table 7.1* shows the observed infra-red band frequencies and associated assignments available in the literature.

Perchard and Josien were one of the first groups to carry out a detailed Raman and infrared spectroscopic study of ethanol and its deuterated isotopomers, which they observed in the gas, liquid and solid phases as well as in solution [16, 19]. They published their work in 1968 and proposed 19 assignments for CH_3CH_2OH, many of which were complicated by coupling between the vibrational modes.

A number of theoreticians have followed up on the work by Perchard and Josien and have simulated the vibrational spectra of ethanol [18, 20]. In all cases they found good agreement with the previous work and confirmed the presence of strong coupling between the modes. Dothe et al suggested that the splitting observed may be due to the existence of the two conformers of ethanol [18].

Barnes and Hallam studied the infrared spectra for ethanol and its deuterated counterpart CH_3CH_2OD suspended in an argon matrix at 20 K and focused on the evidence for the two conformers of ethanol [17]. Publishing in 1970, they proposed different assignments to those of Perchard and Josien. *Table 7.1* shows the bands they observed for ethanol along with their proposed assignments. Their spectra were clearer than those previously recorded, as the colder temperature resulted in smaller line widths. However, overlapping peaks still prevented clear assignment of all the fundamental modes and alternative assignments were possible.

Mikawa et al studied polarized infrared spectra of crystalline ethanol and its deuterated derivatives, grown on a diamond window at high pressure [21]. They proposed a crystalline form for ethanol which was based on long chains of alcohols, with eight molecules in the unit cell, four in each chain. They assigned all of their observed bands on the basis of the proposed structure.

There is only one previous surface study of ethanol with relevance to astrophysical ices. In 1998 Boudin et al reported the infrared spectra of ethanol and a number of other molecules thought to be important constituents of interstellar ice matrices or comets [10]. The molecules were studied in their pure state as well as in water-dominated and CO-dominated ices at temperatures of 10 K. The assignments used were all taken from the work of Mikawa [21] and the acquired spectra were compared to ISO observations.

With the growing interest in small organic molecules as future electrochemical fuels, an increasing number of studies of methanol and ethanol have been completed on surfaces. Most of these studies have been performed on transition metal surfaces such as Pd [22], Pt [23-27] and Cu [28] because of their relevance to catalysis, but additional studies have also been performed on semiconductor surfaces [29, 30].

It is generally accepted that ethanol adsorbs molecularly on the Pt(111) surface and that thermal processing causes a proportion of the monolayer to dissociate into a series of products including CO, H and C [24]. The extent of this dissociation is disputed. Lee et al performed a fast XPS study and claim that 34% of the monolayer dissociates [26] and Sexton et al [24], who performed a series of TPD studies on the C_1-C_4 alcohols adsorbed on Pt(111), quote a desorption proportion of less than 10%.

Camplin and McCash performed RAIRS studies of adsorbed ethanol, predominantly concerning themselves with the ethoxy species adsorbed on oxidized Cu(100) [28]. In addition to the ethoxy studies, they also presented spectra of physisorbed ethanol ice and its deuterated counterparts. They found good agreement with earlier vitreous and matrix isolation studies and based their assignments (repeated in *Table 7.1*) on the work of Perchard and Josien [16] and also that of Barnes and Hallam [17].

Eng et al performed a RAIRS study of ethanol adsorbed on Si(100) wafers for its relevance in the generation of microelectronic devices [29]. They found that ethanol adsorbs dissociatively and reported infrared bands for the ethoxy monolayer as well as for multilayers of molecular ethanol on the Si(100) surface. They chose to assign the multilayer features by comparison with the works of Perchard and Josien [16, 19], making slight adjustments to the coupling involved in certain bands following their own ab-initio studies.

Silvestrelli [30] performed a first principles study of the adsorption of ethanol on the Si(100) surface. He found that the ethanol molecule initially physisorbs on the silicon surface by the formation of a barrierless dative bond between the O atom and a “down” Si atom. From this state he found that the cleavage of the O-H bond was kinetically favoured.

Souda [31] performed a temperature programmed time of flight secondary ion mass spectroscopic study of ethanol and heavy-water films deposited on a Ni(111) substrate at 15 K. He reported the heat induced mixing of ethanol and water that begins at around 120 K as the morphology of the ethanol changes, and which is complete by 140 K.

Mixed ethanol and water ices clearly have important implications for astronomy. This chapter presents a RAIRS study of pure ethanol, ethanol deposited onto pre-existing layers of amorphous solid water and of ethanol codeposited with water. In each case the underlying substrate is highly oriented pyrolytic graphite, HOPG.

Table 7.1 Observed infrared vibrational bands and band assignments for ethanol, where υ = stretch, δ = deformation, δ$_s$ = symmetric deformation, δ$_a$ = asymmetric deformation, τ = twist, ρ = rocking and ω = wagging mode.

Perchard Vitreous 80 K [16]		**Mikawa et al liquid [21]**		**Barnes & Hallam Ar matrix (Anti rotamer) [17]**		**Camplin, McCash oxidised Cu(100) [28]**		**Eng et al Multilayer on Si(100) [29]**		**Boudin CsI Solid [10]**		**Coussan, Boutellier, Perchard, Zheng DFT calc [20]**		**Coussan, Boutellier, Perchard, Zheng Ar matrix (Anti rotamer) [20]**	
Assignment	**σ/cm^{-1}**	**Assignment**	**σ/cm^{-1}**	**Assignment**	**σ/cm^{-1}**	**Assignment**	**σ/cm^{-1}**	**Assignment**	**σ/cm^{-1}**	**Boudin CsI Solid**	**σ/cm^{-1}**	**Assignment**	**σ/cm^{-1}**	**Assignment**	**σ/cm^{-1}**
ρ(CH$_2$) + ρ(CH$_3$)	805	ρ(CH$_2$)	802	ρ(CH$_2$)	812	ρ(CH$_2$) + ρ(CH$_3$)	805			ρ(CH$_2$)	804	ρ(CH$_2$) + ρ(CH$_3$)	822	ρ(CH$_2$) + ρ(CH$_3$)	812
υs(CCO)	881 886	υ(CC)	880	υs(CCO)	886	υs(CCO)	882	υs(CCO)	891	υ(CC)	879	υ(CCO)	895	υ(CCO)	888
υa(CCO)	1051	υ(CO)	1050	ρ(CH$_3$)	1025 1083	ρ(CH$_3$) + δ(OH)	1058	υa(CCO)	1061	υ(CO)	1049	υ(CCO) + ρ(CH$_3$)	1030	υ(CCO) + ρ(CH$_3$)	1025 1016
υ(CO) + ρ(CH$_3$) + δ(COH)	1091	ρ(CH$_3$)	1089	υa(CCO)	1092	υa(CCO)	1097	υ(CO) + ρ(CH$_3$) + δ(OH)	1099	ρ(CH$_3$)	1089	υ(CCO) + ρ(CH$_3$)	1095	υ(CCO) + ρ(CH$_3$)	1092 1084 1077
ρ(CH$_3$)	1128	ρ'(CH$_3$)	1149							ρ'(CH$_3$)	1156	ρ(CH$_2$) + ρ(CH$_3$)	1178	ρ(CH$_2$) + ρ(CH$_3$)	1161
				δ(OH)	1240							δ(OH)	1271	δ(OH)	1240
τ(CH2) + δ(OH)	1277	τ(CH$_2$)	1273	τ(CH$_2$)	1250	τ(CH2) + δ(OH)	1277			τ(CH$_2$)	1275				
δ(COH) + ω(CH$_2$)	1331	δ(OH)	1328			δ(OH) + ω(CH$_2$)	1341	ω(CH$_2$)	1335	δ(OH)	1329				
δs(CH$_3$)	1381	δs(CH$_3$)	1381	δs(CH$_3$)	1371	δs(CH$_3$)	1382	δs(CH$_3$) + ω(CH$_2$)	1385	δs(CH$_3$)	1381	δs(CH$_3$)	1410	δs(CH$_3$)	1372
		ω(CH$_2$)	1422	ω(CH$_2$)	1415					ω(CH$_2$)	1424	ω(CH$_2$)	1451	ω(CH$_2$)	1416
δa(CH$_3$)	1410- 1480	δa(CH$_3$)	1450	δa(CH$_3$)	1445 1463	δa(CH$_3$)	1457	δa(CH$_3$) + δs(CH$_2$)	1481	δa(CH$_3$)	1454	δa(CH$_3$)	1488 1505	δa(CH$_3$)	1445 1463
										δ'a(CH$_3$)	1477				
		δs(CH$_2$)	1481	δs(CH$_2$)	1490					δs(CH$_2$)	1487	δs(CH$_2$)	1530	δs(CH$_2$)	1487
υs(CH$_2$)	2873 2894	υs(CH$_2$)	2880	υs(CH$_2$)	2900 2953	υs(CH$_2$)	2874	υs(CH$_2$)	2881	υs(CH$_2$)	2884	υs(CH$_2$)	2991	υs(CH$_2$)	2899
												υa(CH$_2$)	3016	υa(CH$_2$)	2917 2913
υs(CH$_3$)	2928	υs(CH$_3$)	2920	υs(CH$_3$)	2939	υs(CH$_3$)	2927	υs(CH$_3$)	2928	υs(CH$_3$)	2930	υs(CH$_3$)	3042	υs(CH$_3$)	2939
		υa(CH$_2$)	2940												
υs'(CH$_3$)	2970	υa(CH$_3$)	2975	υa(CH$_3$)	2995 2985	υa(CH$_3$)	2974	υa(CH$_3$)	2983	υa(CH$_3$)	2971	υa(CH$_3$)	3104 3111	υa(CH$_3$)	2984 2995 2992
		υ(OH)	3336	υ(OH)	3658			υ(OH)	3267	υ(OH)	3291	υ(OH)	3848	υ(OH)	3661 3656

7.2 Methodology

Experiments were performed in the ultra-high vacuum (UHV) chamber, described previously in Chapter 2. The chamber has a base pressure of 2×10^{-10} mbar. The HOPG sample has been described previously [32] along with the "scotch tape" method of cleaning.

The ices were grown in situ by exposing the cold HOPG surface, held at ≈ 98 K, to a stream of gas by back filling the chamber through a high precision leak valve. The mixed ices were produced by exposing the HOPG surface to the vapour from a pre-mixed water and ethanol solution. The exposures were measured in Langmuir (L), where 1 L = 10^{-6} mbar s, and were recorded during dosing by the mass spectrometer to enable the relative sensitivities, and an accurate measure of the relative exposure of each species, to be determined. The chemicals used during the experiments were distilled, de-ionised water and ethanol (CH_3CH_2OH, 99.7-100% - AnalaR – BDH).

All RAIR spectra were recorded using a Mattson instruments Fourier transform infrared spectrometer coupled to a mercury cadmium telluride detector. The spectra were recorded with a resolution of 4 cm^{-1} following 256 scans. During the annealing and desorption sequence, the sample was held at the set temperature for 3 minutes and then cooled down to base temperature before performing the scan. Between experiments the sample was annealed to 500 K and held for 3 minutes to remove all contaminants from the surface.

7.3 RAIRS Results and Discussion

7.3.1 Pure Ethanol

7.3.1.1 Adsorption

RAIR spectra following adsorption of ethanol on the bare HOPG surface held at 98 K are shown in *Figure 7.2.* At the lowest 5 L exposure of ethanol, four peaks can be distinguished in the low frequency region at 1380 cm^{-1}, 1095 cm^{-1}, 1057 cm^{-1} and 887 cm^{-1}. The most intense of these are the peaks at 1057 cm^{-1} and 1095 cm^{-1}.

Increasing the exposure of ethanol to 10 L results in the appearance of several further spectral bands. Additional bands that are seen are a broad feature at 3280 cm^{-1}, a sharp peak at 2970 cm^{-1} and a low intensity peak at 2875 cm^{-1}. Higher exposures of ethanol, up to 300 L, lead to the appearance of additional low intensity bands across the spectral region. There is a broad feature centred at ≈ 2896 cm^{-1} that appears to comprise 3 distinct peaks at 2927 cm^{-1}, 2896 cm^{-1} and 2875 cm^{-1}. By 100 L it is also clear that the early peak recorded at 1380 cm^{-1} is now centred on a broad feature with additional peaks or shoulders at 1465 cm^{-1} and 1334 cm^{-1}.

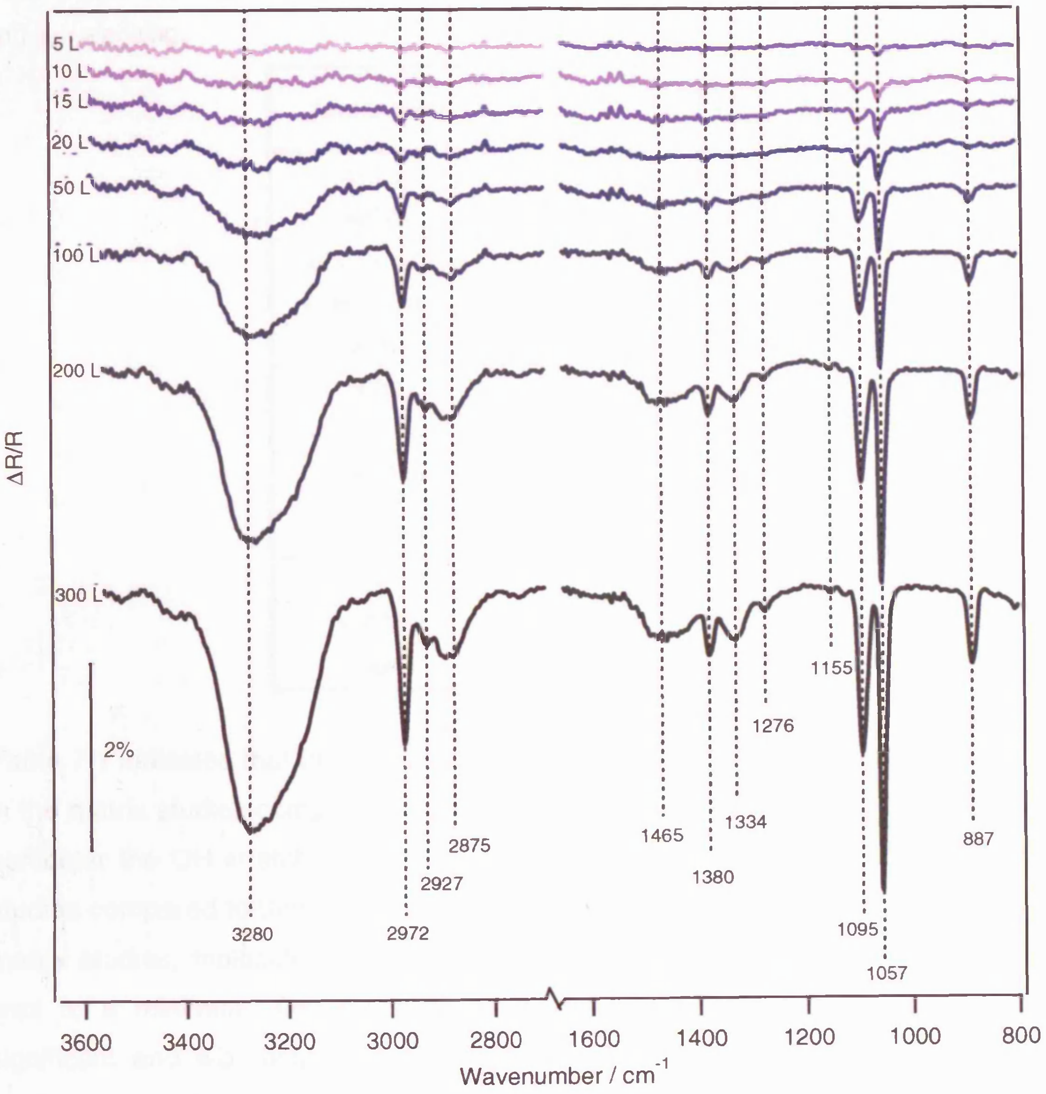

Figure 7.2 RAIR spectra recorded over the wavenumber range from 3600 to 800 cm^{-1}, showing the full adsorption sequence for increasing exposures of pure ethanol adsorbed on HOPG at 98 K. The region between 1700 and 2700 cm^{-1} has been excluded for clarity.

Table 7.2 shows all of the bands recorded in the pure ethanol spectra along with the exposure at which they were first recorded and the proposed assignments. These assignments are also illustrated in *Figure 7.3*. The assignments have been made by comparison with those previously reported [10, 16, 17, 19-21, 28, 29] and are based on both experimental work and ab-initio studies. Most of the assignments made in this study are consistent with those of previous researchers, but in the case of the bands at 1057, 1095, 1328 and 3280 cm^{-1} there has been more uncertainty.

Table 7.2 Infrared vibrational bands and assignments for ethanol adsorbed on a HOPG surface at 98 K, along with the exposure at which each band is first noted. Where υ = stretch, δ = deformation, δ_s = symmetric deformation, δ_a = asymmetric deformation, τ = twist, ρ = rocking and ω = wagging.

Assignment	σ/cm^{-1}	Exposure Threshold
υs(CCO)	889	5 L
υa(CCO)	1057	5 L
υ(CO) + ρ(CH_3)	1095	5 L
ρ(CH_2) + ρ(CH_3)	1155	300 L
τ(CH_2)	1276	50 L
δ(OH)	1328	50 L
δs(CH_3)	1380	5 L
δa(CH_3)	1465	20 L
υs(CH_2)	2896 2875	5 L
υs(CH_3)	2927	15 L
υa(CH_3)	2972	5 L
υ(OH)	3280	10 L

Table 7.1 indicates that there are some clear differences in the peak positions shown in the matrix studies compared to the work on surfaces [10, 16, 20, 21, 28, 29, 33]. In particular the OH stretch is seen at considerably higher frequencies in argon matrix studies compared to those recorded for multilayers on either metal or CsI surfaces. In matrix studies, molecules are kept far apart and so inter-molecular interactions are kept to a minimum. On the surface intermolecular hydrogen bonds will become significant and will result in a broadening of the OH band and a downshifting in frequency. The feature at 3280 cm^{-1} has been assigned to the υ(OH) stretch and is in very good agreement with the values recorded by both Eng et al [29] on an Si(100) surface and by Boudin et al [10] on a CsI surface. Camplin and McCash also recorded this peak but then disregarded it as detector ice contaminant [28].

The bands at 1057, 1095 and 1328 cm^{-1} have been assigned by comparison to the work of Eng et al [29]. This work was chosen for its surface relevance and the very close agreement achieved with band frequencies. Eng et al performed a very convincing study which improved upon the work of Perchard and Josien by undertaking ab-inito studies. The proposed assignments for the work described here are illustrated in *Figure 7.3*, although it is important to bear in mind that alternative interpretations are possible.

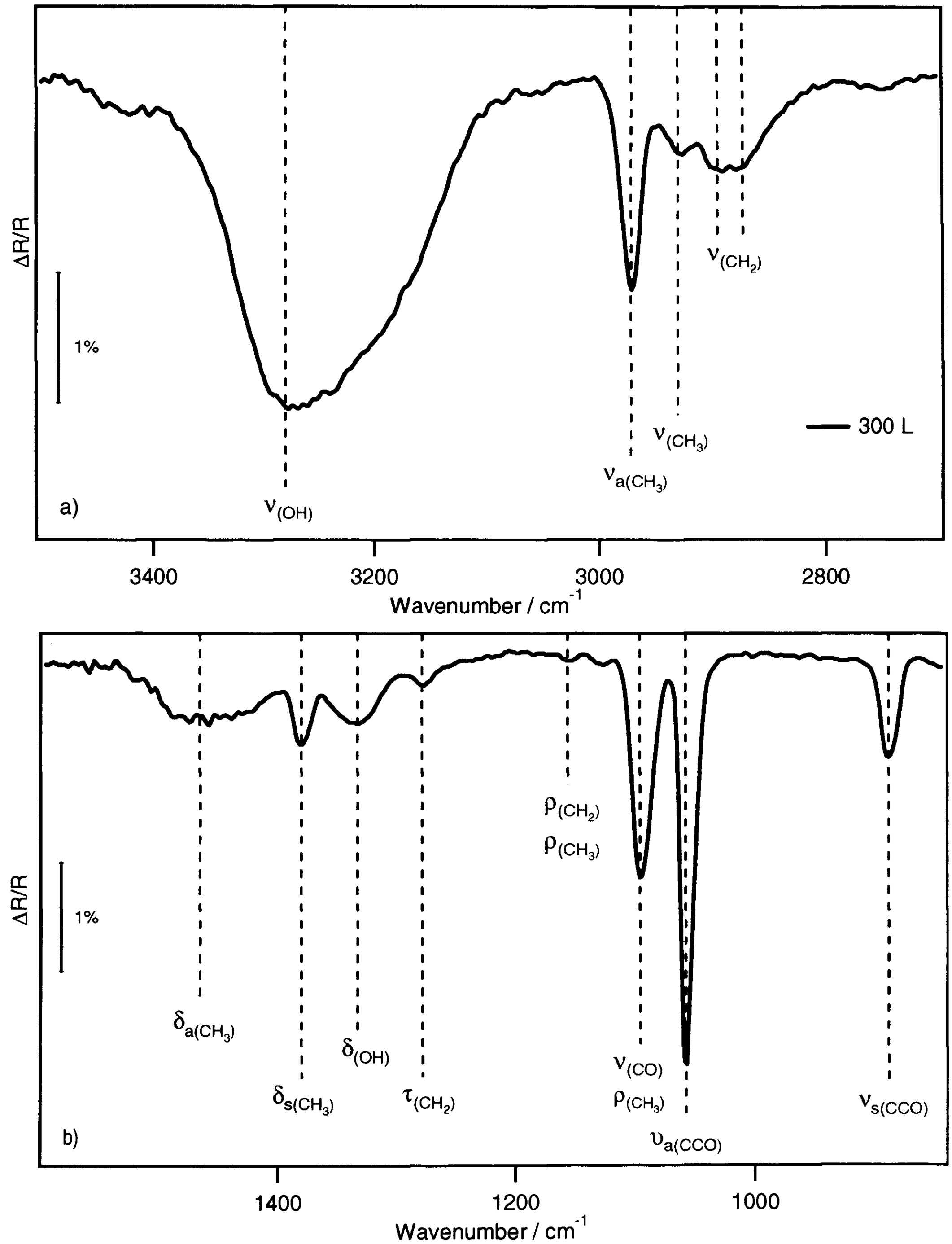

Figure 7.3 Illustration showing the proposed assignments for the vibrational bands observed following the exposure of 300 L of ethanol on to a HOPG surface at 98 K. The high frequency region from 3450-2750 cm^{-1} is shown in a) and the low frequency section from 1500-900 cm^{-1} is shown in b).

During adsorption, increasing the exposure of ethanol results in an increase in intensity of all bands. None appear to saturate, which is indicative of the formation of physisorbed multilayers. In addition to this, there is no change in the frequency of the observed bands with increasing exposure. This indicates that the ethanol is physisorbed on the HOPG surface, even at the lowest coverages. *Figure 7.4* shows the variation of the integrated peak area as the ethanol exposure increases, for the four most intense peaks in the ethanol spectrum. The ethanol exposures have been normalised by integrating each dose area and plotting on a relative scale. All of the bands in *Figure 7.4* increase rapidly in area as the exposure is increased to 20 L. Beyond this exposure the area increase is less rapid, but is still positively linear.

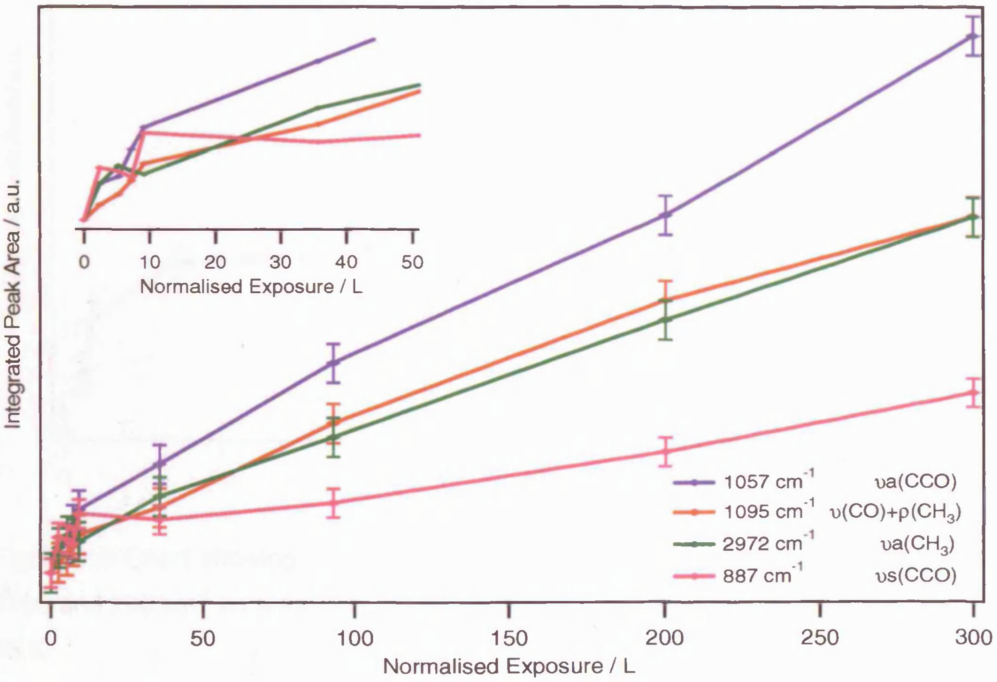

Figure 7.4 Chart showing the integrated peak area for the bands at 887 cm^{-1}, 1057 cm^{-1}, 1095 cm^{-1} and 2972 cm^{-1} as a function of increasing ethanol exposure on the pure HOPG sample at 98 K. The inset focuses on the low exposure region between 0 and 50 L.

Figure 7.5 shows a similar chart for the entire region of the ethanol spectrum between 3700 and 700 cm^{-1} as a function of increasing exposure. It shows the same rapid rise in peak area up to 20 L with a decline in the gradient beyond 20 L. Both *Figure 7.4* and *Figure 7.5* show that there is not a simple linear relationship between the peak areas and the ethanol exposure. A linear uptake chart would typically suggest that the sticking probability remains constant as the exposure increases. In this case, where the gradient of the uptake curve is not constant across the entire exposure region, it could indicate a preferential adsorption of ethanol on the HOPG surface compared to adsorption on existing layers of ethanol. Alternatively, it may indicate that the ethanol molecules are altering their orientation as the exposure increases. Molecules with prominent vertical dipole components will show more intense peaks than randomly oriented molecules. It is possible that the first layers of ethanol show some tendency to order while the multilayers beyond 20 L are in more disarray. It is not expected that a physisorbed molecule will order on the surface, but perhaps at the surface temperature of 98 K the molecules are sufficiently thermalised to assemble in a way that encourages intermolecular bonding.

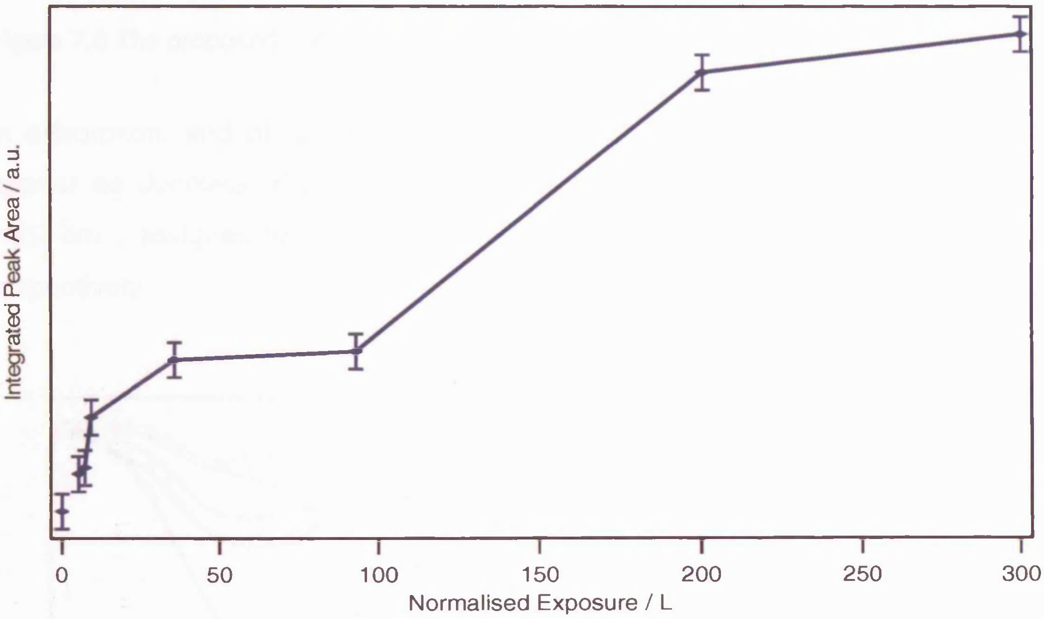

Figure 7.5 Chart showing the integrated peak area for the entire ethanol spectrum between 3700 and 700 cm^{-1} as a function of increasing ethanol exposure on the pure HOPG sample at 98 K.

The observation of vibrational modes for species adsorbed on metal surfaces and indeed graphitic surfaces [34], are subject to the surface dipole selection rule, often termed the metal surface selection rule. This states that only those vibrational modes which give rise to an oscillating dipole with a component perpendicular to the surface will be IR active [35]. This rule can provide information on the orientation of the adsorbate on the surface.

As the most prominent bands to appear at low exposures of ethanol are due to the υ_s(CCO), υ_a(CCO), υ(CO) + ρ(CH_3) and υ_s(CH_2) vibrations, it is possible that the favoured orientation of ethanol on graphite is with the CH_3 group facing down to form a tripod on the surface, see *Figure 7.6*. The exact orientation of the CO group would depend on the conformer present (vertical for anti-ethanol). This orientation would increase the opportunity for hydrogen bonding as the OH group would not be obscured by the surface.

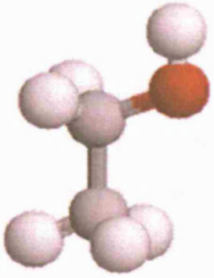

Figure 7.6 The proposed orientation of ethanol adsorbed on a HOPG surface at 98 K.

In adsorption, and at low exposures of ethanol, a number of the assigned bands appear as doublets. *Figure 7.7* shows a close up of the bands at 1095 cm^{-1} and 1057 cm^{-1}, assigned to the $\upsilon(CO)$ + $\rho(CH_3)$ and $\upsilon_a(CCO)$ ethanol vibrational modes respectively.

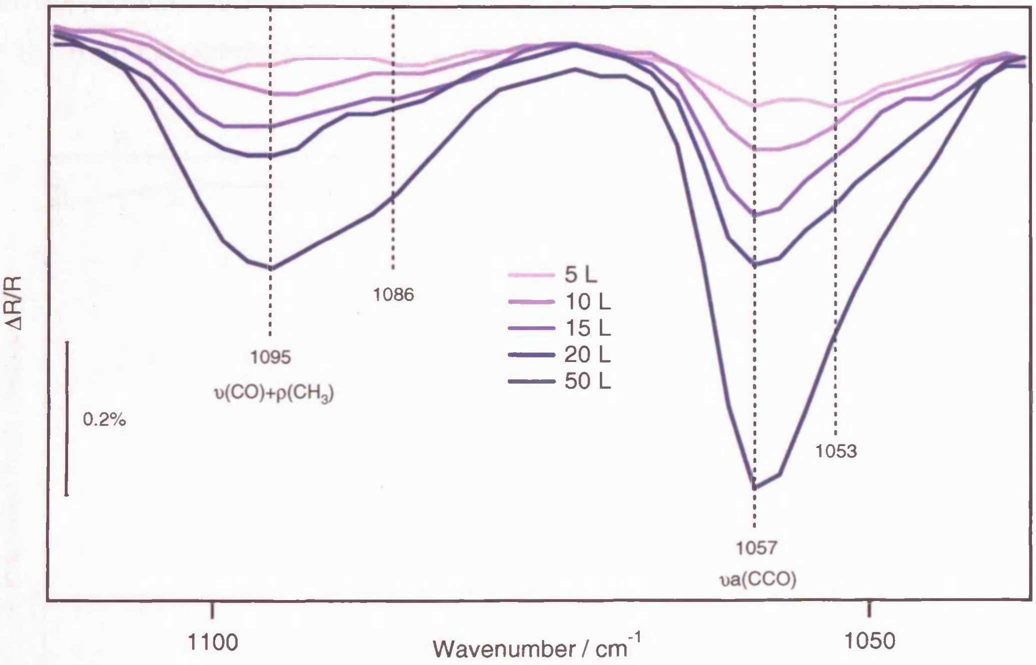

Figure 7.7 The 1140-1040 cm^{-1} RAIR spectrum showing the adsorption sequence for increasing exposures of pure ethanol adsorbed on HOPG at 98 K.

This splitting could be indicative of the ethanol molecules adsorbing in distinct surface environments, but some researchers believe that the doublets are due to contributions from the two separate conformers [20]. Coussan et al recorded highly resolved spectra from matrix studies of ethanol and suggested a possible spectroscopic fingerprint for the two conformers in the region between 1100 and 1000 cm^{-1} [20]. They recorded two doublets in the region around 1030 and 1090 cm^{-1} for the anti conformer and at 1070 and 1060 cm^{-1} for the gauche ethanol. This current study does not fit either of their fingerprints. This may be due to the difference between matrix and surface studies or alternatively may suggest that the conformers are not an important consideration. It is also possible that the splitting is evidence for different neighbouring interactions between ethanol molecules. Redshifts would be expected for vibrations in ethanol molecules that are involved in hydrogen bonded networks, when compared to isolated or disordered ethanol molecules.

7.3.1.2 Annealing the Pure Ethanol Ice

The desorption behavior of pure ethanol from the HOPG surface was studied by annealing the sample to increasing temperatures. Ices formed by exposing the HOPG sample to 300 L, 100 L and 50 L of ethanol were studied in turn. *Figure 7.8* shows the integrated area of the 300 L ethanol spectrum recorded between 3700 and 700 cm^{-1} after the sample has been annealed to increasing temperatures. Above 120 K there is an appreciable decrease in the spectral area. Desorption reaches a maximum at ≈ 127 K and is complete by ≈160 K.

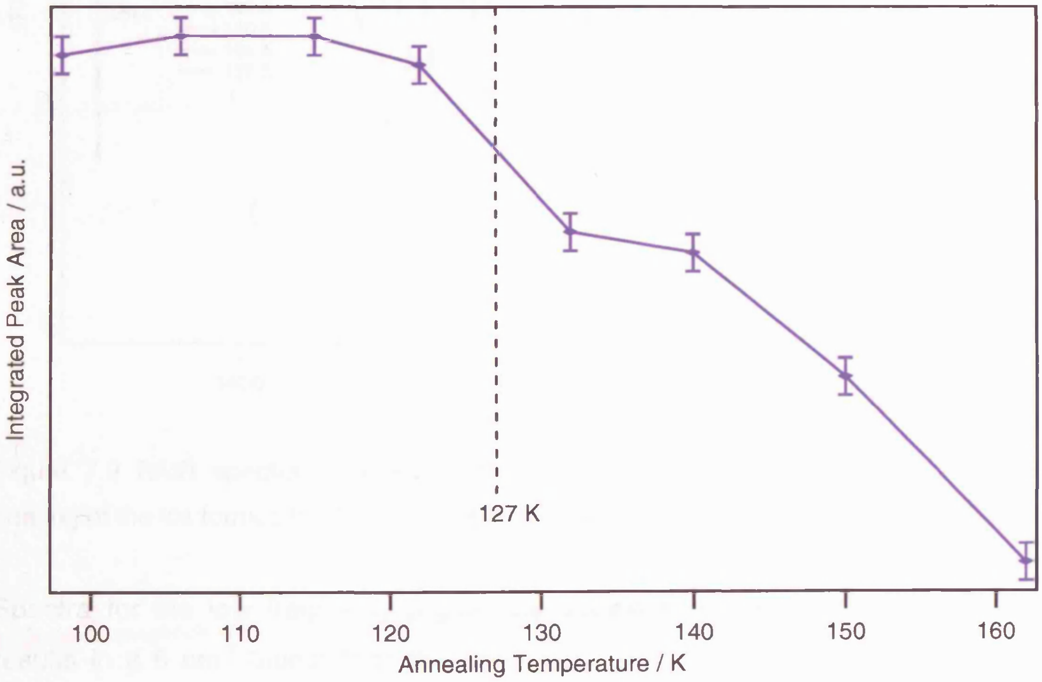

Figure 7.8 Chart showing the integrated peak area for the entire ethanol spectrum between 3700 and 700 cm^{-1} as a function of annealing temperature.

peak appearing at 1047 cm^{-1}. The υ_s(CCO) feature also splits immediately upon heating with peaks appearing at 893 and 883 cm^{-1}.

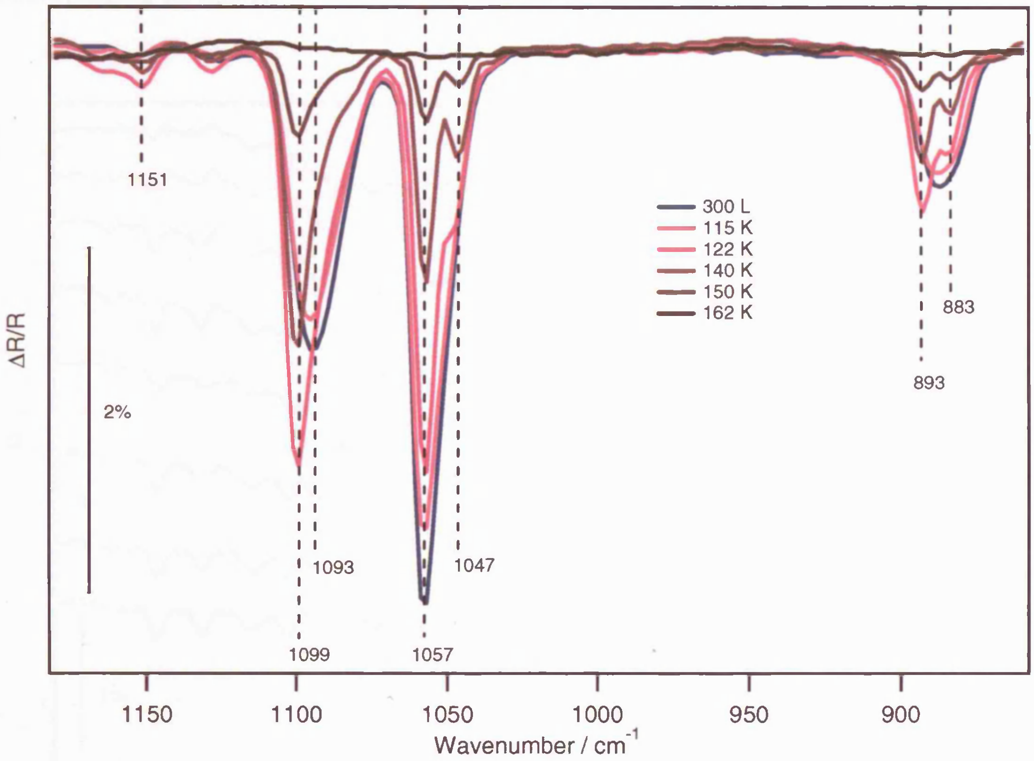

Figure 7.10 RAIR spectra recorded between 1180 and 850 cm^{-1} showing the sequential heating of the ice formed by depositing 300 L of ethanol on a HOPG surface at 98 K.

An expansion of the spectra from the mid frequency region is shown in *Figure 7.11*. In this region there is a very broad feature between 1510 and 1280 cm^{-1}, which comprises a central peak at 1380 cm^{-1}, and is assigned to the symmetric deformation of the methyl group. There is also a high frequency shoulder around 1380 cm^{-1}, which is assigned to the symmetric deformation of the methyl group and a low frequency shoulder at 1328 cm^{-1}, due to the deformation of the OH group.

On heating, the symmetric methyl deformation peak at 1379 cm^{-1} begins to decrease in intensity. By 122 K, its peak area has dropped by more than 50% and a new feature at 1358 cm^{-1} appears. This new feature increases in intensity as the sample is heated to 132 K but then begins to decline by 140 K.

The shoulder at 1328 cm^{-1}, attributed to the deformation of the OH group, shows a slight redshift as it is heated to 122 K and sharpens to a definite peak which is centred at 1325 cm^{-1}. A similar response to heating is shown by the shoulder attributed to the symmetric deformation of the methyl group; this also sharpens into a definite peak by 122 K but the frequency increases to 1479 cm^{-1}. The intensity also starts to decrease by 140 K. None of the spectral features in this region remain after the sample has been heated to 150 K.

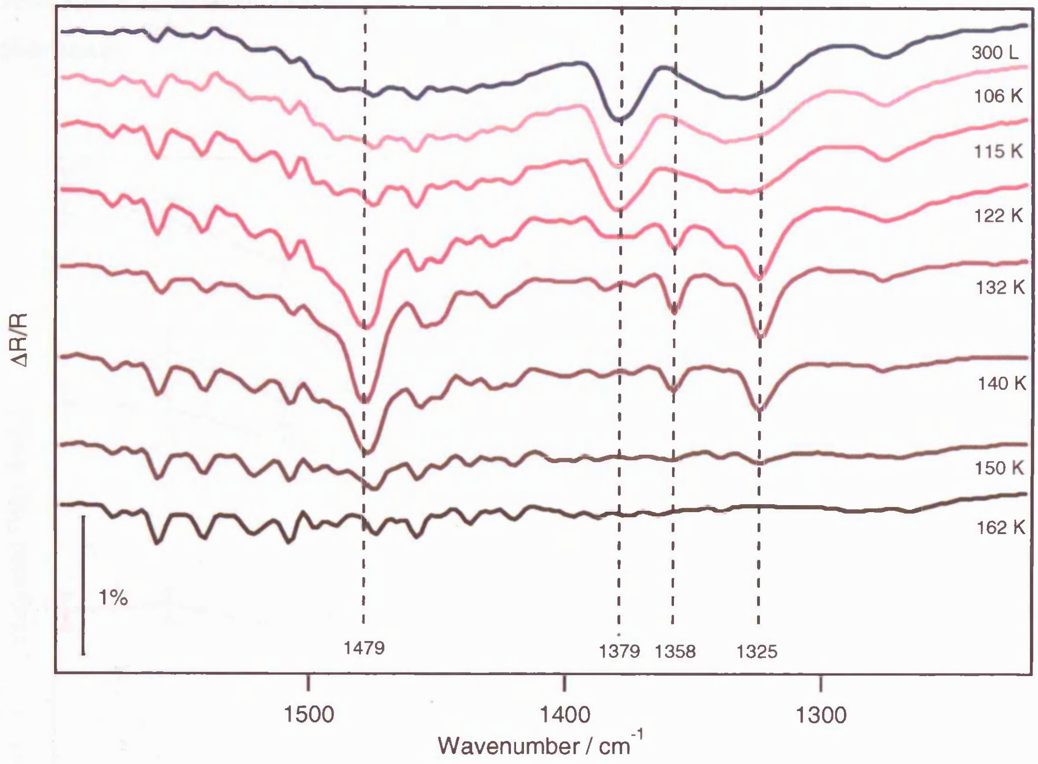

Figure 7.11 RAIR spectra recorded between 1600 and 1200 cm^{-1} showing the sequential heating of the ice formed by depositing 300 L of ethanol on a HOPG surface at 98 K.

Considering the entire spectral region, it is clear that beyond 140 K all of the peaks have started to decrease in intensity, indicating that ethanol is desorbing, with only the features at 3238, 2970, 2877, 1099, 1057 and 893 cm^{-1} still apparent at 150 K. By 162 K the spectra is clear and ethanol desorption is complete.

Figure 7.12 shows the variation in integrated peak areas for the 5 most dominant bands in the ethanol spectra, as a function of increased annealing temperature. The area of the υ_s(CCO) feature at 893 cm^{-1} remains fairly constant until 132 K where it begins to decrease rapidly and is completely desorbed by 160 K. The υ(OH) feature at 3282 cm^{-1} shows a gradual decline as the sample is heated to 132 K, and then it also drops very rapidly, with complete desorption by 160 K.

The peak at 1057 cm^{-1} assigned to υ_a(CCO), drops rapidly from 112 K then seems to stabilise between 120 K and 132 K, after which it begins to drop rapidly again. The remaining two features at 1099 cm^{-1} and 2970 cm^{-1} which are assigned respectively to υ(CO) + ρ(CH_3) and υ_a(CH_3), show an intensity inversion with the band at 1057 cm^{-1}. Between 115 K and 122 K the intensity of both bands increases before stabilising between 122 K and 132 K then, as with the 1057 cm^{-1} feature, the intensities rapidly decrease.

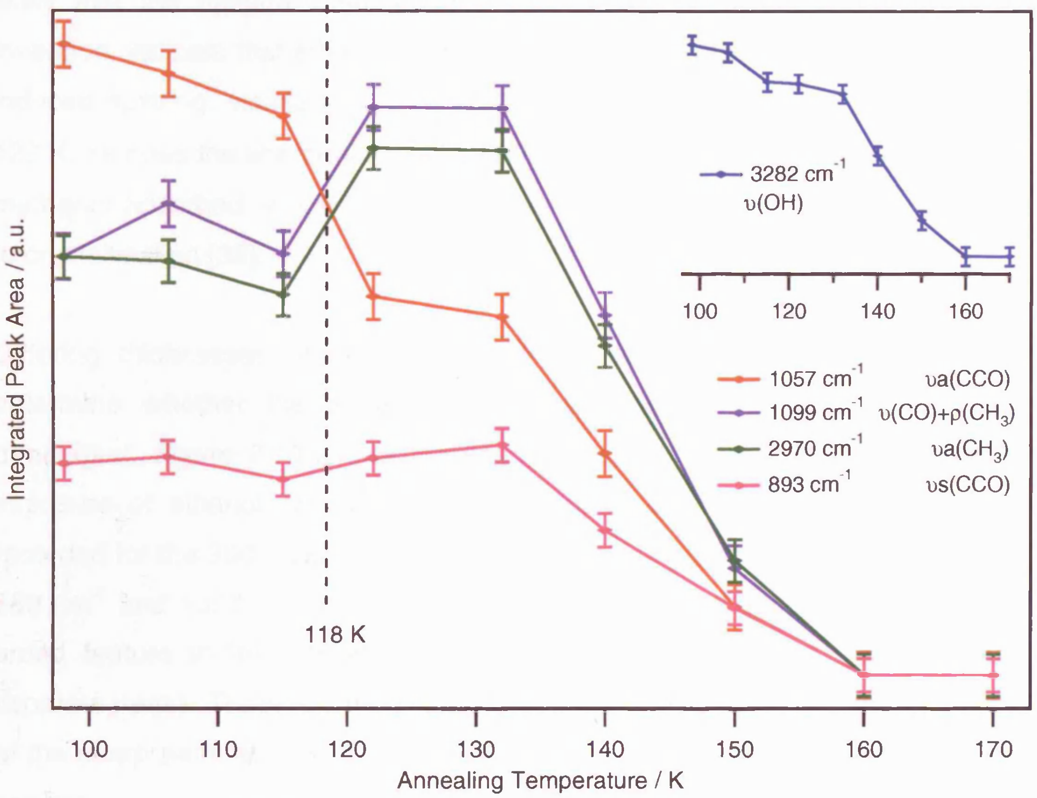

Figure 7.12 Chart showing the integrated peak area for selected bands in the ethanol spectrum as a function of annealing temperature. In the main chart υs(CCO), υa(CCO), υ(CO) + ρ(CH_3) and the υa(CH_3) bands are displayed. The inset shows the integrated area for the 3282 cm^{-1}, or υ(OH), vibration, which is displayed on a larger scale.

The intensity inversion which appears to occur at ≈ 118 K must represent a reordering of the ethanol molecule. Coussan et al [20] have noted a similar intensity inversion with ethanol in a N_2 matrix as it is heated from 8 K to 30 K, which they attributed to a thermally induced interconversion from the anti to gauche conformer. Although annealing the sample in this study has resulted in the splitting of many of the bands into doublets, neither of the characteristic fingerprints for anti and gauche conformers that Coussan et al described have been observed. It is more likely that the reordering is an indication of the glass transition, where ethanol becomes a viscous liquid.

Calorimetric studies by Sugisaki [36] have shown this to occur at 97 K, but Souda [31] found that the morphological changes in ethanol occur at the higher temperature of 120 K.

Heating amorphous solids above their glass transition temperature has been shown to induce crystallisation in water [37, 38], methanol and ethanol ices [39]. Ayotte reported IR spectra of the crystalline transition of amorphous ethanol as it was held at 135 K and described a characteristic sharpening in the υ(OH) band [39]. It seems likely that the spectral changes that are noticed here, in particular the intensity inversion, indicate that ethanol also undergoes crystallisation around 118 K. The heat induced splitting, visible in *Figure 7.9* and *Figure 7.10*, occurs between 115 K and 122 K, as does the sharpening of the υ(OH) band. Similar band splitting was noted for methanol adsorbed on a HOPG surface as it was heated and this was also attributed to crystallisation [32].

Differing thicknesses of ethanol ice on the HOPG sample were also studied to determine whether the annealing features described previously were coverage dependant. *Figure 7.13* shows the spectra resulting from the annealing of a 100 L exposure of ethanol on HOPG. The resolution is not as clear as in the spectra recorded for the 300 L exposure, but all the same features are apparent. The peaks at 889 cm^{-1} and 1057 cm^{-1} both split. The 1095 cm^{-1} peak shifts up to 1099 cm^{-1}. The broad feature in the OH stretching region around 3280 cm^{-1} resolves into three separate peaks. There is a high frequency, low intensity peak at 3282 cm^{-1}, in addition to the sharp peak at 3234 cm^{-1} and the shoulder at 3182 cm^{-1} recorded in the 300 L spectra.

The low frequency spectra following the annealing of 50 L of ethanol are shown in *Figure 7.14*. The resolution is much poorer than for the previous spectra, but there is still evidence for the splitting of the bands at 889 cm^{-1} and 1057 cm^{-1}. The low frequency region is not well defined and shows only a gradual decrease in intensity without the clear splitting shown at higher exposures.

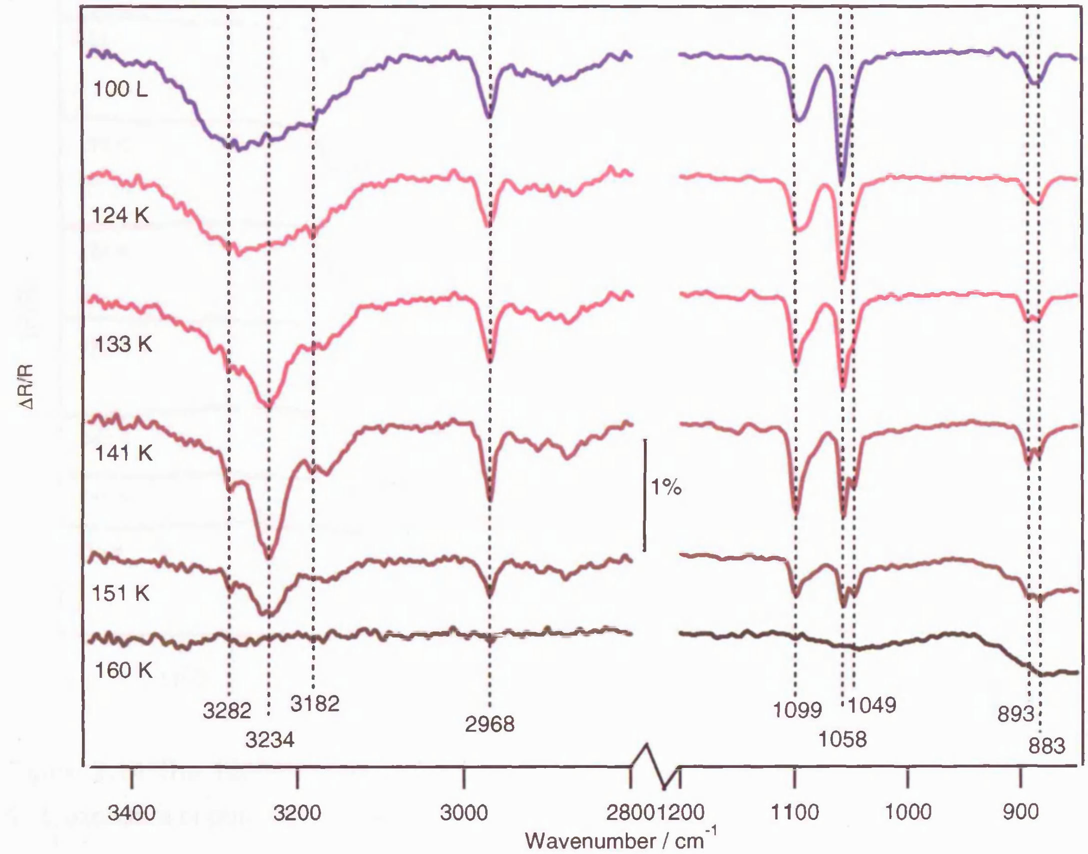

Figure 7.13 RAIR spectra recorded over the range from 3400-850 cm^{-1} showing the desorption of a 100 L exposure of pure ethanol deposited on HOPG at 98 K. The region between 1200 and 2800 cm^{-1} has been excluded for clarity.

Splitting of the υa(CCO) vibrational band at 1058 cm^{-1} is observed in both the 50 L and 300 L systems. The onset of splitting seems to occur approximately 10 K earlier on the thicker ice than on the thinner ethanol layer, although this could be an issue of spectral resolution rather than a physical difference in the ice. In conclusion, it appears that ethanol adsorbed on the HOPG surface crystallises on heating to ≈ 118 K and that this crystallisation is not coverage dependent, at least for ethanol exposures ≥ 50 L. The ethanol has completely desorbed from the HOPG surface at around 160 K.

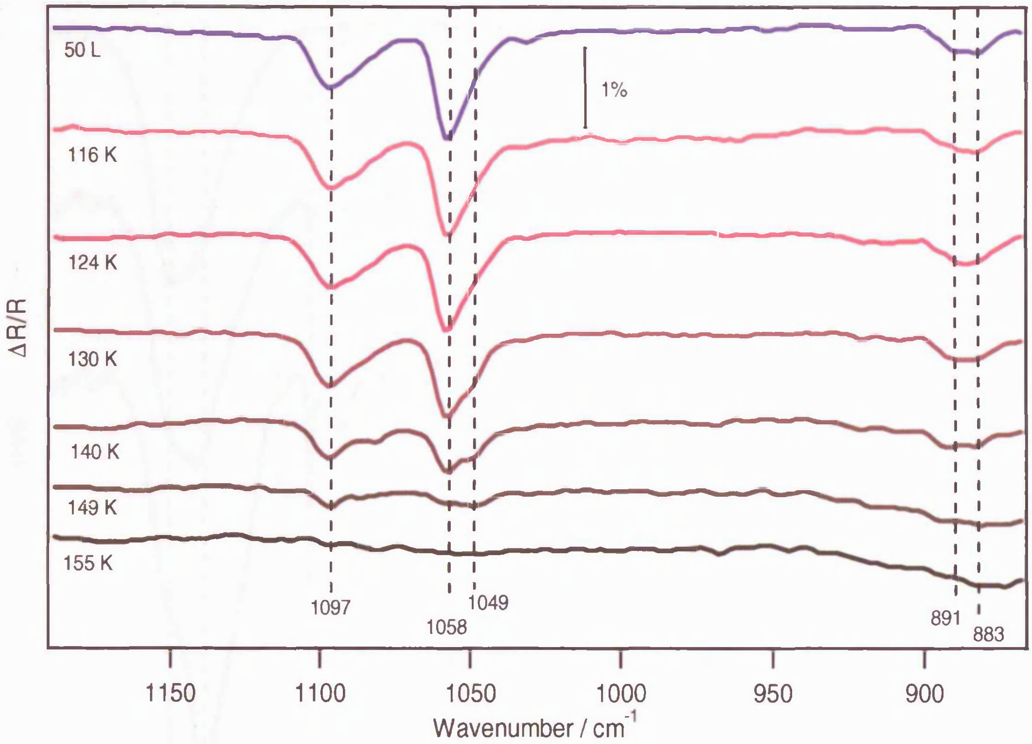

Figure 7.14 The 1200-850 cm^{-1} RAIR spectrum showing the full desorption sequence for a 50 L exposure of pure ethanol deposited on HOPG at 98 K.

7.3.2 Ethanol Sequentially Deposited on Water

In this series of experiments, layered ethanol and water ice systems were studied. These were formed by exposing an existing film of amorphous water ice, deposited at 98 K, to increasing doses of ethanol. In the earlier study of methanol adsorption on a pre-existing layer of water ice, three separate thicknesses of water ice were considered, but the resolution of the spectra was poor in all but the 50 L system. For this reason, in the ethanol studies only a single thickness of water ice was considered, equivalent to a 50 L exposure. The resulting layered ice structure will be described by the following notation: CH_3CH_2OH/H_2O(50 L) as described in Chapter 3.

7.3.2.1 Adsorption of Ethanol on Water

Figure 7.15 shows RAIR spectra of the CH_3CH_2OH/H_2O(50 L) system following increasing exposures of ethanol on the 50 L exposure of water. The initial pure water trace is shown to demonstrate the transition from water dominated spectra through to ethanol dominated spectra. The water features have been discussed in Chapter 3. The broad feature around 3396 cm^{-1} is the OH stretch and the peak at 1677 cm^{-1} is the HOH scissors mode of the pure water layer.

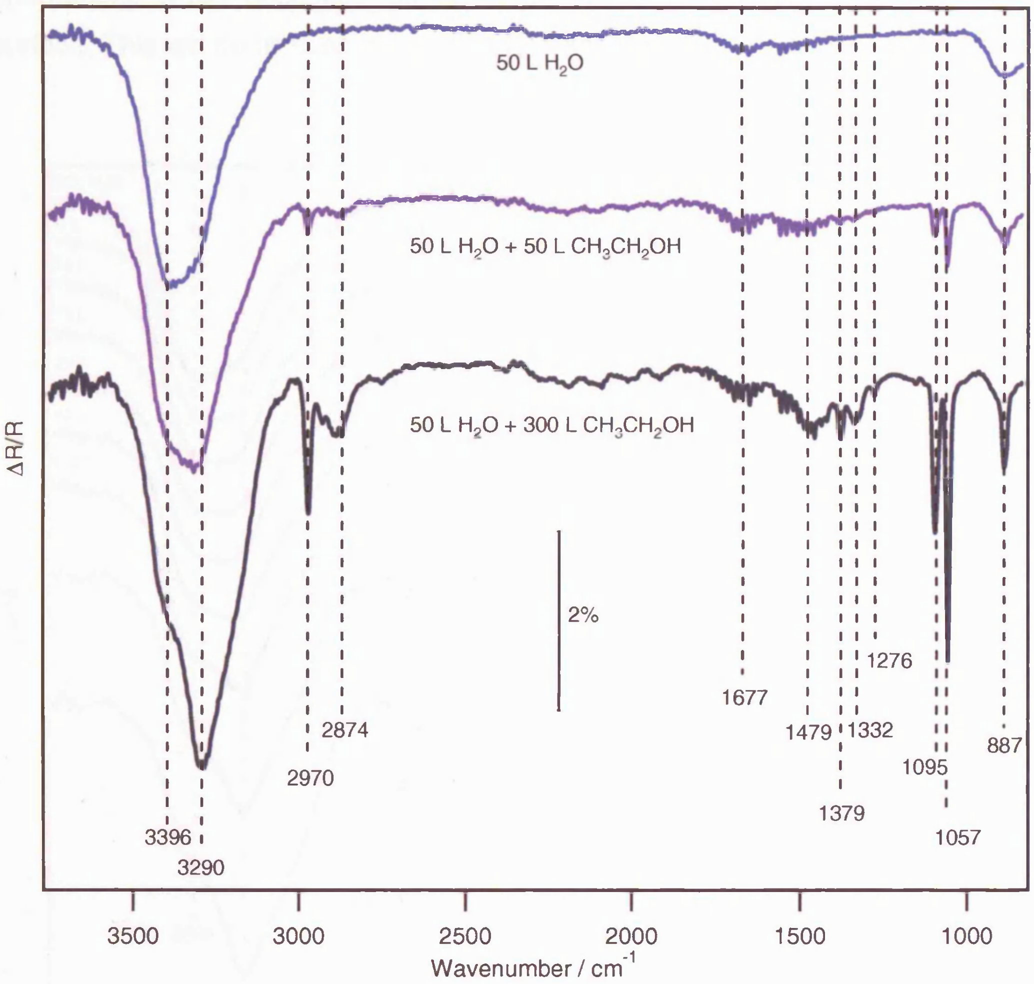

Figure 7.15 RAIR spectra showing the formation of the layered ice produced by depositing increasing amounts of ethanol on a pre-existing 50 L layer of water, all deposited on HOPG at 98 K.

Detailed RAIR spectra for the adsorption of ethanol on an underlying layer of water ice are shown in *Figure 7.16*. The initial trace shown is the 50 L exposure of pure water and the other traces represent increasing amounts of ethanol on top of this. Excluding the OH stretching region above 3000 cm^{-1}, which will be considered separately, all additional spectral features that appear as ethanol is adsorbed are coincident with those reported for spectra of pure ethanol on HOPG and they can be confidently assigned by comparison to *Table 7.2*.

In all cases, except for the $\delta_s(CH_3)$ at 1380 cm^{-1}, the order of appearance of the peaks is the same as for the adsorption of pure ethanol on HOPG. However, the methyl stretch is not apparent until the ethanol exposure has reached 50 L in the layered ethanol and water system. In contrast, it appeared immediately upon exposure of 5 L direct to the HOPG surface. This suggests that the ethanol molecule adopts different orientations when deposited on either a water surface or directly on the HOPG surface. This will be discussed in more detail later.

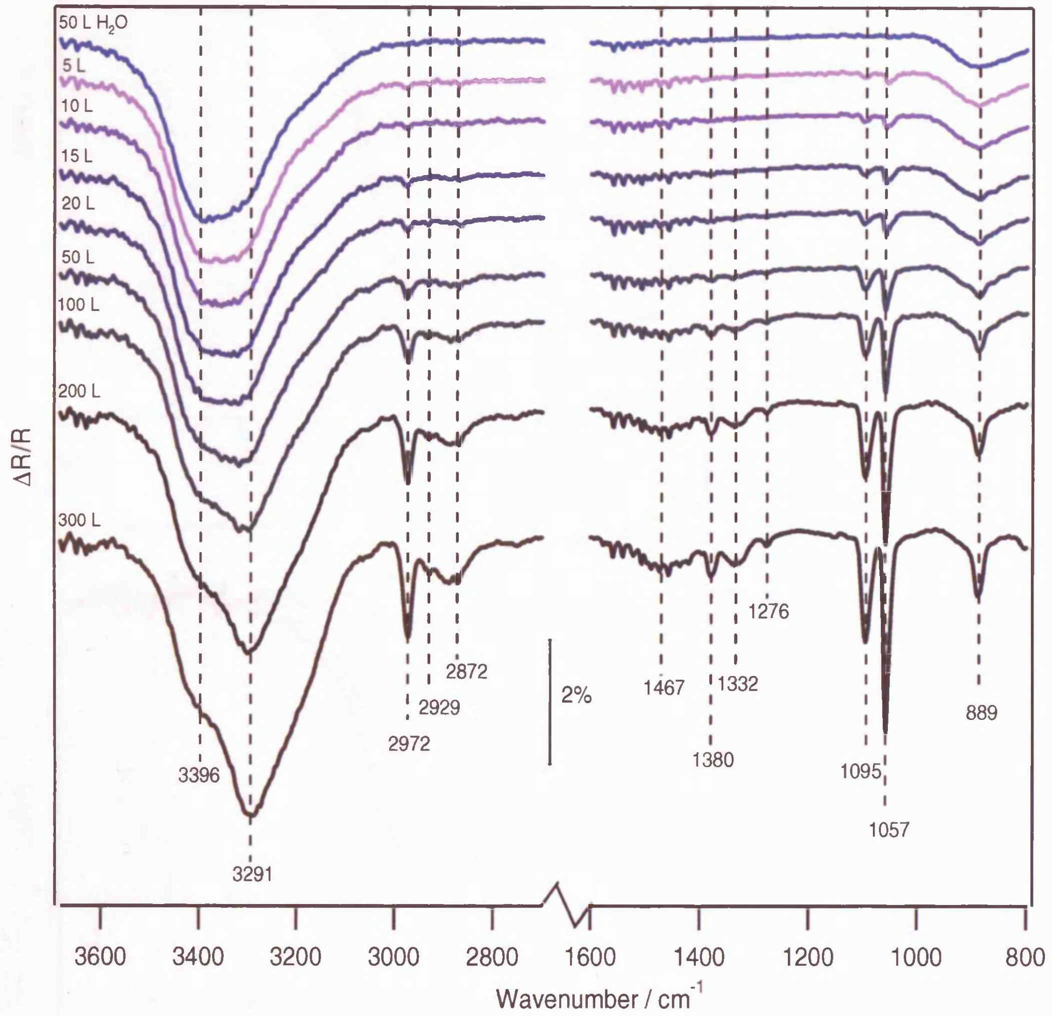

Figure 7.16 RAIR spectra over the range 3600-800 cm^{-1}, showing the full adsorption sequence for increasing exposures of ethanol on a pre-existing layer of water ice (50 L) adsorbed on HOPG at 98 K.

The broad OH stretching region around 3396 cm^{-1} undergoes a number of changes as the ethanol exposure increases, and essentially resembles a simple combination of the pure water and ethanol spectra. *Figure 7.17* shows an attempt to model the OH region of the layered spectra by a simple addition of the pure water and pure ethanol traces. The excellent fits achieved suggest that, as with the sequential dosing of methanol on water discussed in Chapter 3, the sequential exposure of ethanol and water has caused little alteration from the pure systems, and the two species are remaining as layers without any mixing during the adsorption process.

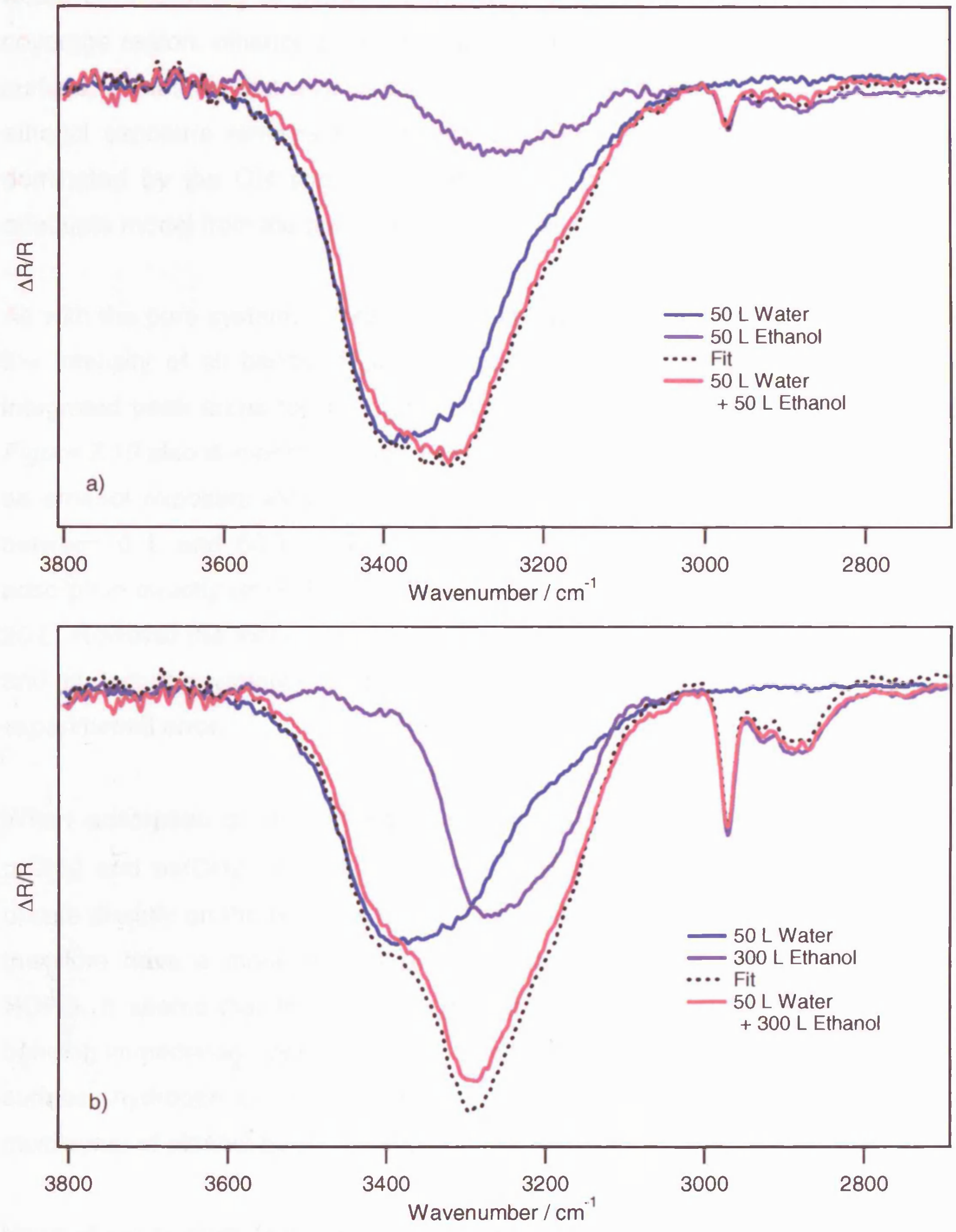

Figure 7.17 RAIR spectra for pure water, pure ethanol and the layered system formed by the addition of 50 L of ethanol to the water ice as shown in a) and 300 L of ethanol above the water ice in b). The region between 3800 cm^{-1} and 2700 cm^{-1} is shown and the combined peak generated by the addition of the pure ethanol and pure water components are shown in both cases as dotted lines.

The 50 L and 300 L exposures of ethanol adsorbed on water, as shown in *Figure 7.17*, represent multilayers of ethanol on water and therefore it is not surprising that the system is modelled well by a simple layered system. It is in the low exposure region, where ethanol is starting to form a monolayer on the water surface, that it would be interesting to model the interaction between the two species. In this low coverage region, ethanol is now able to form hydrogen bonds directly with the water surface, something that is not possible on the HOPG surface. Unfortunately, while the ethanol exposure remains so low, the spectral features of the layered ice are so dominated by the OH stretch from the water that it is impossible to produce an adequate model from the pure system traces as described above.

As with the pure system, increasing the exposure of ethanol results in an increase in the intensity of all bands. *Figure 7.18* and *Figure 7.19* show the variation in the integrated peak areas for the four most intense features in the layered ice spectra. *Figure 7.19* also demonstrates the variation in integrated area for the entire spectrum as ethanol exposure increases. In both cases the inset focuses on the exposures between 0 L and 50 L. The four most intense peaks demonstrate that, as with adsorption directly on HOPG, the increase in intensity is most rapid between 0 L and 20 L. However the increase is not as dramatic as that recorded in the pure system, and in fact the variation in area for the total spectrum is actually linear within experimental error.

When adsorption occurs on water, the vibrations assigned to υa(CCO), υ(CO) + ρ(CH_3) and υa(CH_3) show a less rapid increase in intensity than when adsorption occurs directly on the HOPG surface. The bonds giving rise to these vibrations must therefore have a more prominent vertical component when adsorption occurs on HOPG. It seems that the presence of the water forces the formation of hydrogen bonding immediately upon deposition, whereas when adsorption occurs on the HOPG surface, hydrogen bonding is only an option as the exposure is increased and multilayers of ethanol begin to form.

None of the spectral features saturate, nor do they demonstrate any frequency shifts with increasing coverage. This demonstrates that in adsorption, ethanol forms physisorbed multilayers on top of water as expected.

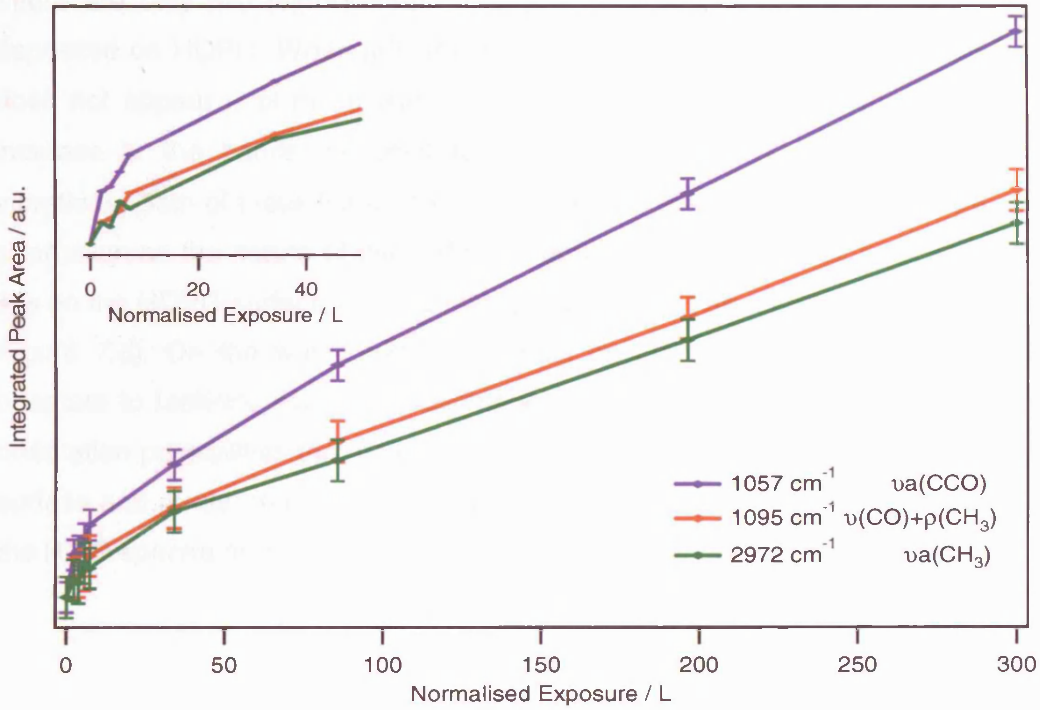

Figure 7.18 Chart showing the integrated peak area for the bands at 1057 cm^{-1}, 1095 cm^{-1} and 2972 cm^{-1} as a function of increasing ethanol exposure on 50 L of amorphous water ice, deposited on HOPG at 98 K. The inset focuses on the region between 0 and 50 L.

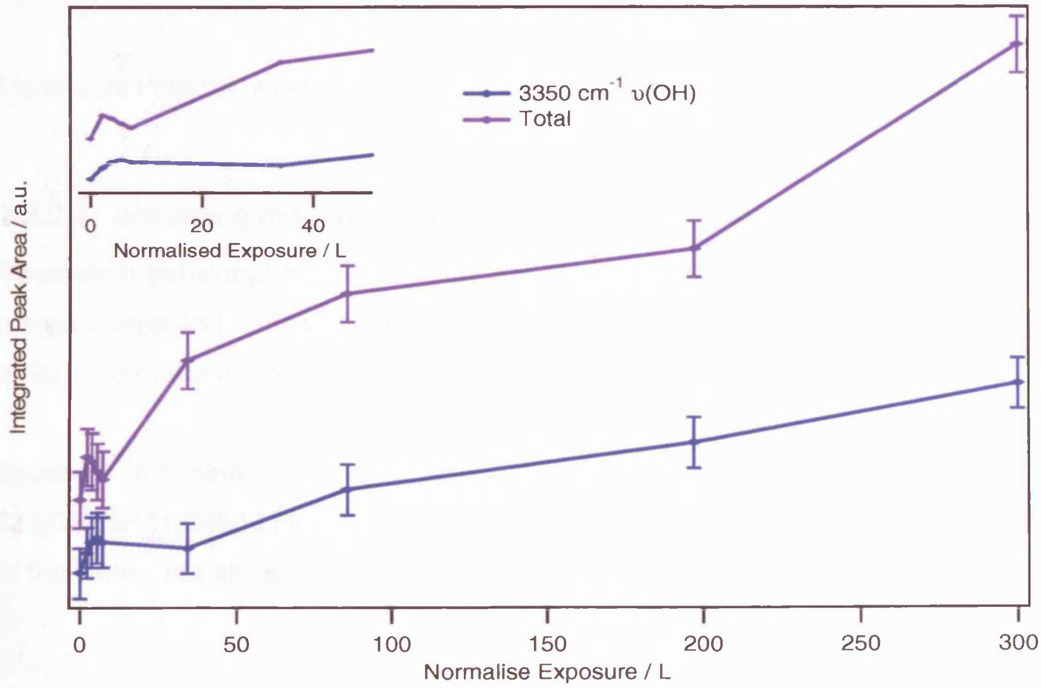

Figure 7.19 Chart showing the integrated peak area for the υ(OH) band at 3350 cm^{-1} and the total spectrum, as a function of increasing ethanol exposure on 50 L of amorphous water ice, deposited on HOPG at 98 K. The inset focuses on the region between 0 and 50 L.

There are only two features that distinguish ethanol deposited on water from that deposited on HOPG. When adsorption occurs on a water surface, the methyl stretch does not appear until much later, and in addition there appears to be a less rapid increase in the bands assigned to the $\upsilon a(CCO)$, $\upsilon(CO) + \rho(CH_3)$ and $\upsilon a(CH_3)$ vibrations. Both of these features suggest that the ethanol molecule adopts a different orientation as the nature of the surface changes. It was proposed earlier that ethanol sits on the HOPG surface with the methyl group acting as a tripod on the surface (see *Figure 7.6*). On the water surface it would be more likely that the ethanol would orientate to facilitate hydrogen bonding with the water layer. There are a number of orientation possibilities that both increase the likelihood of hydrogen bonding with the surface and render the C-CH_3 bond parallel to the surface and therefore absent from the RAIR spectra at low exposures. One possible orientation is shown in *Figure 7.20*.

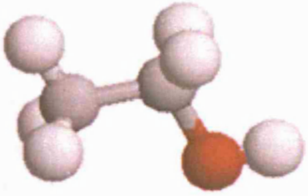

Figure 7.20 Possible orientation of ethanol adsorbed on the water ice surface at 98 K.

7.3.2.2 Annealing the Layered Ethanol and Water System

Desorption behaviour was studied by annealing the layered ice system to increasing temperatures and annealing for 3 minutes. The sample was then allowed to cool back to 98 K before taking a scan.

Spectra focusing on the OH region, resulting from annealing the CH_3CH_2OH/H_2O(50 L) layered ice system, with an exposure of 300 L of ethanol on top of the water, are shown in *Figure 7.21*.

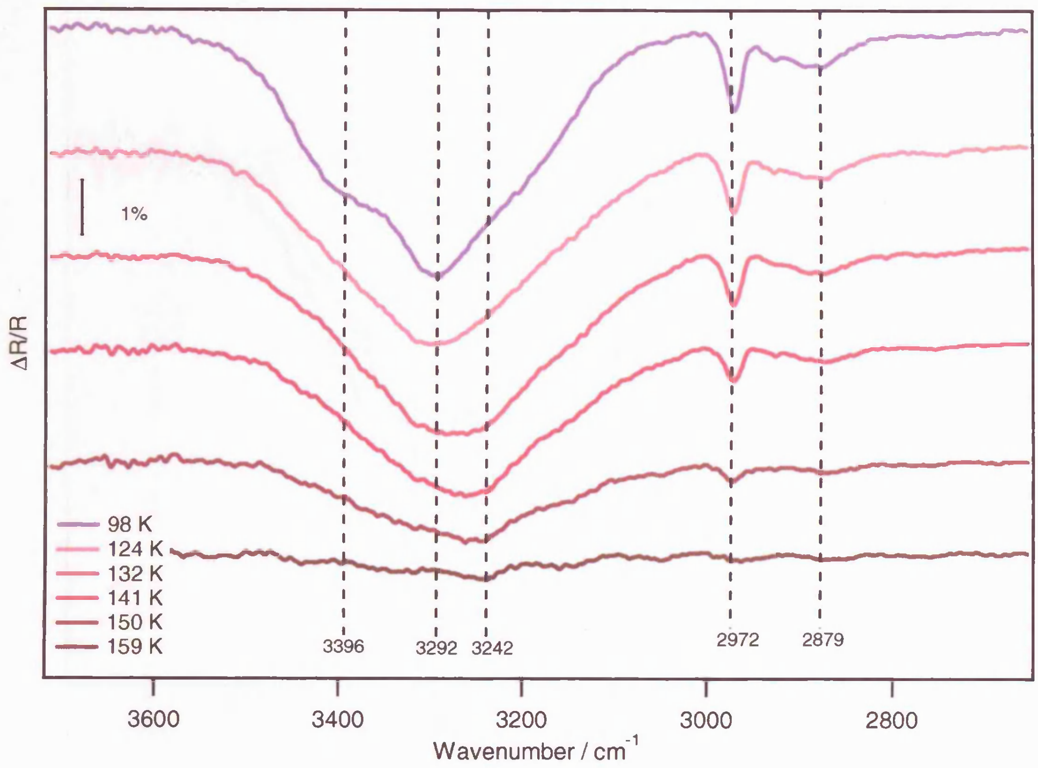

Figure 7.21 RAIR spectra recorded between 3700 cm^{-1} and 2700 cm^{-1} showing the sequential heating of the layered ice formed by depositing 300 L of ethanol on a pre-existing 50 L layer of water, all deposited on HOPG at 98 K.

Heating the water-ethanol layer results in immediate changes to the appearance of the broad OH peak. Prior to heating, the broad peak between 3000 cm^{-1} and 3600 cm^{-1} has a number of features. There is a central peak at 3292 cm^{-1}, and two shoulders either side at 3396 cm^{-1} and 3200 cm^{-1} and, as discussed in the adsorption section, it appears to be a simple spectral combination of the pure systems. As the system is heated to 122 K the features appear to smooth out, with both the high and low frequency shoulders losing intensity, to leave a single broad peak at 3292 cm^{-1}. Further heating is associated with a reduction in intensity of the peak and also results in a downshift in its frequency to 3242 cm^{-1}.

An attempt to model the OH stretch region between 3000 cm^{-1} and 3600 cm^{-1} is shown in *Figure 7.22*, with the dotted line representing the combination of components from the pure ethanol and water annealing experiments. The water trace shows the characteristic shape of crystalline water as discussed in Chapter 3.

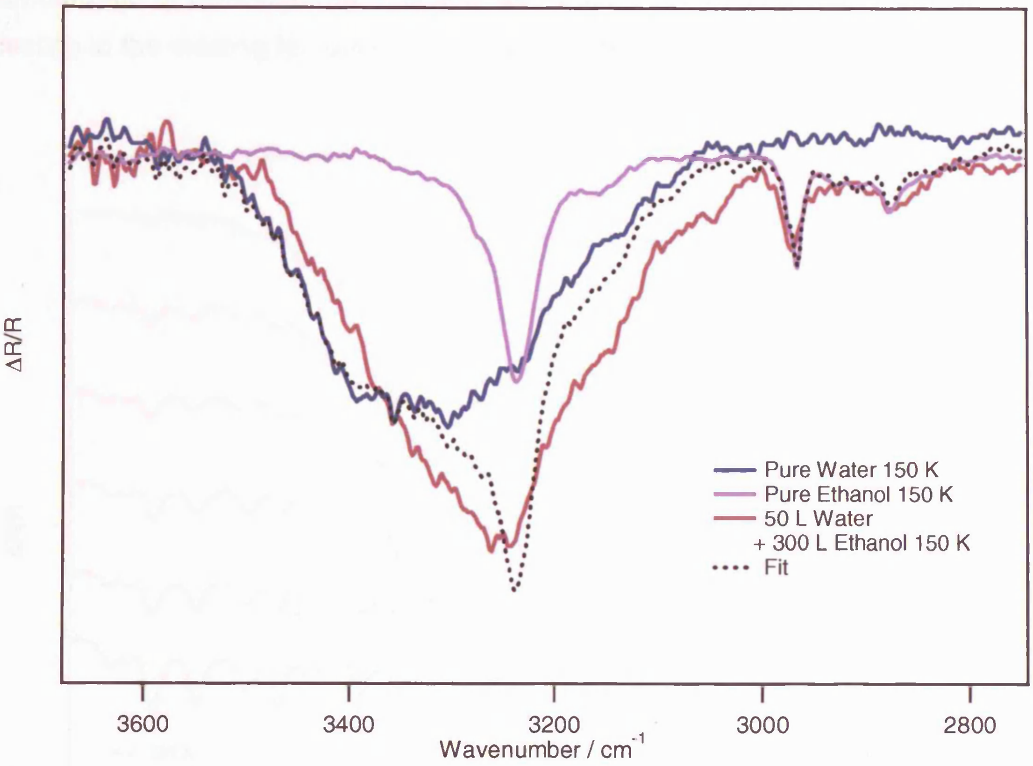

Figure 7.22 RAIR spectra for 50 L of pure water annealed to 150 K, 300 L of pure ethanol annealed to 150 K and the layered system composed of 300 L of ethanol on 50 L of water ice annealed to 150 K, all deposited on HOPG at 98 K. The region between 3800 cm^{-1} and 2700 cm^{-1} is shown and the combined peak generated by the addition of the pure ethanol and pure water components is shown as a dotted line.

The fit shown in *Figure 7.22* is not an adequate representation of the layered spectrum. Even by adjusting the proportions of water and ethanol used in the combination fit, it is not possible to achieve a good match to the rather featureless peak seen with the annealed layered system. The inability to represent the layered system as a combination of the two pure systems indicates that, as expected, processing must have occurred in the ice during the annealing, resulting in the intermixing of the two components to form a hydrogen bonded network. This result was also observed for the annealing of layered methanol/water systems in Chapter 4.

The desorption sequence for the mid-frequency range between 1600 cm^{-1} and 1200 cm^{-1} is shown in *Figure 7.23*. The chart shows a decrease in intensity of all the visible peaks at 1457 cm^{-1}, 1381 cm^{-1}, 1336 cm^{-1} and 1277 cm^{-1}, as the temperature increases. All of the features are absent by 159 K. The corresponding chart for the pure ethanol system is shown in *Figure 7.11*. In the pure ethanol system, heating results in an increase in intensity of the peaks at 1479 cm^{-1} and 1325 cm^{-1} and the appearance of new features. The layered system, in contrast, simply demonstrates a decline in the existing features during the annealing process.

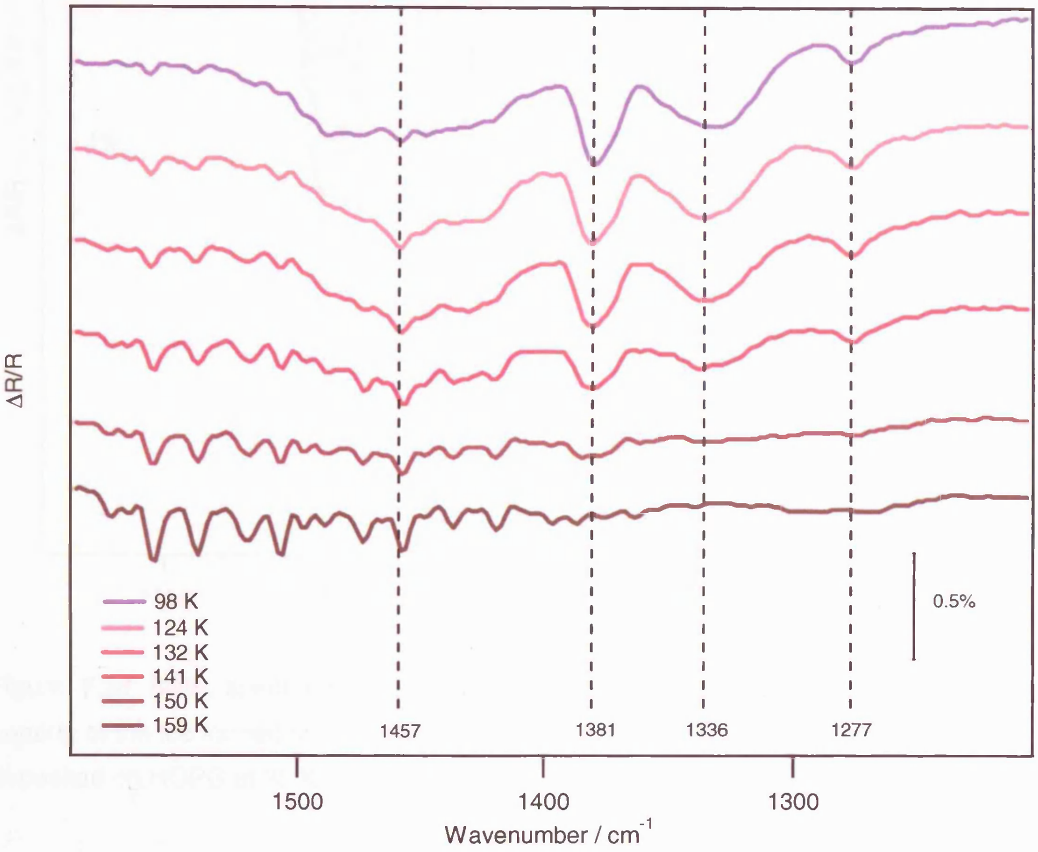

Figure 7.23 RAIR spectra recorded between 1600 and 1200 cm^{-1} showing the sequential heating of the ice formed by depositing 300 L of ethanol on 50 L of pre-existing water ice, both deposited on HOPG at 98 K.

Spectra for the low frequency region are shown in *Figure 7.24*, which can be compared with the equivalent chart for the pure system, *Figure 7.10*. Again, in this region of the spectrum, the layered system is showing only a decrease in intensity of the peaks as the sample is heated, unlike the pure system which shows an immediate increase in intensity as the sample is first heated, followed by desorption and splitting. The absence of heat induced splitting in the layered system is further evidence for the intermixing between the two species that occurs during the annealing process. The interaction between the water and ethanol molecules now inhibits the crystallisation that was observed by the splitting of bands in the pure ethanol system.

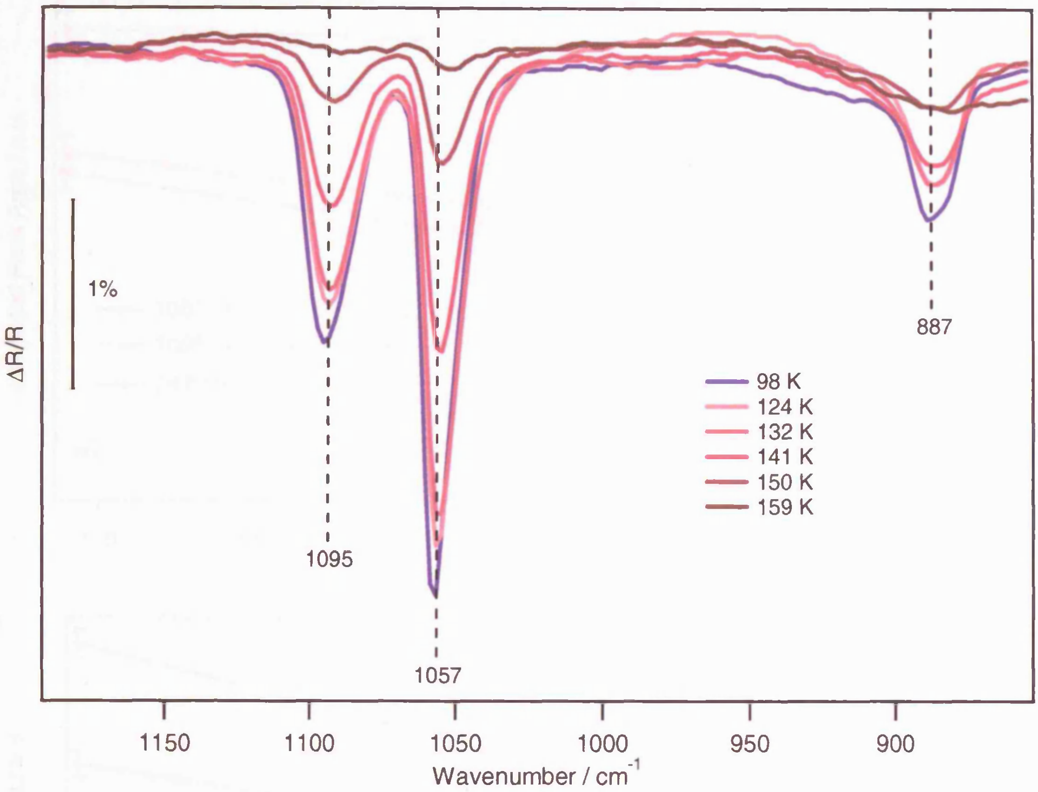

Figure 7.24 RAIR spectra recorded between 1160 and 850 cm^{-1} showing the sequential heating of the ice formed by depositing 300 L of ethanol on 50 L of pre-existing water ice, both deposited on HOPG at 98 K.

The change in integrated peak area as a function of temperature is shown in *Figure 7.25,* for the 4 most dominant bands in the spectrum. The change in area for the entire spectrum is also displayed. In all cases, the trend is for a gradual decrease in peak area as the sample is heated, with the rate of decrease reaching a maximum at around 138 K and desorption complete by 159 K. This again is evidence that, unlike the case for pure ethanol, no crystallisation occurs on heating.

To summarise, in adsorption, ethanol displays almost the same spectral features regardless of whether it has been deposited on HOPG or a pre-existing layer of water. The only difference in the two systems is a delay in the appearance of the methyl stretch, when adsorption occurs on the water surface, possibly indicating an alternative arrangement of the adsorbing ethanol molecules.

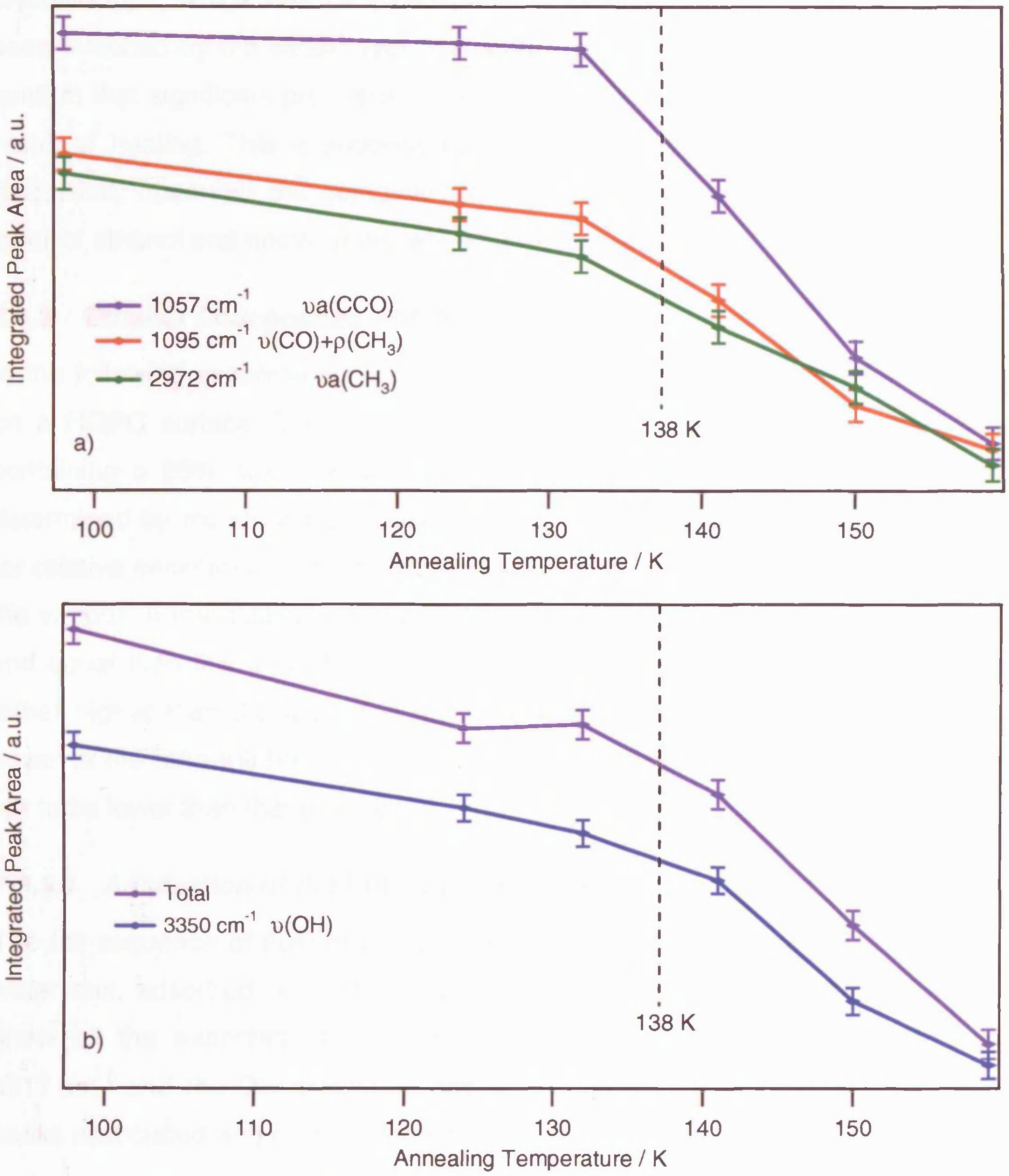

Figure 7.25 Chart showing the integrated peak area for selected bands in the ethanol spectrum as a function of annealing temperature for the ice formed by depositing 300 L of ethanol on 50 L of pre-existing water ice. In chart a) 1057 cm^{-1}, 1095 cm^{-1} and 2972 cm^{-1}, or υa(CCO), υ(CO) + ρ(CH$_3$) and υa(CH$_3$), bands are displayed. Chart b) shows the integrated area for the 3282 cm^{-1}, or υ(OH), vibration along with the integrated area for the total spectrum.

However, the desorption behaviour of ethanol is clearly affected by the presence of the underlying water layer. During the annealing process of the layered system, there is no evidence for the intensity inversion witnessed in the pure system and displayed in *Figure 7.12.* There is also no evidence for peak splitting, which is a clear feature of most peaks present in the pure spectrum. These spectral differences indicate that crystallisation, which was assumed to occur around 118 K in the pure system, has been inhibited by the water layer. Certainly the changes in the OH stretching region confirm that significant processing has occurred between the water and ethanol, as a result of heating. This is supported by the work of Souda [31] who, as previously discussed, observed the complete intermixing and isotope scrambling of a binary layer of ethanol and heavy-water when heated to 140 K.

7.3.3 Ethanol Codeposited with Water

In the following experiments, an intimately mixed ethanol and water ice was studied on a HOPG surface. The sample was exposed to vapour pressure from a vessel containing a 25% mix of ethanol:water. The exact composition of the vapour was determined by monitoring the dose with the mass spectrometer and then correcting for relative sensitivities. The results indicate an upper figure of 15% ethanol:water in the vapour. If the sticking probability of both species are presumed to be both high and equal then this should translate to an equivalent composition in the ice. This is rather higher than the proposed maximum of 5% for astrophysical ices [4, 10, 11], however the ratio will be considerably lower if the sticking probability of ethanol turns out to be lower than that of water.

7.3.3.1 Adsorption of the Ethanol and Water Mix

The full sequence of adsorption spectra for increasing exposures of the ethanol and water mix, adsorbed on a HOPG surface, is shown in *Figure 7.26*. These spectra show all the expected features of water, namely the broad OH stretch around 3317 cm^{-1} and the OH scissors mode at 1677 cm^{-1}. In addition the most dominant peaks associated with ethanol are also visible.

Table 7.3 shows the visible peaks from the 300 L spectrum of the mixed system. Most of the peaks recorded in the pure spectra are visible in the mixed spectra following a 300 L exposure, with only the $\rho(CH_2)$ + $\rho(CH_3)$ feature at 1155 cm^{-1} missing. Comparing the intensity of the 1057 cm^{-1} peak in the mixed spectra with that from the pure system indicates that the dose of ethanol in the 300 L exposure of the mix is equivalent to only a 50 L exposure of pure ethanol, i.e. ≈ 15-20% ethanol. It is therefore expected that the ethanol features will be swamped by the water components.

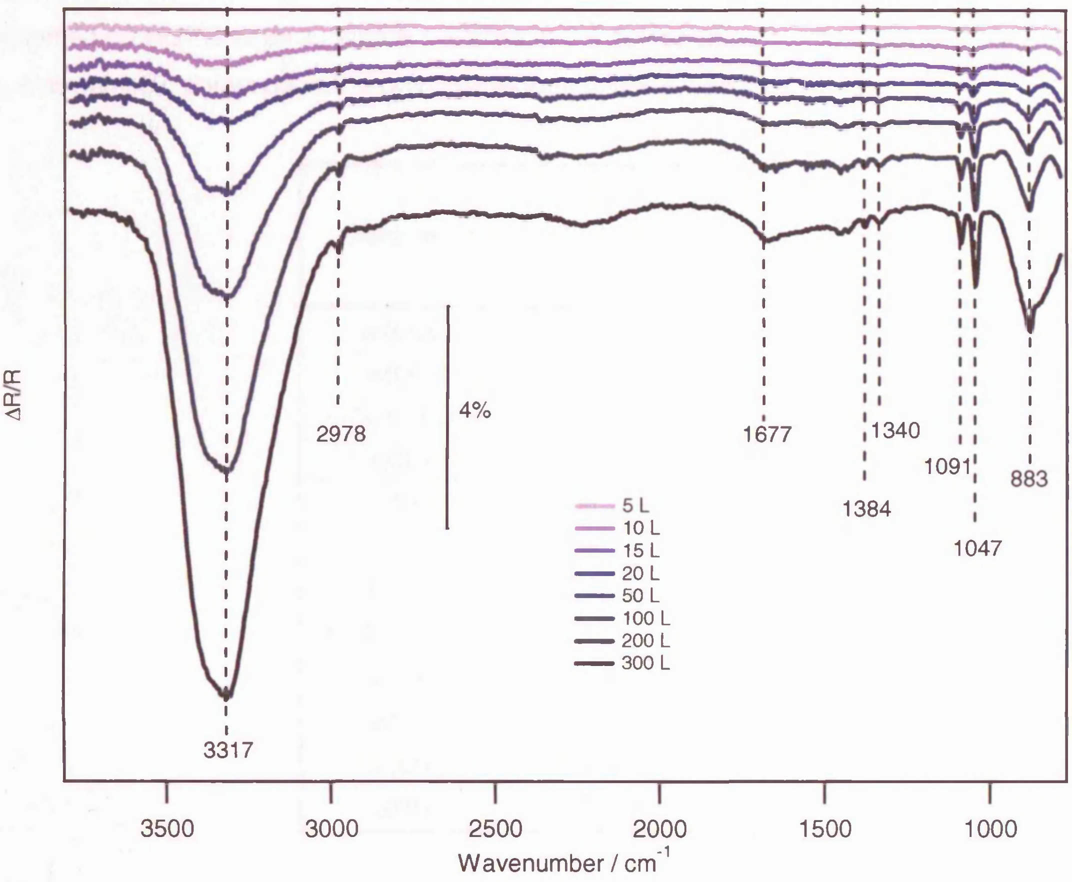

Figure 7.26 RAIR spectra over the 3600-800 cm^{-1} region showing the full adsorption sequence for increasing exposures of the intimate ethanol and water mix, deposited on HOPG at 98 K.

Careful inspection of *Figure 7.26* shows that some of the ethanol-only peaks have been shifted from the frequencies observed in the pure state, and these have been recorded in *Table 7.3* along with the assignments. In the mixed state, the ethanol molecules are in a different environment to those formed on either the HOPG or water surface. This close association with the water molecules will result in increased hydrogen bonding and results in the frequency shifting of individual vibrational bands within ethanol. Hydrogen bonding weakens the OH bond, and therefore lowers the υ(OH) vibration, but inhibits librational and bending vibrations and so those bonds would be expected to shift to higher frequencies [40].

Table 7.3 Infrared vibrational bands and assignments for an intimate mix of ethanol and water, adsorbed on HOPG at 98 K. Where υ = stretch, δ = deformation, δ_s = symmetric deformation, δ_a = asymmetric deformation, τ = twist, ρ = rocking and ω = wagging.

Assignment	σ/cm^{-1}	**Frequency Shift from Pure ethanol /cm^{-1}**
υs(CCO)	883	- 6
υa(CCO)	1048	- 9
υ(CO) + ρCH_3)	1092	+ 3
τ(CH_2)	1277	-
δ(OH)	1336	+ 8
δs(CH_3)	1384	+ 4
δa(CH_3)	1462	+ 3
(OH) scissors	1677	-
υs(CH_2)	2874	-
υs(CH_3)	2907	- 20
υa(CH_3)	2982	+ 10
υ(OH)	3317	N/A

7.3.3.2 Annealing the Mixed Ethanol and Water System

The desorption behaviour of the 300 L exposure of the mixed ethanol and water ice was studied by sequentially heating the sample to increasing temperatures.

Spectra focussing on the OH stretching region are shown in *Figure 7.27*. This can be compared with *Figure 7.28*, which shows the variation of peak area as a function of increasing temperature, to show that there is only a very slight decline in peak area as the temperature is increased to 153 K. The peak shape changes during the annealing process, with the OH peak demonstrating the clear fingerprint of the amorphous to crystalline structural change expected for water, with the low frequency shoulder increasing in intensity as the high frequency shoulder declines. Crystallisation appears to occur between 145 K and 153 K, which is in agreement with previous studies of pure water on HOPG, which quote a temperature of ≈ 145 K [41]. Amorphous water adsorbed at 98 K would typically show a RAIR spectrum with the high frequency shoulder more intense than the low frequency shoulder [41]. This is reversed in *Figure 7.27* as the contribution from the ethanol component is in the region of the low frequency shoulder, at 3250 cm^{-1}.

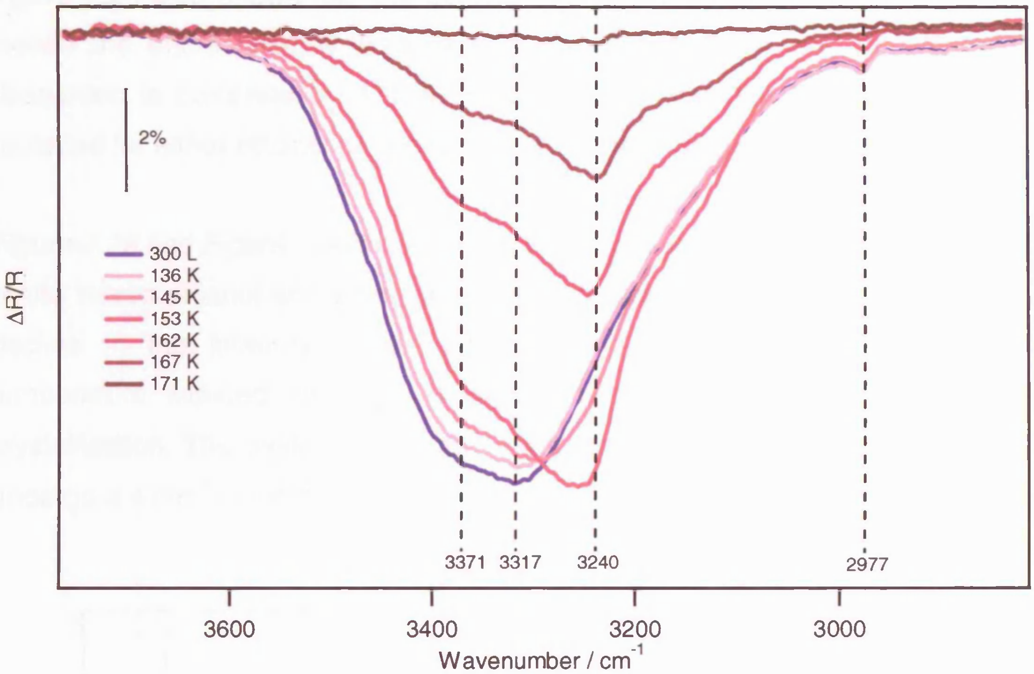

Figure 7.27 RAIR spectra recorded between 3700 cm^{-1} and 2800 cm^{-1}, showing the sequential heating of the ice formed by depositing 300 L of the ethanol and water mix on a HOPG surface at 98 K.

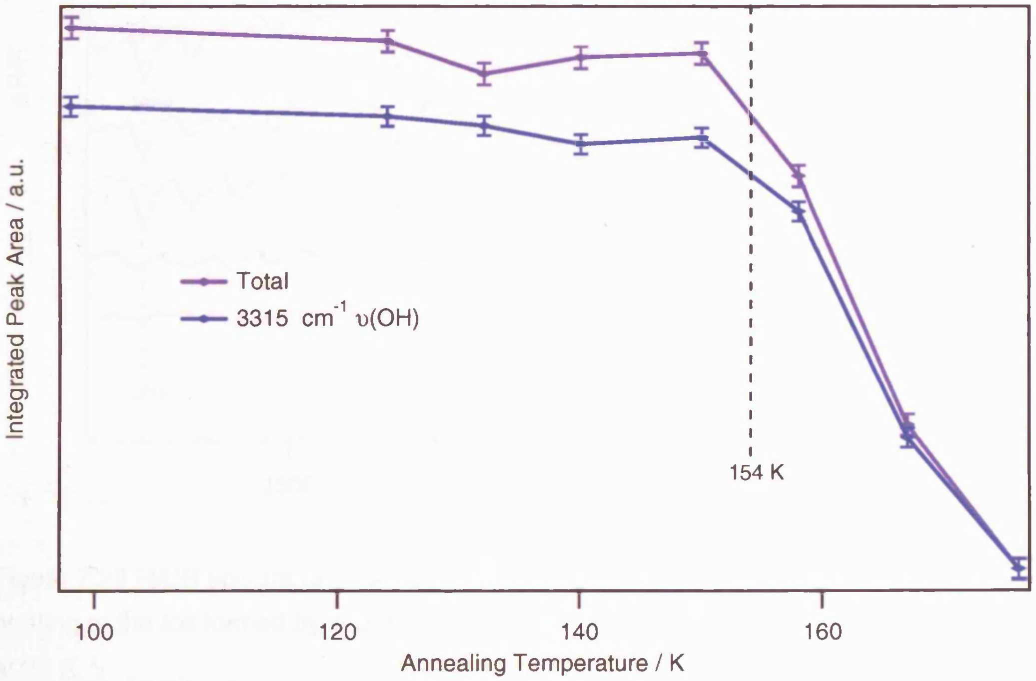

Figure 7.28 Chart showing the integrated peak area for the υ(OH) and the entire mixed ethanol and water spectrum, as a function of temperature, following exposure of 300 L of the mix onto the HOPG sample at 98 K.

Figure 7.28 also shows that the decline in the area of the OH stretching peak and indeed the entire spectral area, is very rapid at ≈ 154 K and demonstrates that desorption is complete by 171 K. This is higher than the desorption temperature recorded for either ethanol on the HOPG or on the water surface.

Figure 7.29 and *Figure 7.30* focus on the mid and low frequency regions, respectively, of the mixed ethanol and water desorption spectra. They both demonstrate a gentle decline in the intensity of the ethanol band vibrations, with no evidence for temperature induced splitting. As expected, there is therefore no evidence for crystallisation. The peak at 1047 cm^{-1}, assigned to the υ_a(CCO) vibration, appears to undergo a 4 cm^{-1} redshift during heating.

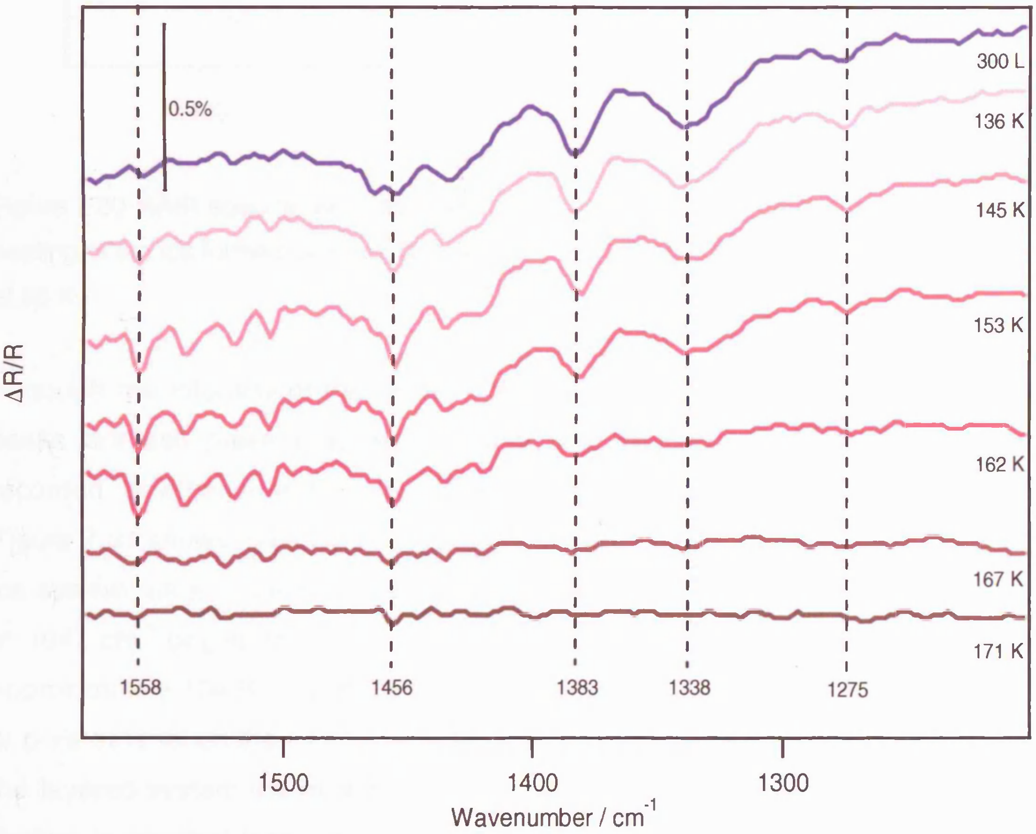

Figure 7.29 RAIR spectra recorded between 1570 cm^{-1} and 1200 cm^{-1}, showing the sequential heating of the ice formed by depositing 300 L of the ethanol and water mix on a HOPG surface at 98 K.

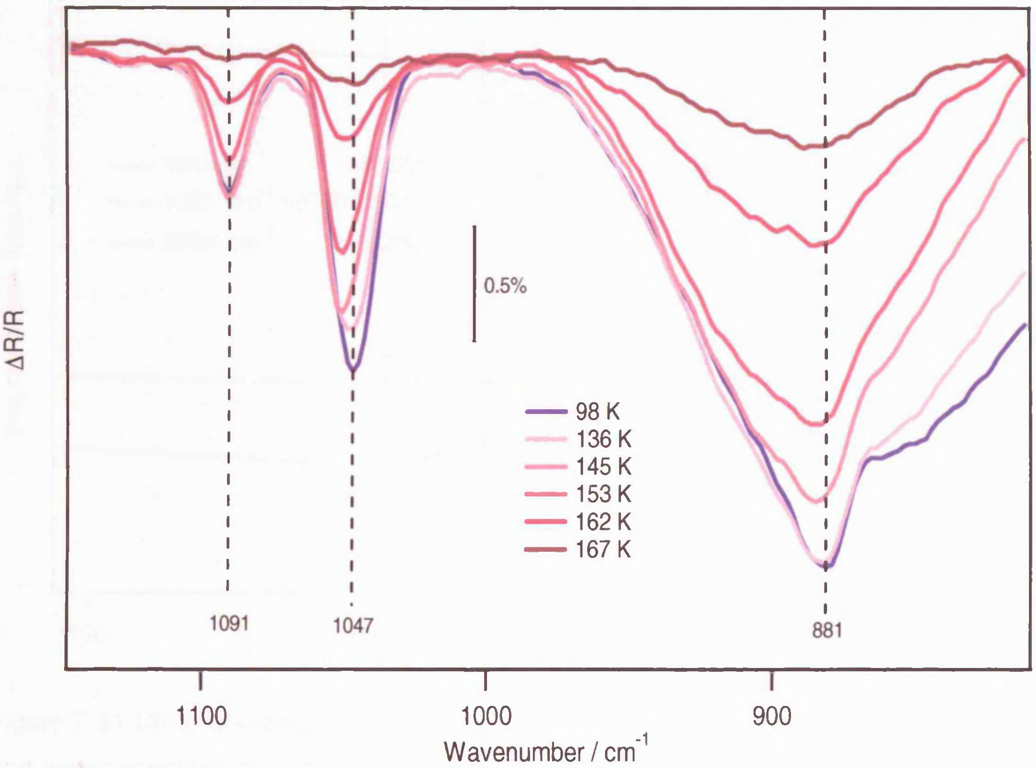

Figure 7.30 RAIR spectra recorded between 1150 cm^{-1} and 800 cm^{-1}, showing the sequential heating of the ice formed by depositing 300 L of the ethanol and water mix on a HOPG surface at 98 K.

Although the intensity of the ethanol-only vibrational bands declines on heating, the peaks are still present at temperatures well beyond the desorption temperature recorded for ethanol in the pure state or adsorbed on the layered water ice system. *Figure 7.31* shows the integrated area for three prominent ethanol peaks in the mixed ice system, as a function of annealing temperature. It is clear that, although the band at 1047 cm^{-1} begins to decline at 137 K, the most rapid rate of desorption begins at approximately 154 K. In comparison, the maximal rate of desorption for a larger dose of pure ethanol on the HOPG sample, was at around 134 K (see *Figure 7.12*), and in the layered system the maximal rate was achieved at 138 K (see *Figure 7.25*). The decline in spectral features for pure ethanol, the ethanol and water layered systems and the codeposited ethanol and water ices as a function of the annealing temperature are displayed in *Figure 7.32*, which also indicates the region of maximal water desorption.

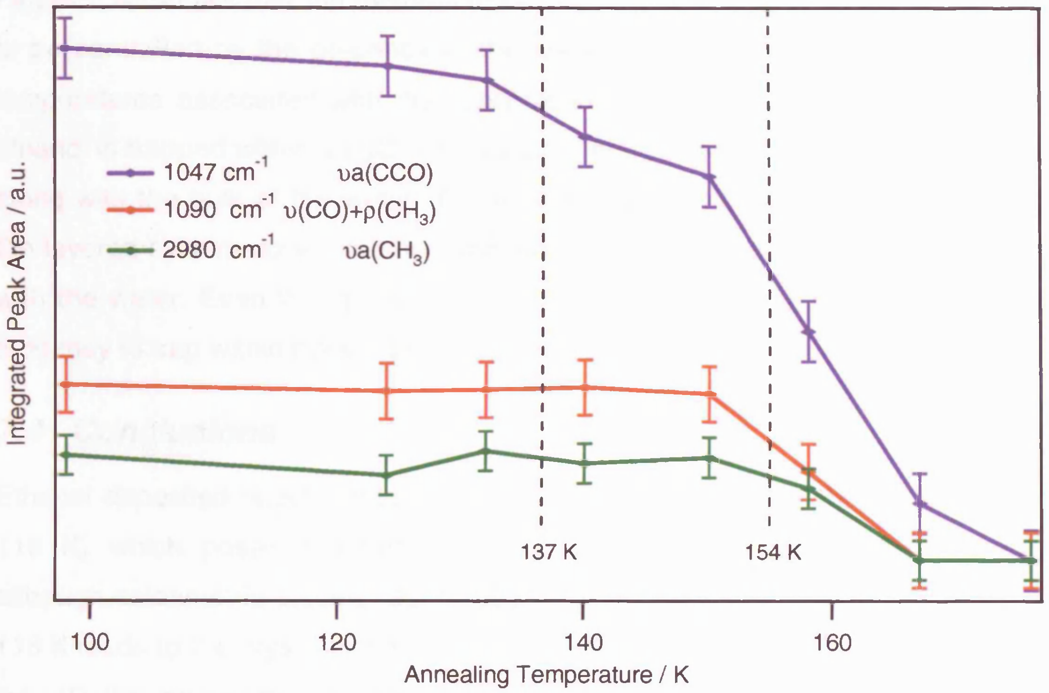

Figure 7.31 Chart showing the integrated peak area for selected bands in the mixed ethanol and water spectrum as a function of annealing temperature. The υa(CCO), υ(CO) + ρ(CH_3) and the υa(CH_3) bands are displayed.

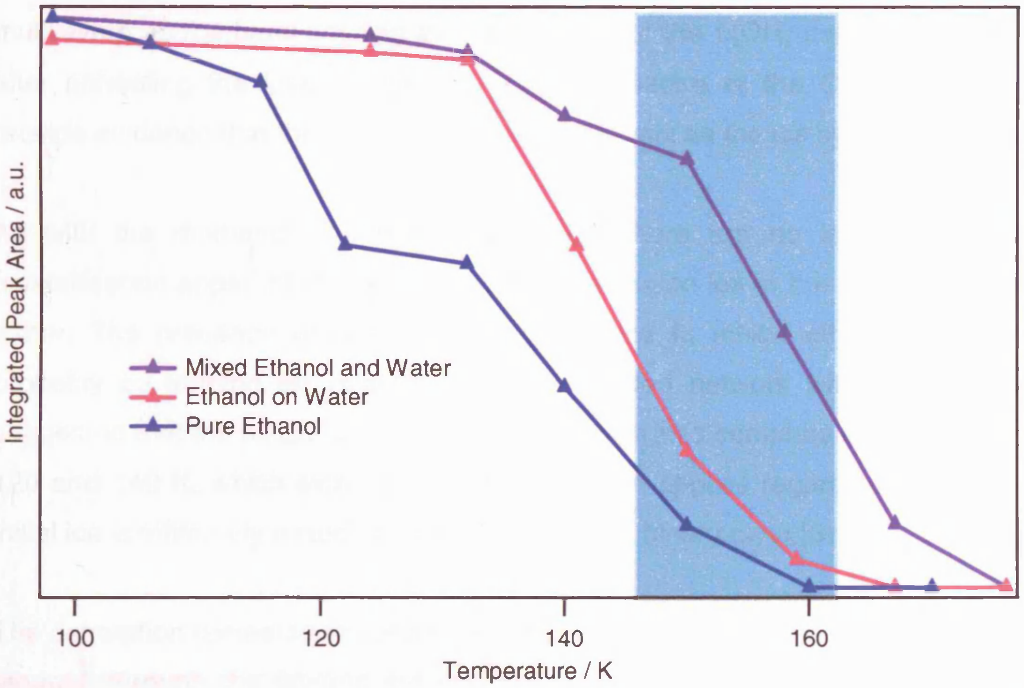

Figure 7.32 Chart showing the integrated peak area for the total spectrum recorded in each of the three systems as a function of annealing temperature. The highlighted band represents the temperature range for which maximal water desorption was observed in the layered and codeposited systems.

Figure 7.32 shows that the desorption behaviour of ethanol in the mixed ice appears to be controlled by the presence of the water. The ethanol only features desorb at temperatures associated with the sublimation of pure water. This suggests that the ethanol is trapped within a H_2O rich hydrogen bonded network and so will only desorb along with the bulk of the water. The elevated desorption temperature for ethanol in the layered system could also be suggestive of a degree of thermally induced mixing with the water. Even though ethanol is larger than methanol, it is showing a similar tendency to trap within the water ice.

7.4 Conclusions

Ethanol deposited directly onto HOPG shows a reordering as the ice is heated to ≈ 118 K, which possibly represents the glass transition temperature for ethanol, although calorimetric studies [36] place the glass transition at 97 K. Heating beyond 118 K leads to the crystallisation of ethanol which is characterised by a sharpening of the υ(OH) band and the splitting of many other peaks.

When ethanol is deposited onto a pre-existing layer of amorphous water ice it remains as a simple binary layered system until the ice is annealed. It appears that the presence of water inhibits the thermally induced crystallisation of the ethanol multilayers as the band splitting and sharpening of the υ(OH) band are not observed after annealing the layered system. The IR spectra of the OH stretching region provide evidence that the two layers begin to intermix as the ice system is heated.

As with the methanol and water mixed ice, there are no indicators of ethanol crystallisation apparent in the spectra of the annealed ice in the codeposited system either. The presence of water in the ice seems to inhibit ethanol crystallisation, probably by forming an intimate hydrogen bonded network with the ethanol. It is suggested that the binary layered system demonstrates complete intermixing between 120 and 140 K, which explains why this inhibition applies regardless of whether the initial ice is intimately mixed or formed as a simple binary layer [31].

The desorption temperatures of the ices shift upwards as the system moves from pure ethanol, through the layered system and up to the codeposited system. Complete desorption of the ethanol features is delayed when the initial ice includes water, whether as an intimate mix or as a binary layer. In this way the ethanol molecule shares a number of similarities in its behaviour with methanol, which clearly demonstrates a tendency to trap within the bulk of the water ice. Further TPD studies of the ethanol systems discussed here are required to confirm trapping behaviour in ethanol and water ices.

7.5 Bibliography

1. Millar, T.J., Olofsson, H., Hjalmarson, A., and Brown, P.D., Astronomy and Astrophysics, 1988. **205**(1-2): p. L5-L7.

2. Millar, T.J., Macdonald, G.H., and Habing, R.J., Monthly Notices of the Royal Astronomical Society, 1995. **273**(1): p. 25-29.

3. Zuckerman, B., Turner, B.E., Johnson, D.R., Clark, F.O., Lovas, F.J., Fourikis, N., Palmer, P., Morris, M., Lilley, A.E., Ball, J.A., Gottlieb, C.A., Litvak, M.M., and Penfield, H., Astrophysical Journal, 1975. **196**(3): p. L99-L102.

4. Charnley, S.B., Kress, M.E., Tielens, A., and Millar, T.J., Astrophysical Journal, 1995. **448**(1): p. 232-239.

5. Charnley, S.B., Tielens, A., and Millar, T.J., Astrophysical Journal, 1992. **399**(1): p. L71-L74.

6. Turner, B.E., Astrophysical Journal Supplement Series, 1991. **76**(2): p. 617-686.

7. Herbst, E. and Leung, C.M., Astrophysical Journal Supplement Series, 1989. **69**(2): p. 271-300.

8. Millar, T.J., Herbst, E., and Charnley, S.B., Astrophysical Journal, 1991. **369**(1): p. 147-156.

9. Brown, P.D., Charnley, S.B., and Millar, T.J., Monthly Notices of the Royal Astronomical Society, 1988. **231**(2): p. 409-417.

10. Boudin, N., Schutte, W.A., and Greenberg, J.M., Astronomy and Astrophysics, 1998. **331**(2): p. 749-759.

11. Hasegawa, T.I. and Herbst, E., Monthly Notices of the Royal Astronomical Society, 1993. **263**(3): p. 589-606.

12. Hasegawa, T.I., Herbst, E., and Leung, C.M., Astrophysical Journal Supplement Series, 1992. **82**(1): p. 167-195.

13. Bernstein, M.P., Sandford, S.A., Allamandola, L.J., Chang, S., and Scharberg, M.A., Astrophysical Journal, 1995. **454**(1): p. 327-344.

14. Truax, D.R. and Wieser, H., Chemical Society Reviews, 1976. **5**(4): p. 411-429.

15. Sasada, Y., Takano, M., and Satoh, T., Journal of Molecular Spectroscopy, 1971. **38**(1): p. 33-&.

16. Perchard, J.P. and Josien, M.L., Journal De Chimie Physique Et De Physico-Chimie Biologique, 1968. **65**(10): p. 1856-&.

17. Barnes, A.J. and Hallam, H.E., Transactions of the Faraday Society, 1970. **66**(572): p. 1932-&.

18. Dothe, H., Lowe, M.A., and Alper, J.S., Journal of Physical Chemistry, 1989. **93**(18): p. 6632-6637.

19. Perchard, J.P. and Josien, M.L., Journal De Chimie Physique Et De Physico-Chimie Biologique, 1968. **65**(10): p. 1834-&.

20. Coussan, S., Bouteiller, Y., Perchard, J.P., and Zheng, W.Q., Journal of Physical Chemistry A, 1998. **102**(29): p. 5789-5793.

21. Mikawa, Y., Brasch, J.W., and Jakobsen, R.J., Spectrochimica Acta Part a-Molecular Spectroscopy, 1971. **A 27**(4): p. 529-&.

22. Davis, J.L. and Barteau, M.A., Surface Science, 1987. **187**(2-3): p. 387-406.

23. Panja, C., Saliba, N., and Koel, B.E., Surface Science, 1998. **395**(2-3): p. 248-259.

24. Sexton, B.A., Rendulic, K.D., and Hughes, A.E., Surface Science, 1982. **121**(1): p. 181-198.

25. Rasko, J., Domok, A., Baan, K., and Erdohelyi, A., Applied Catalysis a-General, 2006. **299**: p. 202-211.

26. Lee, A.F., Gawthrope, D.E., Hart, N.J., and Wilson, K., Surface Science, 2004. **548**(1-3): p. 200-208.

27. Yee, A., Morrison, S.J., and Idriss, H., Journal of Catalysis, 2000. **191**(1): p. 30-45.

28. Camplin, J.P. and McCash, E.M., Surface Science, 1996. **360**(1-3): p. 229-241.

29. Eng, J., Raghavachari, K., Struck, L.M., Chabal, Y.J., Bent, B.E., Flynn, G.W., Christman, S.B., Chaban, E.E., Williams, G.P., Radermacher, K., and Manti, S., Journal of Chemical Physics, 1997. **106**(23): p. 9889-9898.

30. Silvestrelli, P.L., Surface Science, 2004. **552**(1-3): p. 17-26.

31. Souda, R., Journal of Chemical Physics, 2005. **122**(13).

32. Bolina, A.S., Wolff, A.J., and Brown, W.A., Journal of Chemical Physics, 2005. **122**(4): p. art. no.-044713.

33. Barnes, A.J., Journal of Molecular Structure, 1984. **113**(MAR): p. 161-174.

34. Heidberg, J., Warskulat, M., and Folman, M., Journal of Electron Spectroscopy and Related Phenomena, 1990. **54**: p. 961-970.

35. *Surface Analysis - The Principal Tecniques*, ed. J.C. Vickerman. 1997: John Wiley & Sons.

36. Sugisaki, M., Suga, H., and Seki, S., Bulletin of the Chemical Society of Japan, 1968. **41**(11): p. 2586-&.

37. Stevenson, K.P., Kimmel, G.A., Dohnalek, Z., Smith, R.S., and Kay, B.D., Science, 1999. **283**(5407): p. 1505-1507.

38. Smith, R.S. and Kay, B.D., Nature, 1999. **398**(6730): p. 788-791.

39. Ayotte, P., Smith, R.S., Teeter, G., Dohnalek, Z., Kimmel, G.A., and Kay, B.D., Physical Review Letters, 2002. **88**(24).

40. Tielens, A., Hagen, W., and Greenberg, J.M., Journal of Physical Chemistry, 1983. **87**(21): p. 4220-4229.

41. Bolina, A.S., Wolff, A.J., and Brown, W.A., Journal of Physical Chemistry B, 2005. **109**: p. 16836-16845.

Chapter 8 Conclusions and Future Work

8.1 Conclusions

This thesis has described a study of pure, binary layered and codeposited alcohol and water ices on astrochemically relevant surfaces under low temperature, UHV conditions that mimic those found in the ISM. The behaviour of the ices has proved to be quite complex, and the results outlined in the previous chapters have illustrated a number of key features of interest to the astrochemical community.

The data reported has direct relevance to studies of desorption of interstellar ices in star forming regions, hot cores and in cometary objects. The codeposition studies have a direct relevance to astrochemical ices that form by a mixture of freeze out and surface catalysed formation reactions. The layered systems will also be relevant in areas where segregation has occurred and in regions where shocks lead to the sudden yet transient heating of grains which results in desorption followed by subsequent readsorption of the ices [1, 2].

Desorption from the surface is a non-equilibrium process and the temperature at which it occurs is influenced by both the heating rate and the thickness of the ice (for non-first order processes such as multilayer desorption). As a result it is not possible to use the temperatures recorded in our experiments directly in astrochemical models. Viti et al [3] have shown that a typical heating rate for a dust grain in a hot core is on the order of 1 K century^{-1}. In order to use these results in astrochemical models it is necessary to use the kinetic parameters derived from these experiments along with an appropriate heating rate to determine the desorption temperatures under astronomical conditions.

In their most fundamental application, the infrared studies have provided the first spectra of the small alcohols in a water rich environment on a graphitic surface. It is vital for observational astronomers to have suitable laboratory spectra for comparison and this study has provided a number of high quality spectra for varying compositions of methanol and water and also ethanol and water. In both cases the systems have been studied as sequentially deposited layers and as codeposited mixes. Spectra have also been provided following temperature processing of the ices.

A wide variety of ice thicknesses and compositions have been considered, not only to achieve astronomically relevant models but also to ensure a rigorous surface science study. It is only by considering a range of exposures in the determination of kinetic parameters that extrapolation to more extreme exposure ranges becomes feasible. The work presented in Chapters 3 and 4 on the TPD of methanol and water ices has questioned earlier categorisation of the behaviour of methanol within water rich ices. Previous work by Collings et al [4] placed methanol into a H_2O-like category as they recorded a multilayer and a monolayer feature in the layered system and a single peak coincident with water when desorption occurred from the mixed ice. The study by Collings et al [4] was restricted to one exposure range. This thesis has shown that the categorisation of methanol should be as an intermediate species as monolayer, multilayer and codesorption peaks are seen for methanol in the layered system.

Recently astrophysical modellers have begun to consider heating rates in their models of star forming regions and have incorporated experimentally determined kinetic data to model molecular abundances in hot core regions [3]. The new understanding of the behaviour of methanol described in this thesis has been used in such models and was found to be significant for the low mass stars [5]. The work has also indicated, by comparison with the studies by Collings et al [4], that the nature of the grain surface has little relevance to the study of physisorbed multilayers [5]. As the quantitative study in Chapter 3 highlighted, the kinetic parameters for methanol multilayers remain the same within error margins regardless of whether deposition occurs directly onto a graphitic surface or a water surface.

The most notable feature from this study is the observational evidence for trapping of both methanol and ethanol within the bulk of the water ice. Bulk trapping behaviour has been noted for both alcohols when either codeposited with water, or when deposited on top of a pre existing layer of water ice.

The ability of water to trap small impurity molecules has been well documented with a number of groups studying the trapping behaviour of water and its particular relevance to cometary ices [6-9]. The trapped feature is usually described as a clathrate-hydrate structure but as these generally form under high pressure conditions it is arguable that these will not form under interstellar conditions. Without further structural analysis it is impossible to say whether the retained complex observed in this study, is actually a clathrate hydrate or a structure such as an extended hydrogen bonded chain.

Future Work

An obvious extension to the work discussed in this thesis is to complete the TPD studies of the ethanol ices discussed in Chapter 7. These are currently in progress and will be published shortly.

All of the experiments discussed were performed at temperatures of ≈ 100 K. Although this temperature corresponds to that found in cometary and hot core regions, it would be desirable to repeat the investigations at temperatures approaching 10 K, typically associated with dust grains in dense clouds.

As the IR spectra of the ISM shown in *Figure 1.4* illustrates, typical interstellar ices are complex multi-component mixes. The studies presented in this thesis are of simple binary layered and mixed ices. It would therefore be an appropriate extension to consider tertiary mixtures as well. As has been shown throughout the RAIRS studies outlined in this thesis, species interact with each other when processed within mixed ices and it is vital to have suitable laboratory spectra to form comparisons with astronomical observational data.

Further work is planned to determine the effect of the underlying surface substrate. Initial comparisons between this study and that of Collings et al [4] performed on an amorphous gold surface, have already suggested that the surface is unimportant when considering the desorption behaviour of physisorbed multilayers [5]. This thesis has focussed on HOPG as the dust grain analogue surface but silicate surfaces would be an obvious extension as very little work has been completed on silicates.

8.2 Bibliography

1. Viti, S., Caselli, P., Hartquist, T.W., and Williams, D.A., Astronomy & Astrophysics, 2001. **370**: p. 1017.
2. Benedettini, M., Yates, J.A., Viti, S., and Codella, C., Monthly Notices of the Royal Astronomical Society, 2006. **370**(229).
3. Viti, S., Collings, M.P., Dever, J.W., McCoustra, M.R.S., and Williams, D.A., Monthly Notices of the Royal Astronomical Society, 2004. **354**(4): p. 1141-1145.
4. Collings, M.P., Anderson, M.A., Chen, R., Dever, J.W., Viti, S., Williams, D.A., and McCoustra, M.R.S., Monthly Notices of the Royal Astronomical Society, 2004. **354**(4): p. 1133-1140.

5. Brown, W.A., Viti, S., Wolff, A.J., and Bolina, A.S., Faraday Discussions, 2006. **133**: p. 113.

6. Barnun, A., Dror, J., Kochavi, E., and Laufer, D., Physical Review B, 1987. **35**(5): p. 2427-2435.

7. Barnun, A., Dror, J., Kochavi, E., Laufer, D., Kovetz, D., and Owen, T., Origins of Life and Evolution of the Biosphere, 1986. **16**(3-4): p. 220-220.

8. Barnun, A., Kleinfeld, I., and Kochavi, E., Physical Review B, 1988. **38**(11): p. 7749-7754.

9. Barnun, A. and Laufer, D., Icarus, 2003. **161**(1): p. 157-163.